IN TWO SECTIONS—SECTION ONE

Transactions of the ASME

A Clearanceometer for Determining Blade-Tip Clearances of Axial-Flow Compressors . . . . . *A. W. Brunot and R. O. Fulton* 1

Fast Thermocouples as Control-System Elements Sensing Exhaust-Gas Temperatures in Aircraft Gas Turbines . . . . . *J. S. Alford and C. R. Heising* 7

A Study of Burner Oscillations of the Organ-Pipe Type . . . . . *A. A. Putnam and W. R. Dennis* 15

An Energy Basis for Comparison of Performance of Combustion Chambers. . . . . *J. B. Nichols* 29

Comparative Performance of Coals of Different Rank in a Film-Cooled Gas-Turbine Combustor . . . . *T. E. Warren, H. P. Hudson, J. D. Robertson, and J. C. Mulligan* 35

A Nondimensional Correlation of Flame Propagation at Subatmospheric Pressures. . . . . *R. E. Cullen* 43

NACA Sonic-Flow-Orifice Temperature Probe in High-Gas-Temperature Measurement . . . . . *P. L. Blackshear, Jr.* 51

Use of the Centrifugal Governor Mechanism as a Torsional Vibration Absorber. . . . . *O. A. Pringle* 59

Axial Tension and Bending Interaction Curves for Members Loaded Inelastically. . . . . *D. O. Brush and O. M. Sidebottom* 63

Distribution of Mechanical and Thermal Stresses in Multilayer Cylinders. *R. A. Strub* 73

The Stresses in a Pressure Vessel With a Hemispherical Head. . . . . *G. W. Watts and H. A. Lang* 83

Flame Velocities in Carbon Monoxide-Oxygen Mixtures. *T. W. Price and J. H. Potter* 91

Operating Experiences With Mechanical Joints in High-Pressure High-Temperature Steam Piping . . . . . *E. C. Bailey, H. C. Schroeder, and I. H. Carlson* 97

Relative Abrasiveness of the Cast Surfaces of Various Gray-Iron Castings on Single-Point Tools of High-Speed Steel . . . . . *Joseph Datsko and O. W. Boston* 103

The Significance of the Thermal Number in Metal Machining. . . . . *B. T. Chao and K. J. Trigger* 109

TRANSACTIONS OF THE AMERICAN SOCIETY OF MECHANICAL ENGINEERS

VOLUME 75 JANUARY 1953 NUMBER 1

Transactions

of The American Society of Mechanical Engineers

Published on the tenth of every month, except March, June, September, and December

OFFICERS OF THE SOCIETY:

FREDERICK S. BLACKALL, JR., *President*

JOSEPH L. KOPP, *Treasurer* — C. E. DAVIES, *Secretary*
EDGAR J. KATES, *Ass't Treasurer*

COMMITTEE ON PUBLICATIONS:

GEORGE R. RICH, *Chairman*

PAUL T. NORTON, JR. — COLIN CARMICHAEL
OTTO DE LORENZI — W. E. REASER

MORRIS GERR, JOSEPH SCHMERLER } *Junior Advisory Members*

GEORGE A. STETSON, *Editor* — K. W. CLENDINNING, *Managing Editor*

REGIONAL ADVISORY BOARD OF THE PUBLICATIONS COMMITTEE:

KERR ATKINSON—I
JOHN DE S. COUTINHO—II
WILLIAM N. RICHARDS—III
FRANCIS C. SMITH—IV
HENDLEY BLACKMON—V
CHESTER R. EARLE—VI
RAYMOND G. ROSHONG—VII
VENTON L. DOUGHTIE—VIII

Published monthly by The American Society of Mechanical Engineers. Publication office at 20th and Northampton Streets, Easton, Pa. The editorial department is located at the headquarters of the Society, 29 West Thirty-Ninth Street, New York 18, N. Y. Cable address, "Dynamic," New York. Price $1.50 a copy, $12.00 a year for Transactions and the *Journal of Applied Mechanics* to members and affiliates, $1.00 a copy, $6.00 a year. Changes of address must be received at Society headquarters four weeks before they are to be effective on the mailing list. Please send old as well as new address.... By-Law: The Society shall not be responsible for statements or opinions advanced in papers or ... printed in its publications (B13, Par. 4).... Entered as second-class matter March 2, 1928, at the Post Office at Easton, Pa., under the Act of August 24, 1912....

Copyrighted, 1953, by The American Society of Mechanical Engineers. Reprints from this publication may be made on condition that full credit be given the Transactions of the ASME and the author, and that date of publication be stated.

A Clearanceometer for Determining Blade-Tip Clearances of Axial-Flow Compressors

By A. W. BRUNOT[1] and R. O. FULTON,[2] WEST LYNN, MASS.

This paper covers the design and use of an instrument for determining blade-tip clearances of axial-flow compressors. The development of the measuring head and control circuits for operating the probe-type head and the results obtained from the use of this instrument are covered with illustrations and graphs which show clearances in axial-flow compressors under various operating conditions.

THE efficiency of axial-flow compressors and gas or steam turbines is related to the radial clearance between the rotating and stationary parts. This is true both of the clearance between the stator blades and the rotor, and clearance between the rotor blades and the casing of an axial-flow compressor, which has been the principal application of this instrument.

Several different methods have been used in the past to determine the radial clearance between rotating blades and a stationary casing. The manually operated mechanical probe and a lead plug are two methods which have proved useful but have drawbacks which are obvious. Some other methods involving magnetic gages, light beams, sonic reflection, and even x-rays have been proposed, but have not yet been made into a practical gage.

The lead gage is limited to low temperatures and has the added disadvantage that the unit must be shut down to remove the gage for measurement in order to obtain the desired answer. Also, the lead gage would give only the minimum clearance encountered in the interval between insertion and removal. The variation of clearance with time and operating conditions of the machine cannot be determined with this single reading. The mechanical probe again has the disadvantage of being applicable at relatively low temperatures and slow speeds since the operator is required to be alongside the machine to make the reading.

Modern steam and gas turbines and axial-flow compressors operate at high speeds and temperatures and, in many cases, are tested in well-protected test cells from which the test personnel are barred while the unit is under operation. This means that the clearance cannot be measured directly by the tester but some remote indicating instrument must be used if information on the clearance as a function of operating conditions is to be made available to the engineers for analysis. This information, with the performance data, may provide the basis for improved design so that the efficiency of the machine may be increased.

Development of Mechanical Head

After studying several possible systems, the mechanical probe was decided upon as the most practical to use. The system desired was one which could be operated remotely and read remotely. The necessary parts of this system were a probe, a means for driving the probe in and out, a sensing system to indicate contact and stop the probe, a fixed reference point, and finally a simple control system.

After deciding to use a mechanical probe, a material for the probe had to be chosen. The material desired was one which would not cause any nicking of blades in the compressor. Several materials were suggested but, over-all, nickel seemed to have the best properties for this application. Nickel possesses the properties of a good rubbing material and is soft in the annealed state. The next consideration was the system for driving the probe. A reversible synchronous motor was chosen for the drive since this would allow time to be used as a base for indicating the distance the probe traveled. A rate of travel for the probe was of primary importance because if the probe fed too fast there would be too much shock on the probe at contact with the blades, and if too slow the measuring time would be unreasonable. Considering that blade tips passing at the rate of 7000 per sec and 0.9 of the periphery is space, there is a very good chance of feeding down in between blades if the probe were fed too fast. Runout and high blades also were considered as factors limiting the feed rate. A rate of 0.250 ipm was decided upon as a reasonable rate although at times this seems extremely slow.

The method used to drive the probe was a lead screw which was operated by a geared-down shaded-pole reversible synchronous motor. The probe was insulated from the lead screw to permit it to be used as a sensing element to determine contact.

To this point we have a mechanical probe of nickel driven by a reversible synchronous motor through a lead screw at the rate of 0.250 ipm. This is simply a motor-driven micrometer, and, as a micrometer is not much good without an anvil or reference plane, a reference was established on the clearanceometer to make it useful as a measuring device. The reference point took the form of a movable flag which could be operated by means of a solenoid through mechanical linkages to cover or uncover the probe opening as desired. This flag acts much like an anvil on a micrometer giving an automatic zero every time the probe is used. This also compensates for any wear which may take place on the tip of the probe.

Several variations of the measuring head have been made with many changes possible to adapt this head to several measuring problems. Two major designs have been made which are shown in Figs. 1 and 2, each with many possible variations in the adapters to take care of mounting problems which might be encountered. Tests have been run with the head operating at —65 F in a cold chamber and, with a 15-watt heater installed in the vicinity of the motor gear box, the unit operated satisfactorily with the proper low-temperature lubricant. This latter condition was imposed by high-altitude testing and cold-cell testing of compressors.

Development of Control Circuits

With the mechanical head decided upon, the next objective was to control it with an electrical circuit which would operate remotely and simply. The possible cycles were analyzed and the

[1] Mechanical Section Head, Thomson Laboratory, General Electric Company. Mem. ASME.

[2] Thomson Laboratory, General Electric Company.

Contributed by the Aviation, Industrial Instruments and Regulators, and Gas Turbine Power Divisions and presented at the Semi-Annual Meeting, Cincinnati, Ohio, June 15-19, 1952, of The American Society of Mechanical Engineers.

Note: Statements and opinions advanced in papers are to be understood as individual expressions of their authors and not those of the Society. Manuscript received at ASME Headquarters, March 11, 1952. Paper No. 52—SA-16.

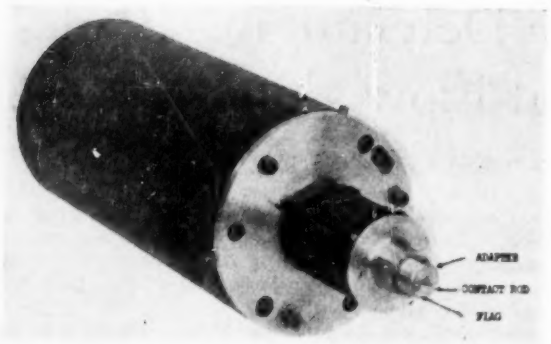

FIG. 1 CLEARANCEOMETER MEASURING HEAD SHOWING ADAPTER, PROBE, AND FLAG

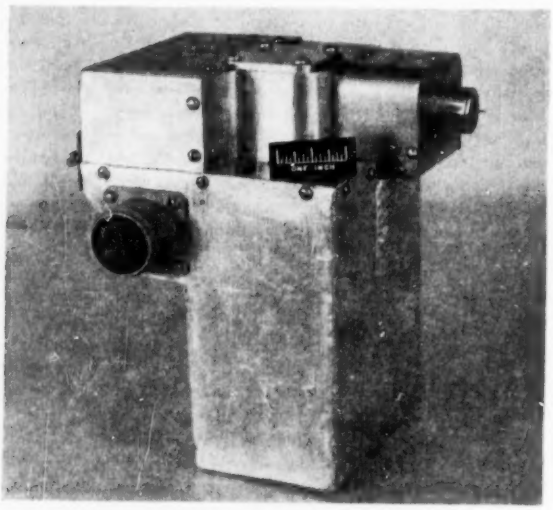

FIG. 2 RIGHT-ANGLE DRIVE CLEARANCEOMETER MEASURING HEAD

cycle decided upon to be used first followed this sequence of events:

1 Probe fed in.
2 Contact indicated.
3 Probe retracted.
4 Measuring counter started to add.
5 Probe reversed again.
6 Flag dropped in front of probe.
7 Measuring counter reversed to subtract.
8 Cycle completed when probe contacts flag.

This cycle required a two-direction indicating device for indicating probe travel. The indicator originally used was a clock with the hour hand removed and the second hand geared to a reversible synchronous motor to indicate 0.001 in. for each second graduation on the clock face. This was replaced by a counter at a later date for convenience in reading.

A second cycle, presently used, was adopted for several reasons, the principal one of which was the desire to set a given clearance to determine a safe minimum without operating the complete cycle. This cycle is substantially the same as the first one except the measuring cycle starts from the final position of the first cycle, that is, at the flag; and the measurement is taken to

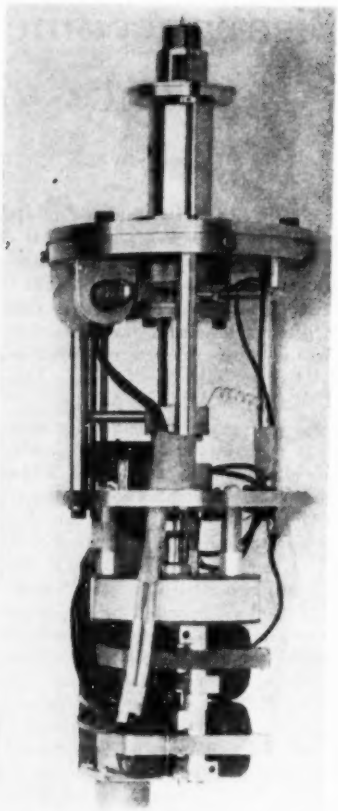

FIG. 3 CONSTRUCTION DETAILS OF MEASURING HEAD SHOWN IN FIG. 1

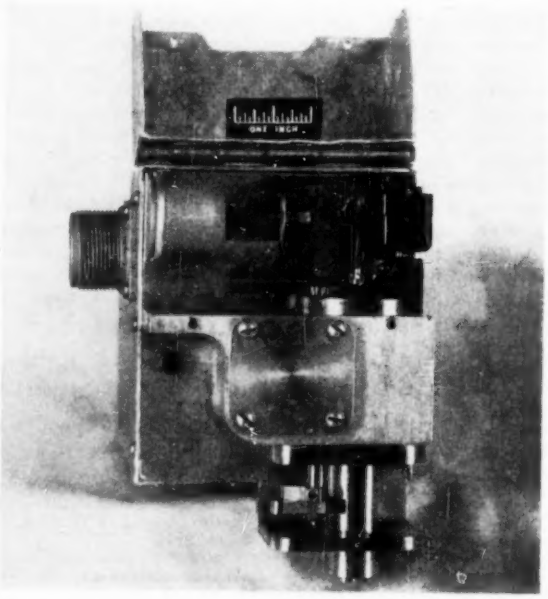

FIG. 4 CONSTRUCTION DETAILS OF MEASURING HEAD SHOWN IN FIG. 2

the contact point. This eliminates the need for a reversible counter as the measurement from the flag to contact is the desired measurement.

Although the two cycles are similar, an extra relay is necessary in the control circuit for the second cycle.

The basic cycle remains the same for the two systems used and it is controlled by an electronic circuit which employs five integrated circuits. These are as follows:

1 The d-c power supply.
2 The probe drive.
3 The sensing circuit.
4 The indicating circuit.
5 The flag-control circuit.

The d-c power supply is used to energize a d-c relay which controls the direction of the probe motor. It is also used as energizing voltage for a thyratron tube which is the heart of the sensing circuit. The thyratron tube is a tube capable of acting as an electronic switch. By maintaining a voltage from cathode to the plate, current flow can be controlled by the bias voltage. This effect is used for a very sensitive sensing device as the bias voltage is impressed on the probe which, when grounded, momentarily decreases the bias voltage of the thyratron, allowing the tube to fire or conduct. After the thyratron fires, it remains conducting until the plate circuit is interrupted when it again becomes nonconducting if the bias voltage returns its original value.

The current which energizes the relay controlling the probe motor must pass through the thyratron tube. This occurs only when the tube has fired. When the thyratron is conducting after the probe makes contact with the grounded rotor, the relay is energized which reverses the probe motor and the probe is withdrawn. To cause the motor to feed the probe forward again, the thyratron plate circuit must be opened to interrupt the current through the probe-motor relay. This is accomplished by a microswitch located in the mechanical head. This switch is opened by the retracting probe thus allowing the relay to return to its starting position, energizing the probe motor to drive it forward.

The circuit controlling the counter motor and the flag can best be followed by examining the wiring diagram shown in Fig. 5.

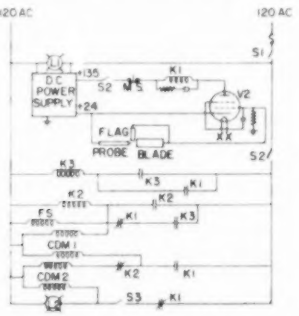

Fig. 5 Schematic Diagram of Control Circuit

The measuring head, Figs. 1 or 2, is connected to the control box Figs. 6, 7, and 8, by an eight-lead cable and 120-volt a-c power is supplied to the control box. The control unit is energized by closing switch S1. After the d-c power supply has had time to warm up, the unit is ready for operation.

When the measuring cycle is to begin, switches S2 and S3 are closed. At this position all three relays are de-energized and the forward field of the probe motor CDM2 is energized causing the probe to feed into the rotating blades until contact is made. This contact reduces the bias voltage on the grid of the thyratron tube V2, causing it to fire. This action causes the relay K1 to energize, which simultaneously reverses the probe motor CDM2

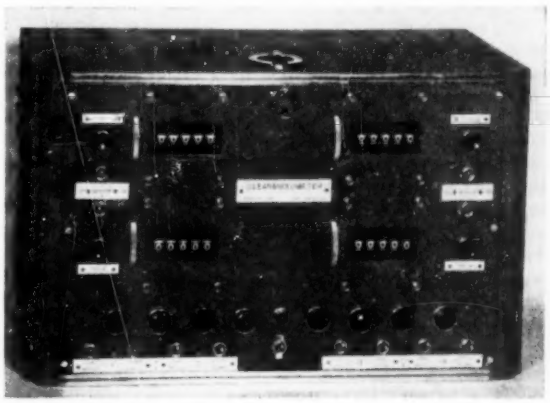

Fig. 6 Control Box Used to Control Four Measuring Heads Simultaneously

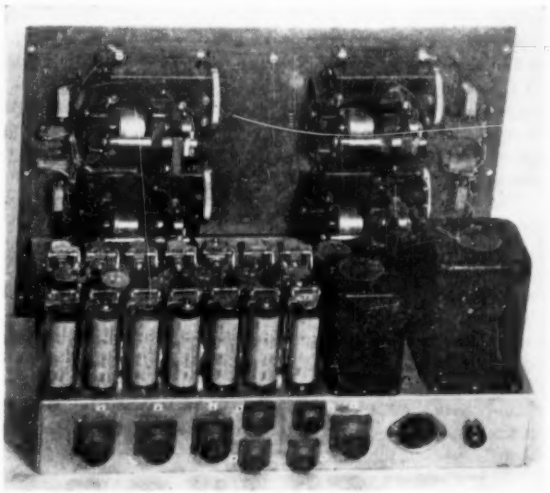

Fig. 7 Rear View of Control Box

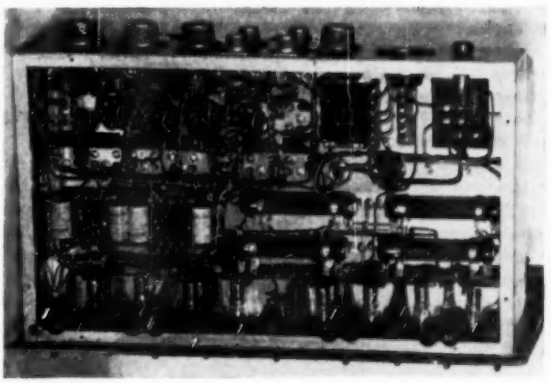

Fig. 8 Bottom View of Control Box

withdrawing the probe, starts counter motor CDM1 which causes a positive reading on the counter, and energizes relay K3 which is locked in by a contact on K3. This will allow relay K2 to be energized when relay K1 is de-energized.

The probe continues to retract and the counter to advance until the microswitch MS, which is installed in the measuring head, is opened by the retracting probe. This simultaneously opens the thyratron circuit and de-energizes K1, which energizes K2, thus opening the reverse field of CDM2, energizes the forward field of CDM2 starting the probe inward again, energizes the flag solenoid, FS, which places the flag across the probe path, and reverses the counter motor CDM1 which causes the counter to subtract. These motions continue until the probe contacts the flag which again fires the thyratron energizing K1 causing the forward probe motor CDM2 to stop and causing the counter motor CDM1 to brake by energizing the two opposing fields. This completes the cycle and the unit remains stopped until switch S2 is opened and closed again to start the measuring cycle. When the cycle has been completed the counter motor shows the distance from the contact point to the plane of the flag, as the distance the probe traveled past the flag in the reverse direction was subtracted from the total travel in the reverse direction from the point of contact with the rotor blade.

To determine the clearance between the rotating blades and the casing one more dimension must be known, that is, the distance from the face of the flag to the inside surface of the casing. This is determined by using two known dimensions, (*a*) the thickness of the casing at the mounting position, and (*b*) the instrument constant which is the distance from the shoulder on the adapter to the face of the flag. The constant used to determine clearances is found by subtracting the instrument constant from the casing thickness.

There are several variations of this circuit which have been made to accomplish other cycles of operation. One, previously mentioned, incorporates a fourth relay to control the counter motor and changes the cycle to permit the reading of the probe travel from the flag to the blade instead of the method described. Another variation is the use of a third switch to stop the probe at any predetermined clearance setting. In addition, a system which would allow a checking device to give an over-all test of the circuit without the necessity of feeding the probe into a rotating blade was desired. This was accomplished by a shorting switch in the sensing circuit to simulate the contact of the probe and blade.

There is one more change in the cycle which has been suggested which would allow this instrument to approach the type of measurements desired. This is a system for oscillating the probe to take a reading and back off a known distance and recontact the blades in a succession of readings to get several points close together. Although this would cause some inaccuracies to occur, experience has shown that a single contact of the probe only removes a very small quantity of material from the probe tip so that a series of 10 to 20 contacts could be made before returning to the reference flag without appreciable loss of accuracy.

Methods of Use

The principal use to which the clearancemeter has been put is the measuring of operating clearances of blade tips in axial-flow compressors. To use either type of clearancemeter a special mounting hole must be made in the location where the measurement is desired. As mentioned previously, this mounting adapter may be changed in many ways to suit given conditions. However, the two types which have found acceptance for the testing which has been performed are shown in Figs. 1 and 2. Fig. 1 shows a threaded adapter with a $^{3}/_{4}$-in. 16 thread, and Fig. 2 shows adapter of a flange type which must have a flat section with an $^{11}/_{16}$-in. hole to pass through the casing. The lengths of the projections have been specially chosen for the compressor casings used.

The change of clearance on axial-flow compressors is caused by temperature changes, centrifugal effects, and pressure. The instrument described will measure clearances with an accuracy of ± 0.001 in. at the location chosen for study. There is no assurance that this is the absolute minimum clearance since there may be variations around the periphery due to local changes in casing deformation.

The clearances, measured under stabilized conditions, of an axial-flow compressor in the 2nd, 6th, and 11th stages are shown in Fig. 9. An increase in clearance as the speed increases is shown in the latter stage. This is not necessarily true in all compressors. Another compressor shows a reduction of clearance

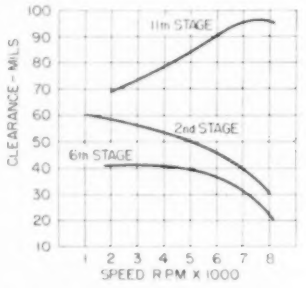

Fig. 9 Graph Showing Tip Clearances of an Axial-Flow Compressor During Operation Under Steady-State Conditions

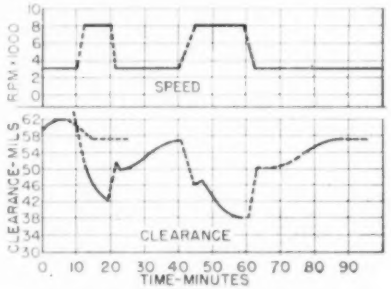

Fig. 10 Graph Showing Effect of Rapid Speed Changes on Clearances

in the 11th stage with the increase of speed as shown in Fig. 10. This is more nearly the ideal condition as higher speeds of a compressor cause higher pressures and less loss in efficiency will occur with lower clearances on the latter stages.

An interesting use of the clearancemeter is to make a clearance versus time run with speed changes made after equilibrium has been reached. Fig. 10 shows such a curve determined by operating the compressor at idle speed until equilibrium and then rapidly accelerating to top speed, taking clearance readings at intervals; then after reaching equilibrium, reducing speed to idle and taking another series of clearance readings. This type of test will show the effect of centrifugal force, temperature effects on the stator and rotor, and effect of pressure changes. Fig. 11 shows a similar curve on a different compressor.

The greatest effects seem to be due to temperature on compressors which have been tested. This effect is clear in Fig. 11 where clearance and temperature curves have the same shape and is shown more clearly in Fig. 12, which shows a plot of temperature of the casing versus clearance between the blade tip and casing.

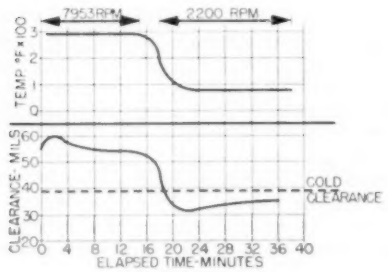

FIG. 11 GRAPH SHOWING EFFECT OF RAPID DECELERATION ON TIP CLEARANCES

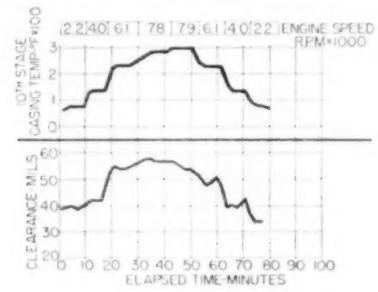

FIG. 12 GRAPH SHOWING CASING TEMPERATURE AND TIP CLEARANCES VERSUS TIME AND SPEED

As in most instruments, there are limitations and precautions in their use and this instrument is no exception. Some of the precautions in the use of this instrument are obvious and others have been acquired through experience. The time of reading is one factor which should be taken into consideration when installing this instrument. As the travel is only 0.250 ipm, the closer the starting position of the probe is to the blade tips the shorter the time cycle of measurement. The flag is the limiting factor in setting this distance as it is approximately $^1/_{16}$ in. thick; thus the minimum travel which could be established is this $^1/_{16}$ in. plus the clearance of the blade tips. As the probe must travel in and out this $^1/_{16}$ in. plus clearance, the minimum reading time can be computed. The instrument constant must be known within the accuracy of measurement desired and the installation constant must be determined before the readings are of any value. The determination of these constants was discussed previously.

Another consideration which should be noted is that the mounting of the instrument should not bind the adapter in any manner as this may cause the flag to bind and give false readings or cause damage to the instrument.

RESULTS FROM USE OF THIS INSTRUMENT

The determination of operating clearances has enabled the design engineer to control the compressor clearances accurately by controlling factors which affect the clearances of an axial-flow compressor. Thus more efficient axial-flow compressors can be made by reducing the tip clearances under all operating conditions and still maintain some clearance to avoid rubbing.

The advantage of knowing the clearance of any axial-flow compressor under all conditions of operation is not yet a reality because the instrument in its present form is not readily adapted to flight testing owing to the power requirements and the auxiliary equipment required to operate the instrument.

This disadvantage of weight and power for flight-test information will be overcome in the future by a simpler system for measuring clearances. However, for accuracy and simplicity in test-cell operation this instrument does the work required, and the data which have been accumulated in numerous tests have proved the value of such an instrument.

Discussion

B. R. ANDERSON.[3] It is important that rotor-blade tip clearances can be measured so that the compressor may be operated at minimum clearance insuring maximum efficiency without the possibility of rubbing. The clearancecometer described in this paper has measured these clearances satisfactorily and has proved itself in giving important and useful information to design engineers.

This instrument has several advantages over other systems. The simplicity of both the mechanical head and control circuit makes it a practical instrument to use. This is an important feature when it is necessary for nontechnical personnel to operate and service the instrument. The simplicity of the unit likewise leads to a rugged and durable instrument. Because of this the mechanical head can easily withstand the vibration and other severe operating conditions. The accuracy of the readings is excellent, giving errors of only ±0.001 in. However, as the authors point out, reference measurements first must be made between the reference flag and blade tip. Then, since the control circuit contains no amplifiers, no calibration is necessary. Only the speed of the probe need be known, and this is always constant.

As for disadvantages, the first is the seemingly long time one must wait for readings. This is due to the fact that the probe travel is only $^1/_4$ in. per min. Therefore, if the tip clearance is, say, 0.1 in., the total time between readings is at least

$$2/1/4 \times (\text{tip clearance} + \text{flag thickness}) = 8\ (0.1 + 0.062) = 1^1/_8 \text{ min.}$$

This assumes that the inside face of the flag is exactly flush with the inside surface of the compressor casing and that the flag is dropped immediately in front of the probe when the probe is retracted far enough. This long length of time may not necessarily be a disadvantage if the changes in clearance are slow. This is not usually the case though if an engine is started cold and immediately brought up to full speed. Therefore the best application for this type clearancecometer would be for measuring clearances under stabilized conditions, or clearance versus time measurements when the time involved is 10 min. or greater. Another disadvantage is that the instrument cannot measure turbine-bucket clearances because of the high gas temperatures.

The clearancecometer is a useful and practical instrument. Any other instrument which could be built to give continuous indications or more accurate readings probably would be so complicated in design and costly to build as well as difficult to use and maintain, that its general usefulness would not be as great as the probe-type clearancecometer.

S. M. COHEN.[4] Although the paper presents the clearancecometer as used to measure the tip clearance of axial flow compressors, its application can be more widespread than this one function. However, used as presented, the device is of great value to the design and development of the gas-turbine engine by providing a means of obtaining accurate information from an engine under actual operating conditions.

The authors not only state their understanding of the appli-

[3] Electro-Mechanical Unit, Lockland Plant Laboratory, Aircraft Gas Turbine Division, Cincinnati, Ohio.

[4] Curtiss-Wright Corporation, Wright Aeronautical Division, Wood-Ridge, N. J.

cation of the clearancometer, but offer modifications in design that will improve the over-all utility of the instrument. Their suggestion that a revision in the control circuit be made to make possible a greater number of readings per unit of time by cycling the movement of the probe from a known secondary position would eliminate the disadvantage of the probe speed. This also would allow the mechanical head to be mounted further from the position of actual measurement. Direct readings may not be possible with an oscillating probe, but oscillographs or similar recorders could be used to measure more transient conditions of engine operation than are now possible.

If minimum clearance or casing distortions are to be investigated, the clearancometer is unwieldy by nature of its fixed position. Of course, several heads mounted in the same lateral plane could be used to indicate the amount and location of minimum clearance, the distortion of the mounting shell, and the concentricity of the rotor.

This paper demonstrates effectively that temperature and rotor speed are the prime factors in changes in compressor-tip clearances. Since these effects are equally important in the turbines that drive the compressors, an investigation of turbine clearances would yield valuable information. Here the factors of circumferential temperature distribution and, perhaps, cooling air flow with the resulting shroud or housing distortions are introduced that need evaluation at all operating conditions of the engine. If turbine temperatures are too severe for the mechanical and electrical mechanisms of the measuring head, cooling modifications could be made to accommodate the requirements of turbine clearance measurements. Another interesting possibility mentioned for use of this clearance-measuring device is the application to a flight test engine. Investigation made under flight maneuvers with an oscillating probe would be of unquestionable value. The clearancometer is a cleverly conceived and developed electromechanical instrument that accomplishes valuable measurements not before readily obtained. The possibilities in its future development will mean an increase in the scope of information available for analysis.

Authors' Closure

We would like to thank Messers. Anderson and Cohen for their interest in commenting on this paper.

The disadvantage of time of reading as pointed out by Mr. Anderson is not as critical as might be supposed for gas-turbine compressors. The curves in Fig. 11 indicate that there is a period of approximately 5 min in which the clearance is changing from maximum to minimum for a rapid shutdown which would give the maximum change in clearances. By having the flag of the clearancometer mounted flush with the inside of the casing, clearance readings up to 0.060 in. may be taken in 1 min, giving a possibility of taking five readings over the entire time of change. With such slow changes taking place it is only necessary to mount the clearancometer properly to achieve the desired results.

The desirability of measuring turbine-bucket tip clearances has been considered in the design of the instrument and provisions have been made for air cooling the adapter. In the only attempt known to the authors to use this instrument for measuring turbine clearances, the probe was extended too far and no cooling air was used which resulted in a jam, caused either by the hot gases or contact with the bucket, and the probe was bent so that it could not be withdrawn. Further attempts will be made to obtain this measurement with this clearancometer by the application of improved techniques.

As pointed out by Mr. Cohen, the determination of the minimum clearance point is difficult. To scan the clearance properly it would be necessary to have the gage rotate with the wheel. Since no gage has been proposed which will do this, it is necessary, at least for the present, to measure as many points around the circumference as possible. From these readings the minimum clearance may be estimated which is much better than no measurement at all. The problems encountered in flight-testing measurements with this clearancometer have not been solved satisfactorily. The power supply on planes is not satisfactory for the present design. Also, the psychological effect on the pilots of a probe moving in on blades has to be overcome. A new principle is now being investigated for flight-test use which will overcome these objections.

The possibility of using the oscillating probe has not been attempted as yet, but if it is used, it will only be necessary to record the maximum reading of the counter for each oscillation as it would be synchronized with the motion of the probe until the probe was brought back to the reference.

Fast Thermocouples as Control-System Elements Sensing Exhaust-Gas Temperatures in Aircraft Gas Turbines

By J. S. ALFORD[1] AND C. R. HEISING,[2] LOCKLAND, OHIO

Factors which favor the use of thermocouples as control-system elements sensing exhaust-gas temperatures in aviation gas turbines are presented, as well as the development of a construction having adequate strength to withstand vibration. The authors give analytical and experimental determinations of the time constant of thermocouples and present a mathematical analysis of the effect on time constant of conduction along the thermocouple wire to the support. The paper also includes a discussion of the recovery factors of thermocouples and an evaluation of the error introduced when a number of thermocouples that read different temperatures are connected in parallel.

Introduction

THE thrust of turbojet engines has been increased substantially by burning additional fuel in an afterburner. The greatest thrust is produced when the turbine inlet or firing temperature is maintained at the maximum specified value for all operating conditions. To accomplish this requires increasing the jet-nozzle area more or less proportionally to the fuel burned in the afterburner. The balance between these two factors is maintained by a control system which senses the temperature of the gases discharged from the turbine. In order to prevent large overtemperature surges during the transient operation, the thermocouples must respond quickly to a change in exhaust-gas temperature. By improving the stability of the entire system, fast response reduces the possibility of hunting and overheating of the engine. The magnitude of the transients imposed on the cycle and control is indicated by the fact that volume flow of hot gas flow is doubled by maximum afterburning, and that the jet-nozzle area must be increased by nearly 50 per cent to pass this increased volume flow.

Even during normal or unaugmented operation there are problems which are partially or entirely solved by a control which adjusts jet-nozzle area or engine speed so as automatically to limit the maximum exhaust-gas temperature. Among these problems are the following:

1 At a fixed speed, the turbine-inlet temperature tends to change with ambient temperature.

2 The flow coefficient of some jet nozzles increases with increased pressure ratio across the jet nozzle. Higher flight speeds increase the jet-nozzle pressure ratio and therefore the effective flow area of the nozzle. Adjustment of jet-nozzle flow area or speed is necessary to maintain the exhaust-gas temperature constant.

3 When operating conditions are such as to cause deterioration of the jet-engine components, an increase in jet-nozzle area is required to keep exhaust-gas temperatures within specified limits at maximum engine speed.

4 Higher peak temperatures for short durations make available higher acceleration torques, provided compressor and other components have sufficient operating margins. However, there is a hazard to buckets and other parts exposed to the hot gas if excessive temperatures persist too long. Experience and testing usually determine the permissible values.

Reasons for Choice of Thermocouples as Control-System Elements Sensing Exhaust-Gas Temperature

The principal advantages of thermocouples for measuring the exhaust-gas temperature of aircraft gas turbines are as follows:

1 The construction is relatively rugged and is able to withstand the vibrations to which the thermocouples are subjected.

2 The bare thermocouple wires can be exposed in the hot exhaust gases. This reduces the time constant for changes in gas temperature.

3 A relatively high degree of accuracy can be maintained with appropriate amplifying equipment, and there is but little change of calibration.

4 When the average gas temperature is desired, a number of thermocouples may be connected in parallel to provide an average reading with small error. An open-circuit failure of one thermocouple causes little or no error in temperature measurement.

5 In field service, thermocouples can be replaced readily if a change is necessary.

6 The cost is moderate.

Recent developments in methods of converting and amplifying small d-c voltages have gone a long way to remove an early difficulty of using thermocouples in control circuits. Electromagnetic and electronic devices having no moving parts and utilizing voltage or current references as standards have been applied successfully to the amplification of the small error voltage obtained from balancing the thermocouple electromotive force (emf) against the standard.

Description of Thermocouple

Chromel and alumel have been favored because their characteristics are good in the temperature range of exhaust gases. The relatively large electromotive force developed by this combination is of course desirable. Chromel and alumel are relatively stable up to 1800 F and even a little higher for short periods. The thermocouples are installed in the exhaust cone or tail pipe upstream of any injection of fuel into the exhaust system to augment the thrust by afterburning. Consequently, the thermocouples are not exposed to the afterburner-exit blasts which may approach 3500 F.

[1] Design Engineer, General Electric Company.

[2] Design Engineer, General Electric Company. Jun. ASME.

Contributed by the Aviation, Industrial Instruments and Regulators, and Gas Turbine Power Divisions and presented at the Semi-Annual Meeting, Cincinnati, Ohio, June 15–19, 1952, of THE AMERICAN SOCIETY OF MECHANICAL ENGINEERS.

NOTE: Statements and opinions advanced in papers are to be understood as individual expressions of their authors and not those of the Society. Manuscript received at ASME Headquarters, April 14, 1952. Paper No. 52—SA-35.

In the vicinity of the hot junction the round thermocouple wire is flattened so that in the cross section the width is approximately twice the thickness. The loop is formed so that the long dimension is parallel to the axis of the loop. The plane of the loop is located perpendicular to the direction of the gas stream, which places the narrow dimension of the wire perpendicular to the gas stream.

The advantages of the loop-junction construction are as follows:

1 The response rate is improved, primarily because the flattened wire has greater surface heat-transfer area per unit of wire mass. The exposed or naked wires have no entwining mating wire to reduce the gas velocity over the surface.

2 The aerodynamic drag is reduced because of the improved streamline form of the flattened section. There is also a reduction of frontal area, because of the flattening. The aerodynamic force on a round wire is mostly form drag which is parasitic in nature, contributing little to the heat-transfer process.

3 Improved mechanical construction is provided by the loop construction. The increase in wire width in the direction of the principal aerodynamic forces increases the rigidity and reduces the bending stresses in the wire. An additional benefit is that the natural frequency is raised. If the comparison of mechanical strength is made on the basis of equal time constants, the loop construction can be made of heavier wire, and this contributes toward increased mechanical strength.

4 A superior junction weld is produced by the butt-welding possible with the loop construction.

5 There is reduced working of the wires in fabrication. This avoids the large strains and stresses caused by tightly twisting wires together.

Fig. 1 shows a thermocouple having the loop-junction construction. Fig. 2 shows a typical installation of a section of the exhaust pipe. There are 14 thermocouples in all. Seven equispaced thermocouples are connected to the bus bars enclosed in one of the circular rings, and are connected as temperature sensors in the control circuit. The other seven equispaced thermocouples are connected to the bus bars in the other circular ring, which in turn is connected to the temperature indicators.

Fig. 1 Thermocouple of Loop-Junction Construction

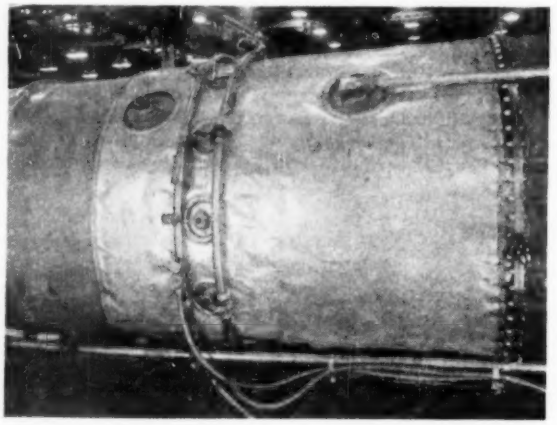

Fig. 2 Typical Installation of Section of Exhaust Pipe

Forced Vibration of Thermocouples

A major problem was that of obtaining adequate endurance from the thermocouples when mounted in the tailcone of the turbojet. An early design of thermocouple was found to give satisfactory endurance when mounted in the tail pipe close to the jet nozzle. However, mounting the thermocouple in the tailcone was found to reduce the life substantially.

The first type of thermocouple applied to gas turbines used conventional two-hole insulators to separate the wires from each other and from the supporting metallic sheath. When installed in the tailcone of turbojets of increased rating, the vibration was frequently so severe that the insulation severely chafed the wires, resulting more or less in the complete abrading away of wires in a relatively short while. An appreciation of the importance of avoiding relative motion between the wires, insulation and support tubes led to the development of a construction using magnesium oxide as a filler which is swaged to form a strong bond between wires, insulation, and outer tube.

An experimental investigation of the vibration of the thermocouple mounting bosses on the tailcone disclosed vibrations at a high frequency. The resulting accelerations were in the hundreds of g. The accelerations resulting from vibrations were found to decrease with increased distance from the turbine. However, when afterburning is used to augment the thrust, the thermocouples are located upstream of the burning in the afterburner, which places the thermocouples only about 15 in. downstream from the turbine. Therefore other solutions to the vibration problem had to be found than merely locating the thermocouples far downstream.

Methods were developed of reproducing in the laboratory the types of vibration which occur in the tailcone during engine operation. Measurements under these conditions showed a large number of resonances in the tailcone structure such that all surfaces are highly active at one frequency or another. Since a wide band of frequencies is known to be present in the exciting forces of the gas stream, it appears that no part of the tailcone will remain inactive and hence there is no ideal location for placement of thermocouples or similar instrumentation.

Circular stiffening bands located close to the thermocouples have been found to be effective in reducing the vibration at the bosses where the thermocouples are mounted. Insulating blankets fitted snugly to the outer surfaces of tailcones were found to improve the life of some of the earlier and less robust types of thermocouples.

Rate of Response

Satisfactory exhaust-gas temperature sensing for aircraft gas-turbine control systems requires rapid rates of response. A series of actions often occur sequentially in a servomechanism or control system. This means that the time delays of those elements in series are added together. An example of this is one arrangement of controls for an electric actuator operating the variable-area jet nozzle. When fuel is introduced into the exhaust system for pur-

pose of thrust augmentation by afterburning, there is a large momentary rise in exhaust pressure when this fuel ignites. To keep the engine speed substantially constant requires a momentary large increase in fuel flow to the main engine combustion system. This of course produces a very rapid increase in exhaust-gas temperature. There is a time delay during which the temperature of the sensor is following the abrupt rise in exhaust-gas temperature. The more time delay here means more delay before the actuator moves the variable-area jet nozzle at a rate and to the extent which ideally would be required by the sudden change in exhaust-gas temperature. Adequate protection of the gas turbine of course requires that the cumulative time delays of temperature sensors plus other elements in the system be less than the time constant of the metal parts exposed to the hot gas streams. Decreasing time constants is fundamental to reducing the magnitude of overshoot transients.

Time delays may have an adverse effect upon the stability of servomechanism and amplifying systems. This problem may be particularly acute when the phase shift due to time delays makes amplifiers having feedback unstable for part of the frequency range of applied signal.

Exposing the thermocouple wires directly to the high-velocity gas stream has a very favorable effect in reducing the time constant. This of course is due to the relatively high surface heat-transfer coefficients when hot gases flow across the thermocouple wires. The design is made to take the best advantages of heat transfer.

The time constant τ is defined as the time required for the junction temperature to change $1 - (1/\epsilon) = 0.632$ of its final change when an instantaneous change in gas temperature occurs. Theoretical analysis for the time constant is given in Appendix 1. This derivation neglects any axial conduction effect, and assumes that the thermal properties are constant. The following equation shows the relationship of factors which define the time constant τ. Fig. 3 exhibits the manner in which the thermocouple temperature varies with time.

$$\tau = \frac{c\rho v}{hA} \qquad [1]$$

where

h = surface heat-transfer coefficient
A = surface area exposed to hot gas per unit length of wire
c = specific heat of wire
v = volume of metal per unit length of wire
ρ = density of wire

The accuracy to which the heat-transfer coefficient is known is the major factor influencing the accuracy of the calculated time constant. For a particular thermocouple, the heat-transfer coefficient is a function of the gas-weight velocity per cross-section area, as shown in Fig. 4. The time constant, in general, will vary inversely as the square root of the gas-weight velocity per cross-section area. This simple relationship can be used to extrapolate experimental data.

The effect of radial conduction in the thermocouple wires has been found to introduce an error of less than 0.5 per cent for a typical case. This result justifies ignoring this factor.

Fig. 5 shows a comparison of experimental and calculated time constants for a particular thermocouple over a range of gas-weight velocity. The graphical curve was calculated by the Schmidt method.[3]

Since the thermocouples are subjected to a large amount of vibration, there is a real possibility of fatigue failure of the thermocouple wire or disintegration of the surrounding packed in-

[3] "Heat Transmission," by W. H. McAdams, McGraw-Hill Book Company, Inc., New York, N. Y., 1933.

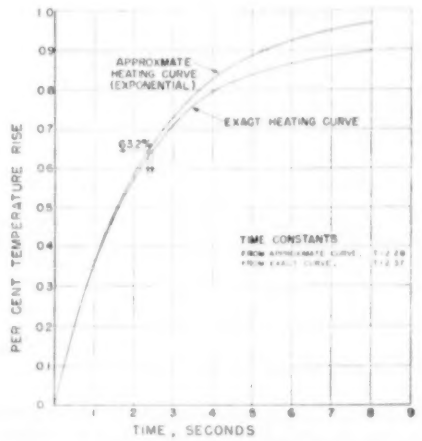

FIG. 3 COMPARISON OF EXACT AND APPROXIMATE HEATING CURVES FOR TYPE A THERMOCOUPLES

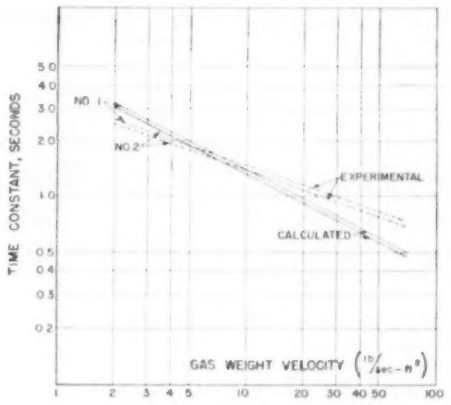

FIG. 4 COMPARISON OF CALCULATED AND EXPERIMENTAL TIME CONSTANTS FOR TYPE B THERMOCOUPLES; MEAN TEMPERATURE, 850 F

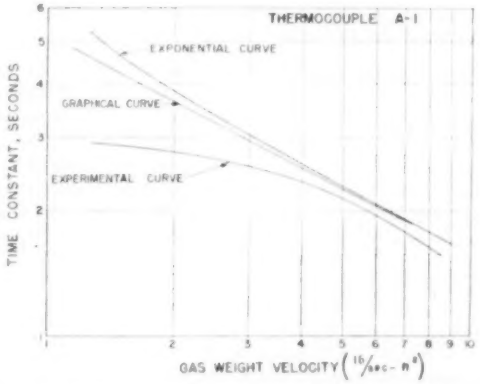

FIG. 5 COMPARISON OF CALCULATED AND EXPERIMENTAL TIME CONSTANTS FOR THERMOCOUPLES

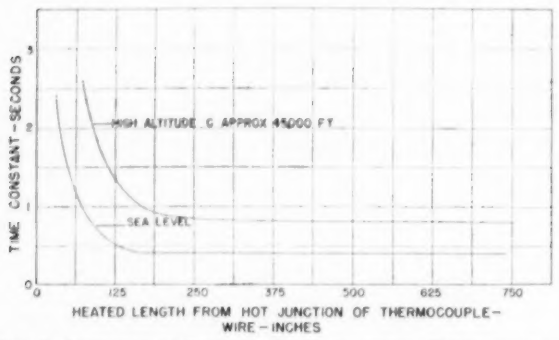

FIG. 6 RESPONSE OF TYPICAL SWAGED MAGNESIA THERMOCOUPLE IN AN AIRCRAFT GAS-TURBINE TAILCONE

sulation. These hazards are of course reduced if the length of the unsupported wire is kept small. The rate of response is slowed if the unsupported length is made too short, the relationship being shown in Fig. 6. Evidently the loop length can be reduced to approximately 1/4 in. without increasing the time constant. As shown in the illustration of the loop junction, the unsupported length is made long enough to avoid any significant loss in response rate due to axial heat conduction to or from the junction. The analyis of this heat-conduction problem is given in Appendix 2.

RECOVERY COEFFICIENT OF THERMOCOUPLE

An ideal temperature sensor in aircraft gas turbines will read total temperature (static temperature plus the kinetic energy of the moving gas stream). The actual thermocouples read a temperature somewhere between the static and total temperatures. The recovery coefficient is defined as

$$\frac{\text{Thermocouple temp—static temp}}{\text{Total temp—static temp}}$$

Tests have shown that most thermocouples used in aircraft gas turbines have a recovery coefficient of around 0.8. A fast-response thermocouple, as shown in Fig. 1, has a recovery coefficient of 0.7, whereas a slow one can be as high as 0.98.

A high-recovery-coefficient thermocouple usually will have a low heat-transfer coefficient between the gas and thermocouple. A low heat-transfer coefficient will cause a thermocouple radiation error (to the tailcone).

Thus the thermocouple that has the greatest accuracy will not have a recovery coefficient of 1.0. Some lower value will give the best compromise between radiation error and recovery error. Tests have shown this to be true.

ACCURACY OF PARALLEL ARRANGEMENT

With gas turbines having individual can-type combustion chambers, there is a periodic variation of exhaust-gas temperature in a circumferential direction. For example, when eight combustion chambers are used, the temperature-distribution-pattern characteristic of the burner is repeated every 1/8 circumference around the tailcone or tail pipe. There also are large temperature variations in a radial direction. In order to determine an average temperature, it is necessary to use a number of thermocouples so located and connected as to average the group properly. The location of these thermocouples, which are usually connected in parallel, is selected so that circumferential shifting of the temperature pattern will have the least possible effect on the measured average temperature. Changes in engine operating conditions are known to change in swirl in exhaust gases and to cause the temperature pattern to shift positions in an angular direction. When the turbojet has eight can-type combustion chambers, a reasonable arrangement which has given good practical results is the use of seven thermocouples located at equal circumferential intervals.

When a number of thermocouples that read slightly different temperatures are connected in parallel to a bus bar which has appreciable resistance relative to that of the individual thermocouple, the voltage on the bus will vary with position. The ratio of the bus-bar resistance to thermocouple resistance must be made small enough to reduce this difference from the average voltage to within a specified allowable error.

If a temperature distribution is assumed as shown in Fig. 7,

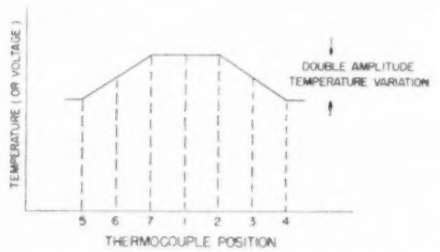

FIG. 7 APPROXIMATE TEMPERATURE DISTRIBUTION IN CIRCUMFERENTIAL DIRECTION

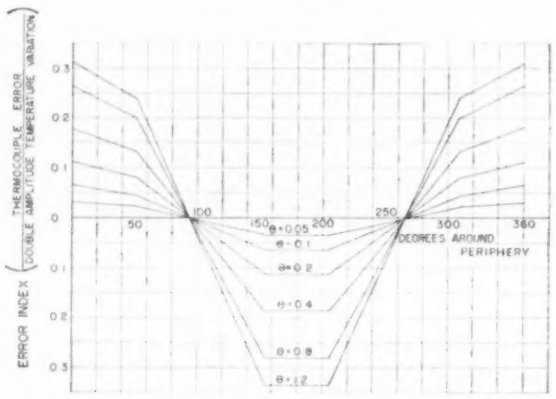

FIG. 8 PLOT SHOWING ERROR IN THERMOCOUPLE BUS INDICATED TEMPERATURE AROUND PERIPHERY OF GAS-TURBINE TAIL-PIPE

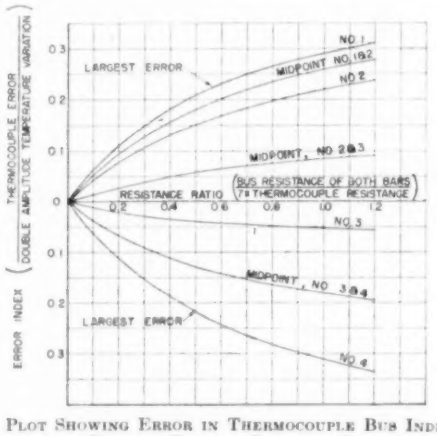

FIG. 9 PLOT SHOWING ERROR IN THERMOCOUPLE BUS INDICATED TEMPERATURE AT VARIOUS TAPS ON BUS AS A FUNCTION OF RESISTANCE RATIO

then the voltage distribution around the circular bus bar is as shown in Fig. 8. The error of the bus-bar voltage from the average thermocouple voltage is shown in Fig. 9. This error is a function of θ, the ratio of resistance of both bus bars to the resistance of the seven thermocouples. Fig. 9 is a cross plot of Fig. 8. The principal design variable is θ, and it must be made small enough to make the paralleling error less than a specified value. However, excessively heavy buses are of course undesirable for aircraft application.

Since the temperature distribution shown in Fig. 8 rotates during various operating conditions, the design should be on the basis of assuming that the bus-bar tap-off point has the greatest possible error.

There are certain symmetrical arrangements and connections of thermocouples which for practical purposes eliminate the error resulting from lead resistance. For instance, consider four thermocouples which are first paralleled in two groups of two thermocouples by connectors of equal resistance. Now if the mid-points of these equal connectors are connected by a third connector as bus bar, the mid-point of this last harness is seen to have a symmetrical location with respect to each of the four thermocouples.

The thermocouple location and connections described are intended to average temperatures in a circumferential direction. Unfortunately, the temperature stratifications in the radial direction are not averaged in this arrangement.

It is desirable to minimize or eliminate entirely the effect of lead resistance from the thermocouple to temperature indicator on the accuracy of the temperature determination. Use of null-point circuits such as in potentiometers often makes it possible to reduce the weight of the lead wires. In this case the lead resistance affects only the sensitivity or stiffness of restoring forces when an unbalanced condition exists.

Conclusions

1 Thermocouples have been developed to have adequate mechanical strength to withstand the severe vibration to which they are exposed in the gas stream.

2 The time-response rate is sufficiently rapid to permit their being used as practical control-system elements sensing exhaust temperature.

3 Thermocouples should be so located in the exhaust-gas system that the average reading is unaffected by changes in the amount of swirl in the hot exhaust gases discharged from the turbine.

4 Practical means are now available for connecting and amplifying the d-c voltage of the thermocouples so as to make them adaptable to control systems.

5 The hot junction can be extended a sufficient distance beyond the support base to eliminate any appreciable error due to axial conduction effects in the thermocouple wires.

6 Radial temperature gradients in the thermocouple wire are small enough to be ignored as a source of error.

Acknowledgment

The authors gratefully acknowledge the valuable assistance and helpful comments of Drs. H. Poritsky and H. Weil. The mechanical design was improved by the work of Messrs. J. H. Baker and F. R. Sias. Excellent project co-ordination and guidance were maintained throughout the development by Mr. R. M. Strock.

References

1 "Test of Chromel-Alumel Thermocouples Supplied by General Electric Company," Air Force Technical Report No. 5738.

2 "Introduction to the Mathematical Theory of the Conduction of Heat in Solids," by H. S. Carslaw, Dover Publications, New York, N. Y., 1945.

3 "Tables of Functions," by Dr. C. Jahnke and F. Emde, Dover Publications, New York, N. Y., 1945.

4 "Gas Tables," by J. H. Keenan and J. Kaye, John Wiley & Sons, Inc., New York, N. Y., 1948.

Nomenclature

The following nomenclature is used in Appendix 2:

a = radius of the thermocouple wire, ft
A = area of heat transfer, sq ft
A = constant c/K
A' = cross-section area of conductor, sq ft
B = constant $\dfrac{2h}{Ka}$
c = specific heat of thermocouple material, Btu/lb-deg F
$c_0, c_1, c_2 \ldots c_n$ = arbitrary constants
G = gas weight flow, lb/hr-sq ft
h = heat-transfer coefficient for air at T deg F, Btu/hr-sq ft-deg F
K = thermal conductivity of thermocouple material, Btu-ft/hr-sq ft-deg F
L = length of wire from thermocouple junction to magnesia shank, ft
P' = perimeter of thermocouple conductor
t = time
t_b = instantaneous temperature of body
T = a function of t
T = temperature, deg F
T_0 = initial temperature, deg F
T_g = temperature of gas, deg F
x = distance along thermocouple conductor axis, measured from junction, ft
X = is a function of x
V = volume per unit length of thermocouple conductor, cu ft
$\alpha_1, \alpha_2, \alpha_3, \ldots$ = arbitrary constants (all are positive)
θ = actual temperature minus gas temperature
θ = bus-bar resistance of both bars divided by 7 times thermocouple resistance
ρ = density, pcf
τ = time constant of thermocouple
τ_c = time constant of magnesia shank

Appendix 1

Derivation of Time-Constant Formula

For this derivation of the thermocouple time constant, the following assumptions are made:

1 The heat radiated to the walls from the thermocouple has little effect on the time constant.

2 Temperature differences in the radial direction inside the thermocouple wires are negligible.

3 Temperature differences in the axial direction along the thermocouple wires are small.

4 The average thermal properties of the two thermocouple wires are used for the entire thermocouple wire.

5 The heat-transfer coefficient between the exhaust gas and the thermocouple may be expressed as a single value which is the average over the surface.

6 The properties of the body do not vary with temperature.

Let us assume that we have a body receiving heat from a gas stream. A heat balance may be written as follows:

Heat flow rate into body = rate of heat storage

$$hA(T_g - t_b) = c\rho V \frac{dt_b}{dt} \quad [2]$$

where

h = heat-transfer coefficient between gas and thermocouple
A = heat-transfer area per unit wire length
T_g = gas temperature
t_b = thermocouple-wire temperature
c = specific heat of thermocouple material
ρ = weight density of thermocouple material
V = volume per unit length of thermocouple wire
t = time

Rewriting Equation [2], we have

$$\frac{dt_b}{dt} + \frac{hA}{c\rho V} t_b = \frac{hA}{c\rho V} T_g \quad [3]$$

The general solution to this equation is

$$t_b = c_1 \epsilon^{\frac{-ha}{c\rho V} t} + T_g \quad [4]$$

The arbitrary constant c_1 may be evaluated from the fact that $t_b = T_0$ when $t = 0$. Thus $c_1 = T_0 - T_g$. Equation [4] may be written

$$t_b = T_g - (T_g - T_0) \epsilon^{\frac{-hA}{c\rho V} t} \quad [5]$$

The time constant of an exponential curve such as this is defined as the time required for the temperature to change 63.2 per cent of its total change. For this to be true, it is seen that

$$\frac{hA}{c\rho V} t = 1.00 \quad [6]$$

This is, therefore, the time constant

$$\tau = \frac{c\rho V}{hA} \quad [7]$$

Appendix 2

Determination of Effect of Axial Conduction on Time Constant

It is obvious that some heat will be conducted axially along the wire of the thermocouple to be absorbed by the ceramic in the thermocouple shank. However, it is difficult to estimate the effect that this will have on the time constant. In order to show the approximate magnitude of this effect, the exact curve for a particular case may be compared to a true exponential curve with a time constant

$$\tau = \frac{c\rho V}{hA}$$

The exact curve will be derived with the following additional assumptions to the ones given in the Assumptions section of Appendix 1:

1 The effect of the steel sheath over the magnesia shank may be neglected.

2 The cooling effect in the magnesia due to the heat conducted away axially by the lead wires is negligible.

Fig. 10 shows an enlarged view of the thermocouple wire loop which extends beyond the magnesia in the shank.

Let us write a heat balance for an element of the wire dx in length

(Heat in) — (heat out) = (heat stored)

$$-KA' \frac{\partial \theta}{\partial x} - hP' dx\, \theta + KA' \left(\frac{\partial \theta}{\partial x} + \frac{\partial^2 \theta}{\partial x^2} dx \right) = A' c\, \rho\, dx \frac{\partial \theta}{\partial t} \quad [8]$$

where

θ = temperature inside wire above gas temperature
x = measured along wire axis from thermocouple junction
A' = cross-sectional area of wire
P' = perimeter of wire
θ_0 = shank and thermocouple initial temperature above gas temperature
τ_c = shank time constant
K = thermal conductivity of thermocouple material
c = specific heat of thermocouple material
ρ = weight density of thermocouple material
h = heat-transfer coefficient between gas and thermocouple
a = radius of thermocouple wire

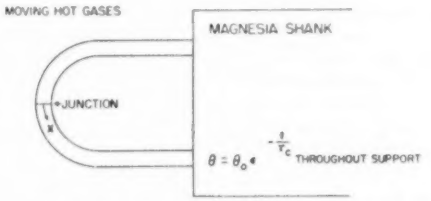

Fig. 10 Thermocouple Loop and Support

Simplifying

$$\frac{\partial^2 \theta}{\partial x^2} - \frac{hP'}{A'K} \theta = \frac{c\rho}{K} \frac{\partial \theta}{\partial t} \quad [9]$$

For a cylindrical wire, $P = 2\pi a$ and $A = \pi a^2$. Thus Equation [9] becomes

$$\frac{\partial^2 \theta}{\partial x^2} - \frac{2h}{Ka} \theta = \frac{c\rho}{K} \frac{\partial \theta}{\partial t} \quad [10]$$

This is the differential equation which describes the heating in the conductor. Let

$$A = \frac{c\rho}{K} \quad [11]$$

$$B = \frac{2h}{Ka} \quad [12]$$

Equation [10] becomes

$$\frac{\partial^2 \theta}{\partial x^2} - B\theta = A \frac{\partial \theta}{\partial t} \quad [13]$$

The boundary conditions which govern the problem are

$$\theta = \theta_0 \text{ at } t = 0 \quad [14]$$

$$\frac{\partial \theta}{\partial x} = 0 \text{ at } x = 0 \quad [15]$$

$$\theta = \theta_0 \epsilon^{-\frac{t}{\tau_c}} \text{ at } x = L \quad [16]$$

where L is the length of the thermocouple wire from the shank to the thermocouple.

The solution to Equation [13] with the boundary conditions of Equations [14] to [16] is

$$\theta = \theta_0 \left\{ \epsilon^{-\frac{t}{\tau_c}} \left[\frac{\cosh \sqrt{B - \frac{A}{\tau_c}}\, X}{\cosh \sqrt{B - \frac{A}{\tau_c}}\, L} \right] + \frac{4(B\tau_c - A)}{A\pi} \sum_{n=1,3,5\ldots}^{\infty} \frac{(-1)^{\frac{n+1}{2}}\, \epsilon^{-\alpha_n t} \cos \frac{n\pi x}{2L}}{(1 - \alpha_n \tau_c)n} \right\} \quad [17]$$

where

$$\alpha_n = \frac{1}{A}\left[B + \left(\frac{n\pi}{2L}\right)^2\right] \quad [18]$$

The solution can be derived as follows: Assume a product solution

$$\theta = XT \quad [19]$$

where X is only a function of x, and T is only a function of t. From Equations [13] and [19]

$$T\frac{\partial^2 X}{\partial x^2} - BXT = AX\frac{\partial T}{\partial t} \quad [20]$$

Dividing both sides by AXT gives

$$\frac{1}{AX}\frac{\partial^2 X}{\partial x^2} - \frac{B}{A} = \frac{1}{T}\frac{\partial T}{\partial t} \quad [21]$$

Each side of Equation [21] must be a constant. Since all the temperature transients eventually must decay, the constant for the right-hand side of Equation [21] must be less than zero. Thus

$$\frac{1}{T}\frac{\partial T}{\partial t} = -\alpha_i \quad [22]$$

Solving for T gives

$$T = c_1 \epsilon^{-\alpha_i t} \quad [23]$$

where c_1 is an arbitrary constant. From Equations [21] and [23]

$$\frac{\partial^2 X}{\partial x^2} + (A\alpha_i - B)X = 0 \quad [24]$$

Since $\alpha_i > 0$, and $A > 0$, and $B > 0$, Equation [24] will have two forms of solution

$$Y = c_2 \cosh \sqrt{B - A\alpha_m}\, X + c_3 \sinh \sqrt{B - A\alpha_m}\, X \quad \text{for } \frac{B}{A} > \alpha_m \quad [25]$$

$$X = c_4 \cos \sqrt{A\alpha_n - B}\, X + c_5 \sin \sqrt{A\alpha_n - B}\, X \quad \text{for } \frac{B}{A} < \alpha_n \quad [26]$$

The boundary condition of Equation [15] will make c_3 and c_4 equal to zero. Thus

$$X = c_2 \cosh \sqrt{B - A\alpha_m}\, X \text{ for } \frac{B}{A} > \alpha_m \quad [27]$$

$$X = c_4 \cos \sqrt{A\alpha_n - B}\, X \text{ for } \frac{B}{A} < \alpha_n \quad [28]$$

The boundary condition from Equation [14] will give a relationship between c_2 and c_4.

The boundary condition for Equation [16] will give the arbitrary constant out front and will also give

$$\alpha_m = \frac{1}{\tau_c} \quad [29]$$

$$\alpha_n = \frac{B}{A} + \frac{1}{A}\left(\frac{n\pi}{2L}\right)^2,\ n = 1, 3, 5 \ldots \quad [30]$$

Equation [29] assumes $1/\tau_c < B/A$; this is the case for the physical constants τ_c, A, and B.

The results from the foregoing analysis were given back in Equations [17] and [18].

Equation [13] was evaluated at $x = 0$, the thermocouple junction. Fig. 3 shows a comparison between the exact curve and an exponential curve. The lower portion of the exact curve is almost identical with the exponential curve. The time constant could be predicted within 5 per cent if a true exponential was assumed instead of using the exact curve.

This calculation shows that axial conduction effects are small for a representative case.

Discussion

H. H. Chamberlain.[4] This paper is of considerable interest to those making and using aircraft gas-turbine thermocouples. The authors have covered the subject of long-life fast-response thermocouples quite thoroughly and in addition, their points in favor of thermocouples as primary detectors of temperature rather than the other possible forms, such as resistance detectors or optical methods, are believed to be well taken.

In point 4 under Advantages of the Loop Junction Construction, the authors state that a superior junction weld is produced by the butt-welding possible with the new construction. This seems to the writer to be questionable, and having personally made both types of welds, he has not found any inherent superiority of one over the other. In addition, he knows of no test data which would tend to indicate any superiority in either thermal emf or life; rather, there are considerable data which would indicate no appreciable difference between the two types of of junctions given equal handling and operating conditions, and there is obviously some superiority in the twisted-type junction in so far as damage from poor handling. In point 5 the authors claim a reduced working of the wires in fabrication. Since in forming the loop junction, the wires are flat-dropped and then formed in a punch press before welding, it seems that there is at least as much stress and strain involved here as in the twisting of wires to form a twisted junction.

Under the heading, Forced Vibration of Thermocouples, the authors claim: "It appears that no part of the tailcone will remain inactive, and hence there is no ideal location for placement of thermocouples or similar instrumentation." Actually, measurements indicated considerably less vibration at points on the tailcone skin near the front or back, as compared with regions in the middle of the cone. It would seem that this was due to the stiffening effect of the relatively heavy metal rings at the front and back used to bolt or clamp the tailcone into place.

The section on Accuracy of Parallel Arrangement seems to be of prime importance. The classical method of paralleling thermocouples, namely, equal-resistance thermocouples, all brought to a common junction point, is, of course, capable of theoretical perfection in averaging. However, this system when

[4] Meter and Instrument Department, General Electric Company, West Lynn, Mass.

used with more than a few thermocouples becomes very cumbersome mechanically, and difficult from a manufacturing standpoint. Although the manifold-type harnessing arrangement described by the authors has in theory a greater error than the equal-resistance paralleling method, in practice, as the authors point out, this system can be so designed as to reduce these errors to a completely negligible value. Some of the advantages of the manifold or ladder-type paralleling arrangement would include the following:

1 Thermocouples all identical electrically and mechanically

2 Much cleaner and neater physically.

3 A weight advantage which begins to be felt at about the 4 to 5 thermocouple level and becomes increasingly important as the number of thermocouples is increased.

4 Simplicity of manufacture. Simplified mountings since the harness can be mounted entirely from the thermocouples themselves and each will bear its equal share of the load.

5 Flexibility, since simply by changing the harness itself, the same-type thermocouples may be used in any number from about three up to as many as can be crowded in around the tailcone.

S. S. Stack.[8] The authors of this paper have indicated the vast amount of engineering and test work involved in the development of fast-response thermocouples to meet the present-day requirements for temperature control of aircraft gas turbines.

The basic calculations involved relative to time response, gas velocity, conduction and radiation errors, the averaging of measurements at several points, and so on, are applicable for other types of temperature detectors. Therefore, testing time and the evaluation of future designs and operating characteristics at other than test conditions can be simplified.

In line with the continual changes in design of engines and operating characteristics, we are confronted continuously with corresponding changes in measuring equipment.

One major factor, which has been found difficult to determine in a relatively short time, is the prediction of expected life under various operating conditions from short-time life tests for durability with respect to temperature, heat shock, vibration, and thrust.

The investigation of the vibration of the thermocouple mounting bosses attached to the tailcones, is probably indicative of acceleration due to vibrations in the tailcone itself, and not necessarily that occurring at the junction end of the thermocouple. It is indicated that circular stiffening bands and insulating blankets have been found effective in improving the life of some types of thermocouples. This would indicate that further improvements could be obtained in this direction by means of other than rigidly mounting the thermocouples in bosses which are directly attached to the tailcone.

[8] General Engineering Laboratory, General Electric Company, Schenectady, N. Y.

A Study of Burner Oscillations of the Organ-Pipe Type

By A. A. PUTNAM[1] and W. R. DENNIS,[2] COLUMBUS, OHIO

Three simplified combustion systems have been investigated for acoustical oscillations. The systems are: (*a*) a mixing chamber and multiple-port burner mounted in a combustion tube open at both ends; (*b*) a similar mixing chamber and multiple-port burner which completely blocked the secondary-air inlet of the combustion tube; and (*c*) a system similar to (*b*), but utilizing separate fuel and primary-air inlets, giving a diffusion flame rather than a premixed-gas flame. Oscillations were found to occur only for certain ranges of the variables. In the first system, the pitch differed significantly in adjacent ranges of oscillation. In the two latter systems, the frequency of the oscillations remained fairly uniform and close to the fundamental of the combustion tube, although breaks occurred in the data as the configurations of the inlet supply systems were varied. These results are explained on the basis of (*a*) the time of feedback of pressure pulses which ultimately cause changes in the heat-release rate, and (*b*) the location of the flame relative to a section of maximum pressure amplitude in the combustion tube. In further substantiation of the implications of the test results, the Appendix presents a thermodynamic treatment of the phase requirement between rate of heat release and pressure.

ACOUSTICAL oscillations are frequently generated when a flame is partially or totally confined in a combustion chamber. These oscillations may not only become undesirable from a nuisance or physiological standpoint, but may at times become so violent as to interfere with proper combustion, causing the flame to blow out or even destruction of the equipment. Heat transfer normally is increased by oscillations; this may be beneficial, but uncontrolled increases in heat flux may cause burner walls to melt. On the other hand, the presence of oscillations may lead to improved flame holding, yielding operating ranges greater than those obtained with conventional flame-holding techniques; oscillations also may cause increased mixing, leading to increased efficiency of combustion without increases in residence time in the burner. Therefore investigations of the oscillations associated with combustion equipment should furnish important information for the optimum design of burners, whether oscillations are to be utilized or suppressed.

As a part of such an investigation, a study has been made of flame-driven oscillations that have frequencies corresponding to the organ-pipe frequencies of the system. On the basis of observations and of complementary theoretical studies, it has been possible to develop a comprehensive understanding of some of these oscillations, and thus to establish the requirements of design for either minimizing or increasing the amplitude of oscillations.

Fig. 1 shows sketches of the three systems that have been studied. These will be described in greater detail later. Unit (*a*) is a Pyrex combustion tube with a premixed-gas burner mounted within; this arrangement permits secondary air to flow between the burner head and the combustion-tube wall. Unit (*b*) is a rocket-shaped burner with a premixed-gas flame; this unit is similar to the previous unit, except that the burner head blocks the combustion tube so that there is no inflow of secondary air.

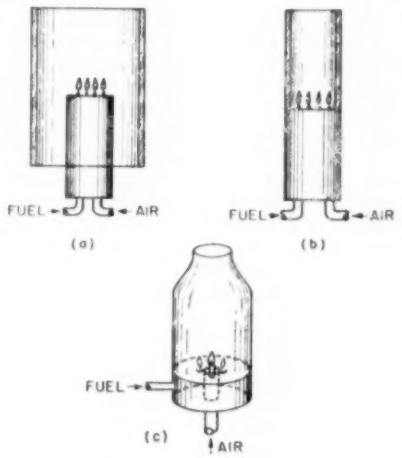

FIG. 1 SKETCHES OF THREE TYPES OF COMBUSTION UNITS INVESTIGATED

Unit (*c*) is a rocket-shaped burner utilizing a diffusion flame; this unit is similar to unit (*b*), except that the fuel and air are brought into the combustion chamber through separate ports. Although burners used in practice are far more complex than those shown, many of them can be reduced, in principle, to the simple configurations shown.

In the mathematical formulation of the acoustic properties of these systems, the fundamental assumption has been made that an oscillating component of the rate of heat release must be in phase with the oscillating component of the pressure. This assumption, which will be discussed later, was first suggested by Rayleigh,[3] and is justified thermodynamically in the Appendix of this paper.

In this study, the only oscillations considered are those for which a column of gases, in the combustion system, is vibrating in the same manner as the gas column in a sounding organ pipe; however, it must be emphasized that this type of oscillation is only one of several types that may occur in combustion systems; other types will not be discussed here.

---

[1] Fuels Research Division, Battelle Memorial Institute. Jun. ASME.

[2] Fuels Research Division, Battelle Memorial Institute.

Contributed by the Fuels and Gas Turbine Power Divisions and presented at the Semi-Annual Meeting, Cincinnati, Ohio, June 15–19, 1952, of THE AMERICAN SOCIETY OF MECHANICAL ENGINEERS.

NOTE: Statements and opinions advanced in papers are to be understood as individual expressions of their authors and not those of the Society. Manuscript received at ASME Headquarters, September 13, 1951. Paper No. 52—SA-12.

[3] "The Theory of Sound," by Lord Rayleigh, Dover Publications, New York, N. Y., vol. 2, 1945, p. 226.

Elementary Considerations

The organ pipe is commonly pictured as a long tube, in relation to its diameter, open either at one end or at both ends. The usual description of the way in which such a tube sounds, for a pipe open at both ends, is that, periodically, air flows inwardly from the ends, building up a higher-pressure region at the center. As the pressure increases, the inflow of air slows down and finally stops. The higher pressure at the center then causes a reversal of flow outwardly toward both ends, accompanied by a lowering of pressure at the center. Because of the momentum of the air, the pressure at the center eventually falls below ambient pressure and with the build-up of this partial vacuum, the outflow of air finally decreases to zero. Thereupon the cycle begins to repeat itself, and periodic oscillation of the column of gases in the tube is established.

Organ-Pipe Theory. More basic considerations[4,5] show that, for small amplitudes of oscillations, wherein the thermodynamic equations can be linearized, the mode of oscillation described in the foregoing is sinusoidal, both in time and, along the tube, in space; that is, the pressure, as well as the gas-particle velocity, varies in a sinusoidal manner with time at each interior point of the tube. Furthermore the pressure, or velocity, is a sinusoidal function of distance along the tube. For the pressure, there is maximum variation in amplitude at the middle of the tube, and no variation at each end. Conversely, for the particle velocity there is no variation in amplitude at the middle of the tube, and maximum variation at each end. This type of oscillation is termed a standing wave; the standing pressure wave, for the fundamental mode just discussed, has a node at each end and an antinode at the center; the standing velocity wave has a node at the center and an antinode at each end. Considering either wave, the frequency ν, and the length of tube L_1 (neglecting certain end corrections to be discussed later), are related as follows

$$2 L_1 \nu = c \qquad [1]$$

where c is the speed of sound.

If two sounding tubes, exactly alike, are connected together and conditions are assumed to be such that the outflow in one tube occurs at the same time as the inflow in the other tube, it will be seen that the tubes will continue to act, in this mode of vibration, as if they were still separated. For this system, using Equation [1]

$$(2 L_1) \nu = c = L_2 \nu$$

where L_2 is twice L_1.

Considering the spacewise distribution of pressures in this system of length L_2, there is, at the appropriate moment, a complete cycle comprising ambient pressure at both ends, maximum pressure at the center of one tube and minimum pressure at the center of the other tube, and ambient pressure at the middle, where they are joined. The length of this complete space cycle is designated as the wave length λ, which is equal to L_2, or $2 L_1$.

Generalizing upon the argument of adding sections of tube to obtain higher modes of oscillation, and realizing that any of these modes is possible in any length of tube, a general equation relating possible frequencies to tube length is obtained

$$\nu = \frac{c}{2 L_1} = \frac{c}{2\left(\frac{L_n}{n}\right)} = \frac{n c}{2 L_n}, \qquad n = 1, 2, 3, \ldots \qquad [2]$$

where n is the number of sections of unit tube, and L_n is the total tube length.

Considering again the fundamental mode of oscillation, it is clear that there is no flow through the cross section of greatest amplitude of pressure change. Thus a wall could be placed at this section without disturbing the oscillation. The frequency for this half-tube with one closed end, of length L_0, would be

$$\nu = \frac{c}{4 L_0}$$

By the process of adding additional lengths of tube, the general equation for the frequencies of a tube open at one end and closed at the other may be determined as

$$\nu = (2n - 1) \frac{c}{4 L}, \qquad n = 1, 2, 3, \ldots \qquad [3]$$

Equations [2] and [3] can be derived in another manner, by considering a pressure pulse as being sent down the tube. It reflects from the open end as a rarefaction, satisfying the conditions of constant ambient pressure at the open end. This rarefaction travels the length of the tube and is reflected from the other open end, becoming a pressure pulse again. This pulse then returns through the tube in the original direction. The time for a complete cycle, returning all conditions in the tube to the initial conditions, is

$$\tau = \frac{2 L}{c}$$

and the frequency is again

$$\nu = \frac{c}{2 L}$$

This argument also can be used for the tube closed at one end, by considering that pressure reflects as pressure at a closed end.

Acoustical Drivers. The considerations just discussed are sufficient for an understanding of the frequency of oscillation observed for simple organ pipes, but are not sufficient for an explanation of the origin and continuation of the oscillations. In other words an intermittent source of energy has been implied to drive the oscillations and to overcome the ever-present damping forces in such a system. The oscillations in the tube will not reach a high intensity unless energy is added periodically to the gases in the tube in such a way as to meet two requirements. First, depending on the type of energy being added, the periodic energy release must be in phase with either the pressure fluctuations or the velocity fluctuations in the tube. For this to be accomplished, the period of the driver must be close to some multiple of the natural period of the tube, but not necessarily equal to it. This is the time condition for resonance.

The second requirement is that the energy must be released near a point of maximum effectiveness. This means that energy in the form of a velocity disturbance must be added near a pressure antinode of the mode of oscillation being driven; conversely, energy in the form of a pressure disturbance must be added near a velocity antinode. One or the other represents the space condition for resonance.

In the case of an organ pipe, and for some other wind instruments, driving may be accomplished in the following way: A jet of air is passed through a slot orifice in such a manner as to impinge upon the edge of a lip extending downward over an opening at the side of the tube.[4] Two oscillatory systems are involved in this driving unit: (1) The jet, after passing through the slot orifice, acquires a characteristic vibration which gives it a sinuous shape. This vibration is caused by alternate shedding of vortexes

[4] "Acoustics," by Alexander Wood, Interscience Publishers, Inc., New York, N. Y., 1941, pp. 93, 397, 406.

[5] "Vibration and Sound," by P. M. Morse, McGraw-Hill Book Company, Inc., New York, N. Y., second edition, 1948, pp. 248, 254.

from the two sides of the slot. However the frequency is not very pure, and the intensity is low. (2) The other oscillatory system consists of the lip and impinging jet; this system also will generate vortexes at a certain frequency.

If the lip has been placed at the proper distance from the orifice, the two vortex-shedding processes will reinforce each other to make the amplitude of oscillation larger and the frequency more definite. The resultant frequency will depend on the position of the lip, relative to the orifice, and on the velocity of the air jet.

If the driver just described has been placed across the open end of a tube whose natural frequency is close to that of the driver, an oscillation will be set up in the tube. This oscillation will be reinforced by the driver and in turn will reinforce the driver, up to the point where all the energy dissipation of the system through damping and sound radiation equals the energy of the air jet that is converted into an oscillatory driving force.

It will be noted that the driver is located, with respect to the tube, at the position of maximum velocity amplitude and minimum pressure amplitude. This position of the driver is optimum for the system because the driving is a result of the pressure fluctuation produced by the alternate shedding of vortexes. The use of this driver in the area of maximum pressure amplitude would be ineffective.

In the case of reed instruments, the driving is accomplished by blasts of air, and the optimum driver position becomes one of maximum pressure amplitude. However, as pointed out by Morse,[5] this entire field of application is not too well understood scientifically and devolves to the art of musical instruments.

In the case of flame-driven oscillations, of the type discussed in this paper, another type of driving mechanism is present. The basic requirement of this mechanism is that the oscillating component of the rate of heat release be in phase with the pressure variation at the point of heat release.[3,4] Theoretical verification of this requirement is presented in the Appendix; this requirement, therefore, is used as a basis for the analysis of the observed results. For this type of driving, energy is added in the form of periodic velocity disturbances. Therefore, as contrasted to the vortex type just described, the maximum effect is obtained in the area of maximum amplitude of the oscillating pressure, as is the case with the vibrating-reed type of driving.

Combustion Tube and Burner Investigation

Apparatus. Fig. 2 shows the open-end combustion tube used in this study; the burner nozzle comprised 29 ports. This apparatus is similar in many respects to the classical "singing-flame" apparatus, in which a single flame orifice is inserted at various distances into the combustion tube. The burner head used could be moved to any desired location L_0, beyond the combustion-tube entrance; to obtain changes in the length of the mixing chamber, different lengths of pipe were used.

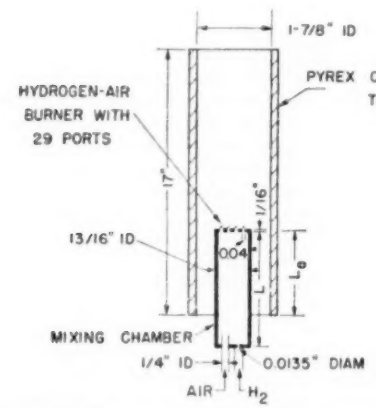

Fig. 2 Schematic Diagram of Combustion Tube and Burner

Oscillations occurred, in this apparatus, only for certain positions of burner head with respect to the end of the combustion tube. These positions were not marked by single points, but each was marked by an interval of displacements for which the observed frequency was nearly constant, but varied widely from that observed at nearby positions. Between such oscillating regions were blank intervals where no oscillation occurred.

Method of Test. In the experimental work, using a stoichiometric mixture of hydrogen and air, the burner head was moved slowly from the entrance to the combustion tube until the first interval was reached where an intense oscillation started. At this point, the frequency and intensity of the oscillation and the distance L_0 were measured. Frequency and intensity of the oscillation were determined, respectively, with a General Radio sound analyzer and a sound level meter, using a crystal microphone placed about 3 ft from the combustion unit. The burner was then moved further into the oscillating interval until the position was reached where the intensity of the oscillation decreased markedly. Returning the burner head to the point of high-intensity oscillation nearest to this point of decreased intensity, the frequency and intensity of the oscillation and the distance L_0 were again measured. The section of combustion tube between the points where the oscillation started and stopped constituted the interval of displacement associated with the particular oscillation. The criterion for establishing the end points of this interval was that the oscillation had been amplified to an intensity equal to or greater than 85 decibels (db), the ambient noise level being approximately 50 db.

Discussion of Test Results. The test procedure just outlined was continued over the entire length of the combustion tube, and was repeated for three lengths of mixing chambers. It was found that several intervals of oscillation existed, and, as previously stated, that the frequency changed markedly from one interval to another. Some intervals of oscillation were so short that the oscillation was generated at only one position of the burner head. It was also noted that the observed oscillations were pure in tone, and that their frequencies and intensities were approximately constant over the interval.

Table 1 shows the data obtained in the manner just described. The data are arranged in three groups corresponding to the three lengths, L, of mixing chamber used; the natural frequency $\nu_m = c/2L$ is shown for each length of mixing chamber. For each interval where oscillation was noted, the distances L_0, corresponding to the beginning and end of the oscillation are given, as are also the observed frequency ν and the ratio ν/ν_m. Since the amplitude of oscillation was at a uniformly high value over each interval, amplitudes have not been tabulated.

The data of Table 1 will now be analyzed from two separate points of view: One will involve only the relations resulting from the time-phase aspects of the resonance established; the other will be concerned with the relations between the point of heat release and the regions of maximum pressure change in the combustion tube.

Analysis of Oscillation Mechanism. The following mechanism is postulated for the observed oscillations: A slight pressure fluctuation caused by any small disturbance in flow in the combustion tube is fed back into the mixing chamber. This pressure pulse travels the length of the chamber, is reflected at the lower end, and returns to the burner ports. The pressure pulse causes an increase in flow rate, which means that an extra slug of gas mixture passes through the ports and is burned. If the burning of this extra slug is "nearly" in phase with some pressure pulse

TABLE 1 FREQUENCIES AND DISPLACEMENT INTERVALS OF OSCILLATION FOR DOUBLY OPEN COMBUSTION TUBE AND BURNER HEAD

(s = 1/16 in.; a = 0.02 in.; V = 117 fps; F = 100 ips; c = 1132 fps)

L, in.	ν_m, cps	Interval of oscillation	Beginning of interval: L_0, in.	Beginning of interval: ν, cps	Beginning of interval: ν/ν_m	End of interval: L_0, in.	End of interval: ν, cps	End of interval: ν/ν_m
11 1/16	615	1	1	2200	3.58	1	2200	3.58
11 1/16	615	2	1 3/4	1650	2.68	2 1/2	1650	2.68
11 1/16	615	3	3	1120	1.82	3 3/4	1120	1.82
11 1/16	615	4	4	1920	3.12	4 3/4	1950	3.17
11 1/16	615	5	6 1/8	2300	3.74	6 7/8	2300	3.74
11 1/16	615	6	7 5/8	1750	2.84	10	1820	2.96
11 1/16	615	7	9	530	0.86	9	530	0.86
11 1/16	615	8	12	1220	1.98	13 1/4	1260	2.05
7 1/16	960	1	1/2	1600	1.67	2 1/2	1660	1.73
7 1/16	960	2	3 3/4	1920	2.00	4 3/4	1920	2.00
7 1/16	960	3	8 1/2	1800	1.88	9 1/4	1800	1.88
4 1/2	1500	1	1/2	2150	1.43	1	2150	1.43
4 1/2	1500	2	6	1450	0.97	6 3/4	1450	0.97
4 1/2	1500	3	12 1/4	1250	0.83	13 1/4	1250	0.83

succeeding the original one, the oscillation originating in the tube will be promoted. The new amplified pulse is then fed back into the mixing chamber and the cycle continues with increasing amplitude, until the driving force balances the losses.

Time Condition for Resonance. The period τ_i of the cycle just described is the sum of the time, $2\,L/c$, required for the pulse to travel the length of the mixing chamber L and back at the velocity of sound c, and the time M for the extra slug of gas to pass through the ports and be burned; thus

$$\tau_i = \frac{2\,L}{c} + M \qquad [4]$$

The time M is, in itself, composed of two terms. One of these is the time for the extra slug of gas to pass through the burner port, that is, the length s, of the ports divided by the gas velocity V through the ports. The other term gives the average time for the gas to be burned, after leaving the port. If the flame is laminar, the approximate length is given by aV/F, where a is the port radius and F is the flame speed. If the mean burning length is assumed to be one third of the total length, the time to reach this mean distance is $(1/3)(aV/F)/V$, or $a/3F$. Therefore

$$M = \frac{s}{V} + \frac{a}{3\,F} \qquad [5]$$

It has been emphasized already that the period τ_i of the driver must be close to the natural period of the oscillating unit. Thus, the time τ_i should "nearly" correspond to the time between two pressure pulses in the combustion tube. This latter time is some multiple n of the observed oscillation period τ of the entire unit. The term "nearly" means that τ_i must differ from $n\,\tau$ by a factor less than $\tau/4$; if the difference were greater, then τ_i would be such that the addition of heat by the additional slug of burned gas would fall between maximum pressure times, or near minimum pressure times, thus damping the oscillation. The condition for resonance can thus be written as

$$n\tau \pm \frac{1}{4}\,\tau\epsilon = \tau_i = \frac{2\,L}{c} + M, \quad \epsilon < 1, \quad n = 1, 2, \ldots$$

A more convenient form of this equation is obtained by using the observed frequency ν as a substitute for the reciprocal of the observed period, and defining the fundamental frequency of the mixing chamber $c/2L$ as ν_m; thus

$$\frac{\nu}{\nu_m} = \left(n \pm \frac{1}{4}\,\epsilon\right) - M\nu, \quad \epsilon < 1, n = 1, 2, \ldots \qquad [6]$$

This is the equation of a set of straight lines, each of slope $-M$, when ν/ν_m is plotted against ν.

Fig. 3 shows the data of Table 1 plotted as ν/ν_m against ν; this

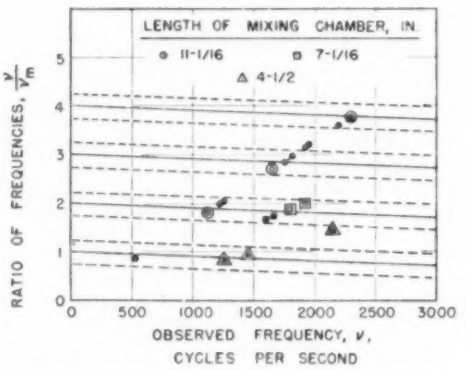

FIG. 3 PERMISSIBLE INTERVALS OF OSCILLATIONS BASED ON PERIOD OF FEED-BACK CYCLE
(Solid lines indicate mid-points of intervals.)

method of plotting is indicated by Equation [6]. From these data it was found, by the least-squares method, that the value of M (slope of the lines shown) which gave the smallest average deviation from lines passing through integral values of ν/ν_m at $\nu = 0$, as required by Equation [6], was $M = 1.05 \times 10^{-4}$ sec. The solid lines shown in Fig. 3 were drawn for $\epsilon = 0$, and dashed lines were drawn for $\epsilon = 1$. With two exceptions, the observed frequencies fall within the regions demarcated by the dashed lines.

The slope M, as determined by direct calculation using the measured or known values for s, V, a, and F, in Equation [5], is 1.1×10^{-4} sec. This value differs from that calculated from the data by less than 5 per cent, which is considered to indicate agreement between data and theory.

In summary, the driving criterion, defined by Equation [6], implies that an oscillation of the gases in the combustion system can be amplified when the oscillating component of the rate of heat release is in phase with the oscillating component of the pressure at the point of heat release. The method of analysis developed so far has shown (*a*) agreement with experimental data in establishing that oscillations of high intensity occur when this driving criterion is fulfilled, and (*b*) agreement in the calculated value of the lag term M with the value obtained by test.

Space Condition for Resonance. An additional requirement, mentioned earlier, that must be met if the oscillation is to build up to a large amplitude, is that the point of heat release must be located near an antinode of the standing pressure wave in the combustion tube. The next step in this development is, therefore, a determination of those regions in which oscillations may occur when account is taken of the reduced efficiency of the driver, that is, the flame, as the burner head is moved in relation to the

combustion tube away from the regions of highest oscillating pressure amplitude. This approach is the one that would be used in analyzing, for the purpose of minimizing or promoting oscillations, any practical combustion systems having the general configuration shown in Fig. 2.

Fig. 4 is the first of a series of figures necessary for the prediction of the permissible regions of oscillation. The calculated frequency ν for a 17-in. combustion tube is plotted as a function of

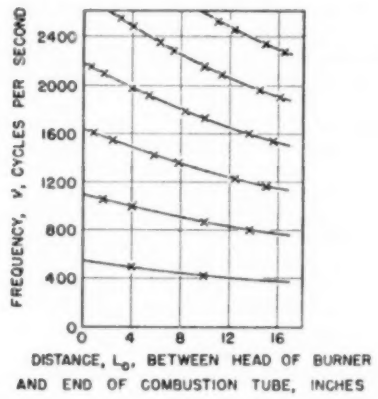

FIG. 4 COMPUTED FREQUENCY OF COMBUSTION TUBE AS A FUNCTION OF BURNER-HEAD POSITION, WITH MIDDLE THIRDS ON PRESSURE LOOPS INDICATED BY PAIRS OF X

the distance L_0, from the burner head to the tube entrance for the first six modes of vibration, by means of the equation

$$\nu = \frac{n\,c}{2\left[L_0 + L_e + \sqrt{\frac{\gamma_a T_a}{\gamma_b T_b}}\,(L_t - L_0)\right]}, \quad n = 1, 2, \ldots \quad [7]$$

where L_e is the total end correction, L_t is the total length of the combustion tube, subscripts a and b refer to ambient and burned-gas conditions, respectively, T is the absolute temperature, and γ is the ratio of specific heats. This equation is of the same form as Equation [2], with the open-end correction L_e added and the length of hot section corrected for the increased velocity of sound. The end correction, for each end, is given by Wood[4] as 0.6 of the radius, so that L_e for the two ends of the tube is 0.6 of the diameter. The easiest way to include the effect of the hot regions is to correct the length to an equivalent cold length. Since the traverse time of a pulse must be the same in the hot and in the equivalent cold sections, the hot length divided by the corresponding speed of sound must equal the equivalent cold length divided by the ambient speed of sound. Since the ratio of these sound speeds varies as the square root of the γT-terms, the equivalent cold length of the hot zone is

$$(L_t - L_0)\sqrt{\gamma_a T_a/\gamma_b T_b}$$

For the tests being discussed, the average temperature T_b of the gases in the hot zone was determined, from measurement with a thermocouple, to be approximately 740 F, or 1200 R. At this temperature, the speed of sound is 1700 fps, as compared with 1127 fps at 70 F. In this calculation, it is assumed that γ_a equals γ_b, so that $\gamma_a/\gamma_b = 1$. The ratio $\gamma_a T_a/\gamma_b T_b$ for these tests is equal to 0.663, so that the equivalent cold length of the hot zone is $0.663\,(L_t - L_0)$. This expression was substituted in Equation [7], which is the equation of the set of the six curves shown in Fig. 4, for values of n ranging from $n = 1$ to $n = 6$.

On the frequency lines of Fig. 4, are also marked the pairs of positions, in terms of L_0, where the burner head just starts to move into the middle third of a pressure loop, or starts to move out. These values of L_0 are given by

$$L_0 = \frac{n'c}{6\nu} - \frac{L_e}{2}, \quad n' = 1, 2, 4, 5, 7, 8, \ldots$$

This marking of the middle thirds of the loops corresponds to an assumption that heat addition only in the middle third of a pressure loop would be sufficiently effective to compensate for damping forces and thus promote oscillations.

Fig. 5 is a replot of Fig. 4, with adjustments to compensate for the fact that the frequencies occurring will not agree exactly with the frequencies computed for the combustion tube only. This is to be expected, since the combustion unit is a coupled system of the supply chamber and of the combustion chamber, and is not a single unit. The middle third of each pressure loop, as located on the mode lines, is extended as an area over the region between the mode lines in the following manner: The ends of the middle-third ranges are connected by lines sweeping upward to the left, to give the regions *A*. In a similar manner, the ends are also connected by dashed lines sweeping upward to the right to give corresponding areas *B*. The overlapping portions of these areas *A* and *B*, the final areas to be considered, are crosshatched. Thus, Fig. 5 shows the areas (crosshatched), in which the pressure amplitude of the oscillations will be large enough to overcome the damping forces, on the basis of the assumption of the preponderant effect of the middle third of the pressure loop. Further research on the methods of computing the exact values of damping and driving forces should lead to a more precise handling of this phase of the problem.

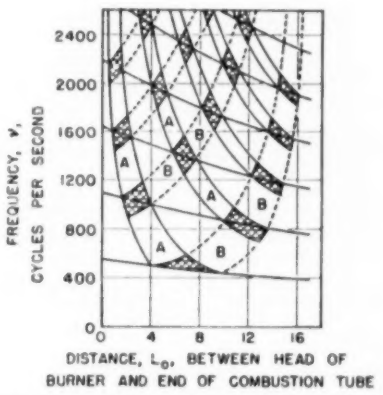

FIG. 5 EXTENSION OF MIDDLE THIRDS ON PRESSURE LOOPS OVER REGIONS BETWEEN MODE LINES

Co-Ordination of Space and Time Conditions. Fig. 6 is a replot of the permitted areas of oscillation, based on the time-phase relation, from Fig. 3. Co-ordinates have been changed to allow direct comparison with Fig. 5. The pairs of curves bounding the lined areas are drawn, using Equation [6], for $\epsilon = 1$. These lined areas correspond to regions in which oscillations can occur on the time-phase basis. For example, the vertical line shown at the computed frequency ν_m of 615 cps, for the mixing-chamber length of $11^1/_{16}$ in., gives the ranges of values of ν, for the first four modes, which are possible for this particular mixing chamber. According to the theory developed, oscillations will occur for only those portions of the crosshatched areas of Fig. 5, which fall within the permitted regions given by Fig. 6. Fig. 7 shows the areas fulfilling these conditions; for comparison, the observed

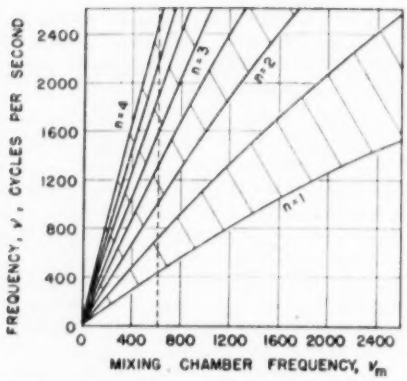

FIG. 6 PERMISSIBLE INTERVALS OF OSCILLATIONS BASED ON PERIOD OF FEED-BACK CYCLE

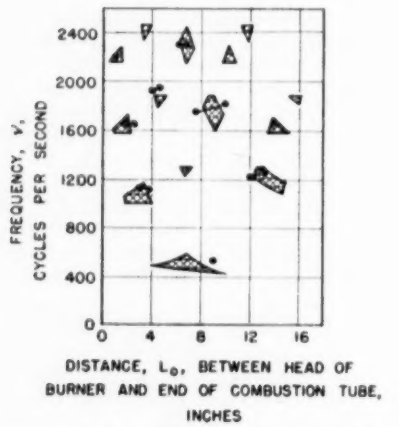

FIG. 7 COMPARISON OF REGIONS OF OSCILLATION PREDICTED BY THEORY WITH TEST RESULTS, FOR 11 1/16-IN. MIXING CHAMBER

frequencies listed in Table 1, for the mixing chamber of length of 11 1/16 in., are indicated by circles. They fall within, or close to, the corresponding permitted region.

At many positions of the burner head in the combustion tube, given by the abscissas in Fig. 7, oscillations might be expected to occur at more than one frequency. However, the tests show that, in most instances, one frequency predominates; to predict which one would require more detailed analysis.

The method of analysis outlined has been found to apply equally well for the two other mixing-chamber lengths studied, and for ports of a different depth. For the deeper ports, the number of oscillation regions observed decreased, probably as a result of increased damping losses.

Practical Application. At least three methods of eliminating a particular oscillation are suggested by these results. They are (*a*) moving the position of the burner head; (*b*) changing the length of the mixing chamber; and (*c*) changing the length or diameter of the burner ports.

Considering the second-mode frequency of 1100 cps at $L_0 \cong 3$ in. in Fig. 7, a practical method of elimination would be either the increase or decrease of this distance L_0 of the burner head beyond the inlet of the combustion tube. It can be seen, from inspection of the figure, that such a change in position might produce another frequency. However, in commercial equipment, not nearly so many higher modes of oscillation are present as in the test equipment described, which was designed to study oscillations; therefore, such a solution would be practical.

Fig. 6 shows that, as the mixing-chamber frequency is increased, the permissible ranges move upward to higher frequencies. It is seen from Equation [2], which is valid for a tube closed at both ends as well as for a tube open at both ends, that the frequency of a mixing chamber 10 in. long would be higher than the frequency of an 11 1/16-in. chamber. The increase in frequency obtained with a 10-in. chamber would raise the permissible range to higher frequencies by an amount sufficient to eliminate the permissible region of Fig. 7, mentioned previously, and thus eliminate the observed frequency of 1100 cps. However, a further decrease of the mixing-chamber length to 7 3/4 in. would result in a still higher frequency, and the oscillation would be reinstated, since another frequency band would be brought into the critical area.

An interesting possibility of eliminating an oscillation is offered by the use of two sizes of burner port, having different diameters and lengths, such that when ports of one size fulfill the conditions of Equation [6], those of the other size cause the two components of the system to be exactly out of phase. This requires that the difference of the M's characterizing the two different port sizes be approximately equal to $1/2\nu$. The size difference may be reduced somewhat in units where different rows of ports are at staggered distances from the far end of the mixing chamber, if the larger deeper ports are put in the farther rows.

Promotion of the oscillations, if that were desirable, would follow from carrying out changes opposite to those described.

ROCKET-SHAPED BURNER WITH PREMIXED GAS

Apparatus. Fig. 8 shows the rocket-shaped burner used in this phase of the investigation. As constructed, the length of the mixing chamber could be varied from nearly zero to about 7 in. by adjusting the position of the movable piston. As shown, the head of the piston includes an annulus for premixing the air and hydrogen; hydrogen enters the annulus through a small orifice, and air through a larger tube. The fuel-and-air mixture passes through an annular slot into the variable-volume plenum chamber. The burner nozzle is recessed so that various tubular com-

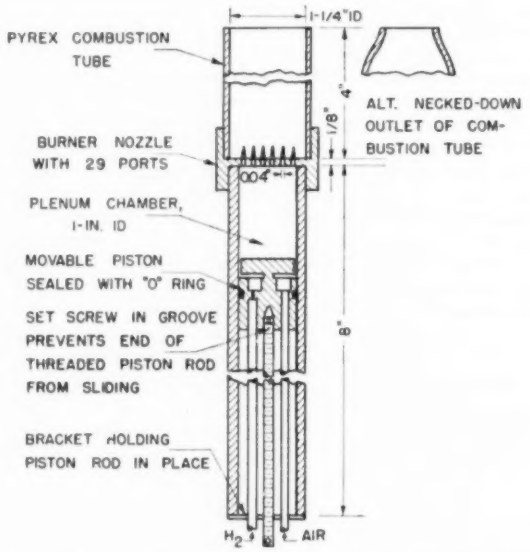

FIG. 8 SCHEMATIC DIAGRAM OF ROCKET-SHAPED BURNER WITH PREMIXED-GAS FLAME

bustion chambers can be placed around the top of the burner. These chambers are closed effectively at the level where the flame is burning, since the total area of the port openings is only a very small fraction of the cross-sectional area of the plenum chamber.

There are two characteristics of this system not present in the previously discussed combustion tube and burner head: (*a*) The flame, and consequently the maximum heat-release rate, is at the closed end of the combustion tube, where the maximum pressure amplitude of any standing oscillation is always found. Thus the requirement of a strong driving potential, as indicated by the crosshatched areas in Fig. 5, for the previously discussed system, is always satisfied in this unit. (*b*) A cut off of the higher modes of oscillation exists in any unit when the quarter wave length is about equal to the diameter of the unit. For the 4-in. combustion tube, the quarter wave length of the second mode is about $1^1/_3$ in., whereas the diameter of the tube is $1^1/_4$ in. Thus, the frequency cut off for the combustion tube will occur at about the second mode of oscillation, and the only oscillation that will be found in the test units will be a first-mode oscillation. As a result, the higher-mode oscillations which had to be considered in the previous section can be disregarded in this section.

Method of Test. Oscillations occurred in the apparatus shown in Fig. 8 only for certain intervals of displacements of the piston; these displacements changed the effective length and hence the natural frequency of the plenum chamber. Between such oscillating regions were blank intervals where no oscillation occurred. However, in contrast to the previously discussed system, the observed frequency did not change markedly from one region to another, and the blank intervals were small. The experimental work was carried out in the same manner as before, with a slow movement of the piston along the plenum chamber corresponding to the movement of the burner head along the combustion tube in the previous system.

Data also were obtained at intermediate points within each interval of oscillation. Combustion tubes of various lengths were used; some of these were necked-down at the outlet, as shown in the diagram at the upper right corner in Fig. 8, so that the area of the outlet was either one half or one fourth as large as the area of the inlet of the tube.

Discussion of Test Results. Table 2 presents data, for several different combustion tubes, on the frequency and plenum-chamber length L, defining the beginning and end of each displacement interval of oscillation. These data were used in a manner exactly analogous to those of Table 1, in obtaining a value of M for use in Equation [6]. The value of M, in this instance, was 3.5×10^{-4} sec, as compared with a value of M computed from Equation [5] of 4.4×10^{-4} sec. The agreement here is not so good as that obtained previously; this is probably caused in part by the assumption of completely closed ends, rather than nearly closed ends, in the computation of plenum-chamber frequency. The experimental value was used in the further treatment.

Table 3 presents the complete frequency and plenum-chamber-length data for the two lengths used of combustion tubes of uniform diameter.

TABLE 2 FREQUENCIES AND DISPLACEMENT INTERVALS OF OSCILLATION FOR ROCKET-SHAPED BURNER AND COMBUSTION TUBE

(s = 0.121 in.; a = 0.02 in.; V = 32.8 fps; F = 55 ipa)

Configuration of combustion tube	Length of combustion tube, in.	Interval of oscillation	—Beginning of interval— L, in.	ν, cps	—End of interval— L, in.	ν, cps
Cylindrical	3	1	$6^5/_8$	1800	$4^1/_2$	1930
Cylindrical	3	2	$3^3/_8$	1730	$^3/_4$	1950
Cylindrical	4	1	6	1550	$5^1/_2$	1550
Cylindrical	4	2	$5^1/_4$	1350	$^3/_4$	1610
OA = $^1/_2$ IA	3	1	$6^5/_8$	1620	$5^3/_4$	1680
OA = $^1/_2$ IA	3	2	$4^3/_4$	1550	$^3/_4$	1680
OA = $^1/_2$ IA	4	1	$6^1/_2$	1430	$6^1/_4$	1330
OA = $^1/_2$ IA	4	2	$5^3/_4$	1200	1	1450
OA = $^1/_4$ IA	2	1	$6^5/_8$	1850	$4^1/_2$	1930
OA = $^1/_4$ IA	2	2	$3^3/_4$	1750	$^3/_4$	1950
OA = $^1/_4$ IA	3	1	$6^5/_8$	1500	$5^3/_4$	1540
OA = $^1/_4$ IA	3	2	5	1370	1	1520

NOTE: OA = outlet area; IA = inlet area.

TABLE 3 FREQUENCIES AND PLENUM-CHAMBER LENGTHS OF ROCKET-SHAPED BURNER WITH CYLINDRICAL COMBUSTION TUBES FOR FIRST AND SECOND DISPLACEMENT INTERVALS OF OSCILLATION

(s = 0.121 in.; a = 0.02 in.; V = 32.8 fps; F = 55 ipa)

Length of combustion tube, in.	—First interval— of oscillation L, in.	ν, cps	—Second interval— of oscillation L, in.	ν, cps
3	$6^5/_8$	1800	$3^3/_8$	1730
3	6	1820	3	1760
3	5	1900	2	1860
3	$4^1/_2$	1930	1	1950
3	...	...	$^3/_4$	1950
4	6	1550	$5^1/_4$	1350
4	$5^1/_2$	1550	5	1350
4	...	...	4	1390
4	...	...	3	1450
4	...	...	2	1490
4	...	...	$1^1/_2$	1610
4	...	...	$^3/_4$	1610

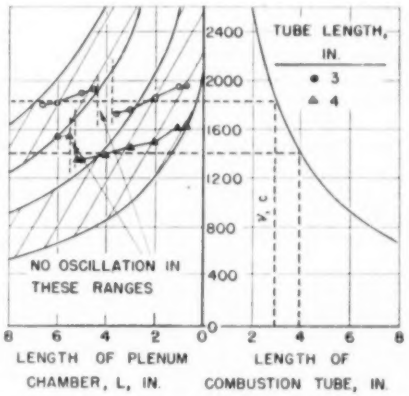

FIG. 9 PREDICTED REGIONS OF OSCILLATION COMPARED WITH DATA FOR THE PREMIXED-GAS FLAME, ROCKET-SHAPED BURNER (Combustion tubes are cylindrical and port length is 0.121 in.)

Fig. 9, on the left side, shows the oscillation data of Table 3 and the predicted regions of oscillation for the 3-in. and for the 4-in. cylindrical combustion tubes. As previously indicated, this figure is more easily obtained than Fig. 7, for the open-end combustion tube, because the space condition of the flame, near the pressure antinode, which is the optimum point for oscillation build-up, is fixed, and only the time condition need be considered. On the right half of Fig. 9, the fundamental frequency of the hot combustion tube, considered as being closed at one end, is plotted as a function of length, using the relation

$$\nu = \frac{(2n-1)\, c\sqrt{\gamma_b T_b/\gamma_a T_a}}{4(L_t + L_e)}, \quad n = 1, 2, \ldots\ldots \quad [8]$$

where the symbols are defined in the same manner as in Equation [7]. Equation [8] is of the same form as Equation [3], with the open-end correction L_e added and the speed of sound c at ambient temperature corrected for the increased temperature in the combustion tube. The end correction L_e for the single open end is 0.6 of the radius. As previously stated, the speed of sound varies as the square root of the product γ_T, and it is again assumed that γ_a/γ_b equals 1. An average temperature T_b was determined, by measurement with a thermocouple, for each of seven different combustion tubes varying, at 1-in. intervals, from

2 in. to 8 in. in length. These values of T_b were used in Equation [8] for plotting the curve shown on the right side of Fig. 9. The higher-mode curves are omitted for the previously stated reason that the higher-mode wave lengths are too short. Dashed lines corresponding to the tube lengths of Table 3 are drawn in.

The curves bounding each of the crosshatched regions on the left side of Fig. 9 are obtained from Equation [6] by substituting $c/2L$ for ν_m and plotting ν against L for $\epsilon = 1$ and for the value of M obtained from the data. The regions shown are between the curves for $(n + 1/4)$ and $(n - 1/4)$; these regions are those in which oscillations should occur, and correspond to those in Fig. 6. The hyperbolic shape of these curves is due to the use of L, the primary variable in this test, as a co-ordinate, rather than the frequency ν_m, with which L varies in an inverse manner.

In Fig. 9, the dashed horizontal lines are extended from the right side into the left half of the plot at the frequency corresponding to the length of the combustion tube. In each instance, the measured frequencies fall within, or close to, the permitted regions, and also fall close to the fundamental frequency of the combustion tube. Too much significance should not be attached to data at the lower values of mixing-chamber length, since in this range the plenum chamber is roughly spherical and, in combination with the orifices, probably acts more like a Helmholtz resonator than a long tube and should be considered as such.

The upward sweep of the data points, as length of plenum chamber decreases, is caused by the coupling of the combustion tube, the frequency of which is given by the horizontal dashed line, with the plenum chamber, frequencies of which are given by mean curves through the upward-sweeping lined areas. This slope of the observed frequency curves, caused by the coupling described, allows them to remain in the "permitted" areas for a greater range of lengths of the plenum chamber than otherwise might be expected. Because of the approximation made in the theory, and of the possible error in some of the measured values, the small deviations of some of the data points which place them outside of permitted regions did not warrant closer investigation.

Results similar to those in Fig. 9 also were obtained with combustion tubes necked-down to varying degrees at the outlet and with burner ports of twice the depth of those in Fig. 9.

Diffusion-Flame Rocket-Shaped Burner

In the rocket-shaped burner just discussed, fuel and air were premixed. The phase of the investigation to be described now concerns observations of the oscillations produced with a combustion system in which fuel and air are introduced separately into the combustion chamber.

Apparatus. Fig. 10 shows the combustion system used in this phase of the study. In this burner, hydrogen enters the combustion chamber through four small jets equally spaced around a larger air-supply opening. These jets are connected to an annular slot, filled with hydrogen, built into the burner nozzle. Air is supplied through an acoustically padded cylindrical plenum chamber 13 in. long with an outside diameter of 8¾ in., thus simulating an infinite chamber. A ¼-in-ID tube of variable length, attached to the air chamber, extends through the center of the burner to the upper surface of the nozzle. The length of this air-supply tube was varied from about 14 in. to 2 in., using the same test procedure as for the two combustion systems discussed previously. Both cylindrical combustion tubes and tubes necked-down at the outlet were used.

With this apparatus, oscillations occurred when the rates of flow of hydrogen and air were such that a diffusion flame burned at the upper surface of each of the hydrogen jets. It was found that variations in the length of the air-supply tube caused significant changes in the intensity of oscillation.

Analysis of Oscillation Mechanism. The analysis of the oscillation mechanism presented in the first section of this paper showed that a time condition for resonance must be satisfied if an oscillation is to occur. A similar development is necessary for the diffusion-flame rocket-shaped burner.

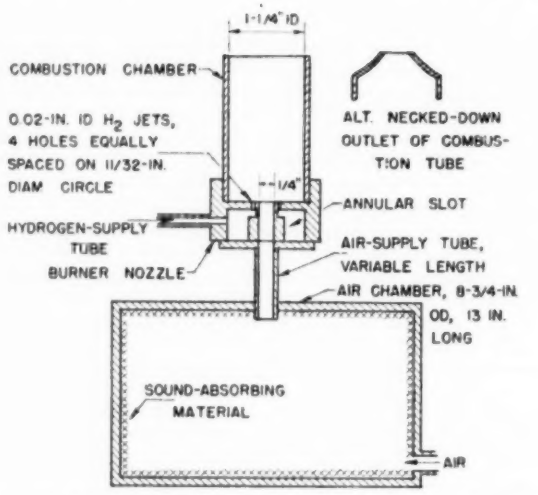

Fig. 10 Schematic Diagram of Diffusion-Flame Rocket-Shaped Burner

The period τ_t of the cycle in the air-supply tube is given by

$$\tau_t = \frac{2N}{c} - \frac{1}{2}\tau + M \qquad [9]$$

where

$$M = \frac{h}{V}$$

and N is the air-supply-tube length, c is the velocity of sound at room temperature, τ is the observed period of oscillation, h is the mean length of the flame, and V is an average velocity of the air in the region of the flame. The factor $\tau/2$ accounts for the phase shift occurring at the upstream end of the tube; that is, the fact that the open end of the tube reflects a pressure pulse as a rarefaction, and conversely. If the tests on the previously discussed combustion tube and burner head had been run with a large volume substituted for the closed upstream end of the plenum chamber, the factor $\tau/2$ would have been used in Equation [4] also.

Equation [9] also can be expressed as

$$\frac{\nu}{\nu_a} = \left(n + \frac{1}{2} \pm \frac{1}{4}\epsilon\right) - M\nu, \quad \epsilon < 1, n = 1, 2, \ldots \qquad [10]$$

where ν_a is the fundamental frequency of the air-supply tube, and ν is the observed frequency. This is the equation of a set of straight lines of slope $-M$ when ν/ν_a is plotted against ν.

In computing the mean length h, it was assumed that the equations which had been developed by Hottel and Hawthorne[6] could be used for the rate of diffusion of gas from one stream tube to another. The mean length was considered to be the distance to the point at which a stoichiometric fuel/air ratio is reached on the axis of the fuel jet, since the combustion front slanted across the

[6] "Diffusion in Laminar Flame Jets," by H. C. Hottel and W. R. Hawthorne, Third Symposium on Combustion, Flame, and Explosion Phenomena, Williams & Wilkins Company, Baltimore, Md., 1949, Appendix I, p. 254.

hydrogen jet from one side. A precise result cannot be expected from this calculation because of the difference between required theoretical conditions and test conditions.

From the foregoing reference,

$$C = 1 - e^{-\frac{1}{4\theta}} \qquad [11]$$

where C is the fuel concentration, and θ is a nondimensional time defined by the relation $\theta = Dt/a^2$; D is the diffusion coefficient; a is the radius of the fuel jet; and $t = h/V$, or M. Since, for a stoichiometric hydrogen-air mixture, $D = 0.0621$ sq in. per sec, the expression for θ can be written as

$$\theta = \frac{0.0621\,(M)}{a^2} \cong \frac{3}{4}$$

where $\theta \cong {}^3/_4$ corresponds to the stoichiometric value of C of 0.296 as obtained from Equation [11]. It is seen from this equation that M depends only on the radius of the fuel jet.

Discussion of Test Results. Table 4 is a compilation of the end points of the displacement intervals of oscillation for several combustion tubes. These data were treated as were the data of Table 1 in obtaining a value for M; however, comparison of Equation [10] with Equation [6] shows that $(n + {}^1/_2)$ must be used in place of n in calculating M. The value of M from the data is 1.0×10^{-3} sec, whereas the value of M obtained from theory is 1.2×10^{-3} sec. The two values show good agreement, considering the assumptions necessarily made in obtaining the theoretical value. As in the previous instances, the value determined from the data was used in the further development.

TABLE 4 FREQUENCIES AND DISPLACEMENT INTERVALS OF OSCILLATION FOR DIFFUSION-FLAME ROCKET-SHAPED BURNER AND COMBUSTION TUBE

(a = 0.01 in.)

Configuration of combustion tube	Length of combustion tube, in.	Interval of oscillation	Beginning of interval: Length of air-supply tube, in.	Beginning of interval: ν, cycles per second	End of interval: Length of air-supply tube, in.	End of interval: ν, cycles per second
Cylindrical	3	1	2 3/8	1200	6	1200
Cylindrical	3	2	7 1/8	1300	9 10 3/4	1200
Cylindrical	3	3	11	1300	14	1300
Cylindrical	6	1	2 3/8	800	8 5/8	750
Cylindrical	6	2	9 1/4	800	15	750
OA = 1/2 IA	3	1	2 3/8	1200	6 3/8	1100
OA = 1/2 IA	3	2	7 13/16	1200	14 13/16	1150
OA = 1/2 IA	4	1	2 3/8	950	7 1/8	850
OA = 1/2 IA	4	2	8	1000	15	900
OA = 1/4 IA	3	1	2 5/8	1050	7 1/8	1000
OA = 1/4 IA	3	2	7 5/8	1100	11 15/16	1000
OA = 1/4 IA	3	3	12 1/8	1100	14 5/8	1050

NOTE: OA = outlet area; IA = inlet area.

Table 5 presents the complete frequency and air-supply-tube-length data for two combustion tubes, one 3 in. long and one 4 in. long; the outlet area equaling one half the inlet area for each of these tubes.

Fig. 11 shows the data of Table 5 and their relation to the predicted permitted regions. The lined areas to the left of the ordinate show the regions, in terms of length of the air-supply tube, in which oscillations should occur. The curves bounding the lined areas were obtained by plotting frequency against length of air-supply tube, using Equation [10], with $\epsilon = 1$ and ν_a replaced by the ratio of the speed of sound to twice the length of the air-supply tube.

The curve to the right of the ordinate in Fig. 11 represents the fundamental frequency of the combustion tube as a function of length. The procedure for calculating the natural frequencies of the necked-down combustion chambers is as follows: The solid lines in Fig. 12 show the actual configuration of a necked-down

TABLE 5 FREQUENCIES AND LENGTHS OF AIR-SUPPLY TUBE FOR DIFFUSION-FLAME ROCKET-SHAPED BURNER, USING COMBUSTION TUBES WITH OUTLET AREA EQUAL TO ONE-HALF INLET AREA

(a = 0.01 in.)

Length of combustion tube, in.	Interval of oscillation	Length of air-supply tube, in.	ν, cps
3	1	2 3/8	1200
3	1	3 1/4	1200
3	1	4	1200
3	1	5	1200
3	1	6	1100
3	2	7 13/16	1200
3	2	8 1/4	1200
3	2	9 1/4	1200
3	2	10 1/8	1200
3	2	11 1/8	1100
3	3	11 7/8	1200
3	3	12 7/8	1150
3	3	14	1150
4	1	2 3/8	950
4	1	3 3/8	950
4	1	5	900
4	1	6	900
4	1	7 1/8	850
4	2	8 1/4	1000
4	2	9	950
4	2	11	950
4	2	12 1/8	900
4	2	13 3/8	900
4	2	13 1/8	900
4	2	14	900

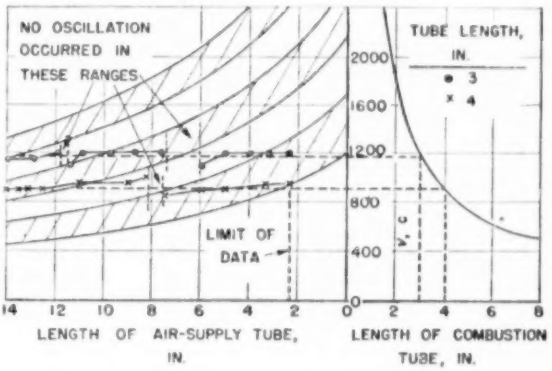

FIG. 11 PREDICTED REGIONS OF OSCILLATION COMPARED WITH DATA FOR DIFFUSION-FLAME ROCKET-SHAPED BURNER
(Outlet area of each combustion tube equals 1/2 inlet area.)

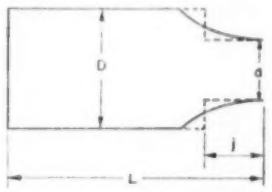

FIG. 12 SKETCH OF APPROXIMATE CONFIGURATION USED TO COMPUTE NATURAL FREQUENCIES OF NECKED-DOWN COMBUSTION CHAMBERS

chamber, while the dashed lines show a hypothetical configuration. The included volume for each configuration is the same. Using the hypothetical case, an approximate expression for the frequency ν of the actual chamber can be computed, by a trial-and-error procedure, from the relation

$$\tan \frac{2\pi\nu}{c\sqrt{\gamma_b T_b/\gamma_a T_a}}(L - j) \tan \frac{2\pi\nu}{c\sqrt{\gamma_b T_b/\gamma_a T_a}}(j + 0.3d) = \left(\frac{d}{D}\right)^2 \qquad [12]$$

where L, j, d, and D are shown in Fig. 12, and $0.3d$ is the end correction for the single open end. The speed of sound c at ambient temperature is corrected in Equation [12] for the increased temperature of the gases in the chamber. The approximate values of ν obtained from Equation [12] have been used successfully in the reduction of the data obtained using necked-down combustion chambers.

As before, an average temperature T_b was determined, by measurement with a thermocouple, for each of seven different combustion chambers. These values of T_b were used in Equation [12] to obtain the approximate values of ν, which are plotted on the right side of Fig. 11.

The dotted horizontal lines extending from the right side into the left half of the plot show the frequencies corresponding to the lengths of combustion tube used. In general, the measured frequencies fall within, or very close to, the permitted regions, and also fall close to the fundamental frequency of the combustion tube at all the lengths used for the air-supply tube.

Practical Applications. The results of the investigation of the two rocket-shaped burners disclose further possibilities for eliminating oscillations beyond those discussed in connection with the doubly-open combustion tube and burner. From inspection of Figs. 9 and 11, it is seen that changes in the lengths of the plenum chamber, for the premixed-gas flame burner, and of the air-supply tube, for the diffusion-flame burner, would not be helpful in eliminating oscillations for the lengths shown, unless the supply system were made extremely short. This is true because (*a*) the ranges in which no oscillations occur are, in general, very narrow; (*b*) in terms of the time-phasing conditions, shown on the left sides both of Fig. 9 and of Fig. 11, many modes of oscillation of either of the supply systems are possible; and (*c*) the flame is located at the optimum point for driving.

An increase in length of the combustion tube will lower the natural frequency of the tube, and also will increase the width of the ranges in which no oscillations can occur. Thus, this increase will allow the first-mode oscillation to be eliminated more easily by decreasing the length of the supply system. However, an appreciable increase in length of the combustion tube will cause the quarter wave length of the second-mode oscillation to be greater than the diameter of the tube. Thus, it would be possible for this second-mode oscillation to occur, and its elimination would be a problem. However, if the distance from the flame to the exit of the combustion tube is maintained constant, and the length of the tube is increased, the flame will be moved away from the optimum driving position and the amplitude of oscillation will be reduced.

The tests on the two rocket-shaped burners also show the effect of the diameter on the cut-off frequency. Thus, the highest observed frequency plotted in Fig. 7, for the doubly-open combustion tube and burner, could be eliminated by increasing the diameter of the combustion chamber.

For promotion of oscillation, if that is desired, methods opposite to those previously described for suppression of the oscillations would be used; that is, the length of the supply system would not be decreased; the flame would be located at the closed end of the combustion tube, and the diameter of the combustion tube would be decreased relative to the length of the tube.

Conclusions

This study shows that natural-frequency oscillations which occurred in three simple combustion systems, having different configurations, can be explained by elementary considerations of both (*a*) the time of travel of a pressure pulse through the system, and (*b*) the position of the flame in relation to the combustion tube. The basic assumptions used in these considerations are that (*a*) an oscillating component of the rate of heat release must be in phase with the pressure variation, and (*b*) the point of heat release must be near the point of maximum pressure amplitude in the combustion tube. The first assumption is confirmed by the thermodynamic proof given in the Appendix.

It was found, from analysis of the test results, that oscillations were amplified in the systems studied when both of the requirements just stated were fulfilled simultaneously, thus confirming the validity of the assumptions. From knowledge gained in this study of the manner of promotion of these oscillations, the amount and type of change in apparatus configuration necessary either to eliminate or to encourage the oscillation can be determined.

Acknowledgment

The work described in this paper was conducted under the sponsorship of the Flight Research Laboratory, Wright Air Development Center, United States Air Force. The assistance of R. W. Baker, Battelle staff, in the preparation of the Appendix, is gratefully acknowledged.

Nomenclature

The following nomenclature is used in the Appendix:

A = cross-sectional area; arbitrary constant
B = arbitrary constant
E = internal energy per unit mass
F = function of x
G = function of t
K = arbitrary constant
M = arbitrary constant
N = arbitrary constant
P = instantaneous pressure
P_0 = equilibrium pressure
Q = heat energy per unit mass
R = gas constant
S = entropy per unit mass
T = instantaneous temperature
T_0 = equilibrium temperature
$\Delta T = T - T_0$
X = function of x
c = velocity of sound
c_p = specific heat at constant pressure
h = enthalpy per unit mass
$p = P - P_0$
t = time
x = distance along channel
α = damping factor
γ = ratio of specific heat at constant pressure to specific heat at constant volume

$$\delta = \frac{\rho - \rho_0}{\rho_0}$$

λ = wave length
ρ = instantaneous density
ρ_0 = equilibrium density
ω = angular frequency
θ = function of t
ξ = displacement of gas due to sound wave, $\xi = \xi(x, t)$
φ = phase angle

Thermodynamic Analysis of Phase Requirement for a Heat-Driven Oscillation

It can be assumed, for obvious reasons, that, in an oscillating combustion system, if an oscillation is driven by the periodic component of the rate of heat addition, phasing of the rate of heat addition with the pressure variation is necessary. If this phasing requirement is not met, the periodic heat addition will tend to

damp out the oscillations. This requirement in phasing is indicated but not proved in the literature.

Mathematically, and neglecting damping forces, this concept requires that the time integral, over a cycle, of the instantaneous product of the rate of heat release and of the oscillating component of the pressure be greater than zero. It is the purpose of this Appendix to offer thermodynamic proof of this phasing requirement. The proof is accomplished by extending a customary derivation of the wave equations for acoustic oscillations.

Nonadiabatic Expansion Law

The first law of thermodynamics may be written as

$$dE + Pd\frac{1}{\rho} = dQ$$

where dE is the change of internal energy per unit mass of fluid, $Pd(1/\rho)$ is the increment of work done by unit mass of the fluid, and dQ is the heat added per unit mass of fluid. Since, by definition

$$dh = dE + Pd\frac{1}{\rho} + \frac{1}{\rho}dP$$

where dh is the change of enthalpy per unit mass, the First Law may be rewritten as

$$dh - \frac{1}{\rho}dP = dQ \qquad [13]$$

Assuming a perfect gas, wherein dh equals $c_p dT$, and P/ρ equals RT, Equation [13] becomes

$$\frac{c_p}{R}\frac{dT}{T} - \frac{dP}{P} = \frac{dQ}{RT} \qquad [14]$$

Integrating Equation [14] between the equilibrium state (subscript $_0$) and some instantaneous state (no subscript) gives

$$\ln\left[\left(\frac{T}{T_0}\right)^{c_p/R}\left(\frac{P_0}{P}\right)\right] = \frac{1}{R}\int_0 \frac{dQ}{T} = \frac{\Delta S}{R} \qquad [15]$$

where ΔS represents the entropy change from the equilibrium state. From Equation [15], it follows that

$$\frac{T}{T_0} = \left(\frac{P}{P_0}\right)^{R/c_p} e^{\Delta S/c_p} \qquad [16]$$

Assuming $c_p = \gamma R/(\gamma - 1)$, Equation [16] can be expressed as

$$\frac{T}{T_0} = \left(\frac{P}{P_0}\right)^{\frac{\gamma-1}{\gamma}} e^{\left(\frac{\gamma-1}{\gamma}\right)\frac{\Delta S}{R}} \qquad [17]$$

From the equation of state for a perfect gas, and from Equation [17]

$$\frac{\rho}{\rho_0} = \left(\frac{P}{P_0}\right)\left(\frac{T_0}{T}\right) = \left(\frac{P}{P_0}\right)^{1/\gamma} e^{-\left(\frac{\gamma-1}{\gamma}\right)\frac{\Delta S}{R}} \qquad [18]$$

Equations [17] and [18] are the general equations for the nonadiabatic expansion of the fluid.

The region of small deviations from the average values is now considered. Using the relations $\rho = \rho_0(1 + \delta)$, and $P = P_0 + p$, Equation [18] becomes

$$1 + \delta = \left(1 + \frac{p}{P_0}\right)^{1/\gamma} e^{-\left(\frac{\gamma-1}{\gamma}\right)\frac{\Delta S}{R}} \qquad [19]$$

If the term within parentheses on the right side of Equation [19] is expanded, and terms of higher order than the first are neglected, Equation [19] can be written in the form

$$p = \gamma P_0\left[(1 + \delta)\, e^{\left(\frac{\gamma-1}{\gamma}\right)\frac{\Delta S}{R}} - 1\right] \qquad [20]$$

Equation of Continuity. Consider a small volume of gas in a cylindrical pipe of cross-sectional area A. At equilibrium, let the co-ordinates of the bounding surfaces be x and $x + dx$. When the volume is displaced, the bounding surfaces will have co-ordinates $x + \xi(x)$ and $x + dx + \xi(x + dx)$, respectively. If $\xi(x + dx)$ is expanded in a Taylor's series, and terms of higher order than the first are neglected

$$\xi(x + dx) \cong \xi(x) + \frac{\partial \xi(x)}{\partial x}dx$$

The mass of gas in the undisplaced volume is $\rho_0 A\, dx$, and the mass of gas in the volume when displaced is

$$\rho A\left(1 + \frac{\partial \xi}{\partial x}\right)dx = \rho_0(1 + \delta)\left(1 + \frac{\partial \xi}{\partial x}\right)A\, dx$$

Since these masses must be equal

$$1 = 1 + \delta + \frac{\partial \xi}{\partial x} + \delta\frac{\partial \xi}{\partial x} \qquad [21]$$

The final term in this equation is of second order and can be neglected, so that Equation [21] reduces to

$$\delta = -\frac{\partial \xi}{\partial x} \qquad [22]$$

Equation of Motion. The force on an increment of the gas will have a resultant equal to $-\frac{\partial p}{\partial x}A\, dx$. This force will accelerate a mass $\rho_0 A\, dx$ at a rate $\partial^2\xi/\partial t^2$. Thus

$$-\frac{\partial p}{\partial x}A\, dx = \rho_0 A\, dx\frac{\partial^2 \xi}{\partial t^2}$$

or

$$\rho_0\frac{\partial^2 \xi}{\partial t^2} = -\frac{\partial p}{\partial x} \qquad [23]$$

Modified Wave Equation. If the expression for δ given in Equation [22] is substituted into Equation [20], and the partial derivative with respect to x is taken

$$\frac{\partial p}{\partial x} = \gamma P_0\frac{\partial}{\partial x}\left[\left(1 - \frac{\partial \xi}{\partial x}\right)e^{\left(\frac{\gamma-1}{\gamma}\right)\frac{\Delta S}{R}}\right] \qquad [24]$$

Carrying out the differentiation with respect to x on the right side, Equation [24] becomes

$$\frac{\partial p}{\partial x} = \gamma P_0 e^{\left(\frac{\gamma-1}{\gamma}\right)\frac{\Delta S}{R}}\left[-\frac{\partial^2 \xi}{\partial x^2} + \left(1 - \frac{\partial \xi}{\partial x}\right)\frac{\gamma - 1}{\gamma R}\frac{\partial}{\partial x}(\Delta S)\right] \qquad [25]$$

Using Equation [23], Equation [25] can be written as

$$e^{\left(\frac{\gamma-1}{\gamma}\right)\frac{\Delta S}{R}}\left[\frac{\partial^2 \xi}{\partial x^2} - \left(1 - \frac{\partial \xi}{\partial x}\right)\left(\frac{\gamma - 1}{\gamma R}\right)\frac{\partial}{\partial x}(\Delta S)\right] = \frac{1}{c^2}\frac{\partial^2 \xi}{\partial t^2} \qquad [26]$$

where $c^2 = P_0\gamma/\rho_0$.

Equation [26] is a form of the wave equation in which addition and withdrawal of heat from the gas are taken into account. If ΔS is zero at all times, Equation [26] reduces to the general wave equation.

Solution to Modified Wave Equation. Neglecting higher-order terms, for small ΔS

$$e^{\left(\frac{\gamma-1}{\gamma}\right)\frac{\Delta S}{R}} \cong 1 + \frac{\gamma - 1}{\gamma}\frac{\Delta S}{R} \quad [27]$$

and, similarly, using the perfect-gas law and neglecting higher-order terms

$$\frac{\Delta S}{R} = \frac{1}{R}\int\frac{dQ}{T} \cong \frac{1}{RT_0}\int\left(1 - \frac{p}{P_0} + \delta\right)$$

$$dQ \cong \frac{1}{RT_0}\int\frac{dQ}{dt}\,dt \quad [28]$$

Equation [26], the wave equation, can now be expressed as

$$\frac{1}{c^2}\frac{\partial^2\xi}{\partial t^2} = \left(1 + \frac{1}{c_p T_0}\int\frac{dQ}{dt}\,dt\right)\left[\frac{\partial^2\xi}{\partial x^2} - \left(1 - \frac{\partial\xi}{\partial x}\right)\left(\frac{1}{c_p T_0}\frac{\partial}{\partial x}\int\frac{dQ}{dt}\,dt\right)\right]$$

by using Equations [27] and [28], and by substituting c_p for $\gamma R/(\gamma - 1)$. Then, when second-order terms are dropped, this equation becomes

$$\frac{1}{c^2}\frac{\partial^2\xi}{\partial t^2} = \frac{\partial^2\xi}{\partial x^2} - \frac{1}{c_p T_0}\frac{\partial}{\partial x}\int\frac{dQ}{dt}\,dt \quad [29]$$

Letting

$$\frac{1}{c_p T_0}\frac{dQ}{dt} = F(x)\,G(t) \quad [30]$$

and

$$\xi = X(x)\,\theta(t)$$

Equation [29] becomes

$$\frac{1}{c^2}\frac{\ddot{\theta}}{\theta} = \frac{1}{X}\frac{d^2X}{dx^2} - \frac{dF}{dx}\frac{1}{X\theta}\int G\,dt \quad [31]$$

where the dot denotes differentiation with respect to time.

Only two nontrivial assumptions will allow a separation of variables and a consequent solution; these assumptions are

$$\frac{dF}{dx} = MX \quad [32]$$

and

$$\int G\,dt = K\theta \quad [33]$$

where M and K are arbitrary constants. Since the point of interest is the possible phasing of the heat input with respect to pressure, the assumption of Equation [33] is not considered. However, the assumption of Equation [32] can be made, and it can be shown that this amounts to an assumption of an amplitude of rate of heat input proportional to the pressure amplitude at each point.

Using Equation [32], Equation [31] may be split as follows

$$\frac{1}{c^2}\frac{\ddot{\theta}}{\theta} + M\frac{\int G\,dt}{\theta} = \frac{1}{X}\frac{d^2X}{dx^2} = -\frac{4\pi^2}{\lambda^2} \quad [34]$$

Solving for X

$$X = A\sin\frac{2\pi x}{\lambda}$$

and from Equation [32]

$$F = -MA\frac{\lambda}{2\pi}\cos\frac{2\pi x}{\lambda} \quad [35]$$

In solving for θ, the derivative with respect to time is taken; thus, Equation [34] becomes

$$\dddot{\theta} + c^2 MG + \left(\frac{2\pi c}{\lambda}\right)^2\dot{\theta} = 0 \quad [36]$$

It is now assumed that

$$\theta = B\,e^{\alpha t}\sin\omega t$$

and

$$G = N\,B\,e^{\alpha t}\sin(\omega t + \varphi) \quad [37]$$

Substituting these equations and their derivatives into Equation [36], it is found that the following equations must be satisfied

$$\alpha(\alpha^2 - 3\,\omega^2) + c^2\,M\,N\cos\varphi + \left(\frac{2\pi c}{\lambda}\right)^2\alpha = 0$$

and

$$-\omega(\omega^2 - 3\alpha^2) + c^2\,M\,N\sin\varphi + \left(\frac{2\pi c}{\lambda}\right)^2\omega = 0$$

Solving for α

$$\alpha = \frac{3\,c^2\,M\,N\cos\varphi}{8\,\omega^2 - 2\left(\frac{2\pi c}{\lambda}\right)^2 + \frac{c^2 M\,N\sin\varphi}{\omega}}$$

Since $\omega \cong 2\pi c/\lambda$

$$\alpha \cong \frac{3\,c^2\,M\,N\cos\varphi}{6\,\omega^2 + \frac{c^2\,M\,N\sin\varphi}{\omega}}$$

In this development, the amplitude of heat-input rate is assumed to be small, that is, $M\,N$ is small, and

$$\alpha \cong \frac{\lambda^2\,M\,N\cos\varphi}{8\,\pi^2}$$

Since a positive value of α indicates an increasing amplitude of oscillation, the oscillation will increase in amplitude when $\cos\varphi > 0$, or $-\pi/2 < \varphi < \pi/2$.

By substituting Equations [35] and [37] into Equation [30]

$$\frac{1}{c_p T_0}\frac{dQ}{dt} = -N\,M\,A\,B\frac{\lambda}{2\pi}\,e^{\alpha t}\sin(\omega t + \varphi)\cos\frac{2\pi x}{\lambda} \quad [38]$$

Using the relation for p given by Equation [23], and neglecting the smaller terms occasioned by small values of α

$$p \cong -\rho_0\,B\,A\,\omega^2\frac{\lambda}{2\pi}\,e^{\alpha t}\sin\omega t\cos\frac{2\pi x}{\lambda} \quad [39]$$

By comparing Equations [38] and [39], it is seen that α is positive, and driving of the oscillations will occur, when the phase difference between dQ/dt and p is less than 90 deg. Also, the maximum effect will occur when $\varphi = 0$, or when dQ/dt and p are directly in phase. This conclusion is the same as the previous statement that a component of the rate of heat input must be in phase with the pressure to drive the oscillation.

Discussion

W. V. Hanzalek.[7] The authors are to be congratulated for conducting this study and preparing this paper in a manner such that the obvious applications to turbojet and rocket combustion chambers were evidently kept constantly in mind. Since the use of oscillations someday may lead to improved combustion systems, it is refreshing that this paper reports a study in a way calculated to speed the use of this information in future design and development procedures.

In view of the fact that the three combustion chambers used were designed to the same principles employed in industry, it should be pointed out that this study was carried out at 1200 R, a relatively low combustion-chamber discharge temperature compared with the modern turbojet values of 2000 R. One wonders therefore how these particular burner oscillations affected the combustion process which was an essential part of this test setup. It would appear to be in order to incorporate these observations in this paper if at all possible. Either at 1200 R or at some higher temperature where there is less excess air, a study of the effect of burner oscillations on flame structure, combustion efficiency, inflammability range, and total pressure loss across the combustion zone would be a significant extension of this paper.

Although the authors have made every attempt to simulate typical combustion-chamber systems, no provision was made to duplicate the introduction of excess air at right angles to the through-flow. Admittedly this would tend to destroy any organ-pipe-type oscillations set up but it also might provide some measure of the strength and action of these oscillations in a turbojet chamber. Similarly a study of the effect at the burner head of controlled turbulence, swirl or vortex flow on organ-pipe oscillations also would be a useful amplification of this work and tend to orient it within the operating regime of a more complex design.

The fact that this paper has stimulated these comments directed toward a broader use of its findings is a sign that it has filled a gap in the thinking concerned with the problem of oscillations in combustion-chamber systems. The number of practical suggestions for ways to effect a particular oscillation phenomenon, included in this paper, also testify to its value and contribution to the subject.

J. A. Johnson.[8] Recently the problem of suppressing burner oscillation has become more important for both military and industrial developments directed toward higher rates of heat release. The advantages of burner oscillation from the standpoint of the development of some types of wave machines and of the possibility of increased heat transfer represent another direction of endeavor. Greater urgency is attached to the problem of suppressing burner oscillation and a definite contribution has been made in the analysis of the organ-pipe type of oscillation by the authors.

In addition to oscillations of the organ-pipe type, to which the paper is limited, some remarks on the important type of oscillation associated with appreciable movement of the flame front may be interesting to those faced with a burner-oscillation problem. These frequencies in combustion units as shown in Fig. 1 (*b*) of the paper, are ordinarily much lower than the organ-pipe frequencies and are associated with high gas velocities in elongated confining tubes having small damping forces. It is known that this type of oscillation may be changed by variations in design. Simple corrective measures for unstable oscillations of this type have included the use of a flame-stabilizing baffle in the fuel-air mixture parallel with the direction of flow but terminating at the flame front. Vanes to cause a rotating flow at the point of flame holding and downstream of the burner also have been reported to improve combustion stability. Another device used with some success is a type of muffle about the burner discharge point.

However, apparently many unknown factors are involved in combustion stability. The authors' comments on the effect of the following factors on both types of burner instability would be interesting:

1 Inherent low-frequency combustion oscillations upon which recently developed electronic flame-failure devices are based and the cause of this oscillation.

2 Blower or air-source pressure-flow characteristics and the stability of flow due to this characteristic.

3 Size of flow passage at the point of flame holding.

4 Use of liquid fuel-burners in which the fuel is not vaporized at the point of flame holding.

The writer wishes to congratulate the authors on an able presentation of factors involved in the increasingly important burner-oscillation field of study.

Authors' Closure

Messrs. Hanzalek and Johnson have effectively pointed out the many complicating factors entering into the study of oscillations in combustion systems. It is clear that much work remains to be done, both in obtaining new information, and in extending results such as those reported in this paper. To obtain the desired answers, the efforts of many additional investigators will be needed, beyond the relatively small number presently engaged in work in this field.

In reply to Mr. Hanzalek's question regarding temperature, it might be mentioned that although tests on the burner configurations shown in Figs. 1(*a*) and 1(*c*) were conducted at about 1200 R, temperatures as high as 2000 R were attained with the burner shown in Fig 1(*b*). The results of these tests, as well as tests on other combustion systems over wide ranges of temperature, have shown that the hypothesis concerning the required phasing of the rate of heat release with the oscillating component of the pressure can be applied equally as well at temperatures of 2000 R or higher as at 1200 R, to explain flame-driven oscillations.

As for the effect of oscillations on such factors as flame structure and combustion efficiency, the following comments are offered: As a direct result of oscillations, the flame front of a laminar flame in a low-velocity stream changes in shape. This effect could be seen in the tests, since each time an oscillation started, the flames immediately became appreciably shorter and wider than the corresponding flames without oscillation. The change in shape for this type of flame can be explained by the fact that oscillations in the region of the flame tend to shift the flow pattern from a laminar type, with a parabolic velocity profile, toward a type of potential flow which has a relatively flat velocity profile. However, there has been no evidence that there is any change in fundamental variables, such as burning velocity, when an oscillation is imposed.[9,10,11]

For flow patterns in high-velocity streams, where the velocity profile tends to be flat, the oscillations do not affect the flow pattern directly. However, as a consequence of an increased mixing of

[7] Project Engineer, Curtiss-Wright Corporation, Wright Aeronautical Division, Wood-Ridge, N. J. Jun ASME.

[8] Vice-President and Chief Engineer, Thermal Research and Engineering Corporation, Conshohocken, Pa.

[9] "The Effect of High-Frequency Sound Waves on an Air-Propane Flame," by C. J. Kippenhan and H. O. Croft, Trans. ASME, vol. 74, 1952, pp. 1151–1155.

[10] "The Effect of Sound on Laminar Propane-Air Flames," by S. Loshaek, R. S. Fein, and H. L. Olsen, *Journal of the Acoustical Society of America*, vol. 21, 1949, pp. 605–612.

[11] "Interaction of Flame Propagation and Flow Disturbance," by G. H. Markstein, Third Symposium on Combustion, Flame, and Explosion Phenomena, Williams and Wilkins, Baltimore, Md., 1949, p. 162.

fuel and oxidant caused by oscillations, or an increased mixing of burned and unburned gases, an increase in apparent flame speed and flame thickness may be obtained, as also an increase in rate of heat transfer to the surrounding gas stream, and to the combustor walls. Therefore the oscillations not only may cause a change in flame structure and an increase in combustion-chamber discharge temperature, but also, indirectly, may cause a change in flow pattern. These effects would be similar to the effects obtained by increasing turbulence. Increased mixing might cause premature quenching of the outer mantle of the flames in the tube configuration of Fig. 1(*a*), where a large amount of excess air is present, but it is believed that the effect of this quenching on discharge temperature is insignificant, at least for the hydrogen-air flames used.

It should also be mentioned that oscillations may cause a decrease in flame holding ability,[10] in much the same way that increased turbulence may cause the flame to be less stable in some types of burners.[12]

It is difficult to give specific answers to the questions raised by Mr. Johnson. However, some broad general statements can be made. Several types of low-frequency oscillations have been observed in various combustion systems, the Helmholtz type being one of frequent occurrence. This oscillation can be obtained with a burner configuration similar to that shown in Fig. 1(*c*).

Another type of low-frequency oscillation has been observed in which the burning zone undergoes such violent changes in shape and size during a cycle that the region of combustion acts, in so far as frequency analysis is concerned, as an additional equivalent length of pipe. Because of this effective increase in the length of the system, the natural frequency of the pipe without combustion, computed using the nominal length, is higher than the observed frequency with combustion. This type of oscillation might occur in any of the three configurations used, as well as in many others.

The flame can also act as an amplifier, either for pulses from other components of the system, such as a blower, or for random pulses traveling from the surrounding atmosphere into the combustion zone. This amplification may give rise to a troublesome pulsation at low frequency.

In regard to the air-source pressure-flow characteristics of a system, some excellent information is available in a paper by Bailey[13] dealing with the surging, pulsation, and blowout of semistable and unstable flow and combustion systems. In this paper the principles of fluid dynamics are used to determine the conditions for instability in flow systems such as a furnace and stack and a blower discharging into a plenum chamber. Flow and entrainment instability and high-temperature dynamic instability in combustion systems are also discussed.

If the flow passage is not greatly restricted at the point of flame holding in a combustion chamber, there is little effect on the calculated natural frequency of the system. If a large restriction is imposed, the system will be effectively closed at this point, as far as oscillations are concerned, and the chamber will act as a quarter-wave tube.

The last question proposed by Mr. Johnson brings up some interesting possibilities regarding flame-driven oscillations. Since the evaporation rate of fuel droplets changes with their velocity, it is reasonable to expect that with an oscillation present, there might be a periodic change in evaporation rate, and a corresponding periodic change in the concentration of fuel vapor at the flame front. This can lead to the satisfaction of the requirement regarding phasing of the rate of heat release and of the pressure which must be fulfilled to drive an oscillation. Thus combustion systems, such as afterburners, may have oscillations driven by this mechanism as well as by other combinations of feedback cycles.

[12] "Flame Stabilization and Propagation in High-Velocity Gas Streams," by G. C. Williams, H. C. Hottel, and A. C. Scurlock, Third Symposium on Combustion, Flame, and Explosion Phenomena, Williams and Wilkins, Baltimore, Md., 1949, pp. 21–40.

[13] "Flow and Combustion Stability," by N. P. Bailey, ASME paper No. 51—A-83, presented at the Annual Meeting, Atlantic City, N. J., November 25–30, 1951.

An Energy Basis for Comparison of Performance of Combustion Chambers

By J. B. NICHOLS,[1] PALO ALTO, CALIF.

The energy loss in a combustion chamber, as a result of pressure drop, is generally found to be of relatively greater importance than the losses from combustion inefficiency. Therefore it must be included in any parameter which claims to state the efficiency of the burner. Combustion efficiency alone does not serve this purpose. A method of comparison is suggested and developed which allows combustion chambers to be compared on an over-all basis. By this method, any combustion chamber is assigned a single energy efficiency for each inlet condition, which includes the effects of both combustion efficiency and pressure drop.

Nomenclature

The following nomenclature is used in the paper:

- AE = available energy in gas, Btu per lb
- c_p = specific heat at constant pressure, Btu/lb/deg F
- C_n = velocity coefficient of nozzle
- C_v = velocity coefficient of burner-nozzle combination
- F = thrust of jet, lb
- g = acceleration of gravity = 32.2 fps^2
- J = Joule's constant, 778 ft-lb/Btu
- M = mass flow, slugs/sec
- r = total pressure in atmospheres—may be used as a pressure ratio in certain instances
- R = gas constant ft/deg F = 53.3 for air
- T = temperature, deg F abs, total
- V_j = jet velocity, fps
- V_b = velocity of burner relative to air source (applicable only when burner is on such devices as helicopter rotors), fps
- k = ratio of specific heats
- η_c = combustion efficiency
- ϵ = energy efficiency or combustor effectiveness
- Φ = over-all energy efficiency of burner-nozzle combination = $C_v^2 = \epsilon C_n^2$

Subscripts:

- 1 = upstream of burner
- 2 = inside burner
- th = theoretical

Introduction

How good is a combustion chamber? The quality of a combustion chamber is usually defined by the combustion efficiency or the energy represented by air temperature rise compared to the heating value of the fuel used.

If temperature rise is the only desired result of combustion, then the combustion efficiency is the only parameter of concern.

In general, however, the purpose of a combustion chamber is to take in air with a certain energy and deliver this air with a higher energy to a nozzle for expansion, where it provides thrust directly or operates a turbine. For these applications, pressure drops cause decreases in available energy comparable to those due to combustion inefficiencies, and, therefore, should be included in any parameter which describes the actual worth of the combustion chamber.

There is no doubt that an energy concept must finally be used in comparing combustion chambers. To give a combustion chamber an energy efficiency of, say, 90 per cent tells exactly how good it is, while to give a combustion efficiency without also mentioning pressure drop is of far less value. Even given both combustion efficiency and pressure drop, the comparison of burners is vague, since energy is the desired result of burning and it is difficult to weigh mentally the relative effects of combustion efficiency and pressure drop on the over-all energy, Fig. 1.

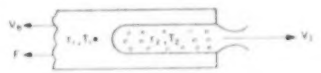

Fig. 1 Schematic Diagram of Combustion Chamber and Nozzle

Evaluation of Combustor Effectiveness

The combustion chamber-energy efficiency or combustor effectiveness[2] can be shown[3] to be given by

$$\epsilon = 1 - \frac{\dfrac{\Delta T}{T_1}}{1 + \dfrac{\Delta T}{T_1}}(1 - \eta_c) - \frac{k-1}{k}\,\frac{dr/r_1}{\dfrac{k-1}{r_1^{\,k}} - 1} \qquad [1]$$

where

- ΔT = theoretical temperature rise
- T_1 = burner-inlet total temperature
- η_c = combustion efficiency
- r_1 = burner-inlet total pressure, atm
- $\dfrac{dr}{r_1}$ = per cent pressure drop in burner

for small values of $(1 - \eta_c)$ and dr/r_1. When either of these terms becomes large (over 10 per cent) the exact equation should be used

$$\epsilon = \frac{T_2\left(r_2^{\frac{k-1}{k}} - 1\right)\left(r_1^{\frac{k-1}{k}} - 1\right)}{T_{2_{th}}\left(r_1^{\frac{k-1}{k}} - 1\right)\left(r_2^{\frac{k-1}{k}} - 1\right)} \qquad [2]$$

---

[1] Hiller Helicopters: formerly, Thermal Power Systems Division, General Engineering Laboratory, General Electric Company, Schenectady, N. Y. Jun. ASME.

Contributed by the Gas Turbine Power and Fuels Divisions and presented at the Semi-Annual Meeting, Cincinnati, Ohio, June 15–19, 1952, of The American Society of Mechanical Engineers.

Note: Statements and opinions advanced in papers are to be understood as individual expressions of their authors and not those of the Society. Manuscript received at ASME Headquarters, April 7, 1952. Paper No. 52—SA-37.

[2] Term suggested by Prof. D. G. Shepherd, of Cornell University, to prevent confusion with combustion efficiency.

[3] Derived in Appendix.

The last two terms of Equation [1] are plotted in Figs. 2 and 3 in terms of percentage change in available energy for a per cent change in either $(1 - \eta_c)$ or dr/r. The relative effects of combustion efficiency and pressure drop on combustor effectiveness can be quickly obtained from these figures. For example, at a temperature-rise ratio $\Delta T/T_1$ of 2:1 and a pressure ratio of 2.5, a 1 per cent combustion efficiency change is equivalent to a 0.66 per cent change in available energy, whereas a 1 per cent change in pressure drop is equivalent to a 0.97 per cent change in available energy. It is seen, therefore, that a given percentage of pressure drop is 50 per cent more detrimental to combustor effectiveness in this case than the same per cent change of combustion efficiency, Figs. 2 and 3.

Equation [2] is plotted in Fig. 4 for a theoretical temperature-rise ratio $(\Delta T/T_1)$ of 2:1 and for a pressure ratio r_1, of 2.5.

At this pressure ratio and temperature rise, it can be seen that a combustion chamber with a 95 per cent combustion efficiency and a 6 per cent pressure drop is no better than one with a 92 per cent combustion efficiency and a 4 per cent pressure drop—in each case, a 91 per cent energy efficiency.

It is proposed, therefore, that the use of Equations [1] and [2] be examined as a possible method of comparison of combustion chambers.

This method has been applied to the test data of three stages of development of an actual burner. Combustion efficiencies are shown in Fig. 5 and pressure drops in Fig. 6. Note that the values of ϵ as shown in Fig. 7, are considerably less than the combustion efficiency.

Application to Test Data

In all applications under consideration, the combustion chamber is followed by a nozzle. Generally, the combustion chamber is designed for a particular nozzle and it is a well-known fact that changing the nozzle often alters the characteristics of the burner. This is true particularly for nozzle-area variation which directly

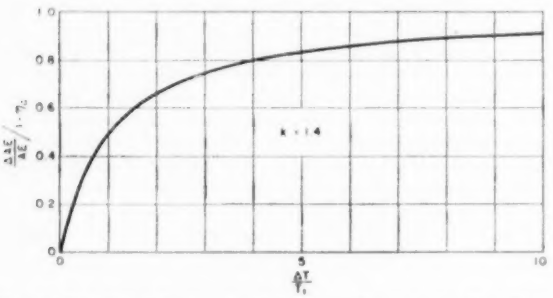

Fig. 2 Per Cent Change in Available Energy per Per Cent Change in Combustion Efficiency as a Function of Temperature-Rise Ratio

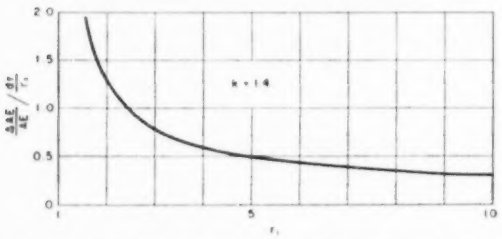

Fig. 3 Per Cent Change in Available Energy per Per Cent Change in Pressure Drop as a Function of Pressure Ratio

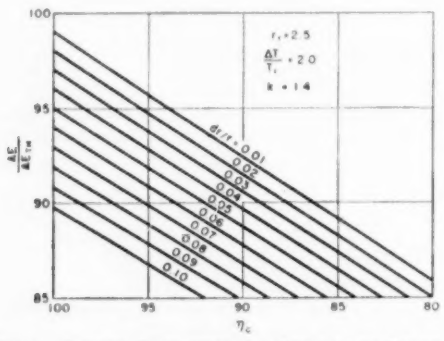

Fig. 4 Energy Efficiency of a Combustion Chamber

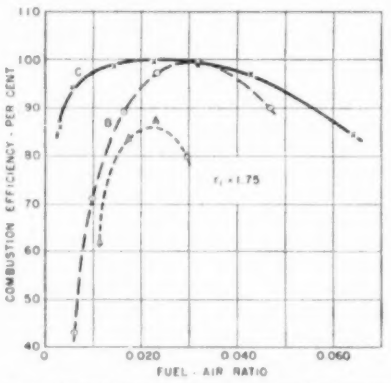

Fig. 5 Test Values of Combustion Efficiency

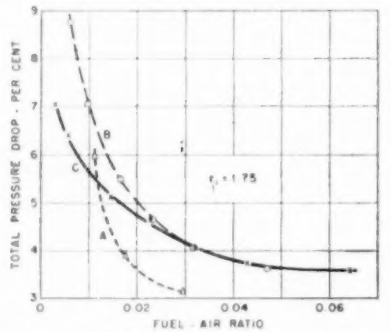

Fig. 6 Test Values of Total Pressure Drop Across Combustor

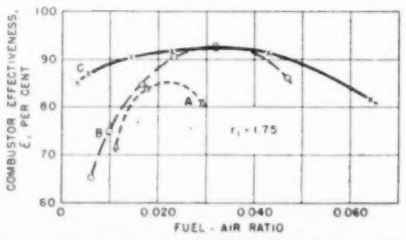

Fig. 7 Variation of Combustor Effectiveness

affects flow capacity and pressure drop and indirectly affects combustion efficiency. It is almost impossible to obtain valid combustor test data without using a nozzle similar to, if not identical with, the nozzle which is to be actually applied with the combustion chamber. Let us assume that our combustion chamber is followed by a fully expanding nozzle with a velocity coefficient C_n. The nozzle-jet velocity is given by

$$V_j = C_n \sqrt{2gJ\ \mathrm{AE}_2}$$

but

$$\mathrm{AE}_2 = \epsilon \mathrm{AE}_{2\mathrm{th}}$$

or

$$V_j = C_n \sqrt{2gJ\epsilon \mathrm{AE}_{2\mathrm{th}}}$$

We can combine ϵ and C_n into an over-all energy efficiency

$$\Phi = C_n^2 \epsilon \quad \ldots\ldots [3]$$

or into an over-all velocity coefficient

$$Cv = C_n \sqrt{\epsilon} = \sqrt{\Phi} \quad \ldots\ldots [4]$$

The value of any burner-nozzle combination can be given by a single coefficient Φ, which has a definite meaning based on firm energy concepts.

The actual determination of this over-all energy efficiency from test is exceptionally simple to obtain. The test data are reduced to the form

$$\frac{F/M + V_b}{\sqrt{2gRT_{2\mathrm{th}}}} \quad \ldots\ldots [5]$$

where

F = measured thrust

M = mass flow $\dfrac{W_A\,(1 + f/a)}{g}$

$T_{2\mathrm{th}}$ = theoretical temperature obtained from burner inlet temperature and fuel-air ratio, f/a

V_b = velocity of burner

The theoretical value of this function, which is merely a nondimensional representation of jet velocity, is given by[3]

$$\sqrt{\frac{k}{k-1}\,\frac{r_1^{\frac{k-1}{k}} - 1}{r_1^{\frac{k-1}{k}}}} \quad \ldots\ldots [6]$$

and is plotted in Fig. 8 for various values of k. Test values may be plotted on this curve and the ratio of the test values is Cv, the over-all burner-nozzle velocity coefficient. The over-all energy efficiency is given by $\Phi = Cv^2$.

The merit of this method of specifying the value of a burner is evident in that it requires measurement only of burner-inlet conditions and thrust, which is more conducive to accuracy than measurement of exhaust temperatures. If the nozzle-velocity coefficient is known, as is often the case, then the energy efficiency of the burner can be determined accurately, Equation [3]. If the nozzle velocity coefficient is not known, then a valuable over-all efficiency is still obtained, which can be compared with any other combustion chamber-nozzle combination with real meaning.

Considering the present status of high-temperature measurement techniques, it is not difficult to realize that accuracy is increased and time saved during test by the replacement of a profile survey by a single thrust measurement. Thrust is a true integration of a velocity profile, and the average velocity so obtained is a true indication of average temperature.

Some question may arise as to the effect of k on the results. As shown in Fig. 8, the effect of k is definitely second order. Since k can be obtained quite accurately from rather rough approximations of pressure, temperature, and fuel-air ratio, it should cause no errors greater than the experimental errors. Exception must be taken, however, to the effects of dissociation, which causes difficulties in interpretation, no matter what the technique.

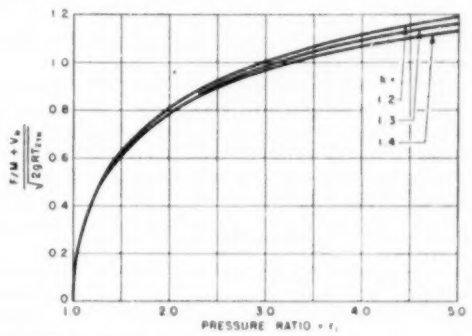

FIG. 8 $\dfrac{F/M + V_b}{\sqrt{2gRT_{2\mathrm{th}}}}$ VERSUS PRESSURE RATIO FOR FULLY EXPANDING NOZZLE

CONCLUSIONS

A definite disagreement exists in the combustion field as to the method of measuring and specifying combustion-chamber performance. A large amount of time and money has been spent in trying to solve the high-temperature measurement problem. This development time is well spent. Accurate temperature measurements are a necessity if combustion chambers are to be developed with good temperature profiles, as is so necessary for gas-turbine applications.

Once a satisfactory temperature profile is obtained, however, the question of efficiency arises. Ordinarily, the emphasis is placed on high combustion efficiencies, with a lesser attention paid to the pressure drop. Also, the present test techniques seem to favor temperature measurements (no matter how difficult they are to obtain) as a method of obtaining these combustion efficiencies.

As shown in this paper, however, the pressure drop usually has a greater relative effect than the combustion efficiency on the effectiveness of the combustion chamber. In any burner development, it often occurs that combustion efficiency can be traded for pressure drop. This paper presents a method of determining where the best bargain is obtained in this trading process. It also is of use in comparing the performance of two basically different burners competing for the same job.

Equations [1] or [2], or Figs. 2 and 3, may be employed in reducing pressure drop and combustion efficiency to an energy efficiency which we shall call combustor effectiveness, so as not to confuse it with the combustion efficiency.

The use of combustor effectiveness as the specification of the performance of a burner should be considered for the following reasons:

1 It is based on fundamentally firm energy concepts.

2 It defines a realistic and practical property of a combustion chamber.

3 It can be obtained from various test techniques, and is applicable to all existing test data.

4 While including combustion efficiency, it can be obtained without the measurement of a single combustion temperature.

The last reason is most significant and bears further explanation. The effectiveness can be obtained from a knowledge of the inlet conditions of the burner and the thrust obtained from the burner-nozzle combination, applied either as a gas-turbine combustor or a direct-thrust device.

The substitution of thrust for temperature measurements considerably simplifies test procedure. It replaces a large number of temperature traverses by a single thrust measurement. Considering the presently available temperature-measurement techniques, the measurement of thrust is considerably more accurate.

Specific thrust is an integral of the true velocity profile and is an exact indication of true average temperature. As such, a thrust measurement, taken simultaneously with a temperature-profile survey, can be used to correct temperature measurements which, while they may yield a valid indication of profile shape, may at the same time have an absolute error.

Acknowledgments

The author wishes to offer sincere thanks to Prof. D. G. Shepherd of Cornell University, for his pertinent comments on this paper. He also wishes to thank Messrs. J. K. Salisbury, G. S. Bahn, R. W. Macaulay, and F. H. Kindl, of the General Electric Company, for their assistance and comments.

Appendix

Derivation of Equation [1]

The available energy of the air in expanding through a pressure ratio r, is given by

$$\mathrm{AE} = c_p T \frac{r^{\frac{k-1}{k}} - 1}{r^{\frac{k-1}{k}}} \quad [7]$$

Differentiating

$$d\ \mathrm{AE} = c_p T \left(\frac{k-1}{k}\right) \frac{dr/r}{r^{\frac{k-1}{k}}} + c_p \frac{r^{\frac{k-1}{k}} - 1}{r^{\frac{k-1}{k}}} dT \quad [8]$$

The actual available energy of the air after combustion is given by

$$\mathrm{AE}_2 = c_p T_{2th} \frac{r_1^{\frac{k-1}{k}} - 1}{r_1^{\frac{k-1}{k}}} - d\ AE$$

$$\mathrm{AE}_2 = c_p (T_{2th} - dT) \frac{r_1^{\frac{k-1}{k}} - 1}{r_1^{\frac{k-1}{k}}} - c_p T_{2th} \frac{\frac{k-1}{k}}{r_1^{\frac{k-1}{k}}} \frac{dr}{r_1} \quad [9]$$

The theoretical available energy after combustion is given by

$$\mathrm{AE}_{2th} = c_p T_{2th} \frac{r_1^{\frac{k-1}{k}} - 1}{r_1^{\frac{k-1}{k}}} \quad [10]$$

We can now define combustor effectiveness as

$$\epsilon = \frac{\mathrm{AE}_2}{\mathrm{AE}_{2th}} = 1 - \frac{dt}{T_{2th}} - \frac{\frac{k-1}{k} \frac{dr}{r_1}}{r_1^{\frac{k-1}{k}} - 1} \quad [11]$$

It can be shown that

$$\frac{dT}{T_{2th}} = \frac{\frac{\Delta T}{T_1} \frac{dT}{\Delta T}}{1 + \frac{\Delta T}{T_1}} \quad [12]$$

where ΔT = theoretical temperature rise and by definition

$$\frac{dT}{\Delta T} = (1 - \eta_c) \quad [13]$$

Substituting Equations [12] and [13] in [11] we obtain ϵ in the form of mutually independent pressure and temperature terms

$$\epsilon = 1 - \frac{\frac{\Delta T}{T_1}}{1 + \frac{\Delta T}{T_1}} (1 - \eta_c) - \frac{k-1}{k} \frac{dr/r_1}{r_1^{\frac{k-1}{k}} - 1} \quad [14]$$

Derivation of Function

$$\frac{F/M + V_b}{\sqrt{2gRT_{2th}}}$$

The thrust of a fully expanding nozzle is given by

$$F = M (V_j - V_b) \quad [15]$$

but V_j for a fully expanding nozzle is equal to

$$V_j = C_v \sqrt{2gJ\mathrm{AE}_{th}} \quad [16]$$

where

$$\mathrm{AE}_{th} = c_p T_{2th} \frac{r_1^{\frac{k-1}{k}} - 1}{r_1^{\frac{k-1}{k}}}$$

so that

$$V_j = C_v \sqrt{2gJc_p T_{2th} \frac{r_1^{\frac{k-1}{k}} - 1}{r_1^{\frac{k-1}{k}}}}$$

or

$$V_j = C_v \sqrt{2gRT_{2th} \frac{k}{k-1} \frac{r_1^{\frac{k-1}{k}} - 1}{r_1^{\frac{k-1}{k}}}} \quad [17]$$

Substituting in Equation [15]

$$\frac{F}{M} + V_b = V_j = C_v \sqrt{2gRT_{2th} \frac{k}{k-1} \frac{r_1^{\frac{k-1}{k}} - 1}{r_1^{\frac{k-1}{k}}}}$$

or

$$\frac{F/M + V_b}{\sqrt{2gRT_{2th}}} = C_v \sqrt{\frac{k}{k-1} \frac{r_1^{\frac{k-1}{k}} - 1}{r_1^{\frac{k-1}{k}}}} \quad [18]$$

The ideal value of

$$\frac{F/M + V_b}{\sqrt{2gRT_{2th}}}$$

is seen to be merely

$$\sqrt{\frac{k}{k-1}\left(r_1^{\frac{k-1}{k}}-1\right)\Big/\left(r_1^{\frac{k-1}{k}}\right)}$$

and is plotted in Fig. 8 for various values of k.

The over-all efficiency of a burner-nozzle combination is found by plotting measured values of

$$\frac{F/M + V_b}{\sqrt{2gRT_{2th}}}$$

on the same chart. The ratio of the actual to the theoretical value is C_v. The over-all energy efficiency Φ, is equal to C_v^2.

If the nozzle velocity coefficient C_n, is known, the combustor effectiveness can be found from the equation

$$\epsilon = \frac{\Phi}{C_n^2} = \frac{C_v^2}{C_n^2} \quad \ldots\ldots\ldots\ldots\ldots\ldots\ldots\ldots [19]$$

Discussion

J. R. Parsons.[4] The author presents a very useful method of combining the effect on combustion-chamber evaluation of pressure drop and combustion efficiency into one term, "energy efficiency." This tool for comparison of combustion chambers on an energy basis is a start in the standardization of evaluation terms. Knowledge of combustion-chamber effectiveness is useful to both the engine designer and the burner designer. The engine designer needs to compare available combustion chambers on an energy basis so that he may select the one with lowest energy losses for his design. The burner designer needs this tool to know which of several competing configurations is best.

After several years of association with the author, the writer is sure that he is cognizant that comparison of burners on an energy basis comes only after each has been made to satisfy many other conditions such as carbon deposition, temperature profile, liner temperature, size, and stability.

For instance, carbon deposition usually cannot be tolerated. However, a rocket engine which employs fuel cooling along the inside wall of the combustion chamber accumulates a small amount of carbon. This fuel does not enter into the combustion process but discharges unburned. Energy efficiency in this example is secondary and is intentionally sacrificed.

Flat temperature profile in a thrust-producing device, such as a rocket or burner exhausting directly to atmosphere, is of no consequence except as it affects liner temperature. Thrust efficiency in this case is paramount in burner comparison. The gas turbine, however, requires a flat temperature profile, but is not penalized by weight or size to the same degree as a burner at the tip of the rotor of a jet-driven helicopter. Once the burner competing for use in a gas turbine has satisfactorily demonstrated (*a*) lack of carbon formation over the range of operating conditions; (*b*) flat temperature profile; (*c*) satisfactory liner life; (*d*) satisfactory stability and ignitibility, it may then be compared with others for acceptance in a given gas-turbine cycle.

It should be noted that the combustion-effectiveness number which is assigned to a liner is significant only for a given compressor-turbine combination. This effectiveness number does not identify the liner at all times regardless of application. Like turbine or compressor efficiency it is applicable only when considered as part of a specific cycle.

Pressure drop occurring in all combustion chambers results principally from incomplete recovery of velocity pressure from impinging jets, or similar entry, required to get sufficient mixing of air and fuel for good burning. The burner designer needs frequently to know during a development how much combustion efficiency he can exchange for pressure drop. The "minimum" pressure drop is determined by instability or carbon deposition; the "optimum" is determined by its effect on energy effectiveness.

[4] Sverdrup & Parcel, Inc., St. Louis, Mo.

Author's Closure

The author expresses his sincere appreciation to Mr. Parsons for his clarifying comments on this paper. In amplification of his discussion, the author wishes to re-emphasize that the purpose of this paper, as Mr. Parsons has clearly described, is to promote and demonstrate the use of a fundamental definition of the performance of a combustion chamber in the strict thermodynamic sense only.

It has been the author's conviction that the combustion systems in gas turbines, and so on, have not enjoyed the common use of fundamental definitions common to other power-plant components, such as turbines and compressors. There is no apparent reason why this should be so. True, the state of the art of combustion-chamber design is not yet advanced to the stage that compressor and turbine design have, but the fundamental thermodynamic laws are available and should be used wherever they apply.

Long before the advent of the gas turbine, and its attendant needs for combustors, compressor and turbine-performance characteristics were defined by fundamentally sound terms, based on energy concepts, which were in common usage in describing performance of industrial compressors, superchargers, and steam turbines. No similar efficiency term was developed for combustion chambers. The combustor effectiveness as developed in this paper, therefore, is suggested for application to combustion chambers in the same manner that compressor efficiency, for example, is applied to a compressor. Neither term can in itself guarantee a good design for a combustor or compressor, but both define the intended or finished product as to thermodynamic value.

Naturally, many other properties of a combustor exist in addition to effectiveness, just as there are other properties of a compressor than efficiency, such as pulsation limit, flow range, and so on. The fact that these other properties are not yet amenable to exact numerical description does not detract from the value of standardized definitions of those properties to which fundamental and numerical descriptions do apply.

For lack of a true efficiency definition the trend has been to use the combustion efficiency as the definition of combustor performance. As shown in this paper, this is not only fundamentally unsound, but in many instances can be misleading. For this reason, the author offers a more basic definition, which he has personally found convenient and accurate, for wider evaluation and possible acceptance in the field.

Comparative Performance of Coals of Different Rank in a Film-Cooled Gas-Turbine Combustor[1]

By T. E. WARREN,[2] H. P. HUDSON,[2] J. D. ROBERTSON,[3] AND J. C. MULLIGAN,[2] OTTAWA, CANADA

Development of a combustor adapted to a coal-burning gas turbine for locomotive use was undertaken for the Locomotive Development Committee by Battelle Memorial Institute some years ago. The coal used in the course of this development was from Ohio No. 8 seam, and no systematic study was made of the effect of variation of coal properties on combustor performance. This phase of the general investigation was undertaken by the Fuels Division of the Mines Branch, Department of Mines and Technical Surveys at Ottawa, Ontario, Canada. The present paper gives a report on 23 coals of various groups within the bituminous class of the ASTM classification by rank.

Introduction

TECHNICAL problems involved in construction of a coal-burning gas-turbine locomotive have been investigated during the past 5 years by the Locomotive Development Committee of Bituminous Coal Research, Inc., under the direction of John I. Yellott. The committee has concentrated its effort on adaptation of the open-cycle gas turbine to coal firing. This cycle has the advantage of direct heating of the working gas but imposes the necessity of developing suitable means for feeding the coal into the combustor, burning it under pressure, and removing ash before it encounters the turbine blading. It has been necessary therefore to undertake studies in diverse fields of technology and some of these have been assigned to established research organizations.

Development of a combustor suited to locomotive requirements was undertaken by Battelle Memorial Institute. In the initial stages of this work it was found experimentally that pressure did not influence the rate of combustion of pulverized coal, and subsequently much of the testing has been conducted at atmospheric pressure.[4] The most satisfactory type of combustor that has been evolved consists of a metallic flame tube made up of overlapping louvers, enclosed in an outer shell.[5] Coal and carrying air are admitted through a burner at the inlet end of the flame tube; excess air passes through the annular space between the flame tube and the outer shell, and part of it flows through the louver slots forming a film of relatively cool air along the inner side of the flame tube; near the outlet end another part of the excess air passes through circular holes in the flame tube so as to mix with the products of combustion and reduce the temperature peak at the center of the combustor outlet. About 10 per cent of the total air is admitted at the burner, about 50 per cent through the film-air slots, and 40 per cent at the mixing section.

The coal used in the course of combustor development at Battelle was from Ohio No. 8 seam and no systematic study was made of the effect of variation of coal properties on combustor performance. This phase of the general investigation was undertaken by the Fuels Division of the Mines Branch of the Department of Mines and Technical Surveys at Ottawa, Ontario. The present paper is a report on tests by the Mines Branch on 23 coals of various groups within the bituminous class of the ASTM classification by rank.

Equipment

Fig. 1 shows the principal items of equipment employed in the tests at the Mines Branch laboratories including a pulverizer, a coal feeder, a blower, an oil-fired preheater, and a combustor. The pulverizer is a high-speed impact mill with a mechanical air separator; it delivers a product, 90 per cent of which passes a 200-mesh screen at a rate of about 250 lb per hr. The coal feeder is a stoker screw operating in a conduit; it is driven by a variable-speed drive and reduction gear. The screw transfers the pulverized coal from the bottom of a 1-ton storage hopper, mounted on a scale, to the mixing box where it is picked up by a stream of air and delivered through a splitter to the burner grid. The blower is a centrifugal fan, rated at 15,000 cfm against 30 in. of water, at 70 F, and barometric pressure 29.8 in. Hg, driven by a 100-hp motor. The output of the blower is controlled by a shutter-type damper.

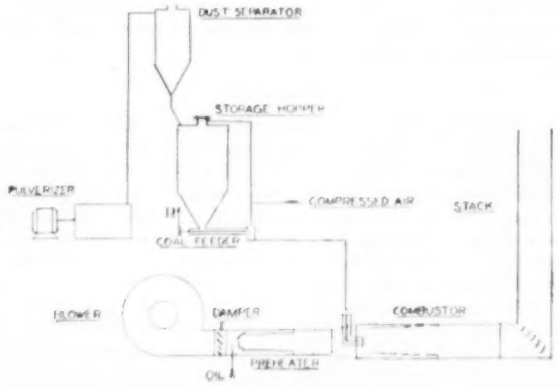

FIG. 1

[1] Published by permission of the Director-General of Scientific Services, Department of Mines and Technical Surveys, Ottawa, Canada.

[2] Department of Mines and Technical Surveys, Canadian Government.

[3] Engineer, Fuels Division, Department of Mines and Technical Surveys, Canadian Government. Jun. ASME.

[4] "Experimental Combustion of Pulverized Coal at Atmospheric and Elevated Pressures," by H. R. Hazard and F. D. Buckley, Trans. ASME, vol. 70, 1948, pp. 729–737.

[5] "A Progress Report on Gas-Turbine Combustors for Pulverized Coal," by H. R. Hazard, presented at the Gas-Turbine Engineering Division, St. Louis, Mo., June 19, 1950, of THE AMERICAN SOCIETY OF MECHANICAL ENGINEERS.

Contributed by the Gas Turbine Power and Fuels Divisions and presented at the Semi-Annual Meeting, Cincinnati, Ohio, June 15–19, 1952, of THE AMERICAN SOCIETY OF MECHANICAL ENGINEERS.

NOTE: Statements and opinions advanced in papers are to be understood as individual expressions of their authors and not those of the Society. Manuscript received at ASME Headquarters, February 19, 1952. Paper No. 52—SA-4.

The function of the preheater is to raise the temperature of the air supply to the combustor to about 600 F in order to simulate conditions that would result from use of a regenerator. The preheater is made up of a perforated stainless-steel flame tube 4 ft 6 in. long and 19 1/2 in. diam contained in an 8-ft length of 24-in. steel pipe. Oil is fed from a storage tank by a rotary gear pump to an atomizing nozzle in the inlet end of the flame tube. The oil-feed rate can be varied plus or minus 20 per cent by varying the pressure at the nozzle. The oil is ignited by a hydrogen flame. Products of combustion from the preheater are mixed with the total air from the blower in the preheater to provide a uniform temperature entering the coal combustor.

Fig. 2 shows the coal combustor which is of the film-cooled type similar to that developed at Battelle.[5] It is 7 ft long and 2 ft

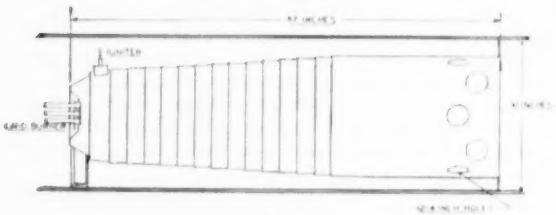

FIG. 2

diam at the open end. The flame tube is supported in a 10-ft length of 30-in. steel pipe. The burner, in the head of the flame tube, is of the grid type with nine nozzles arranged in a 6-in. square. The nozzles are supplied individually by a splitter which divides the stream of coal and carrying air into 9 equal parts. A spark-ignited oil flame is used for ignition of the coal. The combustor differs from that at Battelle in that a 1-in. annular opening was left round the grid burner. The purpose of this was to supply more air for support of combustion in the flame zone.

The main air supply from the blower is measured by means of an orifice, piezometer ring, and manometer. The primary coal-carrying air is measured separately by an orifice and differential manometer. Temperatures are measured by systems of bare chromel-alumel thermocouples, located at the outlets of the preheater and combustor, and connected to a 30-point indicator. Ash samples for ash-balance calculation are collected through a 1 1/2-in. horizontal traversing tube by a single "aerotec" dust-collecting tube, and led through a receiving cup with a canvas-bag filter for removal. Samples were taken by timing the traverse so that the sample would be fully representative of the combustion during the test. Larger samples of ash for other studies are collected by a cyclone separator from the bottom of the exhaust duct. The average coal-feed rate is determined by a continuous record of the time required to deliver 10-lb increments from the storage hopper.

PROCEDURE

At the beginning of each test approximately 1000 lb of coal are pulverized to a size distribution such that 90 per cent passes a 200-mesh seive. The pulverized coal is stored in the feed hopper. The air streams are then turned on and the preheater and oil igniter started. The coal feeder is started and when steady conditions are reached, the test measurements are begun. Temperature traverses are taken at the preheater outlet and the combustor outlet in such a manner that the arithmetic mean of each set of readings is the average temperature. At the same time a traverse is made with the ash sampler at the combustor outlet at such a rate that the sample collected is representative of all the residue leaving the combustor. Observations are also made of the oil-feed rate to the preheater, the main-air-supply rate, the coal-carrying air rate and pressure, and the temperature and relative humidity of the ambient air.

With each coal, separate tests are made at different air and coal rates in order to give different temperature rises. The preheat temperature is maintained at approximately 600 F in all cases. The coal-carrying-air rate is adjusted to give the maximum temperature rise after the main air- and coal-feed rates have reached steady conditions.

With the present equipment and procedure, it was found difficult to maintain steady operating conditions. The principal cause for fluctuating conditions appeared to be due to variations in the coal-feed rate. Usually these could be corrected by discharging all unused air from the compressor to avoid operation of the pressure regulator and give a constant pressure to the coal-carrying air. Adjustments also were made to the pressure-balance line to the storage hopper and the air supply to the aerators around the feeder so that the feed screw gave a more uniform output into the mixing box.

Combustion efficiencies were calculated both by heat balance and ash balance. The heat-balance results, however, were found to be less reliable than those obtained by ash balance, probably because of radiation errors which caused inaccurate mean combustor-outlet temperatures. The ash-balance efficiencies might be expected to have one major source of error, namely, continued combustion after the sample has been taken from the combustor, but the fact that the sample could be collected in a canvas filter is evidence that this source of error did not apply in the present experiments. Efficiencies based on ash-balance data have, therefore, been used for correlation with the properties of the coals.

Efficiency has been expressed by the following equation

$$\text{Efficiency} = \frac{\left(\begin{array}{l}\text{Gross calorific}\\ \text{value of coal,}\\ \text{Btu per lb}\end{array}\right) - \left(\begin{array}{l}\text{Heat loss as combustible}\\ \text{matter in stack dust per}\\ \text{lb of coal charged}\end{array}\right)}{\text{Gross calorific value of coal, Btu per lb}}$$

Where efficiency is shown as a single value for any coal the value is the arithmetic mean of efficiencies obtained in all tests made on the coal. Individual tests on each coal are given in Table 1 in increasing order of coal-to-air ratios.

DESCRIPTION OF COALS TESTED

The samples employed in the tests were typical of various coals in normal use for steam locomotives in Canada. They were supplied by the two major Canadian railways, 12 from the Canadian National Railway, and 11 from the Canadian Pacific Railway. Fifteen of the coals were of Canadian origin and 8 were imported by the railways from the United States. All 23 samples were within the limits of the bituminous class of the ASTM classification according to rank. The properties of the coals, listed in order of combustion efficiency, are shown in Table 2.

DISCUSSION OF RESULTS

The data in Table 1 indicate a major trend toward higher efficiency with decrease in rank of the coals. This is shown more clearly in Table 3 where the average efficiencies for all tests on each coal are listed against classification by rank. Further, if the average efficiency for all coals in each group is listed as in Table 4 the coals are placed in inverse order of rank.

The basis for classification of the five groups of the bituminous class changes between the high-volatile A and medium-volatile groups. Low and medium-volatile bituminous coals are classified according to the percentage of volatile matter; the three high-volatile groups are classified according to calorific value. Therefore the continuous trend throughout the whole class was not

TABLE 1 RESULTS OF TESTS

Coal no.	Test no.	Coal/air ratio × 10^{-3}	Combustion efficiency, per cent	Coal rank	Coal no	Test no.	Coal/air ratio × 10^{-3}	Combustion efficiency, per cent	Coal rank
1	1	14.4	95.5		11	1	7.4	63.3	
	5	14.7	85.3	High vol. bit. C		2	8.7	76.2	High vol. bit. B
	2	16.3	86.9			6	12.6	76.9	
	4	16.4	89.0			4	16.1	74.8	
	3	19.1	92.7			3	18.2	75.1	
						5	22.1	72.3	
2	4	6.7	90.5		12	1	10.2	71.4	
	5	8.5	90.1	High vol. bit. A		3	10.6	74.9	High vol. bit. A
	1	10.8	81.2			2	11.8	77.0	
	2	12.1	88.6			4	18.8	67.6	
	3	14.2	93.5						
					13	1	10.4	72.7	
3	5	11.4	84.0			2	20.0	68.5	Med. vol. bit.
	1	14.1	89.1	High vol. bit. B		3	21.4	66.8	
	2	14.4	83.8			4	26.4	56.0	
	3	16.0	85.5						
	4	19.0	91.2		14	2	11.0	63.0	
						1	11.6	73.0	Med. vol. bit.
4	1	9.8	77.8			3	11.8	60.4	
	2	12.6	89.0			4	15.2	63.0	
	3	14.1	89.5	High vol. bit. C		5	15.9	68.4	
	4	14.5	89.3		15	4	13.4	56.0	
	5	16.1	84.6			1	13.7	71.4	Med. vol bit.
	6	17.4	83.3			2	15.9	62.6	
						3	28.9	44.0	
5	1	9.0	79.8						
	2	11.7	78.0	High vol. bit. A	16	1	11.6	48.0	
	3	12.0	79.4			2	14.1	56.0	Med. vol. bit.
	5	14.1	76.8			3	16.5	63.4	
	6	17.6	76.0			4	22.1	66.0	
	4	18.3	78.4			5	26.2	58.0	
					17	1	13.3	58.8	
6	1	9.1	73.7			2	15.5	62.1	Med. vol. bit.
	2	11.2	79.2	High vol. bit. A		4	16.5	61.5	
	3	14.4	79.5			3	20.8	53.0	
	4	17.1	78.6			5	30.1	54.1	
	5	18.9	77.3						
					18	1	13.1	58.2	
7	1	6.9	63.2			2	16.8	59.3	Med. vol. bit.
	2	9.4	80.2	High vol. bit. B		3	18.4	53.3	
	3	11.1	81.3			4	20.3	59.9	
	6	13.3	79.8						
	4	14.1	81.0		19	1	13.8	45.5	
	5	21.7	77.0			2	15.5	65.2	Med. vol. bit.
						3	22.4	56.0	
8	1	9.8	77.9			4	43.7	50.5	
	2	11.9	79.8	High vol bit. A	20	1	12.4	31.3	
	3	15.1	78.8			2	14.8	43.0	Med. vol. bit.
	4	18.2	75.1			3	17.0	44.5	
	5	22.7	72.3			4	23.9	73.4	
9	1	10.6	77.3		21	1	9.0	—	Med. vol bit.
	6	10.6	78.3	High vol. bit. C		2	20.6	46.0	
	2	13.0	76.1						
	3	14.2	75.7		22	1	15.3	55.2	Low vol. bit.
	4	16.2	74.3			3	24.5	42.0	
	5	16.2	78.6			2	26.6	40.4	
					23	2	11.9	33.2	
10	3	10.7	76.4			1	14.3	49.4	Med. vol bit.
	2	15.1	76.0	High vol. bit. C		3	19.3	45.2	
	1	16.4	76.6			4	32.4	46.8	
	4	22.2	69.3						

TABLE 2 PROPERTIES OF COALS TESTED

Coal no.	Proximate analysis, as-received basis, per cent					Calorific value Btu/lb	Free swelling index	Ash fusibility		
	Moisture	Ash	Volatile	Fixed carbon	Sulphur			Initial, deg F	Softening, deg F	Fluid, deg F
1	8.2	17.1	31.7	43.0	0.2	10,000	NA[a]	2100	2310	2440
2	3.9	10.3	37.4	48.4	3.7	12,500	5+	2060	2300	2420
3	7.9	9.4	36.8	45.9	3.5	11,900	5	1950	2080	2400
4	8.8	13.6	32.8	44.8	0.3	10,510	NA[a]	2170	2320	2460
5	2.0	8.1	38.3	51.6	2.7	13,660	7½	2000	2190	2320
6	3.3	22.3	30.0	44.4	9.6	10,948	5½	1930	2030	2370
7	7.3	6.8	39.7	46.2	3.4	12,465	4	1950	2050	2400
8	1.4	16.5	32.2	49.9	7.6	12,236	5½	1920	2030	2140
9	4.8	13.8	36.7	44.7	3.9	11,765	6	2020	2110	2420
10	11.7	8.5	33.9	45.9	2.7	11,440	4	2100	2220	2500
11	6.1	9.8	37.6	46.5	3.4	12,240	5½	1990	2130	2440
12	1.8	14.5	31.3	52.4	7.2	12,514	5½	1900	2010	2280
13	3.6	16.0	24.4	56.0	1.6	12,130	4½	2500	2680	2750+
14	3.3	11.4	23.2	62.1	0.4	13,090	7½	2750+	2750+	2750+
15	3.1	11.8	24.7	60.4	0.6	13,100	6½	2300	2750+	2750+
16	2.5	17.0	25.7	54.8	0.5	12,080	2	2570	2750+	2750+
17	3.7	12.3	24.4	59.6	0.3	12,720	2	2290	2570	2700
18	3.2	21.8	21.3	53.7	0.3	11,300	1	2750+	2750+	2750+
19	5.6	19.4	23.3	51.7	0.2	10,830	1	2690	2750+	2750+
20	2.6	13.3	21.8	62.3	0.3	12,950	4	2320	2610	2740
21	5.4	15.6	24.1	54.9	0.3	11,750	1	2380	2630	2750+
22	1.6	10.5	16.9	71.0	0.4	13,770	4	2510	2630	2750+
23	3.5	14.9	21.3	60.3	0.3	12,520	2	2320	2750+	2750+

[a] Nonaggiomerating.

TABLE 3 AVERAGE EFFICIENCIES OF COALS TESTED

Coal no.	Coal rank	Average efficiency per cent
1	High volatile bituminous C	89.9
2	High volatile bituminous A	88.8
3	High volatile bituminous B	86.7
4	High volatile bituminous C	85.6
5	High volatile bituminous A	78.6
6	High volatile bituminous A	77.7
7	High volatile bituminous B	77.1
8	High volatile bituminous A	76.8
9	High volatile bituminous A	76.7
10	High volatile bituminous C	74.6
11	High volatile bituminous B	73.1
12	High volatile bituminous A	72.7
13	Medium volatile bituminous	66.0
14	Medium volatile bituminous	65.6
15	Medium volatile bituminous	58.5
16	Medium volatile bituminous	58.3
17	Medium volatile bituminous	57.9
18	Medium volatile bituminous	57.7
19	Medium volatile bituminous	54.3
20	Medium volatile bituminous	48.1
21	Medium volatile bituminous	46.0
22	Low volatile bituminous	45.9
23	Medium volatile bituminous	43.6

TABLE 4 AVERAGE EFFICIENCY FOR ALL COALS OF GIVEN RANK

Rank	Average efficiency for all coals of given rank, per cent
High volatile bituminous C	83.3
High volatile bituminous B	79.0
High volatile bituminous A	78.5
Medium volatile bituminous	55.6
Low volatile bituminous	45.9

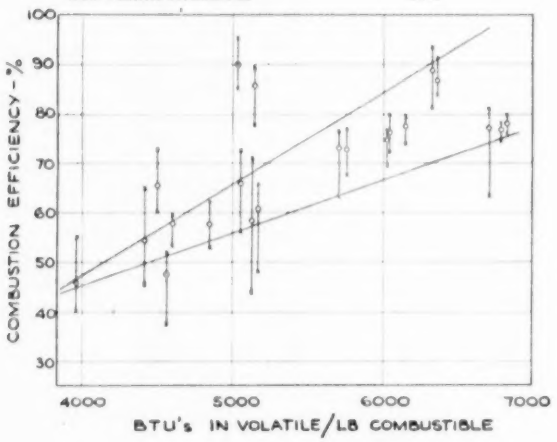

FIG. 3

anticipated, and it is probable that the variation in efficiency is caused by change in the value of some property that varies continuously with changing rank.

The calorific value of the volatile matter is one such property. Heat liberated by combustion of the volatile matter near the burner raises the temperature of the remaining fixed carbon and, therefore, might be expected to influence its combustion rate.

Fig. 3 shows the plot of combustion efficiencies against the total calorific value of the volatile for each coal. In each case the maximum, minimum, and average efficiencies are shown. While there is a great scatter of points a definite trend toward increasing efficiency with high heats in the volatile is evident. The spread also increased in the same manner as evidenced by the arbitrarily chosen boundary curves.

To study further the effect of the volatile content itself together with its calorific value, efficiency was plotted against the specific volatile index (SVI)[5] As can be seen in Fig. 4, a definite

[5] "Classification of Coals Using Specific Volatile Index," by E. J Burrough, E. Swartzman, and R. A. Strong. Canada Department of Mines, Mines Branch, Ottawa, Publication No. 725-2.

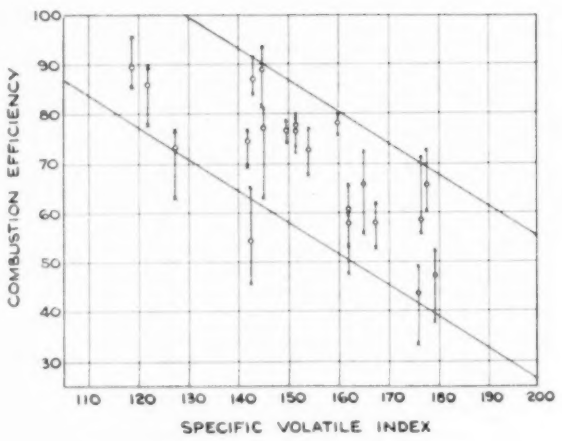

FIG. 4

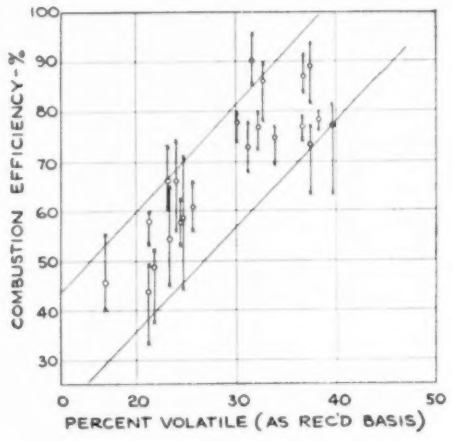

FIG. 5

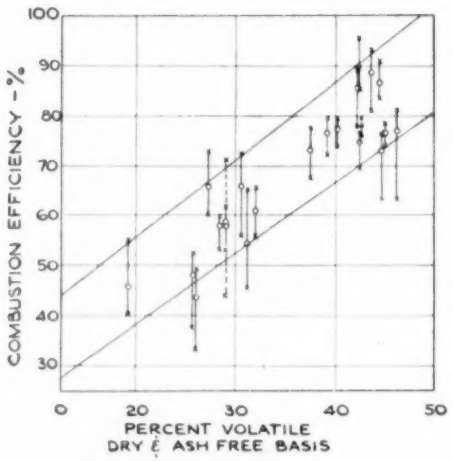

FIG. 6

TABLE 5 RELATION OF EFFICIENCY AND TEMPERATURE

Coal and group (sample no.)	Coal rate, lb/hr	Total air rate, M lb/hr	Temp rise, deg F	Combustor outlet temp, deg F	Efficiency, per cent
	539	50.3	420	1083	81.2
2	536	44.3	430	1117	88.6
A	500	35.6	443	1192	93.45
	240	36	230	970	90.5
(572)	304	36	290	1041	90.1
	643	48.8	303	934	58.8
17	684	44.4	346	982	62.1
M	754	36.5	415	1091	53.0
	614	37.65	348	1019	61.5
(573)	1090	36.8	575	1257	54.1
	487	50.3	352	1002	77.8
4	544	43.3	374	1085	89
	531	38.1	374	1100	89.5
C	548	38.1	381	1188	89.2
	608	38.2	366	1090	84.6
(571)	655	38.1	393	1103	83.3
	685	47.8	416	1004	95.5
1	752	47.0	472	1110	86.9
C	825	43.6	542	1154	92.7
	697	42.7	445	1019	89.0
(574)	647	44.5	367	952	85.3
	732	51.5	303	886	49.4
23	562	47.4	278	872	33.2
M	752	39.4	371	993	45.2
(576)	1255	39.1	487	1289	46.8
	539	51.9	261	815	72.7
13	896	45.1	488	1123	68.5
M	884	41.7	509	1126	66.8
(577)	944	36.1	525	1163	56.0
	773	47.3	558	1104	76.6
10	782	51.6	550	1061	76.0
C	466	44.0	370	910	76.4
(578)	865	39.2	638	1315	69.3
	539	39.6	354	933	71.4
15	616	39.1	417	1009	62.6
M	1112	38.8	590	1206	44.0
(579)	692	51.9	475	943	56.0
22	588	38.8	140	756	55.2
L	1263	47.8	363	884	40.4
(580)	1140	46.8	421	995	42.0
19	667	48.5	216	783	45.5
	690	42.9	312	933	65.2
M	616	27.8	352	1016	56.0
(581)	2010	49.3	740	1244	50.5
	588	45.1	158	735	58.2
18	589	35.3	314	984	59.3
M	700	38.3	267	830	53.3
(582)	720	35.7	394	998	59.9
	625	54.3	283	832	73
14	518	47.5	226	834	63
M	485	41.5	268	886	60.4
(583)	511	34	326	1021	63
	536	34	346	1047	68.4
	595	48.2	174	722	31.2
20	656	44.6	265	822	43.0
M	673	39.9	318	906	44.5
(585)	938	39.5	486	1083	73.4
	537	46.8	202	729	48.0
16	573	41.1	318	909	56.0
M	566	34.7	410	1080	63.4
(586)	745	34.0	514	1198	66.0
	910	34.1	514	1131	58.0
	495	46.1	364	912	77.3
9	517	40.1	424	993	76.1
A	565	40.1	470	1047	75.7
(587)	640	40.1	521	1107	74.3
	572	35.6	426	1143	78.6
	516	49.3	373	838	78.3
	594	42.4	411	869	89.1
3	618	43.1	483	1019	83.75
B	671	42.3	536	1121	85.5
(589)	690	36.7	608	1210	91.2
	496	44.0	423	950	84.0
	420	56.8	196	752	63.3
11	441	51.3	256	812	76.2
B	888	48.7	557	1146	75.1
(590)	710	44.3	490	999	74.8
	850	38.8	641	1217	72.3
	680	54.1	400	823	76.9
	235	46.1	95	660	52.2
	308	45.3	181	758	63.2
	383	40.9	284	857	80.2
B	451	40.3	365	947	81.3
	565	40.5	467	1057	81.0
(591)	841	39.1	678	1281	77.0
	684	51.8	468	937	79.8
5	430	48.4	287	816	79.8
	493	42.4	395	933	78.0
	507	42.4	422	906	79.4
A	760	41.9	627	1204	78.4
(593)	591	42.2	460	1008	76.8
	922	52.7	622	1081	76.0
	486	48.0	301	889	71.4
12	512	43.7	377	978	77.0
A	458	43.7	332	946	74.9
(607)	760	40.7	587	1181	67.6
	482	53.6	273	799	73.7
6	496	44.7	217	882	79.2
A	630	43.9	408	986	79.5
(608)	641	37.9	476	1061	78.6
	837	44.7	544	1041	77.3
	526	54.1	317	832	77.9
8	573	48.6	376	951	79.8
A	650	43.4	469	1069	78.8
(610)	636	35.3	566	1168	75.1
	794	35.4	669	1278	72.3

trend toward higher efficiency with coals of lower SVI is evident but here the spread is more or less constant throughout the range.

Taking the per cent volatile alone, neglecting its calorific value first on the as-received basis and then on the dry-and-ash-free basis, it is even more apparent from Figs. 5 and 6 that the trend is toward increasing efficiency with increased volatile content. It can be seen that in these two plots the scatter is less than in the plots which included the heat of the volatile as well.

Another measurable property, the "free swelling index" of the coals,[7] would appear to have some relationship to the size of the cenosphere formed under the conditions of combustion and so influence combustion rate. Fig. 7 is a plot of efficiency versus this property and, while a trend toward higher efficiency with greater swelling is evident, the spread in the boundary curves is much greater than in any of the previous plots. Also appearing almost as a complete contradiction are the two "nonagglomerate" coals with high efficiency. These coals which do not swell at all and on which a microscopic study of the ash showed no evidence of cenosphere formation, practically rule out the free swelling index as a means of rating the coal.

One plot which, to some, may be conspicuous by its absence is that of efficiency versus temperature rise but inspection of Table 5 will show that no grouping of the coals by rank, or volatile will give any consistent trend toward peak efficiencies at a given temperature rise.

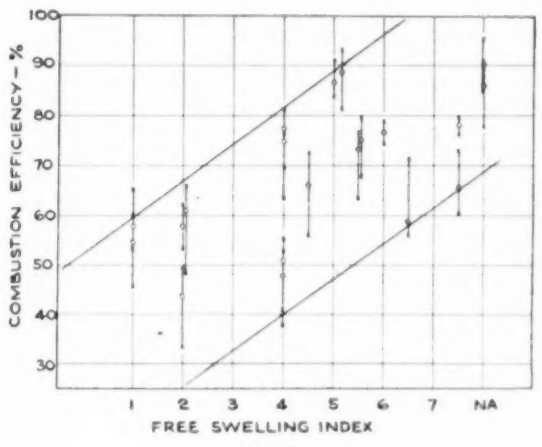

FIG. 7

Another property related to rank which might influence efficiency is the reactivity of the distillation products of the coal.

[7] ASTM Designation: D 720-46.

It is probably the reactivity of the fixed carbon remaining after very rapid distillation of small particles that is of significance in this connection. No samples suitable for reactivity measurements were collected in the present series of tests so that correlation of reactivity with efficiency is not yet possible.

Conclusions

Efficiency of combustion in a film-cooled combustor of a type proposed for use in coal-fired gas-turbine locomotives varies greatly with change in coal rank. The present tests indicate that bituminous coals of the high-volatile A, B, and C groups will, in general, give satisfactory performance. Coals of higher rank appear to be unsuitable because of low combustion efficiency. Tabulation of the coals tested in order of efficiency placed them in descending order of rank.

A definite trend toward higher efficiencies with higher volatile contents and high-volatile heat contents is evident from the test data. Therefore one can safely say that coals of low rank, high-calorific-value volatile and high-volatile content will prove satisfactory in a combustor of this type operated at atmospheric pressure.

To get satisfactory combustion of the higher rank, lower-volatile coals modification of the burner design appears to be necessary. Some increase in efficiency can be expected by operation under pressure but for efficiencies constantly in the 85-95 per cent range over the full range of North American coals considerable modification will be required. This may be expecting too much of any given combustor when one considers that any other existing combustor is designed to burn fuel falling in a comparatively narrow band of variable properties.

Discussion

H. R. Hazard.[8] The authors' data indicate a large variation of combustion efficiency at atmospheric pressure with changes in coal properties, while data from other sources, to the contrary, show little, if any, effect of coal properties on combustion efficiency in gas-turbine tests at elevated pressures. The reasons for these extremely different results are probably the combined effects of burner design and of pressure. It would be of interest to know more about the comparative effects of each of these factors.

The burner used by the authors was similar to the multijet burner used at Battelle during combustor development work for the Locomotive Development Committee of BCR. Although the burner was unsuitable for use in a gas turbine because of its shape and characteristics, it gave the highest efficiency of any burner tested, and, thus served as a basis for comparison. It was felt that no burner would surpass it in efficiency, although improvement in other characteristics was needed. The principal difference between the Battelle burner and that used by the authors was the addition of a 1-in. annular air space around the periphery. Whereas the original burner admitted the coal with air in stoichiometric proportions, it appears, by comparison of areas, that this modification roughly doubled the air/fuel ratio at the burner. This apparently did not affect performance with high-volatile coals, because several values of efficiency above 90 per cent are reported. However, it appears likely that it had a much greater effect on low-volatile coals, as these are particularly sensitive to high air/fuel ratios, and that much higher efficiencies might have been obtained at atmospheric pressure by some modification of air/fuel ratios. Thus the difference in data between those at atmospheric pressure, and those in the gas turbine is probably not entirely due to the favorable effect of pressure in raising flame temperature by reducing the proportion of radiation loss, but is probably influenced greatly by the air/fuel ratios at which the burner was operated.

J. I. Yellott[9] and F. D. Buckley.[10] Early in 1949 the Canadian Bureau of Mines offered to undertake a combustion project to determine the efficiency of the Locomotive Development Committee's combustor with a variety of Canadian coals. Enough components were available from the various programs to help them set up their test stand. The combustor was from Fontana, the burner and preheater were from Battelle, and the igniter was from Dunkirk. These were engineered by the Bureau into a test stand which was the best we knew how to set up at that time, and is the one used in the tests just reported.

The combustor which was used was developed for the Locomotive Development Committee by the Turbodyne Corporation early in 1949. It was tested with a coal burner of its own design at full-flow conditions and under moderate pressure, at Fontana, Calif., where a spare blower in the Kaiser steel mill furnished the air.

The burner described in the paper was of the square multijet type. It was a Battelle version of an English design developed by BCURA for use on Lancashire boilers, and had been used at Battelle in a different combustion design.

All atmospheric combustion work by the Locomotive Development Committee was concluded when the Houdry turbine was ready for operation at Dunkirk, and the combustor development was continued on this unit because full locomotive condition could be obtained for one combustor. The first combustor to be tested on the Houdry was similar to that shown in the paper in Fig. 2, but with a variation of ring supports and dome construction to permit the use of a circular multijet burner.

Fig. 8 Flexible-Ring Combustor Used During Fourth 250-Test of Houdry Unit

After a long series of major and minor changes, in which the air proportion to the various sections and the type of construction were altered, the combustor shown in Fig. 8 of this discussion appeared to give satisfactory efficiency, cleanliness, and life.

The construction of the film-cooled section was changed to permit free radial expansion of each ring and yet hold axial alignment, by the use of 12 radial pins. These pins were supported in a separate cradle which was made of carbon steel. By this means distortion of the elements and consequent maldistribution of air were eliminated, and ash deposition was minimized. Combustors of this design have operated at high firing rates for well over 500 hr with no noticeable deterioration or distortion, and two of this design are now operating in the locomotive test plant.

A number of disappointing experiences with various designs of multijet burners led to its abandonment in favor of an annular type. It appeared that the grid burner was too critical to air proportion, and because of interference in the flow pattern, it caused recirculation within the dome section. To obtain high combustion efficiency the flame front had to be kept close to the

[8] Assistant Supervisor, Fuels Research Division, Battelle Memorial Institute, Columbus, Ohio. Mem. ASME.

[9] Director of Research, Locomotive Development Committee, Bituminous Coal Research, Inc., Baltimore, Md. Mem. ASME.

[10] Assistant Manager, Dunkirk Laboratory, Locomotive Development Committee, American Locomotive Company, Dunkirk, N. Y. Mem. ASME.

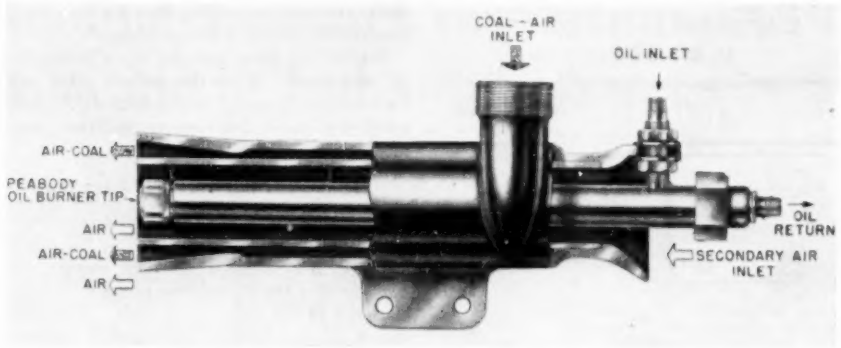

FIG. 9 DUNKIRK ANNULAR BURNER FOR PULVERIZED COAL AND OIL

nozzles which were usually melted away. Higher air velocities through the burner caused low efficiency and blowout. Turndown was very limited, even with an oil flame to maintain ignition.

The annular burner shown in Fig. 9, herewith, was designed to accomplish several purposes. The coal-air mixture was blown tangentially to the burner annulus to obtain uniform distribution at the burner tip. The swirling action was intended to throw the coal out into the combustion air coming through the dome. Auxiliary air was allowed to pass on both the outside and inside of the coal annulus. The air on the outside was whirled by vanes in the dome in a direction counter to the coal-air stream, to produce a short flame. Air was admitted through the inner portion of the burner to prevent recirculation within the flame and to supply a central oil nozzle. This nozzle doubled as an igniter and a burner for oil-fired operation. Many revisions were made in the dome section, in conjunction with burner changes, to supply the proper air proportions and to prevent ash deposits.

The curves in Fig. 10 show the results obtained with the present combustor-burner combination in the Houdry unit with three coals representing high, medium, and low-volatile. These test results were obtained in the period from 1000 to 1250 hr of the Houdry turbine plant operation, with no oil-ignition flame used during the test runs.

Although this combustor has never been operated at atmospheric pressure it can easily be seen that the efficiency and turndown have been much improved over the combustor tested at the Canadian Bureau of Mines.

Fig. 11 shows the results of Fig. 10 superimposed on Fig. 5 of the paper. It can be seen that the improved combustor design has raised considerably the combustion efficiency for the low-volatile coals.

Fig. 12, herewith, is a cross section of the Houdry combustor test stand. No louver separators were used ahead of the ash-sampling points. The combustion efficiency was determined by ash balance from ash collected on a horizontal traverse and, although the sampling point was about 6 ft from the mixing section of the combustor, it had been determined that little additional combustion took place.

In the tests which were made by the authors we feel that the low combustion efficiency was caused mainly by the multijet burner and its installation in the dome of the combustor. The 1-in. annulus, which was left around the burner, would aggravate the already poor characteristics of this type of burner. It is doubtful to us whether many of the low-volatile coals could have been burned at all without the use of an oil-ignition flame.

The combustor development has progressed so far since these Canadian tests were made that it would certainly seem advanta-

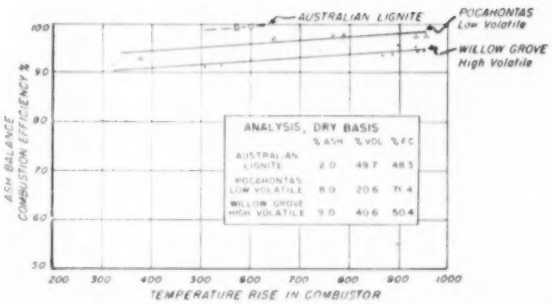

FIG. 10 ASH BALANCE COMBUSTION EFFICIENCY VERSUS TEMPERATURE RISE, COMBUSTOR F 7

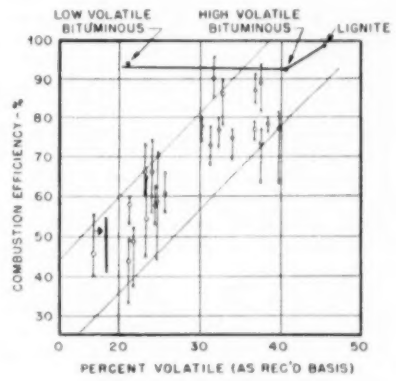

FIG. 11

geous to all concerned if this series of runs could be repeated with the present combustor design.

In conclusion we would like to thank the authors and the group at the Canadian Bureau of Mines for their interest in the gas-turbine combustion problem, and for taking it upon themselves to make this large series of tests. It is felt that these results will be more useful when they are correlated with similar test results from a more advanced type of combustion system.

W. E. YOUNG.[11] The authors are to be commended for an excellent piece of work. Since the properties of bituminous coal vary so widely it is of course necessary that coals throughout the

[11] Westinghouse Research Laboratories, East Pittsburgh, Pa.

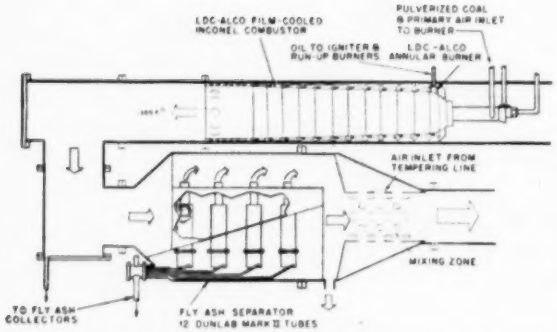
LDC-ALCO FILM-COOLED INCONEL COMBUSTOR
PULVERIZED COAL & PRIMARY AIR INLET TO BURNER
OIL TO IGNITER & RUN-UP BURNERS
LDC-ALCO ANNULAR BURNER
AIR INLET FROM TEMPERING LINE
MIXING ZONE
TO FLY ASH COLLECTORS
FLY ASH SEPARATOR 12 DUNLAB MARK II TUBES

FIG. 12 ARRANGEMENT OF LDC COMBUSTION AND ASH-REMOVAL EQUIPMENT FOR EXPERIMENTAL GAS TURBINE AT DUNKIRK

bituminous range be investigated for satisfactory combustor performance. The present investigation appears to have included any coal which conceivably might be encountered.

Under "procedure" the authors state that all coals were pulverized to a size distribution such that 90 per cent would pass a 200-mesh sieve. For a given coal, the size-distribution curve (which normally is shown as a straight line on Rosin Rammler co-ordinates) has a slope which is characteristic of the pulverizer; hence, for a given coal, various distribution lines should be parallel. Therefore the location of one point, such as 90 per cent through 200-mesh, serves to identify the complete distribution. But for coals of widely varying properties, the question arises as to whether or not the distribution curves for various coals will be parallel. If they are not, they might all satisfy the specification of 90 per cent through 200 mesh, but the average particle size and over-all distribution upon which completeness of combustion depends possibly might be different. Have the authors investigated the over-all distributions of these coals, or at least obtained another point in addition to the 90 per cent through 200-mesh size?

The fact that combustion efficiencies based on heat balances and ash balances do not agree would seem to give cause for some concern. The authors explain the discrepancy as being due to radiation errors presumably in the thermocouple readings. It should be possible to minimize these errors by proper choice of and location of the thermocouples, or at least to compute the radiation error. A question also arises as to the calculation of efficiency by means of an ash balance. The authors express efficiency by the equation

$$E = \frac{\begin{pmatrix}\text{Gross calorific value}\\ \text{of coal, Btu per lb}\end{pmatrix} - \begin{pmatrix}\text{Heat loss as combustible}\\ \text{matter in stack dust per lb}\\ \text{of coal charged}\end{pmatrix}}{\text{Gross calorific value of coal, Btu per lb}}$$

Frequently the combustible matter in the stack dust is assumed to be pure carbon with a heating value of 14,500 Btu/lb. However, at efficiencies less than 80 per cent and at these relatively low outlet temperatures, considerable volatile, with some unknown heating value, may still exist in the stack dust. An error, then, might be introduced if all the remaining combustible were considered to be carbon. Of course this error will not arise if the gross calorific value of the stack dust is used, as this automatically takes into account the heating value of any volatile. Would the authors explain the method they use to determine the heat lost as combustible matter in the stack dust?

Fluctuating conditions due to variations in the coal feed rate are mentioned. Have the authors noted any difference in the various coals in regard to this difficulty? Specifically, have they noted any correlation between moisture, ash, and volatile content, and uniformity of feed?

AUTHORS' CLOSURE

The authors appreciate the written comments on this paper by Mr. Hazard. They point out that the chief difference between our test rig and that at Battelle, namely, the 1-in. annular air space around the burner, was probably the cause of the very low efficiency of the higher rank coals. This space was not present during the first series of runs and a uniform low efficiency resulted throughout the whole range of coals. In the second series, reported in this paper, the 1 in. annulus was provided around the burner and together with improved pulverization, improved efficiency considerably on the first few coals.

The comments by Messrs. Yellott and Buckley are much appreciated and serve to demonstrate the tremendous advances made by the LDC since our test rig was set up. We, at the Canadian Bureau of Mines, are pleased to see the LEC coming within sight of a successful completion to the "Coal-Fired Gas-Turbine Locomotive Project" and are proud to have been associated even in a small way with them.

Mr. Young's comments are constructive and are appreciated. They raise several interesting points, some of which can be answered, others which cannot.

The over-all size distribution was not investigated fully but an unsuccessful attempt was made to correlate efficiency to per cent minus 325 mesh. In these tests all the coals passed 100 per cent through 100 mesh and the per cent through 325 mesh varied between 25 and 65. Thus one can see that the size-distribution curves on the Rosin Rammler co-ordinates were not parallel. In a previous series with the same coals but a different pulverizer, the per cent + 100 mesh was 10-25 and the per cent minus 200 only 60-75, the resultant efficiencies being 10 per cent or more lower in the low-rank coals. In the medium-rank coals, efficiencies with the coarser coal were only slightly lower and in high-rank coals were actually higher than with the finer coals. As pointed out earlier, the 1 in. annulus around the burner was added at the same time as the new pulverizer was installed; thus the conclusion could be made that the changed air/fuel ratio probably canceled out the improvement due to finer pulverization in the high-rank coals which are sensitive to air/fuel ratios.

Heat loss as combustible in the stack dust was determined by assuming all combustible to be pure carbon with a heating value of 14,500 Btu per lb. This, we agree, is not the most accurate method. However, on several of the poorer runs the ASTM test for volatile content was used and the highest analysis showed only 3 per cent volatile which would raise the combustion efficiency by 1 or 2 percentage points above that determined by assuming the combustible to be pure carbon. While our test results are not too conclusive, the value of using the ASTM volatile test for chars in still open to argument. In any future work we believe the best method would be to provide facilities for a calorific determination on the chars.

Since the coal feeder was being modified constantly, no true evaluation of the effect of moisture, ash, and volatile could be made.

A Nondimensional Correlation of Flame Propagation at Subatmospheric Pressures

By R. E. CULLEN,[1] ANN ARBOR, MICH.

The effect of ambient pressure on the propagation rate of Bunsen flames in propane-air and ethylene-air mixtures is described. It is concluded that the normal flame speed for the fuels studied varies inversely with the logarithm of the pressure from atmospheric pressures to as low as 1 in. Hg abs. A nondimensional parameter, the Peclet number, is established that correlates the results with four burner sizes, two fuels, and for the range of pressures investigated. It is concluded that the Peclet number must be kept large to avoid considerable reductions in flame speeds at subatmospheric pressures.

Introduction

THE rate at which a flame front propagates through an unburned mixture of combustible gases, i.e., a process normally termed a "deflagration," is of fundamental importance to the design and operation of jet-combustion chambers. It is the purpose of this paper to describe the effect of ambient pressure on the propagation rate of flames in air mixtures of hydrocarbon fuels similar to the fuels employed in present-day jet-combustion chambers (1).[2] In addition, a correlation of the pressure and scale effects upon flame-propagation rates by means of a nondimensional parameter, the Peclet number, will be shown. The importance of this fact to the operation of jet combustors at extreme altitude conditions will be discussed.

Experimental Equipment and Procedure

In order to carry out an investigation of the pressure and scale on effects on flame-propagation rates, the Bunsen-burner flame was employed because of its inherent experimental advantages.

The combustible mixture was introduced in the bottom of a vertical stainless-steel tube, 24 in. long, with an internal diameter of $1^5/_8$ in. At the top of the tube one of four interchangeable, convergent nozzles with exit internal diameters of $^3/_8$, $^1/_2$, $^5/_8$, and $1^1/_4$ in. was installed, Fig. 1. A copper cooling coil around the retaining head of the burner assembly through which cold water circulated, was employed to keep the temperature of the unburned gases relatively constant. The burner assembly was mounted in the bottom of a pressure vessel constructed of $^1/_2$-in. welded mild steel. The flames were observed through plate-glass windows mounted in the sides of the pressure vessel. The flames were ignited with a high-voltage discharge to the burner exit from a movable electrode.

A sketch of the burner and pressure vessel appears in Fig. 2. A Nash Hytor vacuum pump was used to evacuate the pressure vessel to moderately low pressures. A high-pressure air ejector, operating from two 80-cu-ft pressure tanks at pressures from 1500 psi to 2000 psi was employed to obtain the lowest pressures at which flames were observed, i.e., about 1 in. Hg abs. The fuels used for the investigations were commercially pure propane and medical ethylene. The fuels were premixed with dry air in storage bottles at desired mixture concentrations and at a pressure of 240 psig. Four rotameters of various capacities, calibrated for air at a density of 0.073 lb/ft³ were used to measure the flow rate of the combustible mixture. The temperature of the mixture at the burner exit prior to combustion was obtained by means of a thermocouple.

A Leica 35-mm camera was used to photograph the flame. The film used in the experiments was Ansco Supreme, a moderately fast film with fine-grain characteristics. The photographs of the flames were mounted in glass slides and projected on white tracing paper to between 10 to 15 times natural size. The inner surface of the reaction zone was traced, with care being taken to record the absolute lower limit of the reaction zone near the burner exit. At the lower pressures where the reaction zone became thicker and more diffused, longer exposures were taken to insure that all of the luminous zone was recorded on the film.

Fig. 1 Burner Tube and Nozzles

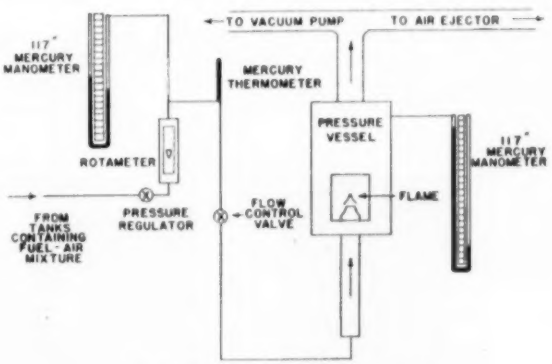

Fig. 2 Line Diagram of Apparatus

[1] University of Michigan, Engineering Research Institute.

[2] Numbers in parentheses refer to the Bibliography at the end of the paper.

Contributed by the Gas Turbine Power Division and presented at the Semi-Annual Meeting, Cincinnati, Ohio, June 15–19, 1952, of The American Society of Mechanical Engineers.

Note: Statements and opinions advanced in papers are to be understood as individual expressions of their authors and not those of the Society. Manuscript received at ASME Headquarters, April 7, 1952. Paper No. 52—SA-39.

The flame surface area was determined by graphical integration using the theorem of Pappus and Simpson's rule.

The normal flame-propagation rate, viz., normal flame speed, can be defined briefly as the rate at which a flame front traverses an unburned mixture of combustible gases normal to itself and relative to the unburned gases. The flame speeds were obtained by the Gouy area method which can be explained as follows: If we assume a constant flame speed over the whole flame surface, normal to the surface, the following continuity relation must apply

$$\rho_0 A_0 \bar{V}_0 = \rho_f A_f V_f \quad \ldots\ldots [1]$$

where the area of the exit of the nozzle is given by A_0 and the average velocity of the unburned mixture at the nozzle exit is given by $\bar{V}_0$. The quantity of gas flowing $A_0 \bar{V}_0$ must be burned at the flame surface A_f. If the density of the unburned gases ρ_0, at the exit of the tube is assumed equal to the density of the gases, ρ_f, immediately upstream of the inner limit of the reaction zone, then the normal flame speed V_f is given by

$$V_f = \frac{A_0 \bar{V}_0}{A_f} \quad \ldots\ldots [2]$$

However, the normal flame speed is not constant over the entire surface of the flame cone; therefore V_f as measured assumes an average value.

The Gouy area relation, Equation [1], then, gives the average normal flame speed from two experimentally determined quantities—the volumetric rate of flow at the nozzle exit and the surface area of the flame.

The runs using the $^3/_8$-in., $^1/_2$-in., and $^5/_8$-in. burners were initiated at atmospheric pressure, while the runs using the $1^1/_4$-in. burner were initiated at 13 in. Hg abs for the propane-air flames and 10 in. Hg abs for the ethylene-air flames. These were the highest pressures at which laminar flames could be burned in the $1^1/_4$-in. burner without the development of turbulence in the flow. The volumetric flow rate to the flame was kept to a fairly constant value except at low pressures where it was reduced slightly to prevent the flame from blowing off. The temperature of the mixture at the burner exit prior to combustion, as measured by a thermocouple, varied between 82 and 91 F for all the runs. These small temperature variations proved to have a negligible effect on flame speed. The lower pressure limit attained with the four burners varied between about 1 in. Hg abs for the $1^1/_4$-in. burner with an ethylene-air mixture and 6 in. Hg abs for the $^3/_8$-in. burner with a propane-air mixture. A fuel-air mixture of 0.067 lb of propane per lb of air, i.e., the mixture for maximum flame speed, was used for all the runs made with propane-air as the combustible. A fuel-air ratio of 0.0836 lb of ethylene per lb of air was used for the ethylene-air runs.

Results and Conclusions

The photographs of ethylene-air flames burning from the $^3/_8$-in. burner are reproduced in Fig. 3 to show graphically the effect of pressure on the shape of the flame and the thickness of the reaction zone. It will be noted that the shape of the flame front changes from that of a pointed cone at atmospheric pressure to a perfectly flat flame at 3.6 in. Hg abs. In addition, the thickness of the reaction zone, i.e., the white band on the photographs, continually increases with decreasing pressures.

Fig. 4 shows a comparison of flames burning from the four different-size burners at the same pressure. In the left column are ethylene-air flames burning from the four different-size burners at 4 in. Hg abs and in the right column are propane-air flames at 6 in. Hg abs. It should be stated that although the thickness of the reaction zone appears much larger for the flames burning from the smaller burners, actually the reaction-zone thickness is

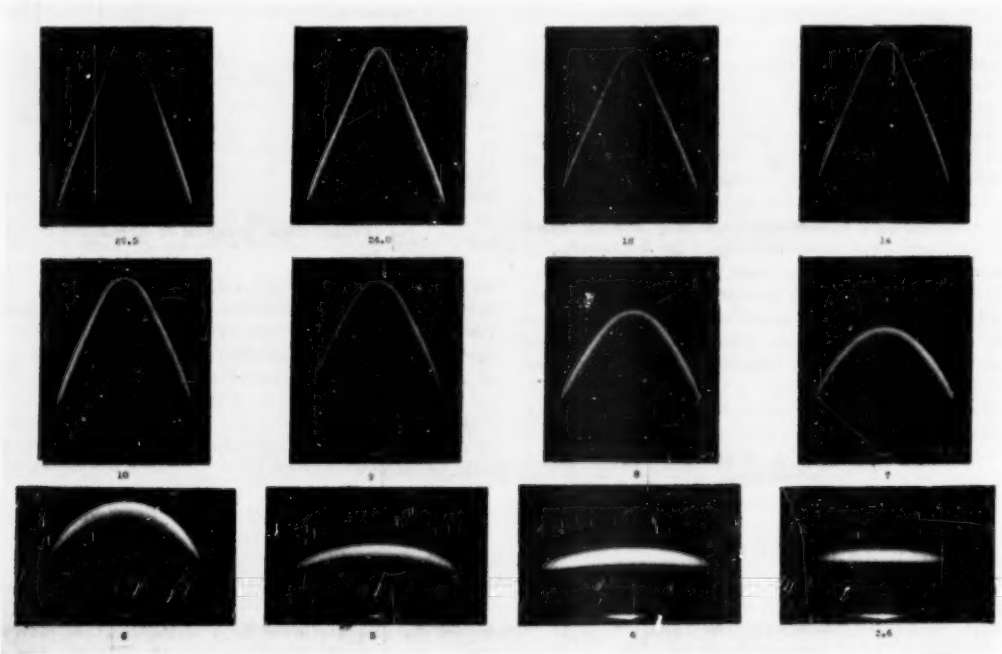

Fig. 3 Ethylene-Air Bunsen Flames at Subatmospheric Pressures With $^3/_8$-In. Burner
(Fuel-air ratio—0.0836 lb ethylene/lb air Numbers under photographs indicate pressure in inches Hg absolute.)

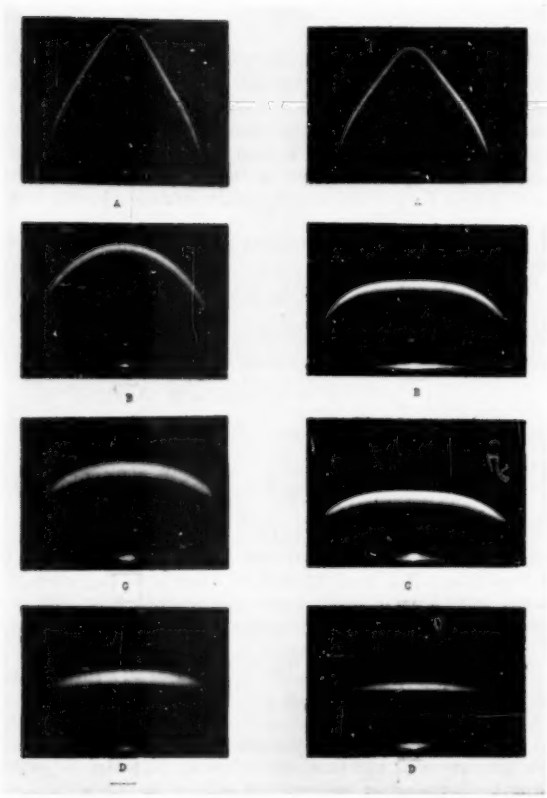

FIG. 4 PROPANE-AIR FLAMES AND ETHYLENE-AIR FLAMES BURNING FROM FOUR DIFFERENT DIAMETER BURNERS AT SUBATMOSPHERIC PRESSURES. FUEL-AIR RATIO—0.0836 LB ETHYLENE/LB AIR

(*Left column:* Ethylene-air flames at 4 in. Hg abs. *Right column:* Propane-air flames at 6 in. Hg abs. Fuel-air ratio—0.067 lb propane/lb air. A, 1¼-in-diam burner; B, ½-in-diam burner; C, ¼-in-diam burner; D, ⅛-in-diam burner.)

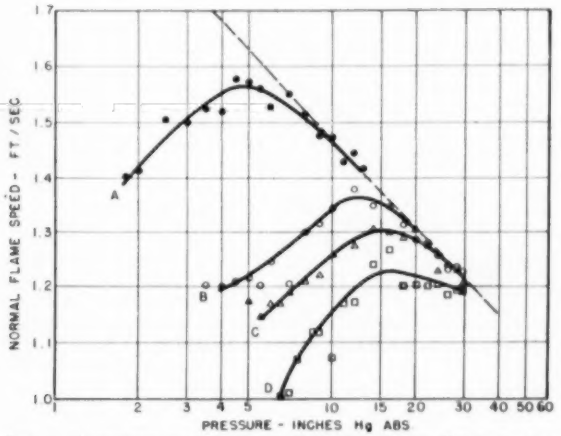

FIG. 5 VARIATION OF NORMAL FLAME SPEED WITH PRESSURE FOR PROPANE-AIR BUNSEN FLAMES

(A, 1¼-in.-diam burner; B, ½-in-diam burner; C, ¼-in-diam burner; D, ⅛-in-diam burner. Fuel-air ratio, 0.067 lb propane/lb air.)

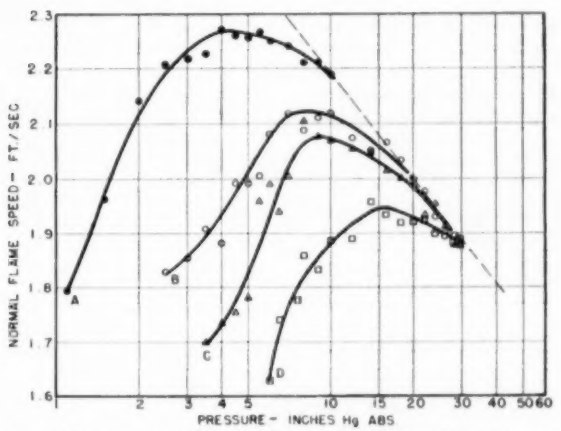

FIG. 6 VARIATION OF NORMAL FLAME SPEED WITH PRESSURE FOR ETHYLENE-AIR BUNSEN FLAMES

(A, 1¼-in-diam burner; B, ½-in-diam burner; C, ¼-in-diam burner; D, ⅛-in-diam burner; Fuel-air ratio 0.0836 lb ethylene/lb air.)

the same at any given pressure. This effect results from the fact that the flames are enlarged to different degrees to make the flames appear the same size for all four burners.

It would appear, then, comparing the flame photographs of Fig. 3 and Fig. 4, that both variables, pressure and burner size, have the same effect on the shape of the reaction zone, i.e., a reduction in pressure holding the burner diameter constant, and a reduction in burner diameter holding the pressure constant result in progressively flatter flames. With this point in mind the experimental results showing the effect of pressure and burner size on flame speed can be pictured more clearly.

Fig. 5 is a plot of normal flame speed versus the logarithm of the pressure for propane-air flames burning from the four different-size burners. Fig. 6 is a similar plot with ethylene-air flames. For any given burner size the normal flame speed increases with decreasing pressure reaching a maximum value at a pressure below which the flame speed drops off sharply. For larger burners this maximum flame speed occurs at progressively lower pressures.

Furthermore, it appears from the curves that there exists an upper envelope whereby at any given pressure, if the burner size is made large enough, a value of flame speed is approached that is independent of burner size. This envelope is represented by the dashed line in both plots. This envelope indicates then, that the normal flame speed which is independent of burner size, i.e., the "true" normal flame speed, varies inversely with the logarithm of the pressure within the range of pressures studied. This effect must be incorrect in the limits because it predicts an infinite flame speed at zero pressure, and at flame speed equal to zero at some large finite pressure. Further experiments with larger and smaller burners would have to be conducted at lower and higher pressures, respectively, to substantiate this logarithmic variation in flame speed with pressure.

In an attempt to understand the mechanism by which the burner size itself can have a pronounced effect on flame speed let us view the phenomenon of flame propagation solely from the standpoint of thermal conduction.

Consider, as in Fig. 7, a stream tube in a small portion of a large combustible mixture moving with linear velocity u, so that the flame front is stationary with respect to a fixed co-ordinate system. Assume that the gases moving from the left are at some temperature T_u, and are heated by conduction to some temperature T_{ig}. At this point chemical reaction commences and the gases burn to some temperature T_b, at which point the combustion is completed. This infers a finite reaction zone thickness, x_b. Confining our attention to the zone immediately up-

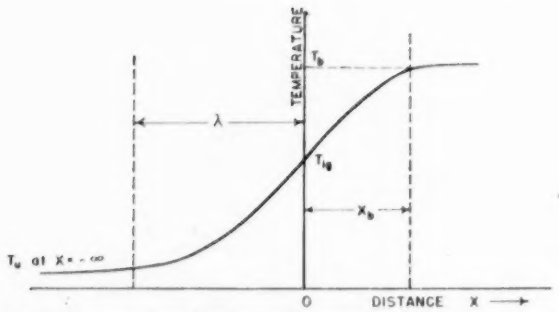

FIG. 7 TEMPERATURE VARIATION THROUGH REACTION ZONE BASED ON HEAT-CONDUCTION THEORY

stream of T_{ig}: if the temperature at any one point is to remain constant with time, then the heat transfer by conduction must be equal to the heat transfer by convection. This can be expressed, assuming T as a function of x only, as a total differential equation

$$\frac{d^2T}{dx^2} - \frac{\rho u C_p}{k}\frac{dT}{dx} = 0 \quad \ldots\ldots\ldots\ldots\ldots [3]$$

where ρ is the density of the gases, corresponding to the temperature T_u of the unburned gases an infinite distance from the reaction zone, C_p is the mean specific heat of the gases at constant pressure, and k is the thermal conductivity.

Equation [3] solves by operators to

$$T = C_1 + C_2 e^{\frac{\rho u C_p x}{k}} \quad \ldots\ldots\ldots\ldots\ldots [4]$$

Putting in the following boundary conditions

$$T = T_u \text{ at } x = -\infty$$

and

$$T = T_{ig} \text{ at } x = 0$$

and solving for the constants C_1 and C_2, Equation [4] reduces to

$$T = T_u + (T_{ig} - T_u)e^{\frac{\rho u C_p x}{k}} \quad \ldots\ldots\ldots\ldots\ldots [5]$$

Since with the case of a stationary flame, $u = V_f$ (the normal flame speed), Equation [5] can be put in the form

$$V_f = \frac{k}{\rho C_p x}\ln\left(\frac{T - T_u}{T_{ig} - T_u}\right) \quad \ldots\ldots\ldots\ldots\ldots [6]$$

Equation [6], however, does not allow for the explicit solution for V_f unless the temperature T is known at some finite distance x, in advance of the flame front. Differentiating Equation [5] with respect to x and putting in the condition that $T = T_{ig}$ at $x = 0$

$$\left(\frac{dT}{dx}\right)_{T=T_{ig}} = \frac{\rho V_f C_p}{k}(T_{ig} - T_u) \quad \ldots\ldots\ldots\ldots [7]$$

Assuming that the temperature is a linear variation with distance through the flame front from Fig. 7

$$\left(\frac{dT}{dx}\right)_{T=T_{ig}} = \frac{T_b - T_{ig}}{x_b} \quad \ldots\ldots\ldots\ldots\ldots [8]$$

Setting Equation [7] equal to Equation [8] and solving for V_f

$$V_f = \frac{k}{\rho C_p x_b}\left(\frac{T_b - T_{ig}}{T_{ig} - T_u}\right) \quad \ldots\ldots\ldots\ldots\ldots [9]$$

Equation [9] is the classical relation of Mallard and LeChatelier treating flame propagation solely from the standpoint of thermal conduction.

Let us now consider how the burner itself in the form of a heat sink can affect the propagation rate of a flame. Assume that some sort of heat sink exists at a distance λ in advance of the reaction zone. Assume further that the heat sink transports away the heat conducted to it from the reaction zone by some means so that the temperature of the unburned gases at a distance λ from the reaction zone is equal to the temperature of the unburned gases at infinity, T_u.

Taking Equation [4] and putting in the new boundary condition that

$$T = T_u \text{ at } x = -\lambda$$

with the previous boundary condition used in the development of the Mallard and LeChatelier relation that

$$T = T_{ig} \text{ at } x = 0$$

Solving for the constants C_1 and C_2, Equation [4] reduces to

$$T = T_{ig} - \frac{T_{ig} - T_u}{1 - e^{-\frac{\rho u C_p \lambda}{k}}} + \frac{T_{ig} - T_u}{1 - e^{-\frac{\rho u C_p \lambda}{k}}}\left(e^{\frac{\rho u C_p x}{k}}\right) \quad [10]$$

Differentiating Equation [10] with respect to x and putting in the conditions that $T = T_{ig}$ at $x = 0$ and $u = V_{fa}$, where V_{fa} is the normal flame speed in the presence of a heat sink at a distance λ in advance of the reaction zone

$$\left(\frac{dT}{dx}\right)_{T=T_{ig}} = \frac{T_{ig} - T_u}{1 - e^{-\frac{\rho V_{fa} C_p \lambda}{k}}}\left(\frac{\rho V_{fa} C_p}{k}\right) \quad \ldots\ldots [11]$$

Equation [11] represents the temperature gradient at $x = 0$ for the case with the heat sink present. Equation [7] represents the temperature gradient at $x = 0$ for the case without the heat sink. Relating Equation [7] and Equation [11] with the assumption that the temperature gradients are the same for the case with the heat sink and without the heat sink

$$(T_{ig} - T_u)\frac{\rho V_f C_p}{k} = \left(\frac{T_{ig} - T_u}{1 - e^{-\frac{\rho V_{fa} C_p \lambda}{k}}}\right)\left(\frac{\rho V_{fa} C_p}{k}\right) \quad [12]$$

which reduces to

$$V_{fa}/V_f = 1 - e^{-\frac{\rho V_{fa} C_p \lambda}{k}} \quad \ldots\ldots\ldots\ldots [13]$$

Equation [13], then, represents the ratio of the normal flame speed V_{fa}, in the presence of a heat sink to the normal flame speed V_f, without a heat sink. It predicts an exponential variation of the ratio of the two flame speeds with the Peclet number $\rho V_{fa} C_p \lambda/k$. It indicates that for small values of this parameter, V_{fa} approaches zero. An examination of the variables that make up the Peclet number shows that it is simply the product of the Reynolds number and the Prandtl number. The Prandtl number $C_p\mu/k$, is practically independent of pressure as is the coefficient of viscosity μ. Therefore, C_p/k is practically independent of pressure. Thus the only pressure-dependent variables appearing in the Peclet number are ρ, V_{fa}, and λ.

In order to correlate the effect of pressure and burner size on flame speed, if, instead of basing the Peclet number on the characteristic distance λ we base it on the burner diameter D_j, then Equation [13] can be rewritten as follows

$$V_{fa}/V_f = 1 - e^{-\frac{\rho V_{fa} C_p (\beta D_j)}{k}} \quad \ldots\ldots\ldots\ldots [14]$$

where $\beta = \text{const with } \lambda = \beta_{D_j}$.

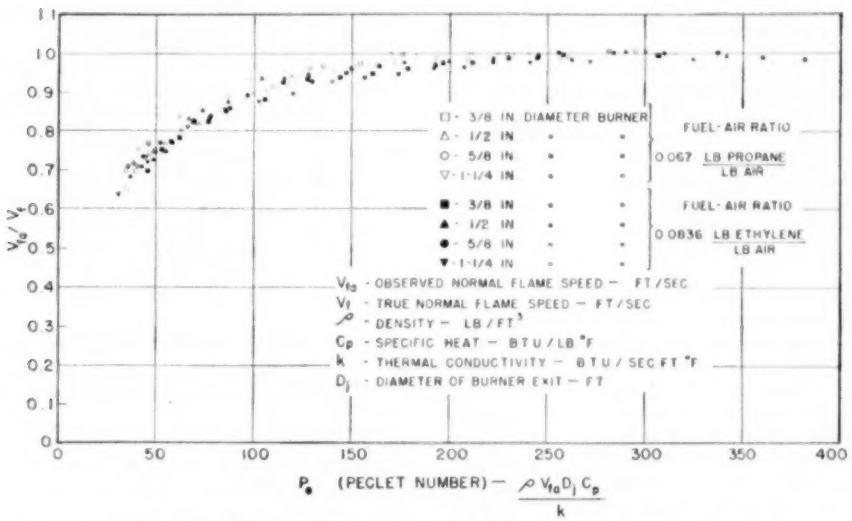
□ - 3/8 IN DIAMETER BURNER
Δ - 1/2 IN " "
○ - 5/8 IN " "
▽ - 1-1/4 IN " "
FUEL-AIR RATIO
0.067 LB PROPANE / LB AIR
■ - 3/8 IN " "
▲ - 1/2 IN " "
● - 5/8 IN " "
▼ - 1-1/4 IN " "
FUEL-AIR RATIO
0.0836 LB ETHYLENE / LB AIR
V_{fo} - OBSERVED NORMAL FLAME SPEED — FT/SEC
V_f - TRUE NORMAL FLAME SPEED — FT/SEC
ρ - DENSITY — LB/FT^3
C_p - SPECIFIC HEAT — BTU/LB °F
k - THERMAL CONDUCTIVITY — BTU/SEC FT °F
D_j - DIAMETER OF BURNER EXIT — FT
V_{fo}/V_f
P_e (PECLET NUMBER) — $\frac{\rho V_{fo} D_j C_p}{k}$

FIG. 8 CORRELATION OF NORMAL FLAME SPEED WITH PECLET NUMBER FOR PROPANE-AIR AND ETHYLENE-AIR BUNSEN FLAMES WITH FOUR DIFFERENT-DIAMETER BURNERS

From Equation [14] we see that there is an exponential relationship between V_{fo}/V_f and the Peclet number whereby V_{fo}/V_f approaches zero as either D_j or ρ approaches zero. Since this is in accordance with the trends of the experimental curves of Figs. 5 and 6, it would seem reasonable that a plot of V_{fo}/V_f versus the Peclet number from the experimental data in Figs. 5 and 6 might correlate all the experimental data.

Fig. 8, then, is a plot of this relationship. The values of V_{fo} used are the actual normal flame speeds as measured while the values of V_f are taken from the envelope of the curves as the "true" flame speed unaffected by the burner size. It appears from the close correlation of all the data that the Peclet number represents a nondimensional parameter that describes the effect of burner size and pressure on flame speed. Large Peclet numbers are desirable if the observed flame speed is to agree with the true flame speed.

CONCLUSION

It is significant that the foregoing correlation by means of the Peclet number could be of considerable importance to the design and operation of jet-combustion chambers at extreme altitude conditions. It would indicate that at high altitudes an increase in the scale of the combustor might tend to eliminate the deleterious effect of heat sink on the processes occurring in the combustion zone.

It is interesting to conjecture that there might be another way of reducing the effect of a heat sink on combustion processes. Present-day combustion-chamber walls are made of metals with structural limits at temperatures well below the temperatures existing in the combustion zone. If a high-temperature ceramic material is used on the inner walls of the combustion chamber, and instead of deliberately cooling the walls by some regenerative process, they are allowed to reach a temperature very close to the temperature of the flame itself, then the walls as a heat sink are virtually eliminated. Preliminary investigations of ceramic-lined ducts without conventional flameholders at the University of Michigan (2) indicate that such a configuration warrants considerable attention.

BIBLIOGRAPHY

1 "The Effect of Pressure on the Propagation Rate of Bunsen Flames in Propane-Air and Ethylene-Air Mixtures," by R. E. Cullen, University of Michigan External Memo, December, 1950.

2 "High Mass Flow, Ceramic Ram-Jet Burner," by H. H. Hicks, Jr., and A. Weir, Jr., University of Michigan External Memo 73, December, 1950.

3[3] "Zur Kenntnis des Innenkegels der Bunsenflamme," by L. Ubbelohde and E. Koelliker, *Journal für Gasbeleuchtung*, vol. 59, 1916, pp. 49–57.

"Zur Kenntnis der Bunsenflamme im Unterdruck," by L. Ubbelohde and L. Andwandter, Ibid., vol. 60, 1917, pp. 225–232.

4 "Die Eigenschaften stationärer Flammen im Unterdruck," by H. G. Wolfhard, *Zeitschrift für technische Physik*, vol. 24, 1943, pp. 206–211.

5 "Experimental Research on the Influence of Pressure on the Speed of Normal Flame Propagation," by L. Khitrin, *Technical Physics of the USSR*, vol. 3, 1936, pp. 926–939 and 1028–1033; vol. 4, 1937, pp. 110–120 and 121–137.

"The Process of the Flame Propagation in 'Constant Pressure Bombs,'" Ibid., vol. 3, 1936, p. 1028.

"Application of the Tube Method for the Measurements of the Normal Speed of Flame Propagation in Gases," Ibid., vol. 4, 1937, p. 110.

"On the Theory of Bunsen Flames," Ibid., vol. 4, 1937, p. 121.

6 "Third Symposium on Combustion and Flame and Explosion Phenomena," by C. Tanford, The Williams and Wilkins Company, Baltimore, Md., 1949, p. 140.

7 "Third Symposium on Combustion and Flame and Explosion Phenomena," by G. W. Culshaw and J. E. Garside, The Williams and Wilkins Company, Baltimore, Md., 1949, p. 204.

8 "Meteor Report UAC-42," by Kurt Wohl, and Numer M. Kapp, U. S. Navy, Bureau of Ordnance, Contract NOrd 9845, 1949.

9 "Flame Propagation Rates at Reduced Pressures," by W. C. Johnston, presented at the SAE summer meeting, French Lick, Ind., June 1–6, 1949, Westinghouse Electric Corporation, Research Laboratories, East Pittsburgh, Pa.

10 "Flame Velocities of Liquid Hydrocarbons," by R. E. Albright, D. P. Heath, and R. H. Thena, as presented before the Joint Symposium on Combustion Chemistry of the Division of Petroleum Chemistry, American Chemical Society, Cleveland Meeting, April 9–12, 1951.

[3] References (3) through (10) include some of the investigations that have been made concerning the effect of pressure on flame-propagation rates.

Discussion

W. T. Olson[4] and Melvin Gerstein.[4] Research on flame-propagation rates at reduced pressures in which particular care and attention has been paid to experimental conditions, as the author has done, is quite pertinent in view of the differences in the pressure effects reported in the literature. In some of the reported studies, burner diameter has not been varied as the author and others have shown to be necessary. Culshaw and Garside[5] find burning velocity to be independent of mixture flow, while Albright, Heath, and Thena[6] do not; the author has held flow rate fairly constant.

A relation for the effect of pressure and burner size on flame speed such as that presented in the paper has obvious engineering usefulness. In reviewing the literature, Dr. D. M. Simon of our laboratory has noted that, although flame velocities for hot flames like acetylene, or ethylene-oxygen are nearly independent of pressure, the pressure dependence of flame velocity for paraffin hydrocarbons in general follows the form $U_f a p^{-n}$, where n is between 0.2 and 0.4 for the various reported data. Such a relation agrees with the small effect of pressure reported by the author.

With regard to the mechanism of flame propagation, the exact mechanism depends on the conduction of heat, the diffusion of molecular and atomic species, and a set of particular chemical reactions. The author has successfully treated his data with an approximate mechanism based on thermal conduction. It would be interesting to see to what extent a mechanism based on the diffusion of molecular and atomic species accounts for the observations.

With regard to the flame shapes of Figs. 3 and 4 of the paper, the effects shown are probably influenced by the velocity profile at the burner outlet as well as by the quenching action of the burner, because the contraction ratios used were too small to assure flat velocity profiles, except for the case of the smallest burner. The flatter flames on the smaller burners also have flatter velocity profiles. Because flame speed was measured by determining total flame area, these data should be independent of the velocity profile.

A. A. Putnam.[7] This paper is of interest both to those who must design and develop combustion chambers operating under varying pressures, and those who are interested in fundamental combustion problems. However, it is believed that the presentation has been oversimplified by neglect of a third dimensionless group, the ratio of jet velocity to flame speed.

Fig. 9, herewith, shows some data on the stability limits of a stoichiometric mixture of propane and air for two different Bunsen-tube diameters. The data are correlated by the dimensionless parameters used, that is, the ratio of jet velocity to flame speed, and the Peclet number based on flame speed. That data for other fuels also will agree with these data is indicated by a comparison in the literature.[8] It should be mentioned that the blowoff section of the data moves to the left as the mixture becomes richer. However, for one mixture ratio, we may conclude that the data can be correlated on one plot. Such a conclusion is also valid for the case of tests on accelerating nozzles.

It appears that the data presented on the change in flame speed were all taken with essentially a constant jet velocity. If the

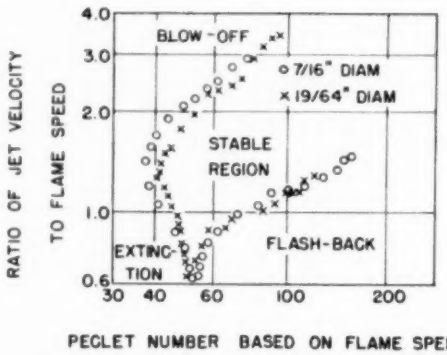

Fig. 9 Stability Data for Two Diameters of Bunsen Tube, Using Stoichiometric Mixture of Propane and Air

true flame speed does not vary too much with pressure, then all the tests results fall on a horizontal line across Fig. 9 of this discussion, and any property of the flame that is measured will be only a function of the one dimensionless parameter, the Peclet number based on flame speed.

This is essentially what has been found in the paper under discussion; that is, that the ratio of observed to true flame speed is a function only of the Peclet number, whether based on observed flame speed or on true flame speed.

It may be further noted in Figs. 3 and 4 of the paper that the flames are held in the region of the edge of the jet, where there is a diffusion mixing of the jet with the ambient atmosphere of the combustion chamber. This tends to lower the flame speed in this region. As the pressure decreases, the diffusion region becomes larger, a greater portion of the flame front is subjected to diffusion effects, amd the average flame speed decreases. Thus the flame speed may be decreased not only by heat loss but by diffusion. Since the Peclet number is related by an essentially constant ratio to the dimensionless groups which control the amount of diffusion, that is, the Reynolds number and a group like the Reynolds number, but with the diffusion coefficient replacing the kinematic viscosity, it is difficult to evaluate the relative influences of the two effects. However, a comparison of curves similar to those of Fig. 8 of the paper, but for different velocities, might lead to a further insight into this problem.

Kurt Wohl.[9] The simple correlation between burning velocity and tube diameter at various pressures expressed in Equation [14] of the paper seems to be new and interesting. The situation is too complicated for an exact treatment; thus short cuts like the one proposed by the author appear welcome.

The author considers the temperature curve upstream of a flame front, Fig. 7 of the paper, and chooses the point at which the temperature equals "the ignition temperature" T_i as zero point for distances perpendicular to the flame front. A laminar stream of combustible gas is assumed to pass perpendicularly through a plane heat sink and to create a plane parallel flame front. An equation is developed, Equation [13], which gives the distance of the ignition point (i.e., the point where $T = T_i$) from the heat sink as a function of the velocity of the stream. The normal burning velocity V_f equals this velocity for the limiting case of an infinite distance. For smaller velocities V_a, the distance acquires the finite value λ.

In deriving this equation the author assumes that the slope of the curve of Fig. 7 at T_i is independent of the distance of the

[4] Lewis Flight Propulsion Laboratory, NACA, Cleveland, Ohio.
[5] Author's bibliography, reference (7).
[6] Author's bibliography, reference (10).
[7] Battelle Memorial Institute, Columbus, Ohio. Jun. ASME.
[8] "Application of Dimensionless Numbers to Flash-Back and Other Combustion Phenomena," Third Symposium on Combustion, Flames and Explosion Phenomena, The Williams and Wilkins Company, Baltimore, Md., 1949, p. 89.
[9] Professor of Chemical Engineering, University of Delaware, Newark, Del.

ignition point from the plane of the heat sink, and that the burning velocity remains finite until the ignition point touches this plane. Both assumptions are true if the effect of the heat sink on the flame front would be restricted to the part of the curve with $T < T_i$ and would vanish at this point. One might ask how far this simplifying assumption is permissible. It would be presumed that the slope at $T = T_i$ is inversely proportional to V_a as long as ignition temperature and maximum flame temperature remain unchanged, as follows from the equation $X_b = V_a t$ (flame-front thickness equals burning velocity times mean chemical reaction period). Equation [13] would then read

$$V_a/V_f = \sqrt{1 - e^{-\rho V_a C p \lambda / K}}$$

It would further be assumed that the equation is restricted to not-too-small values of V_a.

The basic equation developed by the author is applied to Bunsen flames burning above tubes. For this case, V_a means the average burning velocity determined from the total area of the upstream boundary of the burning zone, and λ is replaced by βD (β = const, D = tube diameter). It is interesting that the resulting Equation [14] can be verified within the range of variables studied, Fig. 8 of the paper. However, it would be desirable to extend the range of variables to larger tube diameters at low pressure.

It is difficult to judge the application of the theory of the author to Bunsen flames burning above tubes from the theoretical point of view since the physical situation in this case is so very different from the one underlying his Equation [13]. It may well be that the averaging procedure as such is taken care of by the constant coefficient β in Equation [14]. But quite apart from this point, the relationship between burning velocity and location of the heat sink is as simple as is claimed only if the gas passes perpendicularly through the sink and if the flame front is parallel to it, as was mentioned. In reality, however, the gas flow is about parallel to the surface of the heat sink (i.e., the tube wall) and the flame front forms various angles with this surface which go from very small to 90 deg.[10]

Moreover, the flame actually burns above the tube, and the dead space between the tube port and the flame base is rather large at low pressure. Thus the unbounded atmosphere affects the outer parts of the flame too. The inner parts of the flame usually experience very little quenching since their position is considerably above the tube, and since they are protected against direct influence by the atmosphere through the outer parts of the flame front, Figs. 3 and 4 of the paper. Only with flat flames, the quenching effect may extend to the tube axis.

[10] For part of the arising problems, refer to G. von Elbe and B. Lewis in "Third Symposium on Combustion and Flame and Explosion Phenomena," The Williams and Wilkins Co., Baltimore, Md., 1949, p. 68.

In case of flames, the shape of which is between hemispherical and flat, another difficulty arises. With these flames, which are observed at low pressures and small tube diameters, the velocity profile of the approach stream is flattened and the dead space is relatively large so that a substantial part of the combustible gas does not pass through the primary flame front. The true average burning velocity is thus lower than calculated.

In view of these uncertainties, the following empirical approach may be worth testing: Assume the differential equation

$$\frac{dV_a}{V_f - V_a} = \frac{d\lambda}{x_b}$$

where x_b is the thickness of the flame front according to Equation [8]. Assume that V_a becomes zero when $\lambda = \alpha x_b$, α being a constant which is smaller than 1. There follows by integration

$$V_a/V_f = 1 - e^{-\frac{\lambda}{x_b} + \alpha}$$

If instead of Equation [9] of the paper the approximation is used

$$x_b = \frac{K}{\rho C p V_f}$$

one obtains instead of equation [13]

$$V_a/V_f = 1 - e^{-\frac{\rho V_f C p \lambda}{K} + \alpha}$$

If α is made equal to zero the equation still differs from Equation [13] by containing V_f on the right side instead of V_a.

Author's Closure

The author is in essential agreement with the comments of the discussers. However, one point that was mentioned by Kurt Wohl merits further discussion.

His statement that the gas flow is about parallel to the heat sink and that the flame front forms various angles with the surface is true indeed. It is felt that a more profitable approach than an empirical one can be made experimentally using a porous plug through which the combustible mixture is allowed to flow with a flat flame stabilized above the surface of the plug. Thus the distance λ of the flame front from the heat sink, the temperature of the heat sink, and the flow velocity can be varied at different ambient pressures. Then the effect of a heat sink which affects the flame front equally at every point can be investigated. With this information, coupled with additional information of the temperature gradient in the "dead space" between the flame and the heat sink, it is felt that the relative importance of thermal conduction and active species diffusion can be determined. Interferometric and spectroscopic techniques would undoubtedly be powerful tools in an investigation of this kind.

NACA Sonic-Flow-Orifice Temperature Probe in High-Gas-Temperature Measurement

By P. L. BLACKSHEAR, JR.,[1] CLEVELAND, OHIO

A brief discussion of the problem of measuring temperatures in jet engines is given. A method of measuring these temperatures by pneumatic means is described. This method involves the use of two sonic-flow orifices in series to give, through thermodynamic calculations, the total temperature of the gas entering the first orifice. An evaluation of this method is given including a discussion of the sampling error in nonhomogeneous gases, and an experimental comparison against a thermocouple and the sodium D-line reversal method is made showing favorable agreement. Results of applying this method of measuring temperature in full-scale engines are discussed.

Introduction

In the field of jet-engine research and development there is an ever-present desire to know the temperature of a flowing stream of gas. This temperature generally is loosely and apologetically defined as the temperature the gas would have if its molecules possessed the same average random translation energy at equilibrium. This is referred to frequently as the static temperature of the gas. A term, total temperature, is often used, meaning the temperature a parcel of perfect gas in motion would possess if it were brought to rest adiabatically.

In the hot portion of the jet engine, that is, from the combustion chamber rearward, there are a variety of measurable average temperatures that are of interest. Two examples are: the space and time average of temperature over an entire cross section of the flowing stream, or any portion thereof, and the space average over an entire cross section, or a portion thereof, as a function of time. In the combustion chambers, temperatures can range from 0 to 4000 F. Since the flames are almost always turbulent, there are regions where the gas flows past a reference point in a succession of hot and cold pockets within this range of temperature. To complicate things further, in some of the flow processes the temperature of the gas changes so abruptly that the internal degrees of freedom of the gas molecules lag behind the translational.

Into this thermal chaos we must place our instruments and record a temperature. To measure a static temperature, our instrument should follow the moving parcels, and to measure the total temperatures, our instrument should capture the moving parcel and measure what its temperature would be when brought adiabatically to rest.

The most widely used device to accomplish the latter has been the thermocouple. Great strides have been made in evaluating and improving the performance of the thermocouple at high velocities and moderately high temperatures. Use of noble metals extends the upper limit of utility of the thermocouple to cover an extremely wide range of the temperatures encountered. At its present state of development, however, the thermocouple loses much of its attractiveness as the temperature exceeds 2000 F.

Measurement of static temperature has been accomplished in the upper temperature range by a variety of radiation methods, such as the sodium D-line reversal method, with varying degrees of success. For a number of practical reasons these techniques have not found widespread use in jet-engine research.

In recent years a great deal of interest has been expressed in the use of pneumatic methods of measuring temperature. These methods rely primarily on the obedience of hot gases for certain perfect-gas laws when flowing through a series of water-cooled orifices. A bibliography of these methods may be found in a paper by R. D. Freeze.[2]

Theory of the Sonic Orifice Probe

One method of measuring temperature by pneumatic means is to draw a sample of gas through two sonic-flow orifices in series. We may show that the rate of flow through a sonic orifice can be expressed as

$$W = \frac{PA}{f(\gamma)\sqrt{gRT}}$$

where

P = total pressure
T = total temperature

$$\gamma = \frac{c_p}{c_v}$$

$$f(\gamma) = \frac{\left(\frac{\gamma+1}{2}\right)^{\frac{\gamma+1}{2(\gamma-1)}}}{\sqrt{\gamma}}$$

A = effective area
R = gas constant

Placing two sonic orifices in series we require that the rates of flow through the two be identical, or

$$\frac{P_1 A_1}{f(\gamma_1)\sqrt{gRT_1}} = \frac{P_2 A_2}{f(\gamma_2)\sqrt{gRT_2}}$$

or solving for T_1

$$T_1 = \left[\frac{P_1 A_1 f(\gamma_2)}{P_2 A_2 f(\gamma_1)}\right]^2 T_2$$

(assuming change in R to be negligible).

If the tube connecting the orifices is cool, we may easily measure T_2 with a thermocouple. Then if we know the ratio A_1/A_2 by some calibration procedure and measure P_1 and P_2, we have only to know the value of the ratio of $f(\gamma)$ to solve for T_1. To evaluate this ratio consider the following:

[1] National Advisory Committee for Aeronautics, Lewis Flight Propulsion Laboratory.

Contributed by the Gas Turbine Power Division and presented at the Semi-Annual Meeting, Cincinnati, Ohio, June 15-19, 1952, of The American Society of Mechanical Engineers.

Note: Statements and opinions advanced in papers are to be understood as individual expressions of their authors and not those of the Society. Manuscript received at ASME Headquarters, April 14, 1952. Paper No. 52—SA-38.

[2] "Bibliography on the Measurement of Gas Temperatures," by R. D. Freeze, Circular 513, National Bureau of Standards, August 20, 1951.

If we use a reasonable theoretical model for the acceleration of a particle of gas on entering the nozzle, we see that the static temperature of the particle drops as much as 17 per cent in a very short time. Kantrowitz and Huber[3] and others, have shown, that in general, the rotational degrees of freedom of most molecules, will adjust almost instantaneously to the new temperature. The vibrational degrees of freedom, however, require many more molecular collisions and hence a longer time to adjust to equilibrium. This time to adjust is referred to as the relaxation time of the gas τ. For air-breathing engines we may approximate the relaxation time as the magnitude of the relaxation time for a nitrogen-water vapor mixture, or $\tau \cong 10^{-4}$ sec.

The relationship between the vibrational and translational temperature is then formally written

$$\frac{dT_{vib}}{dt} = -\frac{1}{\tau}(T_{vib} - T_{trans})$$

Employing this relationship we find that while the translational temperature decreases 17 per cent in the orifice, the vibrational temperature decreases less than 1 per cent; in other words, the gas acts, during the acceleration, essentially as though no vibrational degrees of freedom exist. Thus γ is no longer a temperature-dependent term and ratio of the $f(\gamma)$ becomes 1 or

$$T_1 = \left(\frac{P_1 A_1}{P_2 A_2}\right)^2 T_2$$

This T_1 is the average total temperature of the gas contained in the stream tube which enters the instrument. The cross-sectional area of this stream tube A_0, is related to the orifice effective area A_1 by the relationship

$$A_0 = A_1 \frac{\left(1 + \dfrac{\gamma - 1}{2} \mathbf{M}_0^2\right)^{\frac{\gamma+1}{2(\gamma-1)}}}{f(\gamma)\sqrt{\gamma}\,\mathbf{M}_0}$$

where $\mathbf{M}_0$ is free-stream Mach number. A plot of A_0/A_1 against $\mathbf{M}_0$ for $\gamma = 1.4$ is shown in Fig. 1.

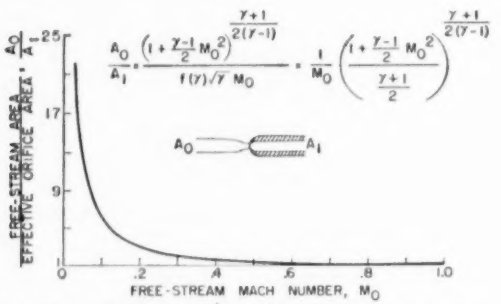

Fig. 1 Ratio of Area of Free Stream Sampled to Area of First Orifice as Function of Free-Stream Mach Number

If the gas were homogeneous, this average would be a representative temperature. From the little that is known of sampling techniques, we learn that in order to get a representative sample of a flowing gas, we must sample at stream velocity. Sampling at stream velocity is in most cases extremely difficult. If we sample at a velocity greater than this, we must expect our sample to contain more of the less dense components of the gas. Since sampling at sonic velocity greatly simplifies the thermodynamics and the calibration of our system, we wish to learn if the sampling error is prohibitive.

To get an idea of this effect, we take the following model:

Suppose the gas passes by the first orifice in pockets at different temperatures, as shown in Fig. 2. Then the ratio of

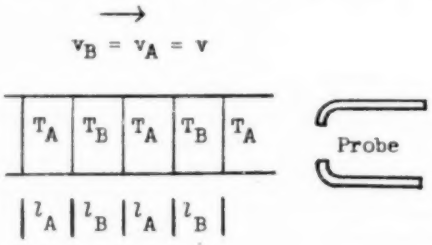

Fig. 2

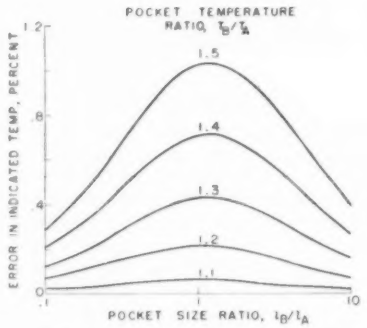

Fig. 3 Error in Temperature Indicated by Probe as Function of Pocket-Size Ratio for Different Values of Pocket-Temperature Ratio

the average temperature, indicated by the probe, to the by-weight average temperature of the successive pockets is found to be

$$\frac{T_{ind}}{T_{act}} = \frac{\left(1 + \dfrac{l_B}{l_A}\right)\left(\dfrac{l_B}{l_A} + \dfrac{T_B}{T_A}\right)}{\left(\sqrt{\dfrac{T_B}{T_A}} + \dfrac{l_B}{l_A}\right)}$$

A plot of the error obtained from this equation is given in Fig. 3.

For an $l_B/l_A = 1$, we get the curve shown in Fig. 4, in which is plotted the approximate maximum error as a function of the temperature ratio of the successive pockets.

The pocket-length ratio for maximum error is

$$\frac{l_B}{l_A} = \frac{2\dfrac{T_B}{T_A} - \dfrac{T_B}{T_A}\sqrt{\dfrac{T_B}{T_A}} - \sqrt{\dfrac{T_B}{T_A}}}{2\sqrt{\dfrac{T_B}{T_A}} - \dfrac{T_B}{T_A} - 1} = \sqrt{\frac{T_B}{T_A}}$$

For an extreme case $T_B/T_A = 4$, the maximum error occurs at $l_B/l_A = 2$, where the indicated temperature is 12.5 per cent high. Thus we see that moderate departure from homogeneity can be tolerated, whereas extreme variations can lead to rather large sampling errors when successive pockets are approximately the same size.

Experimental Evaluation

The probes examined evolved into the sort shown in Fig. 5

[3] "Heat-Capacity Lag in Turbine-Working Fluids," by Arthur Kantrowitz and P. W. Huber, NACA Wartime Report RB 14E29, May, 1944.

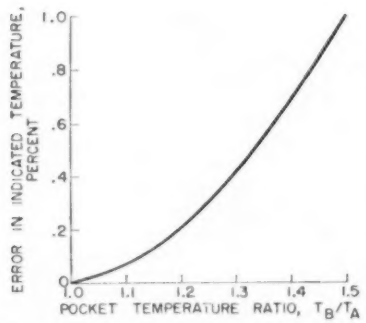

FIG. 4 APPROXIMATE MAXIMUM ERROR IN TEMPERATURE INDICATED BY PROBE FOR $l_B/l_A = 1$ AS FUNCTION OF POCKET-TEMPERATURE RATIO

(see also author's report on probes[4]). A sharp-edged orifice drilled into a thin-walled beryllium copper plug was sweated into the inlet of a water-jacketed probe of 3/8 in. OD. Gas drawn through this orifice at sonic velocity passed through the inner tube of the probe into a 3/8-in. heated copper tube leading to the second orifice. Temperature of the gas at the second orifice was maintained at the wall temperature of this copper tube and the pressure upstream of the second orifice was read on a precision barometer. The gas passed through the second orifice at sonic velocity to a vacuum pump. Actual ratio of orifice sizes was chosen as 1/3, and effective area ratios of the two orifices were found by setting $T_1 = T_2$, from which one obtains $A_1/A_2 = P_2/P_1$.

The selection of an area ratio of 1/3 was made after an exhaustive examination of a variety of orifices all having characteristics as shown in Fig. 6. These tests were exhaustive because the results disagree with those of Perry.[5] In that paper flow coefficients were shown to increase at pressure ratios in excess of 3. Although a number of variations of the curve shape were encountered in the calibration of the orifices used by the author at pressure ratios less than 3, in no case were there any recordable deviations in flow coefficients as pressure ratios exceeded 3.2. The orifices were used, then, such that they were within the constant coefficient range.

The temperature indicated by the probe was compared to that read by a thermocouple in a hot-air stream at temperatures ranging from room temperature to 1100 R and agreed well as shown in Fig. 7. These runs were made at approximately 60 fps stream velocity. This velocity was reduced in search of a minimum allowable value yielding the curve shown in Fig. 8. The value of velocity where error began agrees well with that velocity where the diameter of the stream-tube sample became equal to the outside diameter of the probe. Further reduction in velocity caused this stream tube to become larger than the outside diameter of the probe. It is felt that the prime source of error when this enlargement occurs is heat transfer from the gas to the outside of the tube prior to entering the orifice.

At the time these tests were made there was no intermediate temperature test section available. However, there were facilities for comparing the probe temperature with that measured by sodium D-line reversal techniques. The apparatus used for this method is shown in Fig. 9. Sodium was introduced so that the center portion of the propane-air flame, having an essentially flat temperature profile, was colored. By taking the plane of

[4] "Sonic-Flow-Orifice Temperature Probe for High Gas Temperature Measurements," by P. L. Blackshear, Jr., NACA TN 2167, September, 1950.

[5] "Critical Flow Through Sharp-Edged Orifices," by J. A. Perry, Jr., Trans. ASME, vol. 71, 1949, pp. 757–764.

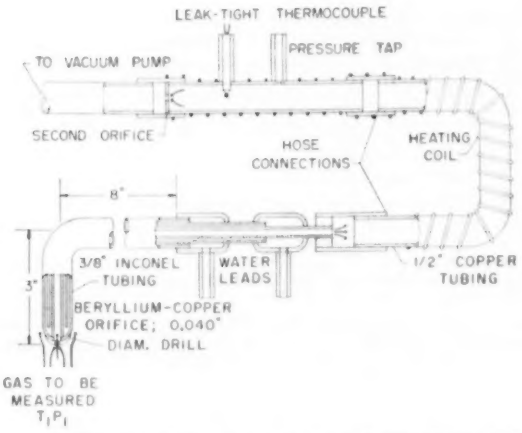

FIG. 5 SCHEMATIC DIAGRAM OF SONIC-FLOW TEMPERATURE PROBE

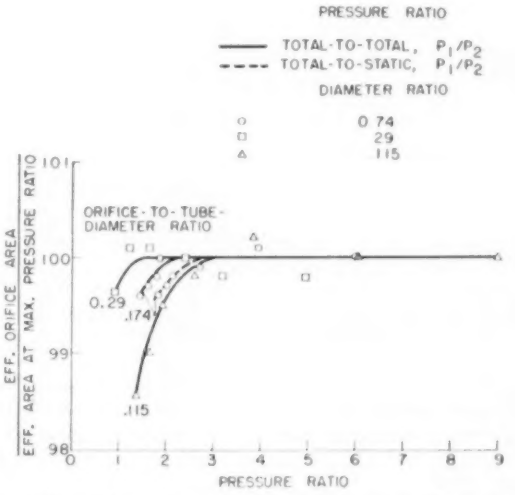

FIG. 6 FLOW COEFFICIENTS OF THIN ORIFICES AS FUNCTION OF PRESSURE RATIO ACROSS ORIFICE

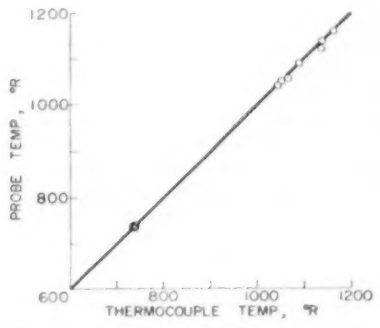

FIG. 7 COMPARISON OF TEMPERATURES OBTAINED BY HIGH-TEMPERATURE PROBE WITH READINGS OF ASPIRATING SHIELDED THERMOCOUPLE IN HOT-AIR STREAM

(Stream velocity, 60 fps; flat temperature profile; parabolic velocity profile.)

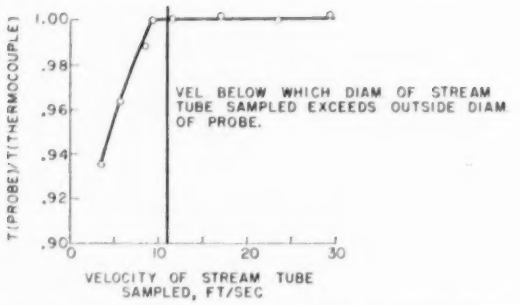

FIG. 8 RATIO OF TEMPERATURE MEASURED BY PROBE TO THAT INDICATED BY THERMOCOUPLE AS FUNCTION OF FREE-STREAM VELOCITY AT STREAM TEMPERATURE, 1090 R

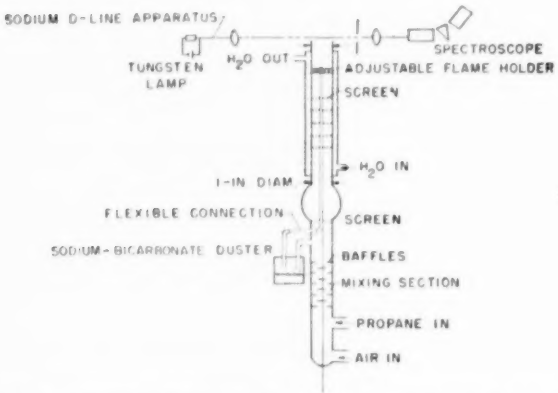

FIG. 9 APPARATUS FOR CALIBRATION OF HIGH-TEMPERATURE PROBE IN PROPANE-AIR COMBUSTION PRODUCTS

measurement at varying distances from the flame holder we were able to compare the two temperature-measuring devices at varying stages of the combustion process. The results are shown in Fig. 10. We see that better agreement is achieved as equilibrium is approached.

USE IN JET ENGINES

In clean burners this probe seems to perform satisfactorily. For example, Richard Koch of the Lewis laboratory, has used a probe of this type successfully over a period of some 70 hr of running time in a propane flame tube. He used the probe alternately as a total-head tube and a temperature probe, obtaining profiles of velocity and temperature downstream of a flame holder of which Fig. 11 is a sample.

Since this is the sort of information designers would like to have concerning the full-scale combustion chamber, this method of temperature measurement seems attractive. There is still much to be desired in the design of an instrument that can be used conveniently in combustion chambers where carbon deposits are likely. For example, William Koffel of Lewis laboratory, recently incorporated probes of this type into rakes for measuring a temperature profile in an afterburner, using 80-octane gasoline as fuel. The precision of the instrument under these conditions was evaluated as 4.4 per cent. This precision was obtained at the price of recalibrating and removing carbon and tar deposits between runs. In addition to this dirty combustion

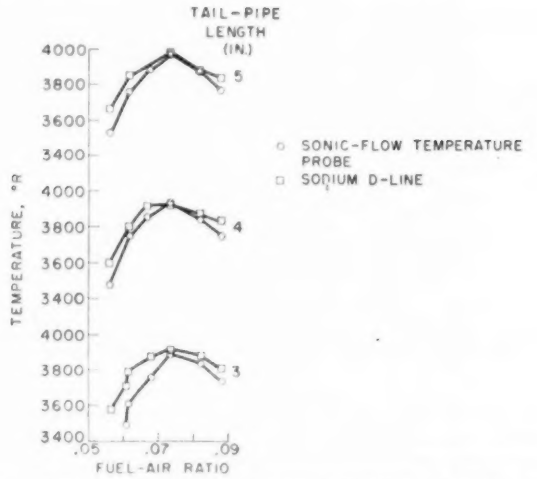

FIG. 10 COMPARISON OF TEMPERATURES OBTAINED WITH SONIC-FLOW TEMPERATURE PROBE AND READINGS OBTAINED WITH SODIUM D-LINE REVERSAL METHOD IN APPARATUS SHOWN IN FIG. 4, WITH VARIOUS FUEL-AIR RATIOS

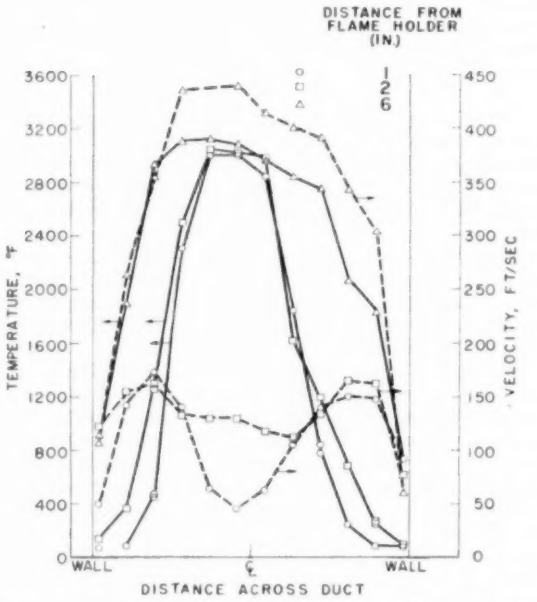

FIG. 11 SAMPLE DATA PLOT OF TEMPERATURE AND VELOCITY MEASURED BY PROBE IN SMALL-SCALE RAMJET WITH INLET VELOCITY OF 88 FPS, FUEL-AIR RATIO OF 0.065, AND PROPANE FUEL

problem, the nature of all the factors affecting the flow coefficient of sonic orifices over the wide ranges of temperature, pressure, composition, and stream velocity encountered in jet engines is still not clearly understood.

The instrument is inexpensive, easily calibrated, and has been found reliable in clean gases. It is hoped that a better understanding of sonic flow through orifices will lead to a design that will extend its utility to the dirtier combustion chambers we would like to investigate.

Discussion

W. K. KOFFEL.[6] The author has done an excellent job of presenting the principle of the sonic-flow-orifice probe and some of its theoretical characteristics and design requirements. It is hoped that others will be encouraged from the results presented in this paper to continue the development of this type probe for measurement of combustion-gas temperatures.

The attractiveness of the sonic-flow-orifice probe lies in its ruggedness and durability at temperatures above those which thermocouples can sustain. In addition, this probe samples the temperature at a point in contrast to some mean temperature along the path of sight as for the sodium D-line method, and the temperature calculated from the thermodynamic equation is independent of radiant heat transfer to or from the probe.

On the other hand, the sonic-flow-orifice temperature probe has some special problems of its own. The effective area of the first orifice can change due to erosion of the sharp edge or to the deposition of carbon or other residues from some liquid hydrocarbon fuels. The deposits on the first orifice vary greatly with different fuels. The unleaded gasoline has been observed to produce a thin, smoke-colored film, and JP-3 fuel sometimes produces sticky, varnishlike coatings. Erosion can be reduced by proper selection of the orifice material, but it may be necessary to restore the sharp edge by periodical polishing of the tip.

The writer has had Inconel and Nichrome first orifices check their initial effective flow areas within 0.1 to 0.2 per cent without repolishing after about 13 hr at gas temperatures from 1800 to 3500 R in a combustion chamber burning clear gasoline.

In the writer's opinion, the sonic-flow-orifice temperature probe is still in the laboratory stage. Quantitative results can be obtained, however, with a probe designed for a specific application and when a high precision is used in measuring the quantities entering the thermodynamic equation for calculating the temperature of the sampled gas.

Special care should be exercised in measuring the gas temperature at the second orifice when heat is applied to prevent condensation of water vapor from the combustion products. The radiation error in this temperature measurement can be appreciable because the thermocouple is in a black-body enclosure and the velocity ahead of the second orifice is usually quite low. The ratio of the effective areas of the two orifices should be checked frequently and this is facilitated if the probe is designed so that the three-orifice method of calibration described by the author[4] can be applied while maintaining the same flow and geometrical conditions that exist in the probe during actual use.

K. L. RIEKE.[7] The author is to be commended for his detailed discussion of the design and performance of a practical and useful tool for investigating combustion under extreme conditions of flow and energy transformation. Anyone studying combustion as it occurs in a jet engine or a gas turbine will be in complete agreement with his statement . . . "there is an ever-present desire to know the temperature of a flowing stream of gas." This knowledge must be obtained under conditions and with a precision which were unthought of 10 years ago.

During the past year experience gained with a sonic temperature probe constructed according to the principles outlined in the author's previous publication[4] has demonstrated that this is one of the most convenient and accurate instruments for the determination of temperature in the highly turbulent reaction zone of a gas-fired combustor for a gas turbine.

Fig. 12, herewith, shows the results of a temperature exploration made with this probe across a combustor tube at a section $3^3/_8$ in. from the point of fuel admission. At this section the tube diameter is $4^1/_4$ in. The indicated temperature at any given position fluctuated within the limits represented by the shaded area, the period of these fluctuations varying from 15 to 30 sec. However, these data are sufficiently reproducible over a range of test conditions so that they may be considered as characteristic of the combustion processes occurring in the actual gas-turbine combustor. With results such as these it is possible to evaluate the utilization of the combustion space and the effect of modifications in combustor design.

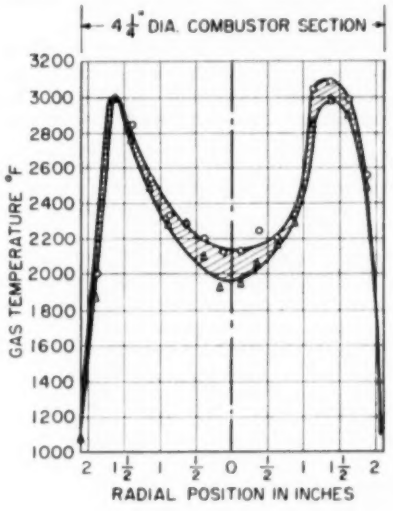

FIG. 12

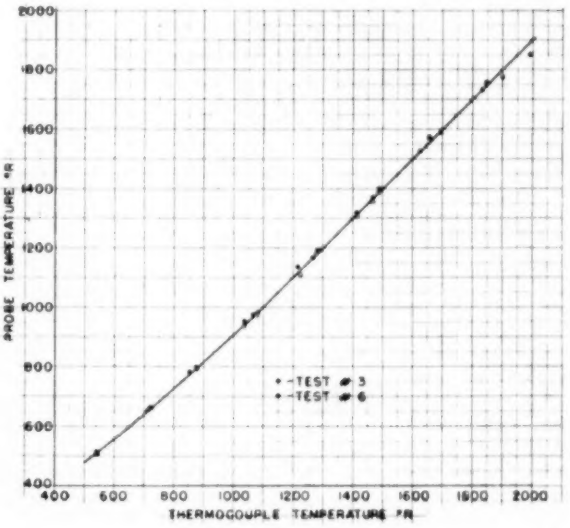

FIG. 13

Fig. 13 shows the calibration curve of the sonic-flow-orifice tem-

[6] Aeronautical Research Scientist, National Advisory Committee for Aeronautics, Lewis Flight Propulsion Laboratory, Cleveland, Ohio.

[7] Westinghouse Research Laboratories, East Pittsburgh, Pa.

perature probe used in the combustion chamber. The probe temperature measurements are compared with those obtained by means of an aspirating thermocouple having a single radiation shield over a temperature range from 500 to 2000 R in a gas stream having a velocity greater than 160 fps. This curve indicates that the probe temperature was approximately 100 F lower than that of the thermocouple at temperatures above 500 F. This does not agree with the author's calibration curve, Fig. 6, in which he shows exceptionally good agreement between the sonic-flow-orifice temperature probe and an aspirating thermocouple. Can the author offer an explanation which would account for this discrepancy? This deviation is not objectionable since the calibration was found to be consistent and reproducible. Calibration at higher temperatures using the line-reversal method for comparison is planned at the first opportunity.

M. D. Scadron.[8] The need of a means to measure high gas temperatures accurately in modern aircraft engines cannot be emphasized too greatly. The pneumatic-probe method does alleviate most of the specific difficulties encountered by the "simple to use" thermocouple, but it is by no means a panacea to the problem of high-gas-temperature measurement. The sonic pneumatic probe described, which is another variation of the basic pneumatic probe, does seem to offer a remedy to some of the difficulties that plague the pneumatic-probe design.

The section where the effect of the speed of the process through the nozzle is discussed, can be better illuminated by referring to a paper by R. B. Spooner.[9] Mr. Spooner shows that for Mach numbers of 0.9 and less and for nozzle-inlet temperatures of 3500 R and less, the ratio of outlet to inlet pressure across the nozzle necessary to obtain a specific outlet velocity was less than 1 per cent smaller than that computed on the basis of the usual assumption that the gas is in temperature equilibrium at all times. The process for a diatomic gas, however, corresponded even more closely to one in which the vibrational energy of the gas was considered entirely unavailable or frozen. A value for the ratio of specific heats of 1.4 can thus be used to yield a closer approximation to the actual case than does the equilibrium value, which includes the effect of the varying heat capacity of the gas. Increases in nozzle-outlet Mach number led to correspondingly greater deviations in pressure ratio from the actual case if the calculations were based on an equilibrium expansion. However, as the outlet Mach number increased toward 1 and the inlet temperature exceeded 3500 R, the value of ratio of specific heats of 1.4 also did not yield a pressure ratio corresponding to that computed on the basis of an equilibrium expansion. Therefore the relation that $[f(\gamma_2)/f(\gamma_1)]^2$ is equal to unity is not a necessary one. The "best" value of γ_1 may lie between 1.40 and the equilibrium value. If this value of γ_1 is about 1.35 instead of 1.40 and the value of γ_2 is 1.40, an error of 3 per cent in the measurement of T_1 is possible.

The author apparently realizes that the pneumatic probe will be used in situations where the flow is not of steady-state nature and he proceeds with an analysis of the effect of pulsating gas temperature upon the temperature indication of the sonic pneumatic probe. In actual use, it is difficult to visualize an application where the pressure and velocity will not pulsate simultaneously with the temperature. The inability to interpret correctly the resulting indication of a sonic pneumatic probe under such conditions is an ailment common to all types of pneumatic probes.

The discrepancy between the author's data regarding discharge coefficients and that of reference 4 should not be of too much concern. The orifices used in the probe were essentially thick-plate orifices (the ratio of hole diameter to plate thickness d/t, was in the order of 4) while those examined in reference 4 were truly sharp-edged orifices (the ratio of hole diameter to plate thickness d/t was between approximately 10 and 20). In addition, the inlet pressure in all of the author's tests was 1 atm, while the inlet pressure in the case of reference 4 was varied with pressure ratio. This essentially means that the author's data were taken at almost a constant value of Reynolds number. However, results obtained by Grace and Lapple[10] on thick-plate orifices ($d/t \approx 1$) agree fairly well with the author's.

A final caution to be observed, in addition to those already mentioned by the author in the use of the pneumatic probe, is the measurement of the gas temperature at the second orifice. If the gas is cooled below the dew point between the orifices, water will condense and drop out, so that the relation $W_1 = W_2$ will not apply. If there is a 1 per cent difference between W_1 and W_2 there will be a 2 per cent error in the measurement of T_1. Also, the ability to measure the temperature at the second orifice with a thermocouple will result in error, unless the thermocouple has a minimum of radiation, conduction, and recovery errors. It also must be able to measure an integrated temperature, i.e., it must measure a mass-flow weighted temperature, since the gas approaching the second orifice will have a radial temperature and mass-flow gradient. It can be seen that a 1 per cent error in the measurement of T_2 will result in a 1 per cent error in the measurement of T_1.

When it becomes difficult to use a thermocouple to measure temperature in a moving gas stream, the pneumatic-probe method becomes a valuable instrument provided it is in the hands of a competent observer.

Author's Closure

The author is indebted to Messrs. Koffel, Ricke, and Scadron for their kind yet penetrating discussions.

The author had the privilege of working rather closely with Mr. Koffel during the time when he was converting a "laboratory-stage" probe into a bank of instruments for installation into a full-scale burner and can fully appreciate the excellent pioneering job Mr. Koffel performed. The problem of carbon and tar deposition is still far from being resolved successfully.

One possible solution, at least over part of the troublesome range, would be to allow the orifice to run hot and correct for thermal expansion of the orifice material. A preliminary investigation of this technique has been made using synthetic-jewel bearings for the first orifice. The results to date are that the jewel (a synthetic ruby of 0.026 in. ID) did not break when exposed to a 3800 R propane-oxygen flame. Carbon formed on the jewel for cool sooty flames but burned off leaving a clean hot jewel when the sooty flame temperature was raised above about 2200 F. The water-cooled probe in which the jewel was mounted continued to collect carbon all the while. Photographs taken before and after the carbon-deposition tests are shown in Figs. 14 and 15, herewith. The flame temperature indicated by probe (without correction for orifice expansion or variations in γ in a nitrogen-free field, which would be compensating errors) was 3460 R as compared to 3420 R obtained with an optical pyrometer and a mirror.[11] The agreement is felt to be fortuitous but added to the foregoing effects offers promise that the jeweled

[8] Aeronautical Research Scientist, National Advisory Committee for Aeronautics, Lewis Flight Propulsion Laboratory, Cleveland, Ohio.

[9] "Effect of Heat-Capacity Lag on a Variety of Turbine-Nozzle Flow Processes," by R. B. Spooner, NACA TN 2193, 1950.

[10] "Discharge Coefficients of Small-Diameter Orifices and Flow Nozzles," by H. P. Grace and C. E. Lapple, Trans. ASME, vol. 73, 1951, pp. 639–647.

[11] "Heat Transmission," by W. H. McAdams, McGraw-Hill Book Company, Inc., New York, N. Y., 1942, p. 75.

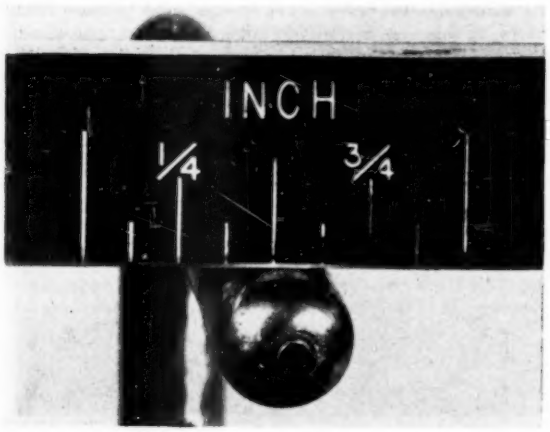

FIG. 14 PROBE BEFORE CARBON-DEPOSITION TESTS

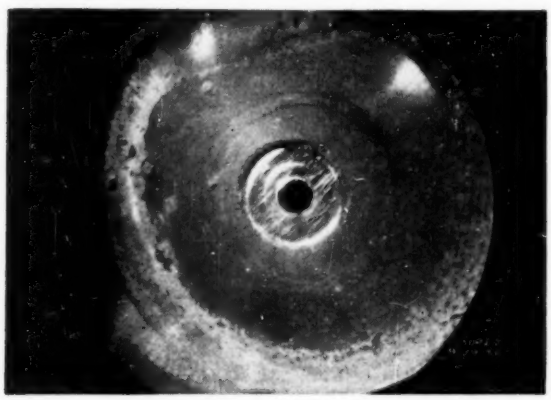

FIG. 15 PROBE AFTER CARBON-DEPOSITION TESTS

orifice may reduce the carbon and tar deposition encountered by Mr. Koffel.

The calibration Mr. Rieke presents is baffling. Presumably the effective area ratio is determined with no heat added before the second orifice and no flow about the probe. Then the probe is calibrated against a thermocouple with the heater turned on and with flow past the probe. Even at 540 R there appears to be a 35-deg error which must be due to either the manner of heating the gas at the second orifice or the nature of flow into the first orifice. Messrs. Koffel and Scadron both mention the importance in measuring the temperature at the second orifice accurately. The system Mr. Rieke used employed an immersion heater upstream of the thermocouple at the second orifice, operated at constant heat input. That the temperature read by a single thermocouple should give a representative temperature in this case seems unlikely. That the error should be as much as 10 per cent and vary in a manner necessary to get the calibration curve (Fig. 13 of his discussion) seems equally unlikely.

One factor that had not been investigated prior to Mr. Rieke's comments was the Mach-number effect on streamlined probes. A preliminary check on this effect has been made. The results are interesting and may have bearing on the mystifying Fig. 13.

Fig. 16 of this closure shows the relative effective area of the first orifice for four different probes plotted against free-stream Mach number. Three of the probes incorporated sharp-edged orifices and the fourth a nozzle so designed that the static temperature distribution along the axis of the nozzle was approximately linear.

The nozzle coefficient appeared unaffected by free-stream Mach number. The three orifices tested are roughly correlated at Mach < 0.7 by $A_{1(\text{effective})}/A_{1(\text{no flow})} = 1 + (\text{ID/OD})^2 M/0.9$, where ID is orifice diameter, OD probe diameter.

The curve labeled $^9/_{32}$ in. was obtained with a probe constructed

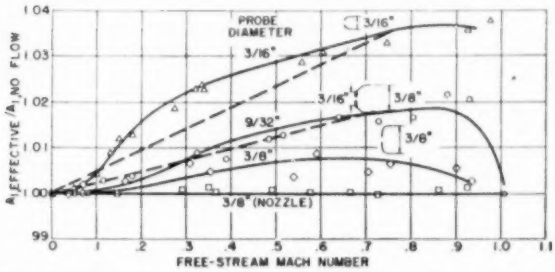

FIG. 16 MACH-NUMBER EFFECT ON FLOW COEFFICIENT OF FIRST ORIFICE FOR THREE DIFFERENT ORIFICE PROBES AND ONE NOZZLE

something like Mr. Rieke's with a button having dimensions as sketched. The $^3/_{16}$-in. and $^3/_8$-in-OD probes were blunt (approximately source shaped) and the correlation obtained with these two probes fits the data for the button probe if we take an effective OD midway between the small button face and the actual OD of the button.

A possible explanation of Mr. Rieke's 10 per cent error at 1000 R and subsequent constant 100-deg error at higher temperatures is that his probe has an effective ID/OD ratio that is fairly large ($\geq$0.3) and in operating his tunnel he first increased, then decreased the tunnel Mach number. This also seems unlikely.

It is conceivable that heat flux to the orifice could increase, then slowly decrease as the gas temperature is raised, which is what Mr. Rieke previously suggested. The effects of heat flux would be to cool the sample, change the orifice coefficient, and alter the size and possibly the shape of the orifice. In each case the indicated temperature would be lower than the actual temperature. Since in the work reported herein, no noticeable difference in the $T_{\text{ind}}/T_{\text{set}}$ was detected, it was concluded that heat transfer to the orifice was a negligible effect.

In all the work reported herein the orifice was made of beryllium copper. Mr. Rieke's orifice was stainless steel.

If the heat loss at the orifice is to be blamed for his Fig. 13, it would seem that the cause would lie in a change in size or shape of the orifice when heated locally, say at the upstream edge.

Mr. Scadron succinctly sums up the status of pneumatic temperature probes. His comments regarding the difficulties and importance in measuring T_2 accurately are well taken. Mr. Scadron is concerned with results Dr. Spooner computed for a nozzle 1.4 in. long. The time involved for a particle to be accelerated in Dr. Spooner's nozzle is about 10 times that involved in the acceleration of a particle with an 0.04-in-diam orifice. The magnitude of the error mentioned by Mr. Scadron is therefore high if the gas is largely nitrogen and the orifice size is as small as discussed herein.

The application Mr. Scadron has difficulty in visualizing, where pressure and velocity remain essentially unaltered, is the very important study of temperatures within a turbulent flame.[13] Herein alternate pockets of hot and cold gases pass a reference

[13] "Flame Stabilization and Propagation in High Velocity Gas Streams," by A. C. Scurlock, M.I.T. Meteor Report 19, Massachusetts Institute of Technology, Cambridge, Mass., May, 1948.

point at stream velocity and at constant pressure. With regard to pressure and velocity pulsations, one of the chief virtues of using a sonic-flow first orifice lies in the fact that small perturbations in pressure and velocity do not cause an appreciable defect in the flow rate. Mr. Scadron has done a great deal of excellent work in evaluating pneumatic probes employing small ΔP across the first orifice. The effect of small pressure disturbances, in this case, is relatively large. As a first approximation the magnitude of the tolerable pressure disturbances must be small compared to the ΔP across the first orifice. In the sonic-flow orifice the tolerable pressure disturbance must be small compared to the total pressure of the stream.

Use of the Centrifugal Governor Mechanism as a Torsional Vibration Absorber

By O. A. PRINGLE,[1] COLUMBIA, MO.

The centrifugal governor mechanism, suitably modified, is shown to be a practical torsional vibration absorber. Equations for predicting its performance are developed, and comparisons are made with other types of absorbers.

Nomenclature

The following nomenclature is used in the paper:

m = mass of absorber, lb sec²/in.
G = center of gravity of absorber mass
R = radius of G from axis of rotation, in.
Ω = angular velocity of disk, radians per sec
θ = angular displacement, radians
θ_o = amplitude of vibration of disk, radians
ω = circular frequency of vibration, radians per sec
t = time, sec
T = torque, in-lb
F = force, lb
a = acceleration, in/sec²
v = velocity, in/sec
r = displacement of mass from equilibrium position, in.
r_o = amplitude of vibration of absorber mass, in.
I = moment of inertia of disk, lb-in. sec²
K_t = torsional spring constant of shaft, in-lb/radian
K = spring constant of absorber system when rotating, lb per in.
k = spring constant of absorber spring, lb per in.
ω_n = circular natural frequency of absorber system, radians per sec
Ω_n = circular natural frequency of main system, radians per sec
N = order number of vibration, cycles per shaft revolution
E_r = theoretical relative effectiveness of two absorbers

Introduction and Description of Absorber Mechanism

If a body is vibrating, one possible way to reduce or eliminate the vibration is by the addition of a dynamic vibration absorber. For torsional vibration, the most common of these devices are the rotating pendulum absorber and the Frahm absorber.[2] It is the purpose of this paper to describe another type of absorber which, although differing in construction from those mentioned, has quite similar characteristics. The mechanism of this absorber is basically that of a centrifugal governor, consisting of a mass elastically mounted on a rotating body and constrained to move in a radial direction when acted upon by centrifugal force.

Fig. 1 shows an idealized diagram of the absorber mounted on a rotating disk. The mass m in the frictionless slot and the spring connecting the mass to the disk make up the absorber. Point G at radius R is the center of gravity of the mass. The disk rotates with a uniform angular velocity Ω, upon which is superimposed an additional velocity $\theta_o\omega \cos \omega t$ due to resonant torsional vibration of the disk. This vibration is excited by a periodic torque $T_o \cos \omega t$ acting on the disk. The radial force acting on the mass is

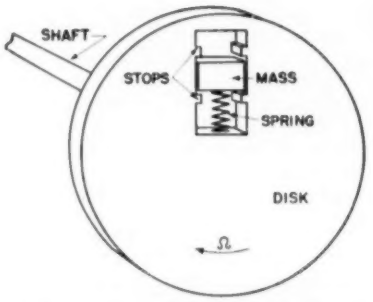

Fig. 1 Vibrating System With Absorber

$$\begin{aligned} F &= mR(\Omega + \theta_o\omega \cos \omega t)^2 \\ &= mR(\Omega^2 + 2\Omega\theta_o\omega \cos \omega t + \theta_o^2\omega^2 \cos^2 \omega t) \\ &= (mR\Omega^2 + \tfrac{1}{2}mR\theta_o^2\omega^2) + (2mR\Omega\theta_o\omega \cos \omega t) \\ &\quad + (\tfrac{1}{2}mR\theta_o^2\omega^2 \cos 2\omega t) \qquad [1] \end{aligned}$$

The total radial force is thus the sum of a constant force, a periodic force of frequency ω, and a periodic force of frequency 2ω. The constant force will determine the extension of the spring and hence the radius R. The two periodic forces will excite vibrations of the mass at their respective frequencies. However, the force of frequency 2ω is very small in comparison with the other, a fact which can be verified by substitution of typical values. Furthermore, it will appear later that the natural frequency of the absorber must be equal to ω; therefore the effect of the force of frequency ω will be magnified due to resonance. For these reasons, the exciting force on the mass is taken as

$$\begin{aligned} F' &= 2mR\Omega\theta_o\omega \cos \omega t \\ &= 2mR\Omega\frac{d\theta}{dt} \qquad [2] \end{aligned}$$

The vibration of the disk thus induces vibration of the absorber mass. The effect of this motion on the disk is shown by writing Coriolis' law between point G and a coincident point G' on the disk

$$a_G = a_{G'} +\!\!\rightarrow a_{GG'} +\!\!\rightarrow 2v_{GG'}\Omega \qquad [3]$$

$$= R\Omega^2 +\!\!\rightarrow R\frac{d\Omega}{dt} +\!\!\rightarrow \frac{d^2r}{dt^2} +\!\!\rightarrow 2\frac{dr}{dt}\Omega \qquad [4]$$

The last two terms of Equation [4] are the result of the motion of the mass. The last term, by virtue of its tangential direction, results in an inertia torque transmitted to the disk by pressure between the slot and mass equal to

$$T_i = 2mR\frac{dr}{dt}\Omega \qquad [5]$$

[1] Assistant Professor, Department of Mechanical Engineering, The University of Missouri. Jun. ASME.

[2] "Mechanical Vibrations," by J. P. Den Hartog, McGraw-Hill Book Company, Inc., New York, N. Y., third edition, 1947, pp. 112–119.

Contributed by the Machine Design Division and presented at the Semi-Annual Meeting, Cincinnati, Ohio., June 15–19, 1952, of The American Society of Mechanical Engineers.

Note: Statements and opinions advanced in papers are to be understood as individual expressions of their authors and not those of the Society. Manuscript received at ASME Headquarters, April 10, 1952. Paper No. 52—SA-34.

In Equation [5] the average angular velocity Ω is used instead of the instantaneous velocity $\Omega + \theta_o \omega \cos \omega t$. The inclusion of the latter term results in an expression similar to the last term of Equation [1] and is not important in the present discussion.

Operation of Absorber

The action of the absorber is shown diagrammatically in Fig. 2. In Fig. 2(*a*), the instantaneous magnitude of a quantity is the projection of its vector upon the *Y*-axis. At resonance, T_o will be in phase with the velocity of $\theta_o\omega$, and will lead the amplitude θ_o by 90 deg. Let the natural frequency of the absorber system equal ω. Then the absorber amplitude r_o lags 90 deg behind its exciting force F', which is due to and in phase with the velocity $\theta_o\omega$. The absorber radial velocity $r_o\omega = (dr/dt)$ is then in phase with T_o. The inertia torque T_i is of opposite sign to $r_o\omega$, and therefore joins with the damping torque T_d in opposing T_o. This is shown more clearly in Fig. 2(*b*), which omits the displacements and velocities.

Equations of Motion

Applying Newton's law to the disk and neglecting damping

$$\Sigma T = I\alpha$$

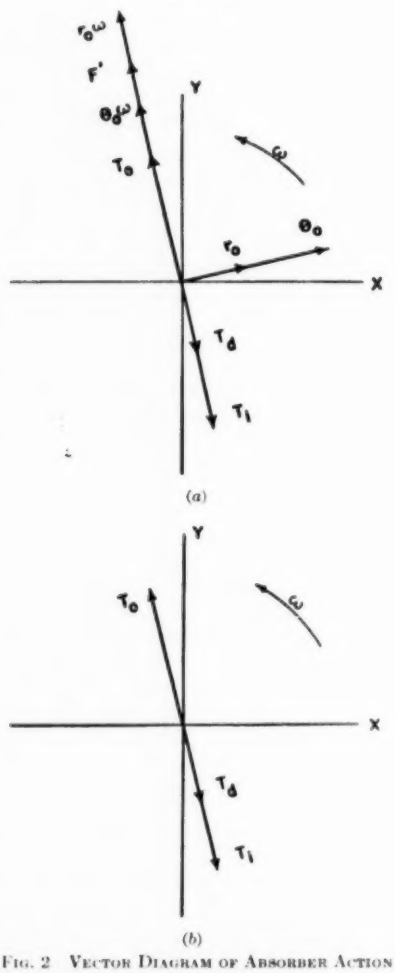

Fig. 2 Vector Diagram of Absorber Action

$$T_o \sin \omega t - 2m R \Omega \frac{dr}{dt} - K_t\theta = I \frac{d^2\theta}{dt^2} \quad \ldots\ldots [6]$$

The corresponding equation for the absorber is

$$\Sigma F = ma_c$$

$$2m R \Omega \frac{d\theta}{dt} - Kr = m \frac{d^2r}{dt^2} \quad \ldots\ldots [7]$$

Inspection of these equations shows that the following will be a solution

$$\theta = \theta_o \sin \omega t$$

$$r = r_o \cos \omega t$$

Also

$$\sqrt{\frac{K}{m}} = \omega_n$$

$$\sqrt{\frac{K_t}{I}} = \Omega_n$$

Making the foregoing substitutions results in

$$\theta_o = \frac{\frac{T_o}{K_t}\left(1 - \frac{\omega^2}{\omega_n^2}\right)}{\left(1 - \frac{\omega^2}{\Omega_n^2}\right)\left(1 - \frac{\omega^2}{\omega_n^2}\right) - \frac{(2m R \Omega\omega)^2}{KK_t}} \quad \ldots\ldots [8]$$

$$r_o = \frac{\frac{T_o}{K_t}\left(\frac{2m R \Omega\omega}{K}\right)}{\left(1 - \frac{\omega^2}{\Omega_n^2}\right)\left(1 - \frac{\omega^2}{\omega_n^2}\right) - \frac{(2m R \Omega\omega)^2}{KK_t}} \quad \ldots\ldots [9]$$

Equation [8] shows that θ_o becomes zero if the natural frequency of the absorber equals the applied frequency.

Owing to the effect of centrifugal force, the absorber-system spring constant and natural frequency vary with the angular velocity as follows

$$K = k - m\Omega^2 \quad \ldots\ldots [10]$$

$$\omega_n = \sqrt{\frac{k}{m} - \Omega^2} \quad \ldots\ldots [11]$$

The action of the absorber is due to the fact that it adds another degree of freedom to the original system. An additional natural frequency is added, making a total of two for the case under discussion, neither of which corresponds to the original natural frequency. These new frequencies are found by setting the denominator of Equation [9] equal to zero. A convenient form of the resulting equation, in which the order of vibration N has been introduced and R is the original desired radius, is

$$\left(1 - \frac{\omega^2}{\Omega_n^2}\right)\left[1 - \omega^2\left(\frac{k}{m} - \frac{\omega^2}{N^2}\right)^{-1}\right] - \left(\frac{4m R^2 \omega^4}{IN^2\Omega_n^2}\right) \times \left(1 - \frac{m\Omega_n^2}{k}\right)^2\left(1 - \frac{m\omega^2}{kN^2}\right)^{-2}\left(\frac{k}{m} - \frac{\omega^2}{N^2}\right)^{-1} = 0 \quad \ldots [12]$$

Solving Equation [12] for ω gives the two natural frequencies.

In a practical design, the undesirable effect of the two new natural frequencies is eliminated by means of stops such as shown in Fig. 1. Initial spring force holds the mass against the inner stop until the speed at which the absorber is to operate is approached, at which time it is pulled away from the stop by centrifugal force. At some higher speed the mass is forced against

the outer stop. Thus the absorber does not operate at speeds which might allow resonance at the two natural frequencies.

Design of Absorber

An equation useful in proportioning the absorber is obtained from Equation [9] when $\omega = \omega_n$

$$2m\,R\,\Omega r_o\omega_n = T_o \quad \ldots\ldots [13]$$

The angular velocity Ω, the natural frequency ω_n, and the torque T_o will be known. The mass m and radius R must be chosen so that the amplitude r_o will be reasonable. The stops will be located to eliminate the natural frequencies of Equation [12]. The spring constant is found from Equation [11]. The initial force in the spring must balance the centrifugal force on the mass at the speed at which the absorber is to begin operating.

The details of construction will vary with the application, but a possible design is shown in Fig. 3. The mass is mounted on a cantilever spring, which transmits the absorber torque to the

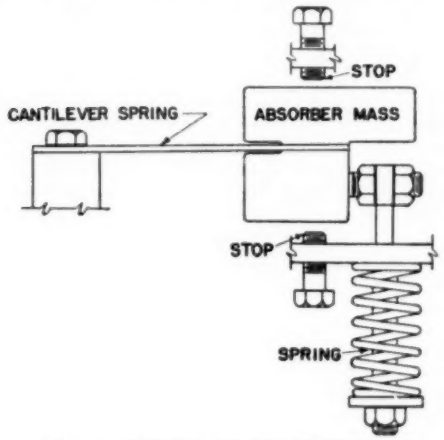

Fig. 3 A Possible Absorber Construction

vibrating body. An alternative construction would have the mass pivot on antifriction bearings. Adjustable stops are above and below the mass. The spring is loaded in compression, the initial load being adjustable. The distance between the center of gravity of the mass and the line of action of the spring force is also adjustable, allowing the spring constant to be varied slightly. The type of mounting depends on the shape of the vibrating body. For greater effectiveness, two or more absorbers may be mounted radially about the center of rotation.

Comparisons

Fig. 3 emphasizes the fact that, if desired, the absorber may be constructed so that its characteristics are somewhat variable. This would facilitate exact tuning to correct for manufacturing tolerances, approximations in calculations, or wear. Other types of dynamic absorbers, particularly the rotating-pendulum absorber, are often difficult to tune exactly.[3]

An important comparison may be made by writing the equation for either the rotating-pendulum absorber or the Frahm absorber which corresponds to Equation [13]. This equation is

$$m\,R\,r_o\,\omega_n^2 = T_o' \quad \ldots\ldots [14]$$

Equation [14] states that a rotating-pendulum absorber of a certain mass, radius, amplitude, and frequency will balance

[3] "Practical Solution of Torsional Vibration Problems," by W. K. Wilson, John Wiley & Sons, Inc., New York, N. Y., second edition, vol. 2, 1941, p. 570.

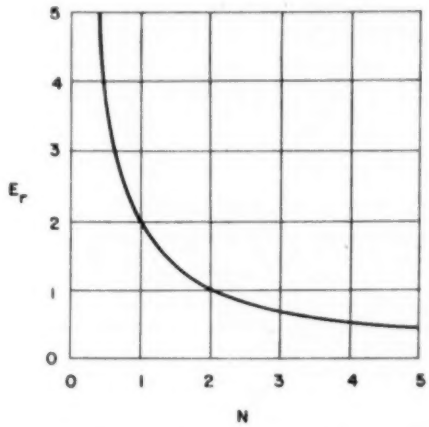

Fig. 4 Absorber Compared With Rotating-Pendulum Absorber

a certain exciting torque T_o'. Equation [13] states that the absorber under discussion of the same mass, radius, amplitude, and frequency will balance a different exciting torque T_o. For the sake of comparison, let the theoretical relative effectiveness E_r be the ratio of T_o to T_o'. Then

$$E_r = \frac{2m\,R\,\Omega\,r_o\,\omega_n}{m\,R\,r_o\omega_n^2} = \frac{2\Omega}{\omega_n} = \frac{2}{N} \quad \ldots\ldots [15]$$

This result is visualized in Fig. 4. For second-order vibration both absorbers are equally effective; in other words, for a given application, the absorbers would be about the same size. For higher orders, the rotating-pendulum absorber would be preferred on the basis of Equation [15]. On the other hand, for orders of vibration lower than the second, the absorber under discussion would be the most effective.

Discussion

R. J. Harker.[4] This paper on the use of a radially oscillating mass to suppress torsional vibrations in rotating systems is novel and appears to present some interesting possibilities, particularly with respect to low orders of excitation. The author is to be congratulated for his ingenious proposal and for his contribution to the theory of the tuned dynamic vibration absorber.

Equations [8] and [9] of the paper may be simplified by defining the main system as a single mass at a radius of gyration equal to the radius R, or $I = MR^2$, and by using the following notation

$f = (\omega_n/\Omega_n)$ = absorber tuning factor

$g = (\omega/\Omega_n)$ = forced-frequency ratio

$\mu = (m/M)$ = mass ratio

Then Equations [8] and [9] become

$$\theta_0 = \frac{(T_o/K_t)\,[1 - g^2]}{[1 - g^2]\left[1 - \left(\frac{g}{f}\right)^2\right] - 4\,\mu\left(\frac{g}{f}\right)^2\left(\frac{g^2}{N^2 + 1}\right)}$$

$$r_0 = \frac{\left(\frac{T_o R}{K_t}\right)\left[\frac{2}{N}\left(\frac{g}{f}\right)^2\right]}{[1 - g^2]\left[1 - \left(\frac{g}{f}\right)^2\right] - 4\,\mu\left(\frac{g}{f}\right)^2\left(\frac{g^2}{N^2 + 1}\right)}$$

[4] Associate Professor of Mechanical Engineering, University of Wisconsin, Madison, Wis. Mem. ASME.

If the tuning of the absorber is correct, $f = 1$, and these equations reduce to

$$\theta_o = \frac{\left(\frac{T_0}{K_T}\right)[1 - g^2]}{[1 - g^2]^2 - \frac{4\,\mu g^4}{N^2 + 1}}$$

$$r_o = \frac{\left(\frac{(T_0 R)}{K_T}\right)\left[\frac{2g^2}{N}\right]}{[1 - g^2]^2 - \frac{4\,\mu g^4}{N^2 + 1}}$$

The resulting frequency equation for the combined system with exact absorber tuning is then

$$g^4\left[1 - \frac{4\mu}{N^2 + 1}\right] - 2g^2 + 1 = 0$$

with the solution

$$g^2 = \frac{1 \pm \sqrt{\frac{4\,\mu}{N^2 + 1}}}{1 - \frac{4\,\mu}{N^2 + 1}}$$

The exciting frequencies corresponding to infinite amplitudes of the system are seen to be a function of the mass ratio and the order of excitation. It is apparent that for high mass ratios and low orders of excitation the factor $\left(\frac{4\,\mu}{N^2 + 1}\right)$ may be greater than unity. Since g^2 can only be positive, this condition apparently would result in a single resonant frequency. In general, however, there would be two resonant frequencies as indicated.

Author's Closure

The author wishes to thank Professor Harker for his comments. The simplification of Equations [8] and [9] and subsequent derivation of an expression for the resonant frequencies added by the absorber is worth while in view of the fact that Equation [12] given in the paper for this purpose is rather tedious to solve.

To avoid confusion in the use of these equations it is necessary to realize that they apply only if the original main system has but a single degree of freedom. Also, the manner in which the exciting torque acts on the system must be defined. If the excitation is of a definite order, its frequency varies with angular velocity. The natural frequency of the absorber system and radius of the absorber mass, which vary with angular velocity, are then functions of exciting frequency. Equation [12] applies to such a case. On the other hand, the excitation may not be of a definite order, but may vary in frequency at constant angular velocity. Then the natural frequency of the absorber system and radius of the absorber mass remain unchanged. In this instance the absorber tuning factor f will equal unity at all times as assumed in Professor Harker's derivation. Inspection of the equations indicates that there is not too much difference in resonant-frequency values obtained by proceeding upon either assumption, and values obtained in either manner will be approximately correct for the other case.

Axial Tension and Bending Interaction Curves for Members Loaded Inelastically

By D. O. BRUSH[1] and O. M. SIDEBOTTOM[2]

This paper presents a theoretical method for constructing dimensionless interaction curves for members subjected to combined tension and bending loads that produce inelastic strains, as well as experimental results which verify the theory. Each interaction curve represents the total range of the ratios of axial load to bending moment which will cause inelastic strains to extend to a given depth in the member. Experimental interaction curves were obtained from eccentrically loaded tension members of rectangular cross sections made from three strain-hardening materials, namely, annealed rail steel and aluminum alloys 24S-T4 and 75S-T6. Good agreement was found between theory and experiment. In order to design a member subjected to combined axial and bending loads by use of the interaction curves, the deflection of the member must be estimated. Three orders of approximation for the deflection of eccentrically loaded tension members are presented. The problem of combined bending and axial compressive loads is discussed and research based on the methods of analysis developed in this investigation is suggested for solving for the buckling load of a member subjected to combined bending and axial compressive loads.

Introduction

MEMBERS of some machines and structures must be designed to resist loads where the weight of the members must be as low as possible. One way of obtaining such members is the use of lightweight metals such as alloys of aluminum and magnesium that have a high strength-to-weight ratio. Another way has been by the improvement in the design of the cross sections of the member by using sections made of thin sheets reinforced with stringers. Another important idea used in designing such a member is to take into account the increased resistance to loads by the member when relatively small inelastic strains are allowed to occur in the most strained fibers. It has been found that many members can resist loads that greatly exceed the maximum elastic load for the member. This method requires the use of a relationship between the loads and the stresses or strains in the member when the strains exceed the elastic-limit strain of the material. The maximum elastic load is the load at which the most strained fiber of the member is on the threshold of becoming inelastically strained. For a member loaded in such a way that it has a stress gradient, the load necessary to produce a small amount of inelastic deformation of the most strained fibers may be appreciably larger than the maximum elastic load especially if the stress gradient is steep at these fibers.

This investigation was undertaken to determine the influence of relatively small inelastic deformation on the loads carried by a member subjected to both an axial load P and a bending moment M. Small inelastic strains are here defined as those of the same order of magnitude as the elastic-limit strain of the material. Some investigations have been made of such members, mostly of aircraft structural elements consisting of cross sections made of thin sheet stiffened by stringers. There are many other types of applications in which a member must be designed to carry combined bending and axial loads such as occur when an eccentric load is applied to a tension member or to a compression member. For members loaded in compression, the failure of the member may be by elastic buckling if the member is relatively long, or by inelastic buckling if the member is relatively short. The behavior of a member that fails by inelastic buckling is complicated. Therefore in this investigation the load P is a tensile load so that buckling failure does not occur. It was felt that the results of this investigation would give a better understanding of inelastic behavior of a member subjected to combined loads and lead to further research in the problem of inelastic buckling.

The failure of members tested in this investigation was by excessive inelastic deformation. None of the members was loaded to fracture, because of the fact that each member tested withstood inelastic strains over a major portion of its length and depth at the maximum loads used. Therefore it was considered that each member failed by general yielding. As will be shown later, this general yielding was assumed to take place when inelastic strains had occurred at the most highly stressed cross section to a certain arbitrarily chosen depth of the section.

When a member is subjected to a combination of two types of loads, such as P and M as used in this investigation, two relationships between the loads are necessary for the design of the member. The first relationship to be considered is that of the interaction curve which expresses the total range of values of load P and moment M which will result in a given depth of yielding. The second relationship expresses the relation between P and M for a given loading of a member so that a point on the interaction curve can be determined.

Method of Obtaining Interaction Curves

Inelastic Strains Impending. If no inelastic strain can be allowed in a member similar to those shown in Fig. 1, the maximum stress σ in the extreme fibers can be written in terms of P and M by using the principle of superposition. This expression is

$$\sigma = \frac{P}{A} + \frac{Mc}{I}$$

in which A is the cross-section area, c is the distance from the centroid to the extreme fiber, and I is the moment of inertia of the area with respect to the centroidal axis. If the value of σ is equal to the elastic limit σ_e of the material, the foregoing equation states the condition that inelastic strain is impending or is on the verge of occurring in the most stressed fibers. The equation is transformed by dividing both sides by σ_e and setting $P_e = \sigma_e A$ and $M_e = \sigma_e I/c$ where P_e and M_e are the elastic limit loads for the member for axial tension only and pure bending only, respectively.

[1] Stress Analyst, Aerophysics Laboratory, North American Aviation, Inc., Downey, Calif. Formerly, Assistant, Department of Theoretical and Applied Mechanics, University of Illinois, Urbana, Ill.

[2] Assistant Professor, Department of Theoretical and Applied Mechanics, University of Illinois. Jun. ASME.

Contributed by the Metals Engineering Division and presented at the Semi-Annual Meeting, Cincinnati, Ohio, June 15–19, 1952, of The American Society of Mechanical Engineers.

Note: Statements and opinions advanced in papers are to be understood as individual expressions of their authors and not those of the Society. Manuscript received at ASME Headquarters, March 3, 1952. Paper No. 52—SA-6.

$$\frac{P}{P_e} + \frac{M}{M_e} = 1 \quad \ldots\ldots [1]$$

Equation [1] is represented by the line DC in Fig. 2 in which ordinates represent values of M/M_e and abscissas P/P_e. The curve DC (straight line in this case) represents corresponding pairs of values of M and P which will cause the member to be on the verge of starting to strain inelastically and is called an interaction curve. Equation [1] constitutes a relationship between P and M for impending inelastic strains, but an additional relationship between P and M must be found for a given member subjected to a combination of bending and axial loads. For the case considered here, namely, eccentric tensile loads, this additional equation is

$$M = P(e_o - \Delta) \quad \ldots\ldots [2]$$

in which e_o (see Fig. 1) is the initial eccentricity and Δ is the deflection of the member at its middle section. For impending inelastic strains Δ is equal to Δ_e. In order to determine the pair of values of P and M that correspond to impending inelastic strain, we must determine[3] Δ_e and then solve Equations [1] and [2] simultaneously. If e_o is relatively large, the effect of Δ_e is usually neglected; that is, Equation [2] is written $M = Pe_o$. If e_o is indefinitely large, the bending moment is so-called pure bending, corresponding to points on the vertical axis in Figs. 2 and 3.

Small Inelastic Strain Allowed. The loads M and P, as given by the foregoing equations, will have to be increased somewhat in order to cause inelastic strains to occur at the extreme fiber and at other nearby fibers in the most highly stressed cross section. Eventually, if the loads M and P are increased sufficiently, the fibers at all depths in the beam at the most highly stressed cross section will become inelastically strained; however, this condition will result in an inelastic deformation which no longer can be considered small, and the member will have failed by general yielding. Therefore some compromise loading between the loads which result in failure by general yielding and the loads that cause inelastic strains to be impending in the extreme fiber is desirable.

[3] "Airplane Structures," by A. S. Niles and J. S. Newell, John Wiley and Sons, Inc., New York, N. Y., third edition, vol. 2, 1943, p. 67.

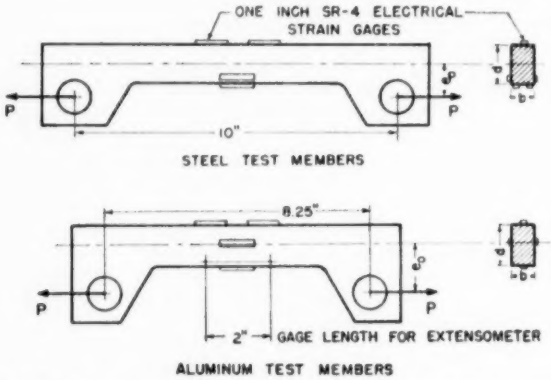

FIG. 1 SKETCHES OF TEST MEMBERS SHOWING MANNER OF LOADING

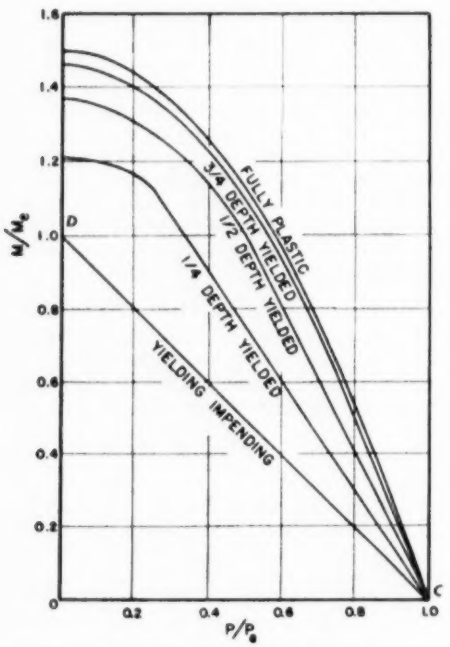

FIG. 2 EFFECT OF DEPTH OF YIELDING ON MOMENT-LOAD INTERACTION CURVES FOR MEMBER OF RECTANGULAR CROSS SECTION MADE OF MATERIAL WITH $\alpha = 0$

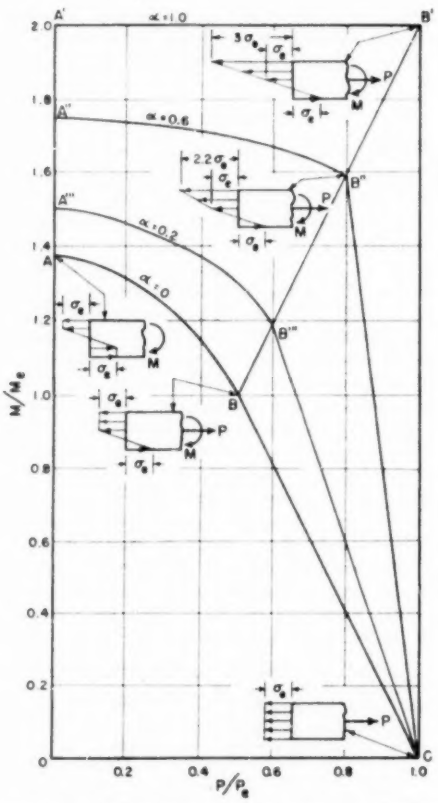

FIG. 3 EFFECT OF STRAIN-HARDENING FACTOR α ON MOMENT-LOAD INTERACTION CURVES FOR A MEMBER OF RECTANGULAR CROSS SECTION WITH HALF DEPTH YIELDED

In this paper the loads chosen are those combinations of M and P that cause inelastic strains to occur over one half the depth of the most highly stressed cross section. This choice of proportions of area covered by elastically strained as compared with inelastically deformed fibers is made because it leaves half of the section elastic which insures that the deformation of the member is of the same order of magnitude as that which occurs under the elastic-limit loads when inelastic strains are impending. Furthermore, this manner of describing the extent and magnitude of inelastic strains is more convenient to use than methods which make use of magnitude of the maximum stress or strain. Also it more closely describes the approach condition of the member to failure by general yielding.

The interaction curve for the condition described in the preceding paragraph, namely, the loads corresponding to inelastic strains in one half the depth of the most highly stressed section, cannot be found by use of the principle of superposition as was Equation [1], and is found here by plotting a few points. The method used is to assume that at this cross section an arbitrary distribution of the strains is chosen which makes half the depth inelastic and half elastic as previously described. The problem is to determine what load P and bending moment M correspond to the assumed strain distribution.

An example is now given which shows how the interaction curve is drawn. ABC in Fig. 3 represents the interaction curve for inelastic strain to one-half depth of the cross section of a member of rectangular cross section made of a non-strain-hardening material having equal yield points σ_s in tension and compression, that is, the slope α, Fig. 4, of the stress-strain curve is zero when the stress becomes σ_s. The ordinate of point A which represents pure bending is obtained by finding the moment $M = \int \sigma y dA$. In this integral y is measured from the centroid and the distribution of the stress σ on the beam cross section is as shown by the figure near the point A. In this case inelastic strains are assumed to occur at the top and bottom of the beam to one fourth its depth, that is, a total of one half. The moment M is divided by $M_s = \sigma_s I/c = {}^2/_3 (\sigma_s bc^2)$. The abscissa of A is zero since $P = \int \sigma dA$ is zero for this stress distribution. Similarly, the ordinate of B is found by determining M from the integral $M = \int \sigma y dA$ in which the stress distribution is shown in the figure near B and y is again measured from the centroidal axis. In this case all inelastic strains are assumed to occur in the upper one half of the cross section and inelastic strains in the lower extreme fiber are impending. This value of M is equal to ${}^2/_3(\sigma_s bc^2)$ for the rectangular section and, since $M_s = {}^2/_3(\sigma_s bc^2)$, the ratio $M/M_s = 1$ is the ordinate of B. The abscissa of B is found by determining the resultant force $P = \int \sigma dA$ for the stress distribution on the section. This value is $P = \sigma_s bc$ for the rectangular section and therefore $P/P_s = {}^1/_3$.

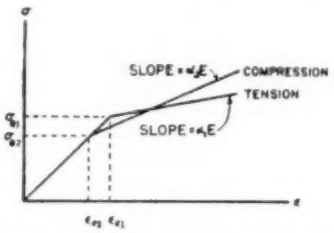

(a) IDEALIZED STRESS-STRAIN DIAGRAMS FOR MATERIAL

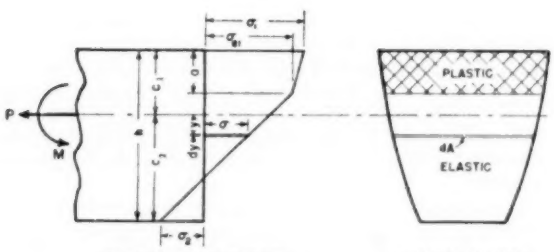

(b) STRESS-DISTRIBUTION (c) CROSS SECTION

FIG 4 DISTRIBUTION OF STRESS IN STRAIGHT MEMBER OF SYMMETRICAL CROSS SECTION WHICH IS SUBJECTED TO AXIAL TENSION AND BENDING LOADS

It is proved later that from B to C the curve is always a straight line. Because of this fact the location of the point B is very important. Other points between A and B can be found in a manner similar to that used in locating A and B. When α is not zero, Fig. 4(*a*), the interaction curve can be drawn in exactly the same way that ABC was drawn. In Fig. 3 the curves $A'''B'''C$, $A''B''C$ and $A'B'C$ represent the interaction curve for materials in which $\alpha = \alpha_1 = \alpha_2$ is 0.2, 0.6, and 1.0, respectively. It will be shown later that curves for values of α between 0 and 1, such as $A'''B'''C$ and $A''B''C$, can be drawn by linear interpolation between $ABC(\alpha = 0)$ and $A'B'C(\alpha = 1)$.

An interaction curve such as ABC in Fig. 3 represents one relationship between P and M. Equation [2], called the moment-load relationship in this paper, is an additional relationship which can be used to solve for the desired values of P and M for a given problem. But in order to use Equation [2] the value of Δ must be known. A value of the deflection Δ can be determined approximately by making use of the assumed depth of inelastic strain in the member. Simple procedures are presented later to give first, second, and third approximations to the deflection of a member loaded eccentrically in tension. The shape of an interaction curve in the inelastic range is a function of the cross section of the member,[4] Fig. 5, the shape of the stress-strain diagram of the material, Fig. 3, and the depth of yielding, Fig. 2.

Several assumptions have been made in constructing these interaction curves. The tension and compression stress-strain diagrams are assumed to be represented by two straight lines as indicated in Fig. 4(*a*). Plane sections are assumed to remain plane during loading. It is further assumed that a plane given by the action line of the load and the centroidal axis of the member is a plane of symmetry of the cross section.

Proof That B-C Is Straight Line. The proof of the linearity of line B-C and the location of point B will now be given for a beam of rather general cross sections such as that shown in Fig. 4(*c*) and for a general case. The beam is subjected to a load P and moment M such that the depth of yielding is a and the maximum compressive stress σ_2 is less than σ_{e2}, Fig. 4(*a*). The equations of equilibrium for the stress distribution are

$$P = \int \sigma dA; \quad M = \int \sigma y dA \quad \ldots\ldots\ldots\ldots [3]$$

where y is measured from the centroidal axis. The stresses in the elastic and inelastic region are, respectively

$$\sigma = \frac{\sigma_{e1} - \sigma_2}{h - a}(c_2 + y) + \sigma_2$$

$$\sigma = (1 - \alpha)\sigma_{e1} + \frac{\alpha(\sigma_{e1} - \sigma_2)}{h - a}(c_2 + y) + \alpha\sigma_2$$

in which σ_2 is negative for compression. If these stresses are put

[4] For a discussion of interaction curves for various types of cross sections see, "Advanced Mechanics of Materials," by F. B. Seely and James O. Smith, John Wiley & Sons, Inc., New York, N. Y., 1952.

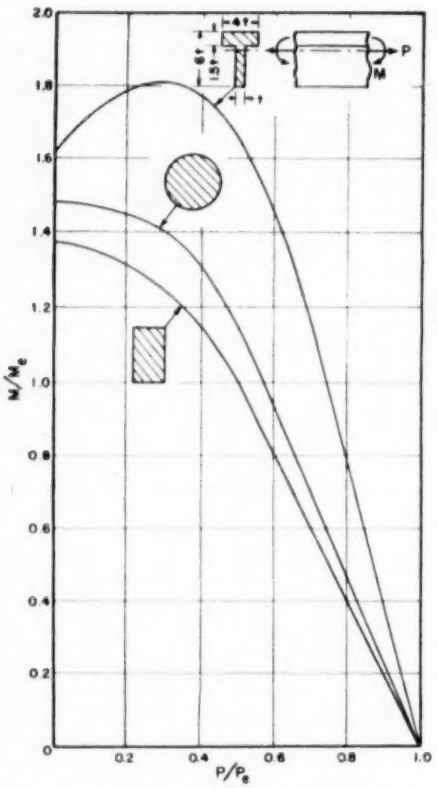

FIG. 5 EFFECT OF CROSS SECTION ON MOMENT-LOAD INTERACTION CURVES FOR MEMBER MADE OF MATERIAL WITH $\alpha = 0$

in Equation [3], the load and moment in dimensionless form are

$$\frac{P}{P_e} = \frac{1-\beta}{A(h-a)}(c_2A_e + Q_e + \alpha c_2A_p + \alpha Q_p) + \beta\frac{A_e}{A} + \alpha\beta\frac{A_p}{A} + (1-\alpha)\frac{A_p}{A} \quad \ldots\ldots [4]$$

$$\frac{M}{M_e} = \frac{c_1(1-\beta)}{I(h-a)}(c_2Q_e + I_e + \alpha c_2Q_p + \alpha I_p) + \frac{\beta c_1Q_e}{I} + \frac{\alpha\beta c_1Q_p}{I} + (1-\alpha)\frac{c_1Q_p}{I} \quad \ldots [5]$$

where

$$P_e = \sigma_{s1}A, \qquad M_e = \frac{\sigma_{s1}I}{c_1}, \qquad \beta = \frac{\sigma_2}{\sigma_{s1}}$$

(negative for σ_2 compression), and Q is first moment of the area about centroidal axis. The subscripts e and p on A, Q, and I refer to the elastic and inelastic (plastic) areas of the cross section.

For a given material, all the terms on the right side of either Equation [4] or [5] are constant except β. Since P and M are both linear in β, the line BC is a straight line. If σ_2 is made equal to $-\sigma_{s2}$, the yield stress in compression, Equations [4] and [5] can be used to locate the point on the interaction curve corresponding to point B in Fig. 3.

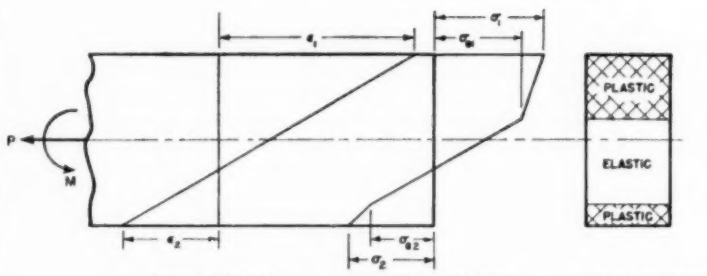

FIG. 6 DISTRIBUTION OF STRAIN AND STRESS IN STRAIGHT MEMBER OF RECTANGULAR CROSS SECTION WHICH IS SUBJECTED TO AXIAL TENSION AND BENDING LOADS

For the special case of a rectangular cross section with $a = h/2$, $\sigma_{s2} = \sigma_{s1}$ and $\beta = -1$, Equations [4] and [5] become

$$\left.\begin{aligned}\frac{P}{P_e} &= \frac{1}{2} + \frac{\alpha}{2}\\ \frac{M}{M_e} &= 1 + \alpha\end{aligned}\right\} \quad \ldots\ldots [6]$$

If α is set equal to zero in Equations [6], point B in Fig. 3 is obtained. Point B' is obtained if α is equal to unity. The load P and the moment M vary linearly with α so that the point, corresponding to point B for a material with $\alpha \neq 0$, must lie on the straight line BB'. It should be observed that the general expression for P and M, Equations [4] and [5], are also linear in α. The point on the interaction curve corresponding to B in Fig. 3 for any value of α is obtained by interpolation between B and B', that is, by laying off a distance along BB' from B equal to $\alpha BB'$.

For any point on the interaction curve from A to B inelastic strains occur on both sides of the member. In the more general case the location of any point on this curve is a function of both α_1 and α_2, the strain-hardening factors in tension and compression. If $\alpha_1 = \alpha_2 = \alpha$, the location of any point from A to B can be computed for $\alpha = 0$ and $\alpha = 1$ and the location of the point for any α can be determined by interpolation in a manner similar to that discussed above for point B. The curves shown in Fig. 3 illustrate the effect of α on the interaction curves for $^1/_2$ depth of yielding in a member with rectangular cross section.

The calculation of a point on the interaction curve for the more general case can be carried out from diagrams similar to that shown in Fig. 6. Assume a strain distribution, Fig. 6(a), which will result in a given depth of yielding. From the strain distributions and the known stress-strain diagrams, Fig. 4(a), the stress distribution, Fig. 6(b), can be obtained. The load P and the moment M can then be calculated for the given stress distribution.

The effect of depth of yielding on the interaction curves is shown in Fig. 2 for a member with rectangular cross section and made of a material with identical properties in tension and compression and $\alpha = 0$. The effect of cross section on the interaction curves is indicated in Fig. 5 by the rectangular, circular, and T cross sections. The material is the same as for the curves shown in Fig. 2, and the depth of yielding is $^1/_2$ the depth of the member.

For a member of given length, cross section, and initial eccentricity, the load or moment on the member necessary to produce a given depth of yielding cannot be determined unless the deflections of the member for these conditions are known. If the deflection is known, the final eccentricity can be calculated and the relation between moment and load obtained. In case the

axial eccentric load is a tension load, simple first, second, and third approximations to the moment-load curves are given later in this paper so that a safe approximation to the load can be obtained. These procedures are presented in the discussion of results.

Materials and Method of Testing

The materials used in the experimental investigations were annealed high-carbon rail steel and aluminum alloys 24S-T4 and 75S-T6. Nine eccentrically loaded tension members were tested, three for each material. The rail-steel test members were machined from the base of an annealed railroad rail. The aluminum test members were machined from six pieces of as-rolled bar stock. All machined surfaces were finish-ground. The over-all dimensions of the test members are shown in Fig. 1. The numerical values of the cross-sectional dimensions and the original eccentricity e_o are listed in Table 1.

TABLE 1 ORIGINAL ECCENTRICITIES AND ORIGINAL CROSS-SECTIONAL DIMENSIONS OF TEST MEMBERS

Material	Test number	b Breadth of section, in.	d Depth of section, in.	e_o Original eccentricity, in.
Annealed rail steel	1	0.753	1.249	1.147
	2	0.753	1.249	0.465
	3	0.753	1.249	0.282
Aluminum alloy 24S-T4	1	0.751	1.252	1.194
	2	0.751	1.252	0.503
	3	0.751	1.252	0.304
Alumaum alloy 75S-T6	1	0.747	1.252	1.194
	2	0.747	1.252	0.504
	3	0.501	1.252	0.304

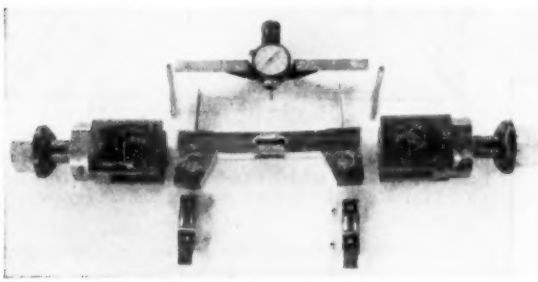

Fig. 7 Layout of Fixtures Used in Loading Test Members

The test members were all tested in a hydraulic type, Amsler testing machine having load ranges of 0 to 10,000, 0 to 20,000, 0 to 50,000, and 0 to 100,000 lb. The load was applied by the fixtures shown in Fig. 7. The two yokes were attached to the heads of the testing machine. The load was transmitted from the yoke through $^3/_8$-in-diam hardened steel balls to the tapered pin and from the pin to the test member. The purpose of the taper on the pin was to permit lateral adjustment of the test member to minimize lateral bending.

Strains in the rail-steel members were measured by 1-in. Type A-11, SR-4 electrical strain gages at the locations shown in Fig. 1. These gages were found to be unreliable for the large tensile strains (up to 0.015 in. per in.) in the aluminum members; therefore a 2-in. gage length mechanical extensometer, with one division on the dial equaling 0.0001 in. per in. strain, was used to measure the strains in the fibers near the most strained fibers. The data from the SR-4 gage were used for small strains, and the extensometer was used for large strains. The deflections of the members were measured by a $^1/_{1000}$-in. dial by the arrangement shown in Fig. 7.

In testing, increments of load were applied and corresponding strains and deflections measured. In the inelastic range the strain and deflection readings indicated that the inelastic deformation continued with time. In such cases an arbitrary time interval of 5 to 15 min was allowed for indicators to become reasonably steady before readings were taken. During this interval a fairly successful attempt was made to hold the load at a constant value.

Properties of Materials

Mechanical properties of the materials were determined from standard tension and compression specimens cut from the bars from which the moment-load test members were made. They were selected so that the center lines of the tension and compression specimens coincided as nearly as possible with the most strained tension and compression fibers of the moment-load test members. Three tensile specimens were tested for the annealed rail steel, one from near the most strained fibers of each of the three test members. From past experience with this material, it was assumed to have the same properties in tension and compression. For each aluminum alloy, three tension and two compression specimens were tested. The stress-strain diagrams of the materials are shown in Figs. 8 and 9. Each diagram is shown approximated by two straight lines. Mechanical properties were taken from these straight lines and are listed in Table 2.

TABLE 2 MECHANICAL PROPERTIES OF MATERIALS

		Tension		Compression	
Material	E, 10^6 psi	σ_{e1}, psi	ϵ_1	σ_{e1}, psi	ϵ_1
Rail steel:					
Test member no. 1	30.9	38600	0.082		
Test member no. 2	30.9	37000	0.077		
Test member no. 3	30.9	36000	0.077		
24S-T4	10.9	49600	0.035	40800	0.123
75S-T6	10.9	72000	0.024	70800	0.100

Discussion of Results

For each of the nine eccentrically loaded tension members, the strain distributions across the depth of the member and the deflections were obtained at increasing loads. The strains were measured at the locations shown in Fig. 1. In the case of the six aluminum specimens, the strains in the most stressed tension fibers for elastic conditions were measured by the SR-4 gages. Thereafter these strains were obtained by extrapolation using the strains as determined by the 2-in. extensometer.

The load P on each member was weighed by the testing machine. The moment M corresponding to P was calculated from the load P, the initial eccentricity e_o, and the measured deflection. Each load P and moment M was reduced to dimensionless form by dividing by the respective quantities $P_s = \sigma_{e1} A$ and $M_s = \sigma_{e1} I/c$ where σ_{e1} is the yield stress in tension as listed in Table 2. Corresponding values of the dimensionless ratios of load and moment are plotted for each of the test specimens in Figs. 10, 11, and 12 for the annealed rail steel, aluminum alloy 24S-T, and aluminum alloy 75S-T, respectively. In each of these figures are shown interaction curves for the loads P and M which, when acting together, will cause inelastic strains of fibers to zero depth, one-quarter depth, and one-half depth, respectively, across the section of the member. For each of the test members a test point was determined for each of the interaction curves and each is shown as a circle with a dot in the center. The test points indicate that the largest error in the calculation of either the moment or load was less than 5 per cent. Also the results show that the load corresponding to one-half depth of yielding is more than 50 per cent greater than the elastic limit load.

Approximate Methods of Determining the Deflection Δ in Equation [2]. In the following paragraphs three approximations of the moment-load curves will be presented for obtaining conservative values of the load necessary to produce a given depth of

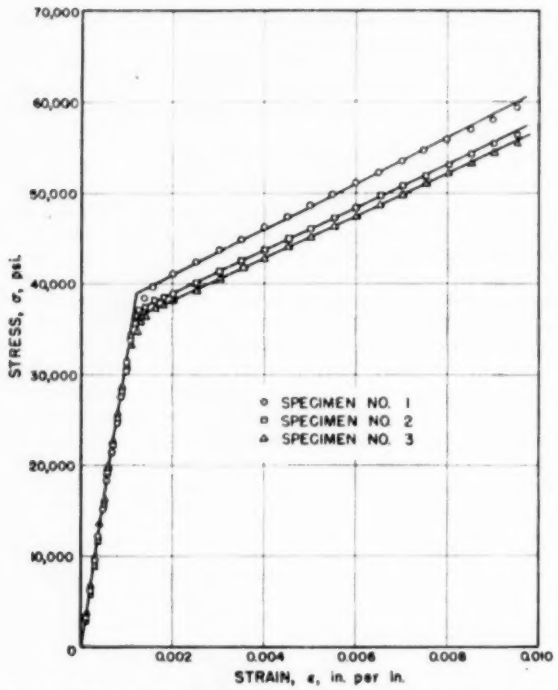

FIG. 8 TENSION STRESS-STRAIN DIAGRAMS OF ANNEALED RAIL STEEL

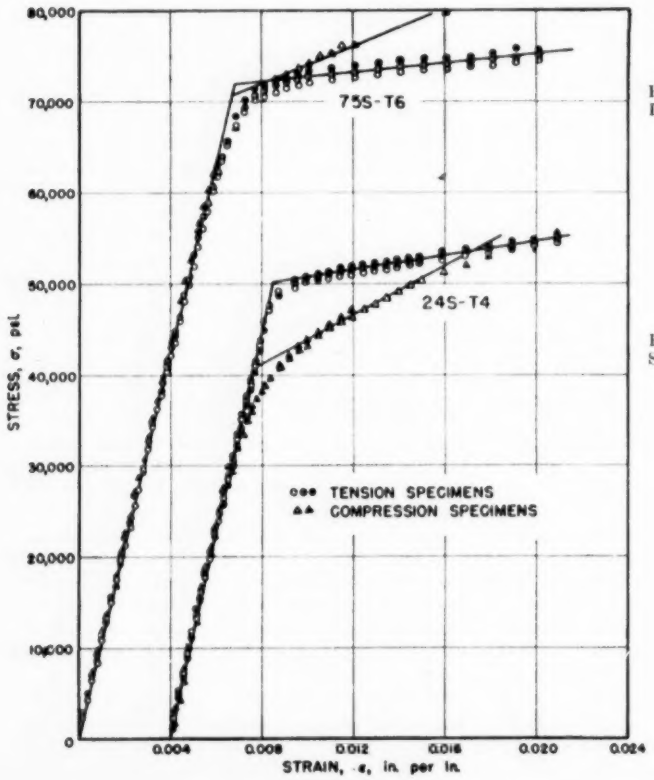

FIG. 9 (*left*) COMPOSITE TENSION AND COMPRESSION STRESS-STRAIN DIAGRAMS OF ALUMINUM ALLOYS 24S-T4 AND 75S-T6

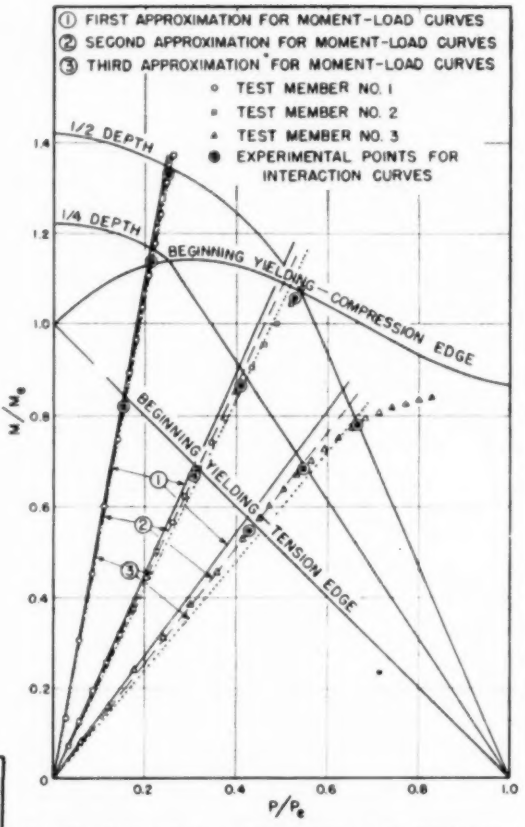

FIG. 10 COMPARISON OF EXPERIMENTAL AND THEORETICAL INTERACTION AND MOMENT-LOAD CURVES FOR RAIL-STEEL TEST MEMBERS OF RECTANGULAR CROSS SECTION

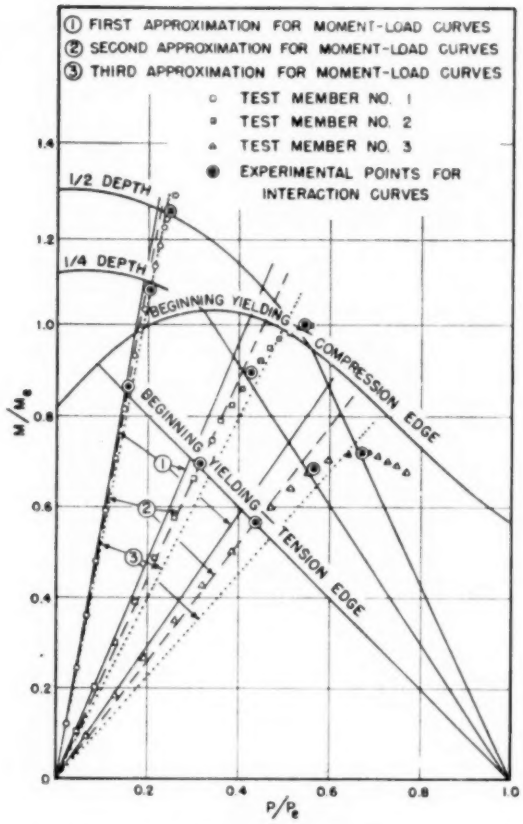

FIG. 11 COMPARISON OF EXPERIMENTAL AND THEORETICAL INTERACTION AND MOMENT-LOAD CURVES FOR ALUMINUM ALLOY 24S-T4 TEST MEMBERS OF RECTANGULAR CROSS SECTION

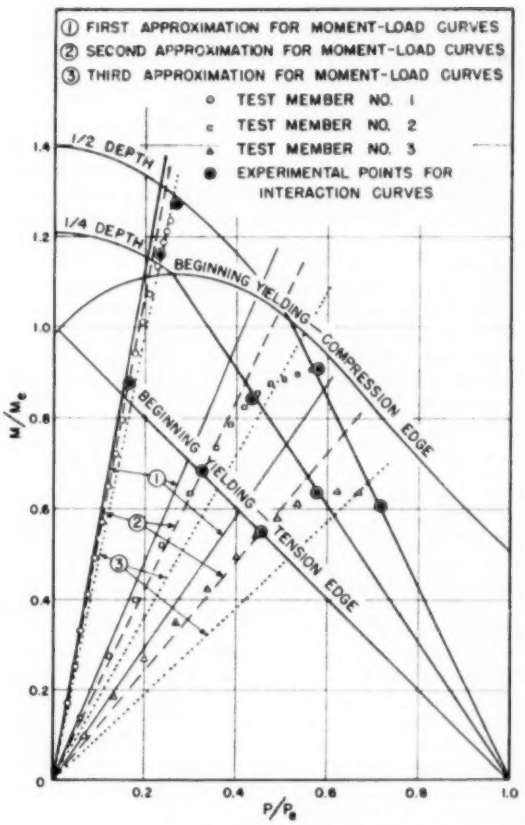

FIG. 12 COMPARISON OF EXPERIMENTAL AND THEORETICAL INTERACTION AND MOMENT-LOAD CURVES FOR ALUMINUM ALLOY 75S-T6 TEST MEMBERS OF RECTANGULAR CROSS SECTION

inelastic strain. In each case the actual deflection is larger than that computed, but the use of an interaction curve such as ABC in Fig. 3 along with Equation [2], in which either of the values of Δ is substituted, will give a conservative value of P; that is, the value of P will be less than that which will be required to cause the actual assumed conditions in the member. This fact will be discussed under the next sideheading.

For the first approximation of the moment-load curve, Equation [2], assume that the member does not deflect so that the relation between load and moment can be calculated from the initial eccentricity. The radial solid lines shown in Figs. 10, 11, and 12 represent the first approximation to the moment-load curves.

For the second approximation of the moment-load curve, we calculate the maximum elastic deflection Δ_e corresponding to a stress of σ_{e1} in the extreme fiber in tension. The relation between load and moment based on the eccentricity corrected for elastic deflection is shown as dashed lines in Figs. 10, 11, and 12.

A third approximation of the moment-load curves is easily obtained for any given depth of yielding. For the special case of pure bending of a beam whose cross section has two planes of symmetry and made of a material with identical stress-strain diagrams in tension and compression, the deflection Δ of the beam is obtained in terms of the maximum elastic deflection Δ_e. From geometrical considerations it easily can be shown that for these conditions

$$\frac{\Delta}{\Delta_e} = \frac{1}{1 - \psi} \qquad [7]$$

where Δ_e is the maximum elastic deflection corresponding to an extreme tensile fiber stress of σ_{e1}, and ψ is the depth of yielding. For $^1/_4$ or $^1/_2$ depth of yielding Equation [7] gives deflection of $^1/_3\ \Delta_e$ and $2\Delta_e$, respectively.

The computation by the more exact method of the deflection after inelastic strains have occurred requires an enormous amount of work. The third approximation of the moment-load curves is also based on a deflection which is smaller than the actual deflection. This fact is explained as follows: It is assumed that the deflection of the member is proportional to the algebraic difference of the strains in the most strained tension and compression fibers of the member. Consider as a special case an eccentrically loaded member in which the strain in the most strained compression fibers does not change as inelastic deformation occurs; the deflection of this member is given by Equation [7]. This special case does not occur except perhaps for small eccentricities accompanied by large depth of yielding, and hence the strain on the compression side increases as yielding takes place so that the algebraic difference in strain is larger than that necessary for Equation [7] to be valid. Hence, in general, the actual deflection will be larger than that given by Equation [7]. The dotted lines in Figs. 10, 11, and 12 were obtained by using Equation [7] in which ψ was made equal to $^1/_2$.

Error Due to Use of Approximate Δ. The load P obtained by using these lines which represent the first, second, and third approximation are all smaller than the actual value of P and the value of M is larger than its actual value as shown by the larger circle with black dot in Figs. 10, 11, and 12.

It is sometimes desirable to use in Equation [2] an approximate value of Δ which is slightly larger than the actual value. This procedure would lead to the computation of values of P and M that are, respectively, slightly larger and slightly smaller than the values that will cause the actual inelastic strained condition of the member that is assumed. The following method is used for determining such a value of Δ:

From calculations for the maximum elastic load, the neutral axis and the strains ϵ_{1e} and $-\epsilon_{2e}$ for most strained tension and compression fibers can be determined. Assuming that the neutral axis does not change, the strains ϵ_1 and $-\epsilon_2$ can be determined for the most strained fibers for a given depth of yielding. The deflection computed by the expression

$$\Delta = \frac{\epsilon_1 - (-\epsilon_2)}{\epsilon_{1e} - (-\epsilon_{2e})} \Delta_e \quad \ldots\ldots\ldots\ldots\ldots\ldots [8]$$

will be larger than the actual deflection since the neutral axis shifts toward the compression side of the member thus reducing both ϵ_1 and ϵ_2 for a given depth of yielding.

Axial Compression and Bending Loads. The results of the investigation reported here do not usually apply to a member subjected to combined bending and axial loads if the axial load is a compressive load. When the axial load is a tensile load its effect is to reduce the deflection due to bending and it thereby tends to reduce the maximum bending moment. This is shown by the fact that in Figs. 10, 11, and 12, where the axial load is a tensile load, the test data representing values of maximum bending moment M versus the axial load P lie in curves which are concave downward and to the right. On the other hand, when the axial load is a compressive load its effect is to increase the deflection due to bending and it thereby tends to increase the maximum bending moment. This is shown in Fig. 13, where some assumed moment-load curves *OBD* and *OFG* resulting from compressive axial loads are shown (no tests were made using compressive axial loads; this important problem requires further research).

In Fig. 13 curve *OAC* represents an actual test of a member of 75S-T6 under combined bending and axial tensile loads, and this curve shows that the tensile axial load reduces the deflection so much that the bending moment reaches a maximum as shown at *A*. On the other hand, the hypothetical[5] curve *OBD* for the same member subjected to combined bending and axial compressive loads is concave upward and to the left, showing that the compressive axial load tends to increase the bending moment. Curve *OBD* shows, by the vertical tangent at *B*, that when the axial load is compressive, the axial load reaches a maximum value instead of the bending moment. This fact means that when the axial compressive load represented by the abscissa of the point *B* is applied to this member it becomes unstable and will collapse by buckling, because points on the curve above *B* show that when the load at *B* is reached, smaller axial compressive loads than at *B* are capable of producing greater bending moments.

It should be noted that the curve *OBD* does not intersect the curve representing pairs of values of M and P that correspond to $^1/_2$ depth of the section being inelastically strained, and hence the results of the analysis in this report do not apply to such members. However, if the member is subjected to a compressive axial load having only a small eccentricity the moment-load curve may be represented by a curve such as *OFG* which does intersect the curve representing $^1/_2$ depth of inelastic strain before the buckling load at *F* is reached. It is of interest here to note that the points *B* and *F* will always be above the line representing the beginning of yielding. This means that the primary buckling (collapse) load for a member subjected to combined bending and axial compressive loads corresponds to a combination of bending moment and axial loads that will produce some inelastic strain in the most highly stressed cross section.

[5] These curves can be constructed for the materials tested in this investigation by a method devised by W. D. Jordan, University of Illinois, Urbana, Ill. Mr. Jordan's method has not been published as yet.

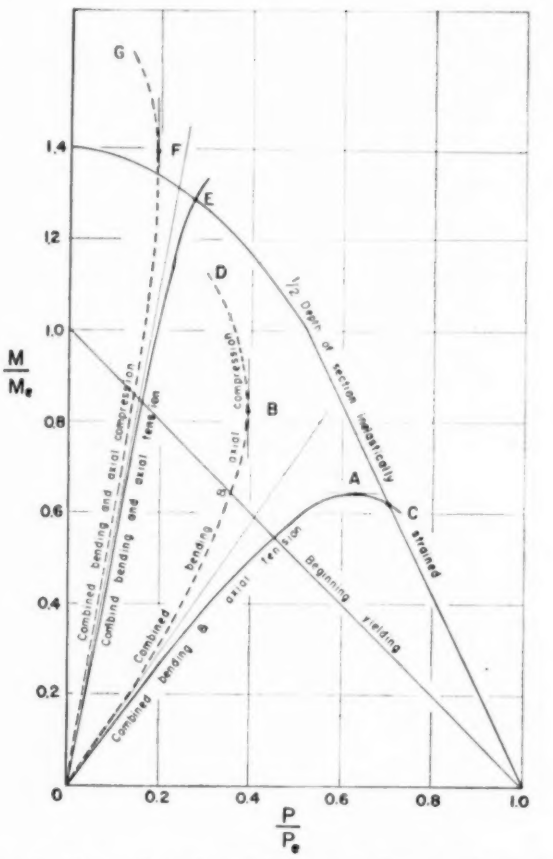

FIG. 13 MOMENT-LOAD CURVES CONTRASTING EFFECT OF TENSILE AXIAL LOADS WITH COMPRESSIVE AXIAL LOADS ON FAILURE OF MEMBER

Additional research is needed for solving the problem of combined bending and axial compressive loads. It is believed that the method of attack used in this investigation can be used for this purpose.

SUMMARY AND CONCLUSIONS

A method is presented for constructing dimensionless interaction curves for members of any cross section having one axis of symmetry and subjected to eccentric axial loads in the plane of symmetry. The theoretical interaction curves for members of rectangular cross section were compared with experimental data for eccentrically loaded tension members of annealed rail steel and aluminum alloys 24S-T4 and 75S-T6. Three specimens of each material were tested to give three points on each interaction

curve. Four approximations to the deflection of a member are presented so that a satisfactory approximation of the loads for a given depth of yielding can be computed. The results presented in this paper are believed to be sufficient to justify the following conclusions:

1 The interaction curve is constructed for a given member subjected to a combination of axial load and bending moment by locating two or more points on the curve. Each point is located by computing the values of P and M for the stress distribution that is assumed to occur for the given depth of inelastic strain. Because of the ease of construction and use, the interaction curve was derived to give the range of corresponding values of moment and load which would produce a given depth of inelastic strain. The tension and compression stress-strain curves for the material are approximated by two straight lines, Figs. 8 and 9.

2 The results obtained from tests of eccentrically loaded rectangular tension members of annealed rail steel and aluminum alloys 24S-T4 and 75S-T6 gave good correlation between theoretical and experimental interaction curves.

3 In designing an eccentrically loaded tension member for a given depth of yielding, the lateral deflection in Equation [2] for the member must be known so that the relation between axial load and bending moment can be determined. Four approximations to the moment-load curve are presented. All approximations give values of P and M that are not greatly different from the values which correspond to the actual conditions assumed in the member.

4 The test results show that for beams of rectangular cross section subjected to combined axial tension and bending loads, more than 50 per cent increase in load at the threshold of the occurrence of inelastic strain in the most highly stressed fibers of the beam is required to cause inelastic strains in the most stressed cross section to occur to a depth of $^1/_2$ the cross section.

5 The results of this investigation are not generally applicable to such members as described in the foregoing conclusions when the axial load is a compressive force. This problem is one of unstable equilibrium because the axial load reaches a maximum and at this load the member will collapse due to inelastic buckling. It is concluded that further research, in which moment-load curves such as *OBD* and *OFG* in Fig. 13 must be used, will be required to solve this problem. The method of analysis developed in this report will be of great value in analyzing the behavior of a member subjected to combined bending and axial compressive load.

Acknowledgments

This investigation was carried out as part of the work of the Engineering Experiment Station of the University of Illinois, of which Dean W. L. Everitt is the Director, in the department of theoretical and applied mechanics, of which Prof. F. B. Seely is the Head. It was part of an investigation sponsored by the Air Development Center, Wright-Patterson Air Force Base, Dayton, Ohio. Special acknowledgment is made to Prof. J. O. Smith, under whose general supervision the investigation was conducted. Acknowledgment is also made to Mr. Che-Tyan Chang for his help in the theoretical analysis.

Discussion

J. M. English.[6] The authors have presented an interesting paper on the interaction curve for bending and direct stress excluding stability. A valuable contribution lies in the approach they took. Ultimately it may lead to a better understanding of the column-interaction curve which does involve stability.

When stability is not a factor, the criterion for failure must be defined by stress. The authors do this by limiting arbitrarily the extent of the inelastic behavior of the cross section of the beam to one half the depth. With this criterion it is then possible to obtain a relationship between P and M which can be plotted as an interaction curve. The interaction curve may be plotted nondimensionally by dividing by chosen reference values of P and M. Because the development of the curve was started from the well-known elastic relation

$$\sigma = P/A + Mc/I$$

it was quite natural to choose P_e and M_e as the reference values. However, a more useful representation of the interaction curve may be obtained by choosing the ultimate moment M_u. The ultimate value of moment, defined by an arbitrary proportion of the section exceeding the elastic limits, will be in excess of the elastic limit value M_e. Consequently, as is shown in the plotted curves, the intercept on the moment axis exceeds unity when M_e is the reference.

If the ultimate value M_u is chosen as the reference moment value, the usefulness of the interaction curve is enhanced. Some interesting relationships become immediately apparent. The ultimate value of the moment for pure bending may be defined either, as before, in terms of a percentage of the section depth behaving inelastically or alternatively as an experimental ultimate. Essentially it makes little difference to the resulting interaction curve.

Consider the case of idealized plasticity, $\alpha = 0.0$, and a fully plastic section. The M_u will be 1.5 M_e. The curve, labeled "fully plastic" in Fig. 2 of the paper, will then be scaled down by this factor to fit the framework of a one-one diagram. Its equation can be shown to be

$$\frac{M}{M_u} + \left(\frac{P}{P_e}\right)^2 = 1 \qquad [9]$$

If the curves of "partial depth yielded" are plotted on the same diagram as Equation [9], the upper portion of the interaction curve in each case is also a parabola and thus is coincident with that of the fully plastic curve.

This fact may readily be seen with reference to Fig. 14 of this discussion, which represents the stress distribution in the cross section for some value of P and M. The only way for P to increase and still satisfy the original postulate, is for the sloping line

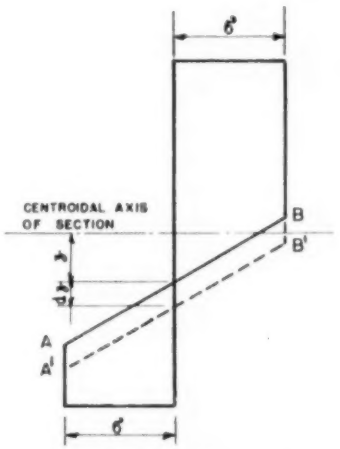

Fig. 14 Stress Distribution Across Section

[6] Department of Engineering, University of California, Los Angeles, Calif.

A-B to shift to A'-B'. Hence the increase in P is

$$dP = 2\sigma dz$$

Likewise, the change in moment will be

$$dM = -2\sigma z dz$$

Integrating each of these expressions and eliminating z, a parabola

$$^1/_4 P^2 + M = c$$

is obtained.

The only effect of the arbitrary limitation of the depth of plasticity is to change the slope of the straight portion of the interaction curve. This also establishes the intersection of the straight line and the parabola. The resulting interaction curve is shown

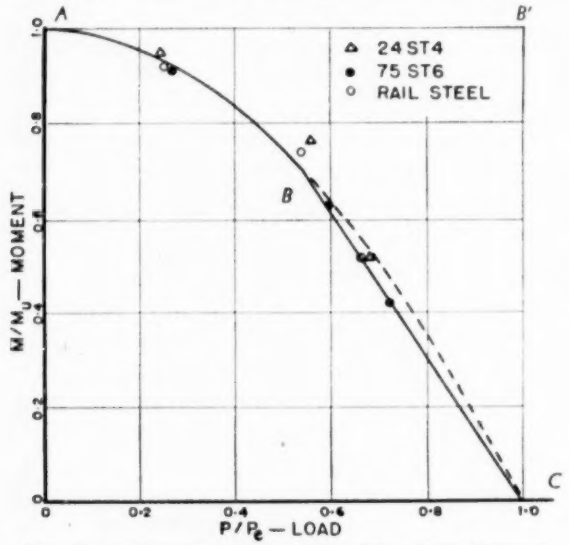

FIG. 15 INTERACTION CURVE—RECTANGULAR CROSS SECTION

in Fig. 15, herewith, for the case of $^1/_2$ the depth yielded. The difference between this and the one having a fully plastic stress in the section is seen by comparison with the completed parabola shown dotted.

The authors kept the problem general by not basing their development on the idealized flat-top stress-strain relation. However, it is interesting to note the results of the tests as plotted [7] on the one-one interaction diagram in Fig. 15. Even for the case of annealed rail steel which did not exhibit a horizontal region in the stress-strain curve, the results lie remarkably close to the interaction curve with the parabolic upper portion and the straight-line lower portion. It may be that this simplified interaction relation will provide a suitable general expression for engineering applications.

[7] The data for replotting the authors' test results were taken directly from the preprint of the paper. There may have been a loss of accuracy in the transcribing.

AUTHORS' CLOSURE

The authors are grateful to Mr. J. M. English for his interesting discussion. His method of representing an interaction curve for a member made of a material with $\alpha = 0.0$ is a simpler relation than that given by the authors, and the one-to-one plot, Fig. 15 of his discussion, is perhaps more appealing to the engineer. Interaction curves for rectangular members made of materials with $\alpha \neq 0.0$ also may be plotted on the same diagram. Curve A-B-C is the interaction curve for $^1/_2$ depth of yielding of a member made of a material with $\alpha = 0.0$. If $\alpha = 1.0$, the corresponding interaction curve is A-B'-C. Interaction curves for rectangular members made of materials having other values of α would lie in the area bounded by A-B'-C-B-A. As indicated in Fig. 3 of the paper, the co-ordinates of point B, the end of the straight line B-C, is very important. In Fig. 3 the co-ordinates of B for a given α were obtained by linear interpolation between points B and B'. Although the abscissa of point B'' for $\alpha \neq 0$ may be obtained by linear interpolation between the abscissa of point B and the abscissa of point B', the ordinate must be obtained from the relation

$$B'' = \frac{BM_u + (B'M'_u - BM_u)\,\alpha}{M_u + (M'_u - M_u)\,\alpha}$$

where B'' is the ordinate of the point for the required α and M_u and M'_u are the ultimate values of the moments for $\alpha = 0.0$ and $\alpha = 1.0$, respectively. The ultimate value of the moment is the magnitude of the pure moment which will produce the given depth of yielding.

The representation of the interaction curves as given by Mr. English has two disadvantages. In the first place the values of M_u would have to be given for each set of curves. These values could be given in equation, tabular, or graphical form. Also, the curve as represented in Fig. 15 of the discussion, conceals the relative increase in load which may be required to produce a given depth of yielding.

There is one point on which the authors wish to differ with the discusser. The criterion for failure was not defined by stress. If α is equal to zero, there is no way in which the magnitude of stress can be associated with depth of yielding, since each depth of yielding results in the same value for the maximum stress.

Distribution of Mechanical and Thermal Stresses in Multilayer Cylinders

By R. A. STRUB,[1] CHARLESTON, WEST VA.

Relations for the optimum proportions of multilayer vessels and the computation of stresses are derived. They are based on the energy of distortion-strength theory which is discussed and illustrated by a photographed model. It is shown that the stress distribution in fully or partially plastic cylinders can be obtained as the limit case of a multilayer vessel with an infinite number of layers of constant or variable yield point. Relations are proposed for the determination of the plastic strains. The problem of thermal stresses is discussed and a graphical method for the rapid computation of transient thermal stresses is explained.

Nomenclature

The following nomenclature is used in the paper:

p = pressure (to be introduced with negative sign!)
p_i = transition radial stress at r_i (if negative = compressive)
$\sigma_1, \sigma_2, \sigma_3$ = principal stresses
$\sigma_r, \sigma_t, \sigma_a$ = radial, tangential, and axial stresses
$\sigma_x, \sigma_y, \sigma_z$ = general normal stresses
$\tau_{xy}, \tau_{yz}, \tau_{zx}$ = shearing stresses
σ_0 = effective stress (yield strength for yielding)
r = radius (Fig. 3)
r_i = transition radius between plastic and elastic zones
$\rho = \frac{r}{r_{k-1}}$ or $1 < \rho < \frac{r_k}{r_i}$ in plastic zone
R = radius ratio
$R_e = \frac{r_a}{r_i}$
$R_p = \frac{r_i}{r_i}$
ϵ = strain
E = modulus of elasticity
ν = Poisson's ratio
T = variation of ambient temperature
T_1 = sudden or total variation of ambient temperature
θ = increase of body temperature
τ = dimensionless time $= t \frac{a}{r_a^2}$
t = time
a = diffusivity $= \frac{\lambda}{\gamma c}$
λ = thermal conductivity
β = coefficient of thermal expansion
c = specific heat
γ = specific weight
α = heat-exchange coefficient from surrounding to body
$h = \frac{\alpha}{\lambda}$
$\sigma_i^* =$ dimensionless stress $= \frac{(1-\nu)\sigma_i}{\beta E T_1}$
$\sum_{k=1}^{k=n} a_k = a_1 + a_2 + \ldots + a_k + \ldots + a_n$
$\prod_{k=1}^{k=n} a_k = a_1 a_2 \ldots a_k \ldots a_n$

Introduction

The tendency in the chemical industry to operate processes under higher and higher pressures has forced the designer to devote more attention to the design of pressure vessels and to diminish the factor of safety (ignorance factor). The stress distribution caused by pressure in the wall of high-pressure vessels is very uneven, and the optimum utilization of the material is far from being reached. Different modifications have been proposed in the past to overcome this difficulty. It is possible to obtain a better distribution of stress by introducing an adequate field of residual stresses. This can be accomplished by autofrettage producing partial or total yielding of the wall of the vessel.

Alternatively, a field of initial stress can be introduced by shrinking several cylinders or layers one upon the other. If the number of layers is large and their thickness relatively small, the vessel can be built by wrapping a sheet or strip of steel round a cylindrical core. Well-known examples of this type are the A. O. Smith vessels and the German design utilizing interlocked narrow steel strips (1).[2] This last type of vessel has the advantage of allowing the use of steel bands which can be evenly heat-treated to maximum strength and inspected for soundness.

The present paper will deal with the distribution of mechanical and thermal stresses in multilayer vessels. The theory will be extended to the autofretted vessel considered as a particular case of a multilayer vessel.

The stress field will be assumed to be symmetrical about the axis and constant along the length of the vessel.

Theory of Strength

The fracture of materials can be separated into two broad classes. The first one consists of materials presenting a brittle fracture. The second one covers ductile materials which break with considerable plastic deformation. Many theories of failure have been formulated in the past in an attempt to reduce different states of stress and strain to a unique comparative stress and strain (2).

In the present paper the material will be considered as ductile and the energy of distortion theory (Maxwell, Hencky) as ap-

[1] Senior Research Associate, Belle Technical Section, Polychemicals Department, E. I. du Pont de Nemours & Company, Inc.

Contributed by the Petroleum Division and presented at the Semi-Annual Meeting, Cincinnati, Ohio, June 15-19, 1952, of The American Society of Mechanical Engineers.

Note: Statements and opinions advanced in papers are to be understood as individual expressions of their authors and not those of the Society. Manuscript received at ASME Headquarters, May 21, 1951. Paper No. 52—SA-5.

[2] Numbers in parentheses refer to the Bibliography at the end of the paper.

plicable.[3] The deformation of a small cube of material submitted to a given state of stress can be reduced to two components of strain.[4] The first one corresponds to a change in volume due to an equivalent hydrostatic state of stress σ_h given by the relation

$$\sigma_h = \frac{\sigma_1 + \sigma_2 + \sigma_3}{3} \quad \ldots\ldots [1]$$

The second type of deformation is a distortion created by an equivalent effective stress σ_0, given by

$$\sigma_0 = \frac{1}{\sqrt{2}} \sqrt{(\sigma_1 - \sigma_2)^2 + (\sigma_2 - \sigma_3)^2 + (\sigma_3 - \sigma_1)^2} \quad [2]$$

A hydrostatic state of tensile stress should produce rupture when the cohesive strength is reached but this represents a stress many times higher than the true tensile stress in an uniaxial test. For this reason, the influence of the hydrostatic component on the strength is assumed to be negligible.

Relation [2] delineates a regular cylindrical surface equally inclined to the axes of co-ordinates, coinciding with the direction of the principal stresses. A model has been built by the author and is reproduced in Fig. 1. Any point P of co-ordinates σ_1, σ_2, σ_3 taken on the cylindrical stress surface (which has been sectioned to show the stress components) corresponds to a state of stress σ_1, σ_2, σ_3. The straight-line distance from this point P to the origin of the co-ordinates is the resultant stress σ_R. This resultant stress can be resolved into two components, one along the axis and one along the radius of the cylinder. It is easy to demonstrate that the first one is proportional to the hydrostatic stress σ_h and the second one to the effective stress σ_0, proportional to the octahedral shearing stress. Since the component σ_h is neglected, the model can be projected on a plane perpendicular to the cylinder axis. Therefore the component σ_h will reduce to a point and vanish and the radius of the cylinder $\sqrt{2/3}\ \sigma_0$ is projected in true length. The principal stresses σ_1, σ_2, σ_3 are reduced by projection in the ratio $\sqrt{2/3}$ and the three co-ordinate axes will appear as three axes at 120 deg apart. A series of concentric circles can be drawn on the plane of projection corresponding to different values of the effective stress σ_0.

If the state of stress is plane, the stress surface is replaced by the ellipse formed by the cross section of the cylindrical stress surface and the plane σ_3 = const, for example.

All computations of the effective stress σ_0 can be carried out in the plane of projection by the vectorial addition of the principal stresses directed along the three isometric axes. Where the principal stresses are not known directly, it also may be interesting to compute graphically the effective stress σ_0 derived from the general relation

$$\sigma_0 = \sqrt{\frac{1}{2}\left[(\sigma_x - \sigma_y)^2 + (\sigma_y - \sigma_z)^2 + (\sigma_z - \sigma_x)^2\right] + 3(\tau_{xy}^2 + \tau_{yz}^2 + \tau_{zx}^2)} \quad [3]$$

which can be written

$$\sigma_0 = \sqrt{S^2 + U^2}$$

Fig. 2 (*a* and *b*) shows that a graphical computation is still easy to achieve. S is directly found by the vectorial addition of vector stresses as indicated in Fig. 2(*a*). Then, U is found as shown in Fig. 2(*b*), and is added at 90 deg to the component S, Fig. 2(*a*). The use of the isometric representation is useful for a rapid discussion of stress problems.

[3] If one prefers to use the maximum shear-strength theory (Tresca), all the succeeding formulas are still valid provided $\sqrt{3}$ be replaced by the value 2.

[4] Reference (2), p. 210.

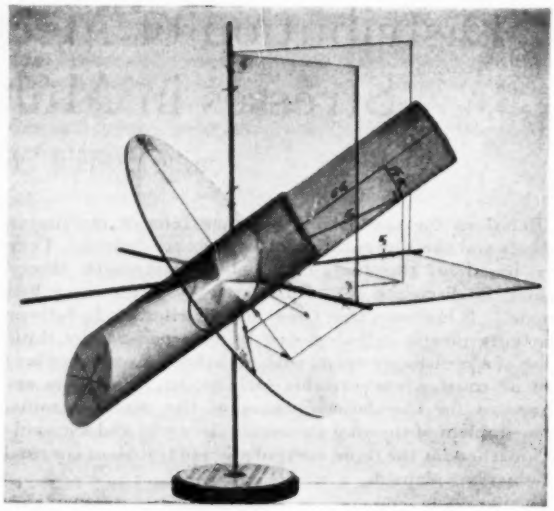

FIG. 1 SPACIAL REPRESENTATION OF THE ENERGY OF DISTORTION STRENGTH THEORY
(Maxwell; Hencky.)

In succeeding paragraphs dealing with vessels, the effective stress defined by Equation [2] will be introduced since the radial, tangential, and axial stresses are principal stresses.

OPTIMUM DESIGN OF MULTILAYER VESSELS

General Case —Effective Stress Varying From Layer to Layer in Any Specified Way. Let us consider Fig. 3, a vessel composed of several closed-end cylinders shrunk one upon the other.

The radius ratio of each layer k is given by

$$R_k = \frac{r_k}{r_{k-1}}, \quad R_{k+1} = \frac{r_{k+1}}{r_k}, \quad \ldots\ldots [4]$$

The stress distribution across the wall of any layer is given by the formulas[5]

for internal pressure

$$\sigma_t = p\,\frac{-1 - (R/\rho)^2}{R^2 - 1} \quad \ldots\ldots [5]$$

$$\sigma_r = p\,\frac{-1 + (R/\rho)^2}{R^2 - 1} \quad \ldots\ldots [6]$$

for external pressure

$$\sigma_t = p\,\frac{R^2 + (R/\rho)^2}{R^2 - 1} \quad \ldots\ldots [7]$$

$$\sigma_r = p\,\frac{R^2 - (R/\rho)^2}{R^2 - 1} \quad \ldots\ldots [8]$$

The axial stress is given by

$$\sigma_z = \frac{1}{2}(\sigma_t + \sigma_r) \quad \ldots\ldots [9]$$

[5] In these relations and the following ones, a pressure p is considered as a negative normal stress!

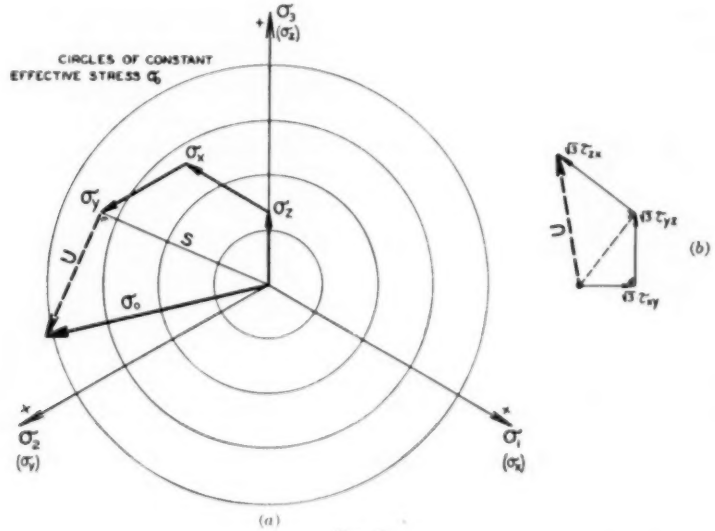

FIG. 2

For a layer k submitted to an internal contact pressure p_{k-1} and an external pressure p_k, the total stress is given by the addition of the stresses given by Equations [5] to [9]. Introducing the total stresses into Equation [2], the effective stress at any radius ratio ρ is

$$\sigma_{0k} = \sqrt{3}\,(p_k - p_{k-1})\,\frac{(R_k/\rho)^2}{R_k^2 - 1} \quad \ldots\ldots [10]$$

The maximum effective stress at the bore ($\rho = 1$) of any layer is

$$\sigma_{0k} = \sqrt{3}\,(p_k - p_{k-1})\,\frac{R_k^2}{R_k^2 - 1} \quad \ldots\ldots [11]$$

To obtain a given value of σ_{0k} in each successive layer, either the pressure difference or the ratio R_k can be selected. Therefore the further condition can be imposed that the volume of the materials composing the wall of the vessel must be a minimum.

Let us first consider two adjacent layers of radius ratios R_k and R_{k+1}. The over-all radius ratio for these two layers is

$$R_0 = R_k R_{k+1} \quad \ldots\ldots [12]$$

which must be a minimum.

Writing Equation [11] for the layer $k + 1$ and introducing R_k and R_{k+1} into Equation [12] we find after eliminating p_k and satisfying the condition $(dR_0)/(dR_{k+1}) = 0$

$$\frac{\sigma_{0k}}{R_k^2} = \frac{\sigma_{0k+1}}{R_{k+1}^2} = \text{const} \quad \ldots\ldots [13]$$

Equation [13] gives the relation between the effective maximum stress at the inner bore and the wall ratio for each layer.

A series of relations Equation [11] can be written for each of the n-layers of a vessel

$$\left.\begin{aligned}
\left(1 - \frac{1}{R_1^2}\right)\sigma_{01} &= \sqrt{3}\,(p_1 - p_i) \\
&\cdots\cdots\cdots\cdots \\
\left(1 - \frac{1}{R_k^2}\right)\sigma_{0k} &= \sqrt{3}\,(p_k - p_{k-1}) \\
&\cdots\cdots\cdots\cdots \\
\left(1 - \frac{1}{R_n^2}\right)\sigma_{0n} &= \sqrt{3}\,(p_a - p_{n-1})
\end{aligned}\right\} \quad \ldots\ldots [14]$$

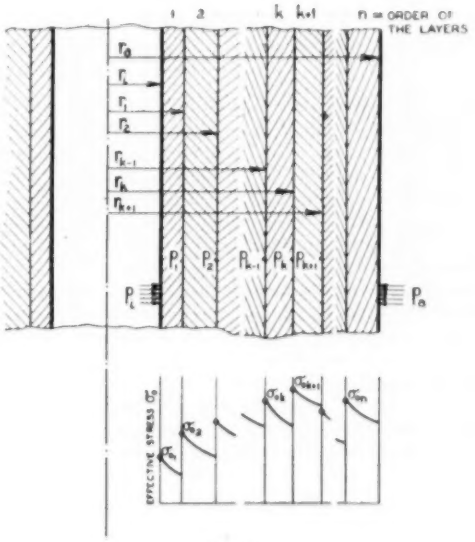

FIG. 3

The summation leads to

$$\sum_{k=1}^{k=n} \sigma_{0k} - \sum_{k=1}^{k=n} \frac{\sigma_{0k}}{R_k^2} = \sqrt{3}\,(p_a - p_i) \quad \ldots\ldots [15]$$

Considering the condition of minimum ratio, as defined in Equation [13]

$$\frac{\sigma_{01}}{R_1^2} = \frac{\sigma_{02}}{R_2^2} = \cdots\cdots = \frac{\sigma_{0k}}{R_k^2} = \cdots\cdots = \frac{\sigma_{0n}}{R_n^2} \quad \ldots\ldots [16]$$

we have

$$\sum_{k=1}^{k=n} \frac{\sigma_{0k}}{R_k^2} = n\,\frac{\sigma_{0k}}{R_k^2} \quad \ldots\ldots [17]$$

Further, considering the over-all ratio

$$R_0 = R_1 R_2 \ldots\ldots R_k \ldots\ldots R_n \quad [18]$$

we can write

$$R_0^2 = \prod_{k=1}^{k=n} \sigma_{0k} \left(\frac{R_k^2}{\sigma_{0k}}\right)^n \quad [19]$$

or

$$\frac{R_k^2}{\sigma_{0k}} = \frac{R_0^{2/n}}{\prod_{k=1}^{k=n} \sigma_{0k}^{1/n}} = \text{const} \quad [20]$$

Combining Equations [17] and [19] we find

$$R_0^{2/n} \sum_{k=1}^{k=n} \frac{\sigma_{0k}}{R_k^2} = n \prod_{k=1}^{k=n} \sigma_{0k}^{1/n} \quad [21]$$

which introduced into Equation [15] gives the following general relation

$$R_0 = \frac{\left(\frac{n}{\sqrt{3}}\right)^{n/2} \prod_{k=1}^{k=n} \sigma_{0k}^{1/2}}{\left[(p_i - p_a) + \frac{1}{\sqrt{3}} \sum_{k=1}^{k=n} \sigma_{0k}\right]^{n/2}} \quad [22]$$

This relation gives the optimum over-all radius ratio R_0 for any distribution of the effective stress σ_{0k} when the operating pressure difference $(p_i - p_a)$ is applied. Then, Relation [20] gives the radius ratios R_k for the different layers, and Relations [14] the contact pressure p_k. Each layer k can then be considered as a separate vessel submitted to an internal pressure p_{k-1} and an external pressure p_k. Formulas [5] to [9] give the corresponding stress distribution at any point.

Generally, σ_0 cannot be taken as constant for every layer. High-pressure vessels can be submitted to pulsating pressure inducing large alternating stresses at the bore, to corrosion, to hydrogen attack, and to thermal stresses. The layers can be made of materials having different strength.

Particular Cases. (*a*) *Constant effective stress σ_{0k} and a finite number of layers:* If, under the working pressure, each of the n-layers is submitted to the same effective stress σ_0, Relation [22] gives

$$R_0 = \left[\frac{\frac{n}{\sqrt{3}} \sigma_0}{(p_i - p_a) + \frac{n}{\sqrt{3}} \sigma_0}\right]^{n/2} \quad [23]$$

It follows that the difference of pressure that the vessel can carry is

$$\frac{p_i - p_a}{\sigma_0} = -\frac{n}{\sqrt{3}} \left(1 - \frac{1}{R_0^{2/n}}\right) \quad [24]$$

This relation is plotted in Fig. 4 for different values of n. Above the limiting curve $A - B$, the effective stress is larger without pressure than under load.

(*b*) *Constant effective stress σ_0 and infinite number of layers:* If the number of layers n, tends to infinity, the limit of Relation [24] is

$$\frac{p_i - p_a}{\sigma_0} = -\frac{2}{\sqrt{3}} \ln R_0 \quad [25]$$

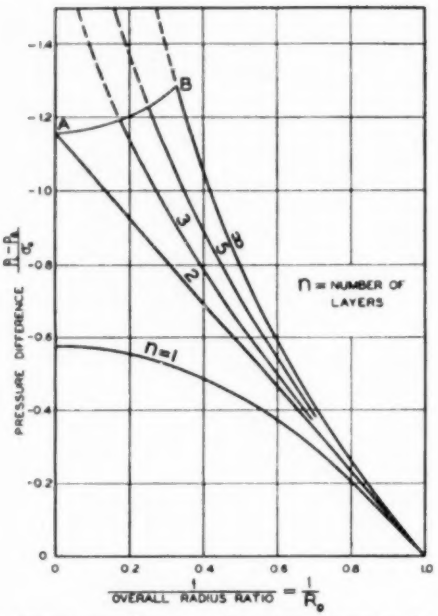

FIG. 4 MULTILAYER VESSEL OF CONSTANT MAXIMUM EFFECTIVE STRESS FOR EACH LAYER

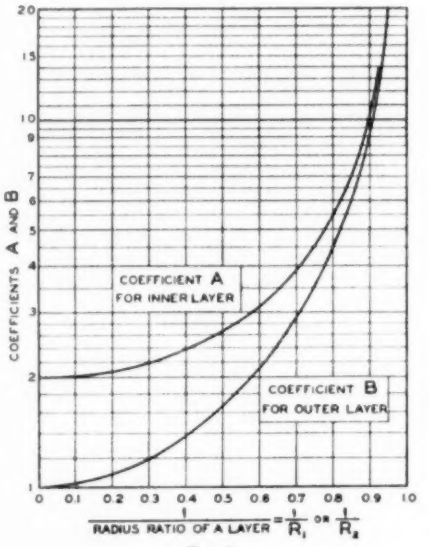

FIG. 5

which is identical with Nadai's relation for solid wall cylinders of constant yield strength σ_0 submitted to full yielding.[6] In case of work-hardening, a solution also can be obtained from Relations [14] to [22].

DETERMINATION OF SHRINKAGE INTERFERENCE

Let us consider a vessel composed of two sleeves of different materials of modulus of elasticity E_1 and E_2. Introducing Relations [5] to [8] into Hooke's law and stipulating that the initial

[6] Reference (2), p. 441.

radial shrinkage stress σ_s must produce a total radial deformation equal to the interference, the following relation is derived

$$\frac{\Delta r}{r} = \frac{1}{E_2}\left[-B - \frac{E_2}{E_1}(A-1) - \nu\left(1 - \frac{E_2}{E_1}\right)\right]\sigma_s \quad [26]$$

This relation introduces the close approximation that Poisson's coefficient ν is equal for both materials and assumes zero axial stress. The factors A and B are dimensionless coefficients plotted in Fig. 5.

If the axial stresses are different from zero, the interference must be corrected by the amount

$$\frac{\Delta r_c}{r} = -\frac{\nu\sigma_{z_1}}{E_1} + \frac{\nu\sigma_{z_2}}{E_2} \quad [27]$$

In Relation [26], the value of σ_s is the shrinkage stress between both sleeves after the pressure has been removed from the vessel and is calculated as follows: The total radial contact stress under operating pressure p_i and p_a is known from the theory outlined in the previous paragraphs, Relations [14]. The following relations derived from Hooke's law will give the reduction of the contact stress p_i when the internal and the external pressures are removed:

Internal pressure p_i removed

$$p' = \frac{\dfrac{E_2}{E_1}(A-2)p_i}{B + \dfrac{E_2}{E_1}(A-1) + \nu\left(1 - \dfrac{E_2}{E_1}\right)} \quad [28]$$

External pressure p_a removed

$$p'' = \frac{(B+1)p_a}{B + \dfrac{E_2}{E_1}(A-1) + \nu\left(1 - \dfrac{E_2}{E_1}\right)} \quad [29]$$

The value of σ_s is then given by

$$\sigma_s = p_i + p' + p'' \quad [30]$$

Relations [26] to [30] are still valid if each of the two sleeves is composed in turn of several layers of the same material shrunk one onto the other, since such a wall can be considered as a solid piece of the same material.

Autofrettage

Stress Distribution at Constant Yield Point. The field of stress is easy to find considering the equilibrium of an element of wall and Relation [25]. The relations obtained are identical with Nadai's formulas[7]

$$\sigma_r = p_i \pm \frac{2}{\sqrt{3}}\sigma_0 \ln \rho \quad [31]$$

$$\sigma_t = \sigma_r \pm \frac{2}{\sqrt{3}}\sigma_0 \quad [32]$$

$$\sigma_a = \frac{\sigma_t + \sigma_r}{2} \quad [33]$$

These relations and the following ones are valid for yielding, under internal p_i, external p_a, or differential pressure. The positive sign is considered if the values of $(\sigma_r - p_i)$ are greater than 1, and the negative sign is valid if they are smaller than 1.

The stress distribution in a cylinder under partial plastic deformation also can be calculated easily if both the position of the transition radius r_t separating the plastic and the elastic regions and the yield point σ_0 are first specified. The radial stress p_t at the transition radius is calculated from Relation [11] which gives

$$p_t = p_a \mp \frac{\sigma_0}{\sqrt{3}}\frac{R_a^2 - 1}{R_a^2} \quad [34]$$

Considering now the plastic zone, Relation [25] is used introducing for p_a the value p_t. The difference of pressure that the vessel can support is found immediately and is given by

$$\frac{p_a - p_i}{\sigma_0} = \pm\frac{R_a^2 - 1}{\sqrt{3}\,R_a^2} \pm \frac{2}{\sqrt{3}}\ln R_\rho \quad [35]$$

The stress distribution at any point can then be computed from Equations [5] to [9] and [31] to [33], considering each zone as a separate vessel submitted to the pressure difference $(p_i - p_t)$ and $(p_t - p_a)$. Residual autofrettage stresses are found by superimposing the elastic field of stress, Equations [5] to [9], as a result of removing pressure p_i and p_a.

Much has been published about the yielding of heavy-wall cylinders (3, 4, 5). The different theories introduce usually approximate relations based on the similarity of the Mohr's circles for stresses and strains. For closed-end cylinders, the stress distribution given by all the theories is in close agreement with the values obtained from the simple Nadai's formulas (2). The radial and tangential stresses are also in good agreement for open-end cylinders. The axial stress, however, is in error but is of small importance since it is acting in the direction of maximum strength of heavy forgings.

Strain Distribution at Constant Yield Point. The determination of the strain in the plastic zone is simple if we first calculate from Hooke's law the elastic strain at the transition radius. The plastified mass situated inside the elastic zone is then supposed to behave like a compressible fluid following the elastic radial and axial displacement imposed by the elastic shell.

The tangential strain at any radius r, corresponding to the radial expansion of the elastic zone, is given by

$$\epsilon' = -\frac{p_i}{E}\left(\frac{r_t}{r}\right)^2 \frac{(1+\nu)R_a^2 + (1-2\nu)}{R_a^2 - 1} \quad [36]$$

p_t being known from Equation [34].

The axial strain ϵ_z of the elastic shell increases the plastic strain by an amount

$$\epsilon'' = \frac{\epsilon_z}{2}\left[\left(\frac{r_t}{r}\right)^2 - 1\right] = \frac{1-2\nu}{2E}\left[\left(\frac{r_t}{r}\right)^2 - 1\right]\sigma_z \quad [37]$$

The elastic stress σ_z is known from Relation [9].

A further correction due to the compressibility of the plastified zone will tend to diminish the strain. It is given by

$$\epsilon''' = -\frac{3(1-2\nu)}{Er^2}\int_r^{r_t} \sigma_r r dr \quad [38]$$

in which the plastic stress σ_r is derived from Equation [33].

The total tangential strain is given by

$$\epsilon_t = \epsilon' + \epsilon'' + \epsilon''' \quad [39]$$

An example is treated and the results are plotted in Fig. 6.

Approximation for Work-Hardening. When a material exhibits work-hardening, it is proposed to introduce an average yield point, variable during the process of yielding and defined as shown in Fig. 7. First, the value of the maximum effective strain at the bore is estimated

$$\epsilon_0 = \frac{\sqrt{2}}{3}\sqrt{(\epsilon_t - \epsilon_r)^2 + (\epsilon_r - \epsilon_z)^2 + (\epsilon_z - \epsilon_t)^2} \quad [40]$$

[7] Reference (2), p. 440.

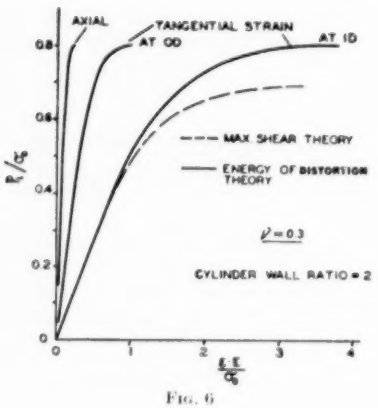

FIG. 6

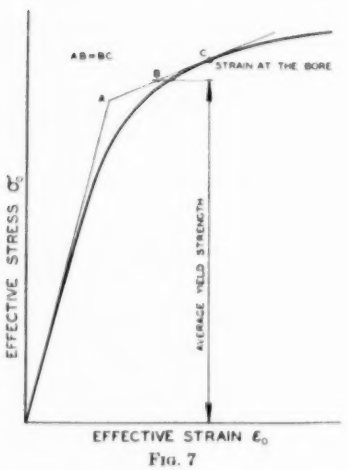

FIG. 7

Then the determination of stresses and strains follow the choice of the yield point which is corrected subsequently if necessary. This choice of average yield point has been found to be in close agreement with experiments.

THERMAL STRESSES IN CYLINDER WALLS

Steady Thermal Stresses. Thermal stresses induced in cylinder walls are of two types. The first type corresponds to a steady flow of heat and produces steady thermal stresses which are easy to calculate from published literature (6), which applies directly to multilayer vessels composed of the same material. If the modulus of elasticity, the coefficients of thermal expansion and of thermal conductivity are different for each layer, the computation is made in two steps.

For two layers of dissimilar materials, for example, the shrinkage interference varies with the change in temperature level. Another variation is introduced by the tangential strains at the shrinkage radius of each layer considered as free, due to the thermal stresses related to the temperature gradients. The foregoing stresses superimposed on those introduced by the total change in shrinkage stress calculated from Equation [26], give the steady thermal stresses.

Transitory Thermal Stresses. The second type of stress takes place during the transitory period preceding the permanent state. Since the relations governing a transient state of temperature in plates, cylinders, or spheres are linear (7), as well as the boundary conditions corresponding to the transfer of heat from the surroundings, the principle of superposition is applicable to the field of temperature.

This is also true for the field or thermal stresses since they are related to the field of temperature by linear equations (6).

A simple graphical method valid for plates, cylinders, or spheres for the determination of the field of temperature or thermal stresses at any instant of time during heating or cooling, will be described.

Let us first consider Fig. 8(*a*), the simple case of a linear variation of the ambient temperature with time. The continuous variation of temperature $T = f(\tau_0)$ can be replaced by infinitely small sudden changes of temperature, $\dot{f}(\tau_0)d\tau_0$, each one starting at time τ_0. The corresponding variation of temperature in the body for a unit sudden variation of the ambient temperature being known from published works (7, 8) is given here in a form suitable for cylinders

$$\theta = T_1\Theta(r/r_a;\ hr_a;\ \tau - \tau_0) \quad \ldots\ldots\ldots [41]$$

Θ is a dimensionless function giving the temperature at any radius r and time τ, having as origin the time value τ_0 at which the corresponding sudden increment of ambient temperature has started.

The total variation of temperature at any point in the body is given by the summation of the effect of each increment

$$\theta = \int_0^{\tau_1} \dot{f}(\tau_0)\Theta d\tau_0 \quad \ldots\ldots\ldots [42]$$

Graphical Solution. A simple graphical solution will be given for solving Equation [42]. Considering first a linear variation of T with time, Relation [42] reduces to

$$\theta = \text{const} \int_0^{\tau_1} \Theta d\tau_0 \quad \ldots\ldots\ldots [43]$$

Let us assume, Fig. 8(*a*), that the straight line $\dot{f}(\tau_0) = \text{const}$, is extended beyond the time τ_1. Each variation of temperature corresponding to an increment $\dot{f}(\tau_0)d\tau_0$ will produce a temperature

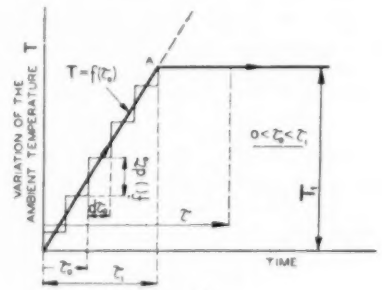

(*a*)

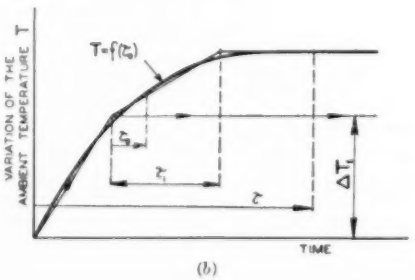

(*b*)

FIG. 8

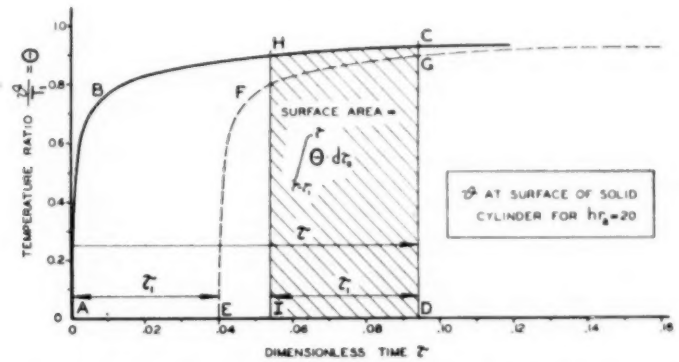

FIG. 9 SURFACE TEMPERATURE θ OF A SOLID CYLINDER AS A FUNCTION OF TIME FOR A SUDDEN CHANGE OF THE AMBIENT TEMPERATURE T_1

change at radius r represented by the ordinate at a point having as abscissa $(\tau - \tau_0)$ and situated on curve *A-B-C* representing the function Θ, Fig. 9. The integration is proportional to the surface *A-B-C-D*. However, if the temperature stops increasing beyond the point *A*, Fig. 8(*a*), we have to subtract the surface *E-F-G-D* corresponding to the time interval $(\tau - \tau_1)$. The value of the temperature θ at time τ is therefore proportional to the surface

$$ABCD - EFGD = ABCD - ABHI = IHCD$$

i.e., to the surface enclosed by the axis of time τ, the curve Θ, and the two verticals *I-H* and *C-D* separated by the lapse of time τ_1. The value of θ can be plotted as a function of time τ after multiplying the areas by the slope $f(\tau_0)$, according to Equation [43].

In case of a nonlinear variation of temperature T, Fig. 8(*b*), the curve is split up into a series of straight lines and the preceding method is applied for each straight-line portion of the polygonal approximation. It must be remembered that each preceding increase of temperature ΔT_1 remains constant when the next sloping line is considered.

The foregoing theory for temperatures applies equally well to thermal stresses.

Example. Fig. 10 is an example applied to the determination of the variation with time of the tangential thermal stresses at the surface of a solid cylinder and for different laws of variation of the ambient temperature. Each stress curve is derived by graphical method from the basic curve 1. It is interesting to note the relatively small diminution of the maximum stress for slower heating.

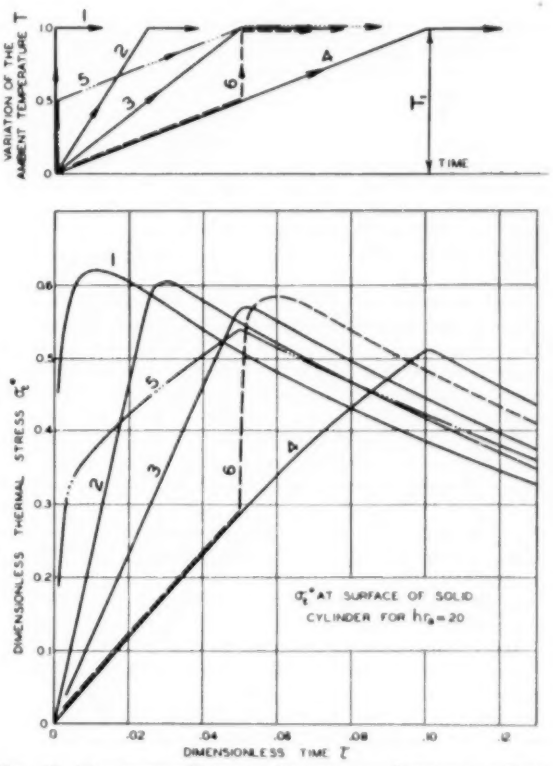

FIG. 10 TANGENTIAL THERMAL STRESSES AT SURFACE OF SOLID CYLINDER FOR DIFFERENT LAWS OF VARIATION OF AMBIENT TEMPERATURE T

BIBLIOGRAPHY

1 "Hochdruckbehälter für die Chemische Industrie," by E. Siebel and S. Schwaigerer, *Die Technik*, vol. 1, September, 1946, pp. 114–118.

2 "Theory of Flow and Fracture of Solids," by A. Nadai, McGraw-Hill Book Company, Inc., New York, N. Y., vol. 1, 1950.

3 "Partially Plastic Thick-Walled Tubes," by C. W. McGregor, L. F. Coffin, and J. C. Fisher, *Journal of The Franklin Institute*, vol. 245, February, 1948, pp. 135–158.

4 "The Theory of Combined Plastic and Elastic Deformation With Particular Reference to a Thick Tube Under Internal Pressure," by R. Hill, E. H. Lee, and S. J. Tupper, Proceedings of the Royal Society, London, vol. 191, November, 1947, pp. 278–303.

5 "A Quantitative Comparison of Flow and Deformation Theories of Plasticity," by P. G. Hodge, Jr., and G. N. White, Jr., *Journal of Applied Mechanics*, Trans. ASME, vol. 72, 1950, pp. 180–184.

6 "Theory of Elasticity," by S. Timoshenko, McGraw-Hill Book Company, Inc., New York, N. Y., 1934.

7 "Heat Transfer," by M. Jakob, John Wiley & Sons, Inc., New York, N. Y., 1949.

8 "Die Grundgesetze der Wärmeübertragung," by H. Gröber and S. Erk, Julius Springer, Berlin, Germany, 1933.

Discussion

T. MCLEAN JASPER.[9] This paper is highly theoretical and the writer's purpose is to supply certain facts which have been obtained in the testing of pressure vessels to destruction so that the author may fit them into his mathematical interpretation of what happens to pressure vessels under the testing conditions, if such a fitting can be made.

The Lamé formula for the maximum stress is the one which we

[9] A. O. Smith Corporation, Milwaukee, Wis. Mem. ASME.

have applied in pipe, relatively thin solid-wall vessels, and thick-layer vessels. We find that it discovers for us the yield and bursting strength when the cylinders are long, are made of steel, are not autofrettaged or precompressed, and are tested at ordinary temperatures. When steel cylinders of pressure vessels are about two diameters long, we find that the heads or ends retard the building up of the maximum stresses in the middle length of the cylinder so that the yield and burst pressure is about 13 or 14 per cent higher than the Lamé formula indicates. However, when the cylinder is about four or more diameters long we have discovered, if the longitudinal weld is as strong or stronger than the steel in the cylinder, that the yield and bursting stress is closely indicated by the normal strength tests such as the normal plate specifications require for and when the Lamé formula is applied.

We have discovered that large thick solid-wall vessels do not follow the foregoing statement. We have burst five such vessels which we had hoped would reach a hydraulic pressure of 20,000 psi before bursting. The highest bursting pressure for the five large solid wall vessels was slightly over 17,000 psi, or approximately 85 per cent of the anticipated value. The average bursting pressures of these five solid wall vessels were about 80 per cent of the anticipated value.

We also have burst five large thick-layer vessels, and the bursting pressures have all been above the minimum of the steel specifications used. Some of these burst vessels have been slightly precompressed so that in these cases the yield and ultimate strengths were slightly increased above the anticipated stress at yield and ultimate bursting pressure when compared with the physical tensile-test properties of the steel and when the Lamé formula was used. It should be mentioned here that the total amount of energy contained in the water and steel at the burst pressures for these vessels was well over 2,000,000 ft-lb in each case. The solid-wall vessels shattered into many fragments, but the layer vessels were always in one piece, thereby presenting a much less dangerous situation should failure occur in any service in which they were used.

We have made several hundred tests on relatively thin solid-wall cylinders about 40 ft long and varying in diameter from 14 to 30 in., on many of which we measured the yield and ultimate pressures and compared them with the actual tensile test properties of the steel. The short cylinders in this series of tests led us to testing nothing shorter than 4 diameters long, if we would wish to check with the material physical tests, and also through the Lamé formula anticipate the minimum bursting pressure of a long cylinder.

About 30 full-size pressure vessels varying in diameter up to 10 ft, and in length up to 50 ft, have been tested to destruction in which the yield and ultimate pressures have been recorded. With the exception of the 5 large thick solid-wall vessels mentioned, and the first 2 vessels tested without proper head shapes and reinforcement of openings, we have found that the Lamé formula will anticipate the yield and burst qualities of such vessels very closely. For these reasons we believe that the Lamé formula not only anticipates the yield strength of a nonprecompressed layer vessel, but it anticipates its bursting strength as well.

Since the author refers to layer vessels in particular, some particular data will be presented on two layer vessels which were made from identical plates. Each plate was cut in half and wrapped upon a 20-in-OD length of pipe $^1/_2$ in. thick. Upon each piece of pipe were wrapped twelve $^1/_4$-in. layers, making a cylinder with a nominal inside diameter of 19 in., and a nominal outside diameter of 26 in. The vessels were marked A and B.

The Lamé formula was applied to the actual dimensions of the cylinder as follows (the actual dimensions were slightly different from those given.)

$$S = P\,\frac{D_1^2 + D_2^2}{D_1^2 - D_2^2} = 3.219\,P$$

Vessel A was tested as wrapped and vessel B was stress-relieved at 1150 F, and held at temperature for $3^1/_2$ hr, and was then cooled slowly.

The test values are given in Tables 1 and 2.[9]

TABLE 1 AVERAGE PHYSICAL PROPERTIES OF STEEL IN VESSELS DURING TEST

Coupons from vessel	Yield strength, psi	Ultimate strength, psi	Elongation in 2 in., per cent	Remarks
A	39770	58845	29.5	(Not stress-relieved)
B	37670	56260	32.3	(Stress-relieved same as vessel B)

TABLE 2 STRESSES AT YIELD AND FAILURE OF VESSELS

	Yield by water column		Ultimate bursting point	
Vessel	Pressure, psi	Stress, psi	Pressure, psi	Stress, psi
A	13400	43100	18800	60400 (not stress-relieved)
B	11500	37000	17375	55900 (stress-relieved)

The calculation of stresses in Table 2 is obtained by multiplying the pressure by 3.219, which is a strict application of the Lamé formula to the original dimensions of the two cylinders. In considering vessel A that was not stress-relieved, it is evident that a slight precompression is obtained in both the yield pressure and ultimate bursting point. This was due to the wrapping method. When vessel B was stress-relieved, however, this small precompression was relaxed which indicated that the Lamé formula applies to layer-vessel stresses due to pressure not only at the yield but at the ultimate also. This had been suspected a considerable time before in the testing of solid-wall relatively thin vessels.

The reader should refer to the publications mentioned for a more complete application of precompression of layer vessels and a general discussion of the same.

In discussing the transitory and steady thermal stresses in vessels, the author has outlined the mathematical considerations quite completely. However, rarely are pressure vessels built in which the restraints necessary to develop large steady thermal stresses are present. At the operating temperature which is constant over the operating period there are not large thermal stresses present unless different steels are involved in the different layers in which the coefficients of expansion may be different. If, for instance, the inner layer is, say, 18-8 corrosion-resistant steel whose coefficient of expansion is, say, 50 per cent greater than that of the remaining carbon-steel layers then if the temperature changes are great there will be a considerable difference. If, however, the inner layer is of 15 per cent chrome steel in which the expansion factor is similar to that of plain-carbon steel, then the temperature stresses for steady operation are negligible. Transitory thermal stresses of large values are often inflicted by careless operation. In the building of welded solid-wall thick vessels the codes require careful handling during stress-relieving. Some operators ignore the implication of care taken in the building of pressure vessels when careless operations are allowed. No one may design to eliminate the danger. Even ice in a pipe will burst it when careless temperature changes are allowed.

The paper should be studied carefully with the possibility of determining where it may help in the proper application of operating conditions, particularly where solid construction is involved. It will be observed how carefully the writer has avoided discussing the mathematics of the author. He is familiar with the references listed. For pressure vessels, and particularly thick walls, we have the problem of the plus-plus-minus zone of the three-dimen-

[9] Test values are taken from a paper, "Multilayer Construction of Thick Pressure Vessels," Trans. AIChE, vol. 37, 1941, p. 889.

sional system. The compression value may be high and is certainly equal to the pressure on the inner surface of the cylinder. This value is slowly reduced in a solid-wall vessel by a diminishing shearing-stress system until at the outer surface it is zero.

The writer adheres to the maximum-energy theory in this discussion. In the plus-plus-minus zone representing this theory, a relatively large compressive stress reduces the pressure at breakdown of a pressure vessel very materially. This has been thought of as contributing to the test values obtained in the five solid heavy-wall vessels referred to early in this discussion.

Something should be said of the thick-layer vessels which also may be considered as being in the plus-plus-minus zone of the stress system. Why do they not act as the thick solid-wall vessels have acted? The writer does not know the complete answer, but it may be suggested that horizontal shear cannot be transmitted from one layer to the other, and therefore, each separate layer acts in a similar manner to that of a catenary of a suspension bridge made of many wires. Suffice to say that in five-layer vessels tested to destruction, each one has acted as if it were a two-dimensional problem within the plus-plus quadrant of the stress system. The facts, therefore, speak for themselves.

The problem which applies to the casing of deep wells with steel tubes is one which involves the plus-minus zone of the two-dimensional system. These structures are relatively thin and therefore the pressure values for failure are relatively small. This problem has been brought to solution by experiment. The results follow very closely the maximum-energy idea. In this case the collapse stress at failure is always within the elastic range of the steel.

We found in the layer-vessel tests, which are reported herein, and which are on cylinders about four diameters long, that if we applied a Poisson's ratio[10] of about 0.25, the Lamé formula also checked within a small value clear to the ultimate bursting pressure if the maximum-energy idea is used. The engineer's method for obtaining the values of yield and ultimate strength are used in these tests. Most theories for failure do not go to the ultimate strength of steel, but break off at the elastic or yield strengths. Very rarely in pressure vessels do we get failure at this point.

Since the author has referred to the distortion theory of Maxwell-Hencky as applicable and since no experimental data are appended, it is to be hoped that some could be forthcoming to help the problem of the layer-vessel solution, or to contribute to the solution of pressure-vessel designs in general.

A. G. Thailing.[11] Has the author ever encountered the following situation? This primarily concerns itself, not with the usual conception of thermal stresses but with stresses created by the inability of a cylinder wall to equalize its temperature due to excessive internal temperature, creating high-temperature differential wall temperatures. These conditions create very high compression stresses on the internal fibers and high tensile stresses on external fibers.

Is it possible, after the use mentioned, for the vessel upon cooling to diminish in diameter internally and externally? Calculations of stresses due to temperature differentials indicate stresses beyond the elastic limits on the inside fibers, and with the material in a semiplastic condition. There could be a diminishing of inside diameters. Field observations indicate a slight diminishing of outside diameters. Do any of the author's calculations substantiate this condition and has he made any tests or field observations to indicate this condition as possible?

[10] "Poisson's Ratio and a Suggestion for Its Use in Stress Analysis," Proceedings of the ASTM, vol. 24, 1924, p. 1012.

[11] Senior Research Engineer, Carbide and Carbon Chemicals Company, South Charleston, West Va. Mem. ASME.

Author's Closure

The theory presented in the paper does not necessarily apply when extensive yielding is involved, and the true stress pattern in the wall of a vessel approaching bursting is not sufficiently well known to allow a rigorous discussion of the subject. However, the author will offer some comments to the interesting and appreciated discussion of Dr. McLean Jasper.

As pointed out in the discussion, Lamé's formula appears to be able to predict, with sufficient accuracy, both the bursting and the initial yielding pressures of vessels of small wall ratios. The relations developed in the paper are based on the energy of distortion-strength theory. However, for vessels of relatively small wall ratios, it will be shown that comparable values to those based on Lamé's formula can be obtained if the relations presented in the paper are used for predicting the bursting pressure.

Lamé's formula for the bursting pressure as proposed in the discussion is

$$p = S \frac{R^2 - 1}{R^2 + 1} \quad \ldots\ldots [44]$$

in which R is the radius ratio of the vessel and S the ultimate strength of the material.

If we assume that Equation [31] of the paper is valid up to the bursting pressure, an average yield point situated between the yield strength and the ultimate strength must be introduced in order to take into account the effect of work-hardening. For simplicity the following formula is proposed

$$p = \frac{2}{\sqrt{3}} \cdot \frac{\sigma_0 + S}{2} \cdot \ln R \quad \ldots\ldots [45]$$

since it is known that neither the yield strength σ_0 nor the ultimate stress S alone will predict bursting with sufficient accuracy.

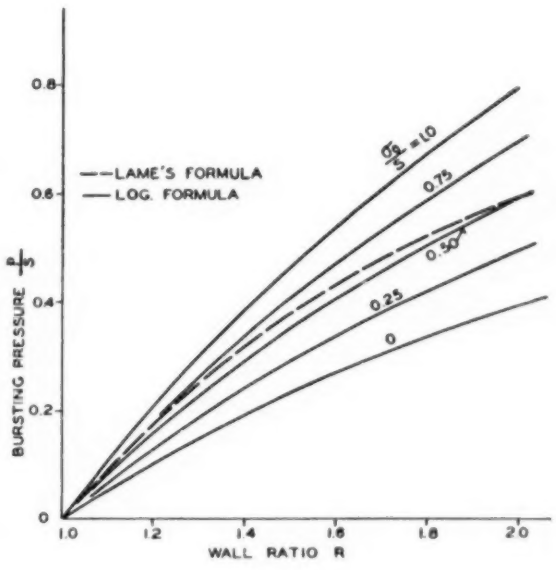

Fig. 11

Fig. 11 of this closure shows that for vessels of small wall ratios and made of steel having a ratio of the yield strength to the ultimate strength situated between 0.5 and 0.8, Relations [44] and [45] will give almost identical results.

From the data of tests carried out with solid-wall cylinders[12] it can be shown that whereas Equation [44] is not valid for wall ratios ranging from 2 to 3, Relation [45] can still be used for predicting the bursting pressure with sufficient accuracy. It is the belief of the author that the lower bursting pressure, observed by Dr. McLean Jasper, for thick solid-wall vessels might be attributed to the influence of the dimensional factor on the mode of yielding and to the yielding pattern which in a layer vessel, may be different from the one occurring in a solid-wall vessel.[13]

As shown in Table 3, herewith, Lamé's formula used for predicting initial yielding at the bore of a vessel of wall ratio larger than 1.17 gives corresponding internal pressures which are greater than those predicted by either the maximum-shear or the energy-of-distortion theories.

It is interesting to note that Dr. McLean Jasper's measurement of the pressure necessary to produce initial yielding at the bore of a layer vessel of wall ratio 1.37 is close to the value predicted by Lamé's formula. Results of tests on heavy solid-wall cylinders of wall ratios 2 to 3, however, reported in the references cited, agree with either the maximum-shear or the energy-of-distortion theories. This fact seems to indicate that a layer vessel starts yielding at a higher internal pressure than a solid-wall vessel. Before reaching a final conclusion on this point, further highly accurate tests on layer and solid-wall vessels are desirable since, owing to the complex mechanism of yielding, an accurate determination of the initial yield is difficult.

TABLE 3 COMPARISON OF FORMULAS FOR PREDICTING INITIAL YIELDING

	Vessel wall ratio				
	1.1	1.17	1.4	2	3
Lamé.....p/σ_s	0.095	0.156	0.325	0.600	0.800
Energy of distortion.p/σ_s	0.100	0.156	0.284	0.433	0.512
Maximum shear....p/σ_s	0.086	0.135	0.246	0.375	0.443

Dr. Thailing's question refers to a rather sharp temperature gradient across a heavy-wall cylinder. It is possible, under a great and rapid increase in temperature of the material adjacent to the bore, that yielding under compression occurs at the inner fibers, without appreciable plastic extension of the outer fibers. This yielding at the bore is made easier by the diminution of the yield strength with increasing temperature. During cooling of the vessel, a stress reversal will occur at the inner fibers which may then be at a sufficiently low temperature to resist complete reversal yielding. As a consequence, residual tensile stresses will appear at the bore together with a reduction in diameter. Therefore the external fibers will be submitted to a compressive stress introducing a corresponding reduction of the external diameter. The author has never observed such phenomenon.

[12] "Influence of Residual Stress on Behavior of Thick-Wall Closed-End Cylinders," by T. H. Faupel and A. R. Furbeck, contributed by the Industrial Instruments and Regulators Division and presented at the Seventh National Instrument Conference, Cleveland, Ohio, September 9-10, 1952, of THE AMERICAN SOCIETY OF MECHANICAL ENGINEERS.

[13] "An Experimental Investigation of Over-Straining in Mild-Steel Thick-Walled Cylinders by Internal Fluid Pressure," by M. C. Steele and John Young, Trans. ASME, vol. 74, 1952, pp. 355–363.

The Stresses in a Pressure Vessel With a Hemispherical Head[1]

By G. W. WATTS[2] and H. A. LANG,[3] CHICAGO, ILL.

This paper, the third of a series, presents the results of computations for determining the stresses in a pressure vessel with a hemispherical head. The bending theory of shells is used to evaluate the maximum stress at the junction between head and shell. Tables show the magnitudes of the shear stress, the axial stress, and the circumferential stress at the junction as multiples of $pd/2t$. The axial and circumferential stress have been computed for both surfaces. Additional results show the magnitude, sense, and location of the maximum stress (of each of the three types) in the shell. The largest value of the diameter-thickness ratio of the head for which computations were made is 40. When the diameter-thickness ratio of the head exceeds 40, well-known approximate theories can be used. The limit of 40 is imposed by the slow convergence of the hypergeometric series. Tables of influence numbers for both the head and shell are included for application to other problems. A brief discussion of the mathematical procedure is included.

Nomenclature

The following nomenclature is used in the paper:

p = internal pressure, lb per square inch
M_0 = bending moment per unit length of circumference exerted by head on cylinder (positive sense is shown in Fig. 1)
Q_0 = shear force per unit length of circumference exerted by head on cylinder (positive sense is shown in Fig. 1)
s = stress, psi
w_0 = radial displacement of cylinder at junction, positive inward
E = modulus of elasticity, psi
d = mean diameter of cylinder
t = thickness of cylinder
T = thickness of hemispherical head
μ = Poisson's ratio (= 0.3 for steel)
δ_0 = radial displacement of mid-plane of head at junction, positive outward
$\beta = \sqrt[4]{\dfrac{12(1-\mu^2)}{(dt)^2}}$
$\alpha_0 = \beta M_0/Q_0$
I = stress ratio or stress divided by $pd/2t$
a_4, a_5, a_6 / b_4, b_5, b_6 = influence numbers for cylinder
a_1, a_2, a_3 / b_1, b_2, b_3 = influence numbers for head
x_s = location of maximum shear-stress ratio in cylinder
x_a = location of maximum axial-stress ratio in cylinder
x_c = location of maximum circumferential-stress ratio in cylinder

Introduction

This is the third paper of a series which considers stresses in pressure vessels. It constitutes part of a continuing program initiated by the Design Division of the Pressure Vessel Research Committee of the Welding Research Council of the Engineering Foundation. This program, which consists of both analytical and experimental investigations, is intended to benefit engineers engaged in the design and manufacture of pressure vessels.

Two previous papers considered pressure vessels with flat and conical heads (1, 2).[4] Each paper contained tables and curves for determining the maximum stress in a pressure vessel under the specified end closure.

The elements of the theory (which are well known)[5] are not repeated here and the paper is limited to a description of the computational procedure together with a discussion of the results. The problem logically consists of two parts: (*a*) The shear force Q_0 and axial bending moment M_0 at the head-cylinder junction, Fig. 1, must be determined from the continuity of the radial displacement and rotation at the junction. (*b*) When these are known we may determine the shear, circumferential, and axial stresses at the junction in the cylinder and in the head. The maximum stresses in the cylinder other than at the junction also can be found. Each stress is divided by $pd/2t$, the circumferential stress in a thin unrestrained cylinder under uniform pressure, to form the stress ratio denoted by I. The values at the junction are distinguished from the cylinder maxima by subscripts

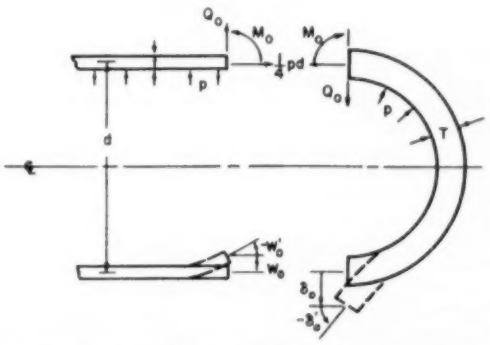

Fig. 1 Convention for Loads and Deformations

[1] This work is part of a continuing program instituted in 1946 by the Design Division of the Pressure Vessel Research Committee of the Welding Research Council of the Engineering Foundation, New York, N. Y.

[2] Director of Engineering, Standard Oil Company (Indiana). Fellow ASME.

[3] Formerly, Project Engineer, Engineering Research Department, Standard Oil Company (Indiana). Mem. ASME.

Contributed by the Petroleum Division and presented at the Semi-Annual Meeting, Cincinnati, Ohio, June 15–19, 1952, of The American Society of Mechanical Engineers.

Note: Statements and opinions advanced in papers are to be understood as individual expressions of their authors and not those of the Society. Manuscript received at ASME Headquarters, February 29, 1952. Paper No. 52—SA-19.

[4] Numbers in parentheses refer to the Bibliography at the end of the paper.

[5] The theory of shells is discussed in reference (3). A general mathematical treatment of pressure vessels will be found in reference (4).

j and m, respectively. The subscripts s, a, c, denote shear, axial, and circumferential, respectively. There are thus nine stress indexes, denoted by I_{sm}, I_{am}, I_{cm} and I_{sj}, I_{aj}, I_{cj}. It will be clear from the context whether the last three of these refer to the shell or the head. The stresses in the head other than at the junction have not been computed.

The stress ratio I has two distinct advantages. It expresses the results in smaller numbers and enables one to tell immediately whether a stress is greater or less than the hoop stress in a thin cylinder. It frequently is substantially linear when plotted against the diameter-thickness ratio d/t of the cylinder. By contrast, a curve of stress divided by pressure is more nearly parabolic.

Conclusions

The analysis of maximum stress in a cylindrical pressure vessel with a hemispherical cap leads to the following general conclusions:

1 The maximum circumferential stress in the cylinder (other than at the junction) is the greatest of the nine stresses computed.

2 This stress decreases slightly as the ratio d/T increases and increases slightly as the thickness ratio T/t increases. To three significant figures, the stress index has the value 1.03 for the range of calculations considered here. It is thus remarkably unaffected by changes in either of the geometric ratios d/T and T/t. Thus, for thickness ratios ranging from $T/t = 0.8$ to 2.0, the curve of stress divided by pressure plotted as a function of the ratio d/t is very nearly a single straight line as shown in Fig. 2.

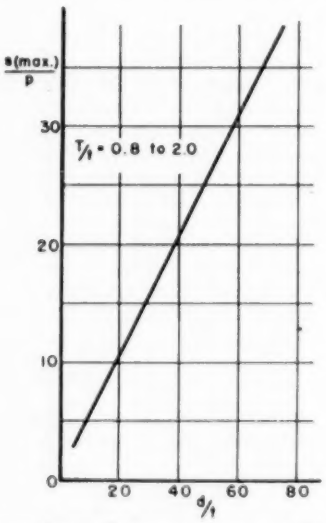

Fig. 2 Maximum Stress-Pressure Ratio as a Function of d/t

3 The location of the maximum stress approaches the junction as either ratio d/T or T/t increases.

4 The present results justify partially the procedure of Meissner,[6] who neglected the bending moment and rotation at the junction and determined the shear force by equating deflections. His result corresponds to a maximum circumferential stress of 1.032 $(pd/2t)$ at a location specified by $\beta x = 1.85$. The average of the twenty-five calculations of this report is $1.033(pd/2t)$. There is less agreement in the location of this stress since the presence of the bending moment affects the location considerably. In terms of the quantity βx, the location of the stress does not vary significantly with an increase of the ratio d/T but it does increase with an increase of the ratio T/t. Thus, if $T/t = 0.8$, the average of five calculations is $\beta x = 1.758$, while if $T/t = 2.0$, the average of five calculations is $\beta x = 2.2912$. The average of the twenty-five calculations is $\beta x = 2.00$.

5 Since the stress exceeds $pd/2t$ by only 3 per cent, present methods of design based on the API-ASME code (or the ASME code) for unfired pressure vessels with hemispherical heads appear adequate. This conclusion should be reinforced by additional computations to determine the maximum stresses in the hemispherical cap, particularly when it is thinner than the cylindrical vessel.

6 All remaining stresses are smaller than $pd/2t$. The second largest stress is the circumferential stress in the cylinder at the junction when T/t is less than 2.0. As T/t approaches 2.0, this stress is overtaken by the axial stress in the cylinder at the junction.

7 The influence numbers for a hemispherical cap are of approximately the same order of magnitude as the influence numbers for a conical head with an apex angle of 90 deg with the exception of b_3 which vanishes. This may be seen by comparing Table 6 of this paper with Table 6 (reference 2). The vanishing of b_3 is a consequence of the fact that a hemisphere under internal pressure does not rotate at its base (or at any other section). This fact, together with the absence of a discontinuity at the junction between the middle surfaces of the cap and cylinder, results in low values of stress.

8 The extension of the radius of a hemispherical cap under pressure is $(pd^2/8Et)(1 - \mu)$. The extension of the radius of a cylinder is $(pd^2/8Et)(2 - \mu)$. The two extensions can be made equal by selecting a thickness ratio $T/t = (1 - \mu)/(2 - \mu) = 7/17 = 0.4117$ for steel. For this thickness ratio the pressure will produce no discontinuity in deflection or rotation at the junction. Consequently there is no shear force or bending moment. The only forces existing are the membrane forces. The greatest stress occurs in the hemispherical cap and is everywhere equal to $(17/14)(pd/2t) = 1.2143(pd/2t)$. Thus, while it is possible to select a head thickness that does not introduce any shear force or bending moment, the uniform stress in the cap is greater than the maximum stress computed for any of the cases in this paper.

Analysis

The upper half of Fig. 1 shows the loads acting upon a long cylindrical pressure vessel and upon its hemispherical cap. The loading consists of the uniform pressure p which produces a radial expansion of the cylinder; a bending moment per unit length of circumference M_0, and a shear force per unit length of circumference Q_0. The bending moment and shear force arise at the junction between the cylinder and the spherical cap because of the unequal expansions the pressure produces in these two elastic structures. The pressure tends also to stretch the vessel, creating axial forces which are readily determined from the equation of axial equilibrium. The upper half of Fig. 1 also defines the positive sense of M_0 and Q_0.

From the theory of the cylindrical shell[7] the displacement w_0, and the rotation

$$-\left(\frac{dw}{dx}\right)_{x=0} = -w_0'$$

at the junction of the cylinder can each be expressed in the dimensionless form

$$\frac{ETw_0}{pd^2} = a_4 + a_5\frac{M_0}{pd^2} + a_6\frac{Q_0}{pd} \quad \ldots\ldots\ldots\ldots [1]$$

[6] Reference (3), p. 407.

[7] Reference (3), p. 393.

$$-\frac{ET^2w_0'}{\beta^2dtpd^2} = b_4 + b_5\frac{M_0}{pd^2} + b_6\frac{Q_0}{pd} \quad [2]$$

where

$$a_4 = -\frac{T}{t}\frac{2-\mu}{8}$$

$$a_5 = -\frac{1}{2}\frac{T}{t}(\beta d)^2$$

$$a_6 = -\frac{1}{2}\frac{T}{t}\beta d$$

$$b_4 = 0$$

$$b_5 = -\frac{T^2}{t^2}\beta d$$

$$b_6 = -\frac{1}{2}\frac{T^2}{t^2}$$

$$\beta d = \sqrt[4]{12(1-\mu^2)}\sqrt{d/t}$$

The quantities a_4, a_5, a_6, b_4, b_5, and b_6 are "influence numbers" which depend only on the ratios T/t and d/T which define the geometry of the pressure vessel. In the present calculations, $\mu = 0.3$, $T/t = 0.8$, 1.0, 1.2, 1.6, and 2.0, while $d/T = 4$, 10, 20, 30, 40. The computed values of influence numbers for the cylinder are listed in Tables 1 to 5.

The deflection and rotation at the junction in the spherical head can each be expressed in a form similar to that for the cylinder

$$\frac{ET\delta_0}{pd^2} = a_1\frac{M_0}{pd^2} + a_2\frac{Q_0}{pd} + a_3 \quad [3]$$

$$\frac{ET^2\delta_0'}{\beta^2dtpd^2} = b_1\frac{M_0}{pd^2} + b_2\frac{Q_0}{pd} + b_3 \quad [4]$$

where the influence numbers for the sphere are

$$a_1 = m_1b_2$$

$$a_2 = -\frac{m_2}{2}\left[\frac{\dot{J}_1^2+\dot{J}_2^2}{\mu[\dot{J}_2J_1-J_2\dot{J}_1]+m_2[J_1\dot{J}_1+J_2\dot{J}_2]}\right]$$

$$a_3 = 0.0875$$

$$b_1 = -\frac{m_1m_2}{2}\left[\frac{J_1^2+J_2^2}{\mu[\dot{J}_2J_1-J_2\dot{J}_1]+m_2[J_1\dot{J}_1+J_2\dot{J}_2]}\right]$$

$$b_2 = \frac{m_1}{4}\left[\frac{\dot{J}_2J_1-J_2\dot{J}_1}{\mu[\dot{J}_2J_1-J_2\dot{J}_1]+m_2[J_1\dot{J}_1+J_2\dot{J}_2]}\right]$$

$$b_3 = 0$$

$$m_1 = \sqrt{12(1-\mu^2)}\,\frac{d}{T}$$

$$m_2 = \sqrt{\frac{m_1^2}{4}-\mu^2}$$

The influence numbers for the sphere are listed in Table 6. The quantities J_1, J_2, and their derivatives ($\dot{J}_1$ and $\dot{J}_2$) occur in the theory of the spherical shell.[6] J_1 and J_2 are, respectively, the values at the junction of the real and imaginary parts of the hypergeometric function which results from this theory.

The quantities J_1 and J_2 converge less rapidly as d/T increases. For this reason the computations are limited to a maximum value of $d/T = 40$. This value requires the summation of 30 terms in order that J_1 and J_2 can be determined to 4 significant figures. The extension of the results by the present method to $d/T = 500$ would require IBM or other high-speed computing machines.

[6] Reference (3), pp. 458–462; and reference (4), pp. 60–65.

TABLE 1 INFLUENCE NUMBERS FOR CYLINDER; $T/t = 0.8$

d/t	a_4	a_5	a_6	b_5	b_6
3.20	- 0.1700	- 4.2298	- 1.3007	- 2.0812	- 0.3200
8.00	- 0.1700	- 10.5745	- 2.0567	- 3.2906	- 0.3200
16.00	- 0.1700	- 21.1491	- 2.9085	- 4.6537	- 0.3200
24.00	- 0.1700	- 31.7236	- 3.5622	- 5.6996	- 0.3200
32.00	- 0.1700	- 42.2981	- 4.1133	- 6.5813	- 0.3200

TABLE 2 INFLUENCE NUMBERS FOR CYLINDER; $T/t = 1.0$

d/t	a_4	a_5	a_6	b_5	b_6
4.00	- 0.2125	- 6.6091	- 1.8178	- 3.6357	- 0.5000
10.00	- 0.2125	- 16.5227	- 2.8743	- 5.7485	- 0.5000
20.00	- 0.2125	- 33.0454	- 4.0646	- 8.1296	- 0.5000
30.00	- 0.2125	- 49.5681	- 4.9784	- 9.9567	- 0.5000
40.00	- 0.2125	- 66.0908	- 5.7485	- 11.4970	- 0.5000

TABLE 3 INFLUENCE NUMBERS FOR CYLINDER; $T/t = 1.2$

d/t	a_4	a_5	a_6	b_5	b_6
4.80	- 0.2550	- 9.5171	- 2.3896	- 5.7351	- 0.7200
12.00	- 0.2550	- 23.7927	- 3.7783	- 9.0679	- 0.7200
24.00	- 0.2550	- 47.5854	- 5.3433	- 12.8240	- 0.7200
36.00	- 0.2550	- 71.3781	- 6.5442	- 15.7061	- 0.7200
48.00	- 0.2550	- 95.1708	- 7.5566	- 18.1359	- 0.7200

TABLE 4 INFLUENCE NUMBERS FOR CYLINDER; $T/t = 1.6$

d/t	a_4	a_5	a_6	b_5	b_6
6.40	- 0.3400	- 16.9193	- 3.6790	- 11.7730	- 1.2800
16.00	- 0.3400	- 42.2981	- 5.8171	- 18.6147	- 1.2800
32.00	- 0.3400	- 84.5963	- 8.2266	- 26.3251	- 1.2800
48.00	- 0.3400	- 126.8944	- 10.0755	- 32.2416	- 1.2800
64.00	- 0.3400	- 169.1926	- 11.6342	- 37.2294	- 1.2800

TABLE 5 INFLUENCE NUMBERS FOR CYLINDER; $T/t = 2.0$

d/t	a_4	a_5	a_6	b_5	b_6
8.00	- 0.4250	- 26.4363	- 5.1416	- 20.5665	- 2.0000
20.00	- 0.4250	- 66.0908	- 8.1296	- 32.5185	- 2.0000
40.00	- 0.4250	- 132.1817	- 11.4970	- 45.9881	- 2.0000
60.00	- 0.4250	- 198.2725	- 14.0809	- 56.3237	- 2.0000
80.00	- 0.4250	- 264.3634	- 16.2593	- 65.0370	- 2.0000

TABLE 6 INFLUENCE NUMBERS FOR HEMISPHERICAL HEAD

d/T	a_1	a_2	a_3	b_1	b_2
4.00	+ 6.9690	- 1.8200	+ 0.0875	- 3.6608	+ 0.5272
10.00	+ 16.7131	- 2.8631	+ 0.0875	- 5.7319	+ 0.5058
20.00	+ 33.2457	- 4.0574	+ 0.0875	- 8.1196	+ 0.5030
30.00	+ 49.7670	- 4.9729	+ 0.0875	- 9.9470	+ 0.5020
40.00	+ 66.2900	- 5.7438	+ 0.0875	- 11.4886	+ 0.5015

Alternatively, it is possible to use several approximate theories for the head. No decision for the procedure to be used for large d/T has yet been reached.

The lower half of Fig. 1 shows the positive senses of the deflection and rotation at the junction in both the pressure-vessel body and the hemispherical cap. Continuity of deflections and rotations require

$$w_0 = -\delta_0$$

$$w_0' = \delta_0'$$

or in dimensionless form (setting $b_3 = b_4 = 0$)

$$a_4 + a_5 \frac{M_0}{pd^2} + a_6 \frac{Q_0}{pd} = -a_1 \frac{M_0}{pd^2} - a_2 \frac{Q_0}{pd} - a_3 \quad [5]$$

$$b_5 \frac{M_0}{pd^2} + b_6 \frac{Q_0}{pd} = -b_1 \frac{M_0}{pd^2} - b_2 \frac{Q_0}{pd} \quad [6]$$

Equations [5] and [6] determine the two dimensionless ratios Q_0/pd and M_0/pd^2. These two ratios are listed in Table 7 and are plotted in Figs. 3 and 4.

The stresses can be computed directly when the dimensionless ratios M_0/pd^2 and Q_0/pd have been determined. It is desirable to introduce a dimensionless stress ratio I, which is defined as the ratio of the stress of any type divided by $pd/2t$, the circumferential hoop stress in a thin cylinder. This ratio, while not as convenient for design purposes as the ratio of stress to pressure s/p, has the advantage that it is numerically smaller. This is a help in computational work, particularly when the diameter-thickness ratio d/t is large.

TABLE 7
BENDING MOMENT RATIO M_0/pd^2, AT JUNCTION

Note: Multiply values in Table by 10^{-3}.

$\frac{d}{T}$ \ $\frac{T}{t}$	0.8	1.0	1.2	1.6	2.0
4.00	- 0.9853	- 0.12828	+ 0.8266	+ 2.4564	+ 3.5507
10.00	- 0.3544	- 0.01093	+ 0.3708	+ 1.0207	+ 1.4546
20.00	- 0.1740	- 0.00287	+ 0.1876	+ 0.5119	+ 0.7285
30.00	- 0.1153	- 0.00127	+ 0.1256	+ 0.3417	+ 0.4860
40.00	- 0.0862	- 0.00071	+ 0.0944	+ 0.2564	+ 0.3646

SHEAR FORCE RATIO, Q_0/pd, AT JUNCTION

$\frac{d}{T}$ \ $\frac{T}{t}$	0.8	1.0	1.2	1.6	2.0
4.00	- 0.02730	- 0.03437	- 0.04029	- 0.05036	- 0.05841
10.00	- 0.01721	- 0.02179	- 0.02562	- 0.03210	- 0.03724
20.00	- 0.01214	- 0.01539	- 0.01810	- 0.02270	- 0.02633
30.00	- 0.00991	- 0.01256	- 0.01478	- 0.01853	- 0.02150
40.00	- 0.00858	- 0.01088	- 0.01280	- 0.01605	- 0.01862

It has been pointed out in previous reports that twelve values of the stress ratio I must be examined in order to determine which corresponds to the maximum stress. There are three types of stress—shear, axial, and circumferential—which are denoted by the subscripts s, a, c, respectively. In addition, each type of stress may be a maximum at any one of four locations. There are two locations at the junction according to whether we refer to the head or to the cylinder. A subscript j is used to indicate this location. Whether the stress ratio I is located in the head or in the cylinder will always be indicated in the tables. Maximum values of I may occur at one point other than the junction in either cylinder or head. These are denoted by subscripts m and require an auxiliary calculation to specify the location completely. The combination of 3 types of stress at 4 locations leads to a total of 12 stress ratios, I.

To simplify the examination of these, reference (5) contains equations for determining the maximum stress ratios in the cylinder and their location. The necessary expressions pertaining to the cylinder are listed in Table 9 of this paper.

Further mathematical, graphical, and computational work is necessary to establish the maximum stress ratio in the head. In the present series of reports, these three ratios have not been considered. By contrast, it is an easy matter to establish the three stress ratios in the head at the junction. In the present problem the shear force and bending moment are continuous across the junction. Furthermore, the center lines of the cylinder wall and spherical wall exhibit no discontinuity at the junction. This means that the circumferential force is continuous across the junction. Also, in both cylinder and head, the circumferential bending moment is μ (Poisson's ratio) times the axial bending moment. The conclusion to be drawn from these observations is that only the effect of a discontinuity in thickness at the junction need be taken into account to deduce each of the three stress ratios in the head at the junction from the corresponding stress ratio in the cylinder at the junction. In addition, the maximum stress ratio of any type at the junction is greater in the thinner elastic member.

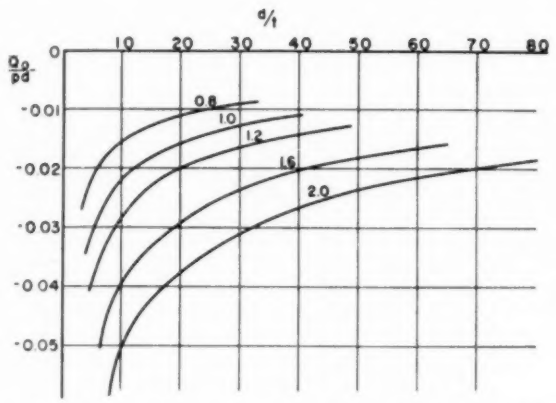

FIG. 3 Q_0/pd AS A FUNCTION OF d/t FOR T/t = 0.8, 1.0, 1.2, 1.6, 2.0

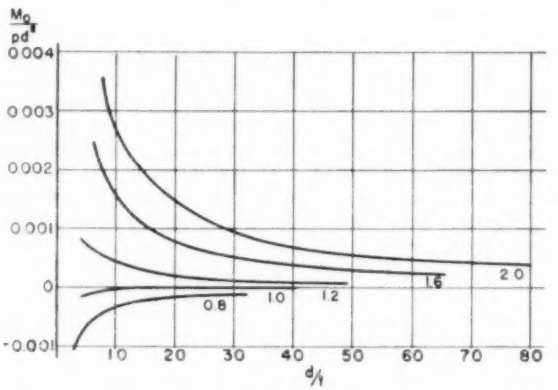

FIG. 4 M_0/pd^2 AS A FUNCTION OF d/t FOR T/t = 0.8, 1.0, 1.2, 1.6, 2.0

The limitations of the analysis should be kept in mind. The elastic theories of cylindrical and spherical shells require that the shell thickness remain small compared to the diameter. Whenever d/T (or d/t) is less than 10, the present results may fail to accurately predict the stresses in the pressure vessel. An additional limitation is that the deflection of either part of the vessel should not be too great. A common requirement is that the deflection nowhere exceed half the shell thickness.

The numerical results contained in the tables were determined by one computer. A second computer made an independent check. All results should be correct to at least four decimal places.

TABLE 8 STRESS INDEXES IN A CYLINDRICAL PRESSURE VESSEL WITH HEMISPHERICAL HEAD, $T/t = 0.8$

d/t	d/T	Cylinder at Junction			Head at Junction		
		Shear I_{sj}	Axial I_{aj}	Circum. I_{cj}	Shear I_{sj}	Axial I_{aj}	Circum. I_{cj}
3.20	4.00	+ 0.0819	+ 0.5378 + 0.4622	+ 0.8130 + 0.7902	- 0.1024	+ 0.6841 + 0.5659	+ 0.8568 + 0.8214
8.00	10.00	+ 0.0516	+ 0.5340 + 0.4660	+ 0.8144 + 0.7940	- 0.0645	+ 0.6782 + 0.5718	+ 0.8576 + 0.8258
16.00	20.00	+ 0.0364	+ 0.5334 + 0.4666	+ 0.8150 + 0.7950	- 0.0455	+ 0.6772 + 0.5728	+ 0.8582 + 0.8268
24.00	30.00	+ 0.0297	+ 0.5332 + 0.4668	+ 0.8152 + 0.7952	- 0.0372	+ 0.6769 + 0.5731	+ 0.8583 + 0.8271
32.00	40.00	+ 0.0257	+ 0.5331 + 0.4669	+ 0.8152 + 0.7954	- 0.0322	+ 0.6767 + 0.5733	+ 0.8583 + 0.8273

d/t	d/T	Maxima in Cylinder			Location of Maxima in Cylinder		
		Shear I_{sm}	Axial I_{am}	Circum. I_{cm}	Shear x_s/d	Axial x_a/d	Circum. x_c/d
3.20	4.00	+ 0.0212	+ 0.6297 + 0.3703	+ 1.0278 + 1.0103	0.4508	0.2093	0.5390 0.8457
8.00	10.00	+ 0.0131	+ 0.6266 + 0.3734	+ 1.0272 + 1.0100	0.2869	0.1342	0.3427 0.5367
16.00	20.00	+ 0.0092	+ 0.6260 + 0.3740	+ 1.0271 + 1.0100	0.2031	0.0951	0.2425 0.3797
24.00	30.00	+ 0.0075	+ 0.6258 + 0.3742	+ 1.0270 + 1.0100	0.1659	0.0777	0.1981 0.3101
32.00	40.00	+ 0.0065	+ 0.6257 + 0.3743	+ 1.0270 + 1.0099	0.1437	0.0673	0.1716 0.2686

TABLE 9 STRESS INDEXES IN A CYLINDRICAL PRESSURE VESSEL WITH HEMISPHERICAL HEAD, $T/t = 1.0$

d/t	d/T	Cylinder at Junction			Head at Junction		
		Shear I_{sj}	Axial I_{aj}	Circum. I_{cj}	Shear I_{sj}	Axial I_{aj}	Circum. I_{cj}
4.00	4.00	+ 0.1031	+ 0.5062 + 0.4938	+ 0.7485 + 0.7449	- 0.1031	+ 0.5062 + 0.4938	+ 0.7485 + 0.7449
10.00	10.00	+ 0.0654	+ 0.5013 + 0.4987	+ 0.7492 + 0.7484	- 0.0654	+ 0.5013 + 0.4987	+ 0.7492 + 0.7484
20.00	20.00	+ 0.0462	+ 0.5007 + 0.4993	+ 0.7496 + 0.7492	- 0.0462	+ 0.5007 + 0.4993	+ 0.7496 + 0.7492
30.00	30.00	+ 0.0377	+ 0.5005 + 0.4995	+ 0.7497 + 0.7495	- 0.0377	+ 0.5005 + 0.4995	+ 0.7497 + 0.7495
40.00	40.00	+ 0.0326	+ 0.5003 + 0.4997	+ 0.7498 + 0.7496	- 0.0326	+ 0.5003 + 0.4997	+ 0.7498 + 0.7496

d/t	d/T	Maxima in Cylinder			Location of Maxima in Cylinder		
		Shear I_{sm}	Axial I_{am}	Circum. I_{cm}	Shear x_s/d	Axial x_a/d	Circum. x_c/d
4.00	4.00	+ 0.0220	+ 0.6503 + 0.3497	+ 1.0323 + 1.0119	0.4283	0.2123	0.5085 0.7817
10.00	10.00	+ 0.0137	+ 0.6475 + 0.3525	+ 1.0317 + 1.0117	0.2728	0.1361	0.3226 0.4962
20.00	20.00	+ 0.0096	+ 0.6469 + 0.3531	+ 1.0315 + 1.0116	0.1930	0.0964	0.2283 0.3510
30.00	30.00	+ 0.0078	+ 0.6467 + 0.3533	+ 1.0315 + 1.0116	0.1577	0.0788	0.1864 0.2866
40.00	40.00	+ 0.0068	+ 0.6466 + 0.3534	+ 1.0315 + 1.0116	0.1366	0.0682	0.1615 0.2483

TABLE 10 STRESS INDEXES IN A CYLINDRICAL PRESSURE VESSEL WITH A HEMISPHERICAL HEAD, $T/t = 1.2$

d/t	d/T	Cylinder at Junction			Head at Junction		
		Shear I_{sj}	Axial I_{aj}	Circum. I_{cj}	Shear I_{sj}	Axial I_{aj}	Circum. I_{cj}
4.80	4.00	+ 0.1209	+ 0.4524 + 0.5476	+ 0.6910 + 0.7196	- 0.1007	+ 0.3836 + 0.4498	+ 0.6704 + 0.6902
12.00	10.00	+ 0.0768	+ 0.4466 + 0.5534	+ 0.6908 + 0.7228	- 0.0640	+ 0.3796 + 0.4537	+ 0.6707 + 0.6929
24.00	20.00	+ 0.0543	+ 0.4460 + 0.5540	+ 0.6911 + 0.7235	- 0.0453	+ 0.3791 + 0.4542	+ 0.6711 + 0.6935
36.00	30.00	+ 0.0443	+ 0.4457 + 0.5543	+ 0.6912 + 0.7238	- 0.0369	+ 0.3790 + 0.4543	+ 0.6712 + 0.6938
48.00	40.00	+ 0.0384	+ 0.4456 + 0.5544	+ 0.6913 + 0.7239	- 0.0320	+ 0.3789 + 0.4544	+ 0.6713 + 0.6939

d/t	d/T	Maxima in Cylinder			Location of Maxima in Cylinder		
		Shear I_{sm}	Axial I_{am}	Circum. I_{cm}	Shear x_s/d	Axial x_a/d	Circum. x_c/d
4.80	4.00	+ 0.0212	+ 0.6584 + 0.3416	+ 1.0340 + 1.0125	0.4166	0.2194	0.4886 0.7391
12.00	10.00	+ 0.0132	+ 0.6561 + 0.3439	+ 1.0335 + 1.0123	0.2653	0.1406	0.3108 0.4692
24.00	20.00	+ 0.0093	+ 0.6556 + 0.3444	+ 1.0334 + 1.0123	0.1878	0.0996	0.2199 0.3320
36.00	30.00	+ 0.0076	+ 0.6555 + 0.3445	+ 1.0334 + 1.0123	0.1533	0.0813	0.1796 0.2711
48.00	40.00	+ 0.0066	+ 0.6554 + 0.3446	+ 1.0334 + 1.0123	0.1328	0.0705	0.1556 0.2348

TABLE 11 STRESS INDEXES IN A CYLINDRICAL PRESSURE VESSEL WITH HEMISPHERICAL HEAD, $T/t = 1.6$

d/t	d/T	Cylinder at Junction			Head at Junction		
		Shear I_{sj}	Axial I_{aj}	Circum. I_{cj}	Shear I_{sj}	Axial I_{aj}	Circum. I_{cj}
6.40	4.00	+ 0.1511	+ 0.3114 + 0.6886	+ 0.5841 + 0.6973	- 0.0944	+ 0.2388 + 0.3862	+ 0.5624 + 0.6066
16.00	10.00	+ 0.0963	+ 0.3040 + 0.6960	+ 0.5824 + 0.7000	- 0.0602	+ 0.2359 + 0.3891	+ 0.5619 + 0.6079
32.00	20.00	+ 0.0681	+ 0.3034 + 0.6966	+ 0.5825 + 0.7005	- 0.0426	+ 0.2357 + 0.3893	+ 0.5622 + 0.6082
48.00	30.00	+ 0.0556	+ 0.3032 + 0.6968	+ 0.5826 + 0.7006	- 0.0347	+ 0.2356 + 0.3894	+ 0.5623 + 0.6085
64.00	40.00	+ 0.0481	+ 0.3031 + 0.6969	+ 0.5826 + 0.7008	- 0.0301	+ 0.2356 + 0.3894	+ 0.5623 + 0.6085

d/t	d/T	Maxima in Cylinder			Location of Maxima in Cylinder		
		Shear I_{sm}	Axial I_{am}	Circum. I_{cm}	Shear x_s/d	Axial x_a/d	Circum. x_c/d
6.40	4.00	+ 0.0191	+ 0.6652 + 0.3348	+ 1.0355 + 1.0131	0.4027	0.2320	0.4651 0.6820
16.00	10.00	+ 0.0120	+ 0.6638 + 0.3362	+ 1.0352 + 1.0130	0.2562	0.1482	0.2956 0.4328
32.00	20.00	+ 0.0085	+ 0.6635 + 0.3365	+ 1.0351 + 1.0129	0.1813	0.1049	0.2092 0.3061
48.00	30.00	+ 0.0069	+ 0.6634 + 0.3366	+ 1.0351 + 1.0129	0.1480	0.0857	0.1708 0.2500
64.00	40.00	+ 0.0060	+ 0.6633 + 0.3367	+ 1.0351 + 1.0129	0.1282	0.0742	0.1479 0.2165

Relation to Code Requirements

The 1943 API-ASME Code or the 1950 ASME Code for Unfired Pressure Vessels determines the thickness of the cylindrical shell[9] from the equation

$$t = \frac{pd}{2s} \text{ or } s = \frac{pd}{2t} \quad \ldots\ldots\ldots\ldots\ldots\ldots [7]$$

where no allowance for corrosion or joint efficiency is made. The allowable stress s is selected from a table when the material of the shell and the metal temperature are known. Equation [7] shows that the design is based entirely on the circumferential (hoop) stress in a thin cylindrical vessel. The allowable stress is sufficiently low to insure a safe design.

The present results show that the maximum stress in the pressure-vessel body, when the shear force and the bending moment at the joint are considered, is only 3 per cent greater than the stress obtained from Equation [7].

The present calculations thus indicate that the code design procedure for a cylindrical pressure vessel need not be modified when the closure is a hemispherical cap. This conclusion applies even if the cap thickness differs considerably from the thickness of the cylinder.

[9] Reference (6), p. 13.

TABLE 12 STRESS INDEXES IN A CYLINDRICAL PRESSURE VESSEL WITH HEMISPHERICAL HEAD, $T/t = 2.0$

d/t	d/T	Cylinder at Junction			Head at Junction		
		Shear I_{sj}	Axial I_{aj}	Circum. I_{cj}	Shear I_{sj}	Axial I_{aj}	Circum. I_{cj}
8.00	4.00	+ 0.1752	+ 0.1591 + 0.8409	+ 0.4848 + 0.6894	- 0.0876	+ 0.1648 + 0.3352	+ 0.4865 + 0.5377
20.00	10.00	+ 0.1117	+ 0.1509 + 0.8491	+ 0.4821 + 0.6915	- 0.0559	+ 0.1627 + 0.3373	+ 0.4856 + 0.5380
40.00	20.00	+ 0.0790	+ 0.1503 + 0.8497	+ 0.4822 + 0.6920	- 0.0395	+ 0.1626 + 0.3374	+ 0.4859 + 0.5383
60.00	30.00	+ 0.0645	+ 0.1501 + 0.8499	+ 0.4822 + 0.6922	- 0.0323	+ 0.1625 + 0.3375	+ 0.4860 + 0.5384
80.00	40.00	+ 0.0559	+ 0.1500 + 0.8500	+ 0.4822 + 0.6922	- 0.0279	+ 0.1625 + 0.3375	+ 0.4860 + 0.5384

d/t	d/T	Maxima in Cylinder			Location of Maxima in Cylinder		
		Shear I_{sm}	Axial I_{am}	Circum. I_{cm}	Shear x_s/d	Axial x_a/d	Circum. x_c/d
8.00	4.00	+ 0.0180	+ 0.6733 + 0.3267	+ 1.0369 + 1.0136	0.3865	0.2357	0.4442 0.6383
20.00	10.00	+ 0.0113	+ 0.6726 + 0.3274	+ 1.0370 + 1.0136	0.2468	0.1502	0.2821 0.4046
40.00	20.00	+ 0.0080	+ 0.6724 + 0.3276	+ 1.0370 + 1.0137	0.1746	0.1063	0.1995 0.2862
60.00	30.00	+ 0.0065	+ 0.6723 + 0.3277	+ 1.0370 + 1.0137	0.1426	0.0868	0.1629 0.2338
80.00	40.00	+ 0.0056	+ 0.6723 + 0.3277	+ 1.0370 + 1.0137	0.1235	0.0752	0.1411 0.2024

For hemispherical heads, the code design formula[10] is

$$T = \frac{pd}{4S} \text{ or } S = \frac{pd}{4T} \quad \ldots\ldots\ldots\ldots\ldots\ldots [8]$$

where no allowance for corrosion or joint efficiency is made. This equation represents the circumferential stress in a thin hemispherical head. A head made of the same material as the body of the pressure vessel need only be half as thick since for the same allowable stress, the ratio of thickness from Equations [7] and [8] is

$$\frac{T}{t} = \frac{1}{2}$$

The present calculations extend only to a thickness ratio of 0.8. Furthermore, the maximum stress in the head probably does not occur at the junction with the vessel body. Approximate theories, developed for a spherical shell having a large ratio d/T, indicate that the rate of decrease of forces and bending moments is about as rapid as in a cylindrical shell. It is probable that when the hemispherical cap is thicker than the cylinder, the maximum stress in the cap will not exceed that in the cylindrical body since forces of the same magnitude and the same rate of decrease will be distributed over the thicker section. The same argument indicates that the hemispherical cap has the greatest stress when it is thinner than the cylindrical body. Additional calculations are necessary to settle this point.

The present calculations indicate that the shear force and bending moment at the junction do not raise the stresses significantly. Consequently, the code design equation for the hemispherical cap probably leads to a reasonably safe design.

Discussion of Results

Influence Numbers. Tables 1 to 5 show the influence numbers for the cylinder for various values of d/t. With the conventions shown in Fig. 1, all coefficients are negative since each of the loadings (M_0, Q_0, p) produces a negative deflection w_0, and a positive rotation w_0', at the junction.

Table 6 contains the influence numbers for the hemispherical cap. Comparison of these numbers with their counterparts for the flat head[11] and for the conical head with a semiapex angle of 45 deg[12] throws considerable light on the deformation of the head. When differences in notation are taken into account, each influence number for a flat head is of opposite sign to that of the conical head. Thus the effect of pressure, shear force, or bending moment on the flat head is to produce a deflection and rotation at the junction precisely opposite to the deflection and rotation produced in the 45-deg conical head by the same type of load. The hemispherical cap deforms in a manner similar to the 45-deg conical head since the signs of each of its influence numbers agree with its counterpart in the 45-deg conical head. This conclusion applies even when the semiapex angle is not 45 deg. The limitation to a 45-deg conical head is made only because it permits comparisons of influence numbers at equal values of the diameter-thickness ratio, d/T.

The influence number a_1 is greater in the hemispherical cap than in the 45-deg conical head. This means that for the same diameter-thickness ratio and the same magnitude of bending moment M_0, the hemispherical cap has the greater deflection at the junction. Similar deductions can be drawn for the remaining five influence numbers a_2, a_3, b_1, b_2, and b_3. These numbers thus enable us to determine which head is more sensitive to deflection or rotation at the junction under any of the three types of loads.

Comparing each of the six influence numbers for $d/T = 4$, 10, and 40 in Table 6 with its corresponding number for the 45-deg conical head indicates that both have approximately the same magnitude except for b_3 which is zero in the hemispherical cap. This indicates that the principal differences between the stresses in these two heads depend on the fact that the hemispherical cap does not rotate when under internal pressure only.

The same effect should require a very small bending moment. Figs. 3 and 4 support this conclusion by showing that the ratio M_0/pd^2 is of the order $^1/_{10}$ or less than the ratio Q_0/pd.

Stresses. The principal results obtained for the 9 stress ratios computed in Tables 8 to 13 are given in the conclusions. Table 14 indicates the variation in all stress ratios as the two geometric ratios d/T and T/t increase.

Convention Used in Tables 8 to 12

While the problem of determining the magnitude of the maximum stress has been primarily emphasized, Tables 8 to 12 include some additional calculations. For each circumferential or axial stress, two figures are listed. The upper figure represents the value of the stress ratio at the external surface of the vessel. The lower figure represents the value of the stress ratio at the internal surface of the vessel. The greater value of the two figures has been computed from the equations of Table 13. All axial and circumferential-stress ratios are positive and represent tensile stresses.

The shear-stress ratio refers to a shear stress at the middle surface. The ratio Q_0/pd is always negative. Consequently the shear-stress ratios at the junction are opposite to the direction of Q_0 in Fig. 1. For the cylinder, this ratio is positive in Tables 8 to 12, denoting that the shear stress is directed toward the axis. The negative sign of the ratio in the head indicates that the shear stress is directed away from the axis. The maximum shear stress I_{sm} is positive, denoting a shear stress and shear force directed toward the axis when material lies on the left in Fig. 1.

BIBLIOGRAPHY

1 "Stresses in a Pressure Vessel With a Conical Head," by G. W. Watts and H. A. Lang, Trans. ASME, vol. 74, 1952, pp. 315–326.

[10] Reference (6), p. 17.

[11] Reference (2), table 6.

[12] Reference (1), table 6.

TABLE 13 EQUATIONS FOR STRESS RATIOS

Stress ratios in cylinder at the junction:

Shear

$$I_{sj} = 3\left|\frac{Q_0}{pd}\right|$$

Axial

$$I_{aj} = \frac{1}{2} + 12\,\frac{d}{t}\left|\frac{M_0}{pd^2}\right|$$

Circumferential

$$I_{cj} = \left|1 + 2\beta d\left(\frac{Q_0}{pd}\right)(1 + \alpha_0)\right| + 12\mu\,\frac{d}{t}\left|\frac{M_0}{pd^2}\right|$$

Maximum stress ratios in cylinder (other than at junction):

Shear

$$I_{sm} = \frac{I_{sj}\sqrt{1 + 2\alpha_0 + 2\alpha_0^2}}{e^{\beta x_s}} \qquad \frac{x_s}{d} = \frac{\tan^{-1}\left(\dfrac{1 + \alpha_0}{\alpha_0}\right)}{\beta d}$$

Axial

$$I_{am} = \frac{1}{2} + 3.4126\sqrt{\frac{d}{t}}\,I_{sm} \qquad \frac{x_a}{d} = \frac{x_s}{d} - \frac{\pi}{4}\,\frac{1}{\beta d}$$

Circumferential

$$I_{cm} = 1 + 0.7326\sqrt{\frac{d}{t}}\,I_{sm} \qquad \frac{x_c}{d} = \frac{x_a}{d} + \frac{1.0720}{\beta d}$$

Stress ratios in hemispherical head at junction:

Shear

$$I_{sj} = 3\,\frac{t}{T}\left|\frac{Q_0}{pd}\right|$$

Axial

$$I_{aj} = \frac{1}{2}\,\frac{t}{T} + 12\,\frac{d}{t}\,\frac{t^2}{T^2}\left|\frac{M_0}{pd^2}\right|$$

Circumferential

$$I_{cj} = \frac{1}{2}\,\frac{t}{T} + 12\mu\,\frac{d}{t}\,\frac{t^2}{T^2}\left|\frac{M_0}{pd^2}\right| + \frac{4t}{T}\left(\frac{a_1 M_0}{pd^2} + \frac{a_2 Q_0}{pd}\right)$$

TABLE 14 VARIATIONS IN STRESS RATIOS AS d/T AND T/t INCREASE

Numbering system	Location	Quantity	T/t constant d/T increasing	d/t constant T/t increasing
1	Cylinder	I_{sj}	Decreasing	Increasing
2	Cylinder	I_{aj}	Slight increase if $T > t$ Slight decrease if $T \leq t$	Decreasing if $T < t$ Increasing if $T > t$
3	Cylinder	I_{cj}	Slight increase	Decreasing
4	Sphere	I_{sj}	Decreasing	Increasing if $T < t$ Decreasing if $T > t$
5	Sphere	I_{aj}	Slight decrease if $T \leq t$ Slight increase if $T > t$	Decreasing
6	Sphere	I_{cj}	Slight decrease	Decreasing
7	Cylinder	I_{sm}	Decreasing	Increasing
8	Cylinder	I_{am}	Decreasing	Increasing
9	Cylinder	I_{cm}	Slight decrease	Slight increase
	Cylinder	x_s/d	Decreasing	Decreasing
	Cylinder	x_a/d	Decreasing	Increasing
	Cylinder	x_c/d	Decreasing	Decreasing

NOTE: Using numbering system of table, stress ratios may be arranged in descending order of magnitude for each value of ratio T/t, as follows:

T/t	
0.8	$9 > 3 > 5 > 8 > 2 > 4 > 1 > 7$
1.0	$9 > 3 > 8 > 2 = 5 > 1 = 4 > 7$
1.2	$9 > 3 > 8 > 2 > 5 > 1 > 4 > 7$
1.6	$9 > 3 > 2 > 8 > 5 > 1 > 4 > 7$
2.0	$9 > 2 > 3 > 8 > 5 > 1 > 4 > 7$

The three location ratios, arranged in order of decreasing distance from junction, are $x_c > x_s > x_a$ for all ratios T/t.

2 "The Stresses in a Pressure Vessel With a Flat Head," by G. W. Watts and H. A. Lang, Trans. ASME, vol. 74, 1952, pp. 1083–1091.

3 "Theory of Plates and Shells," by S. Timoshenko, first edition, McGraw-Hill Book Company, Inc., New York, N. Y., 1940.

4 "The Basic Elastic Theory of Vessel Heads Under Internal Pressure," by G. W. Watts and W. R. Burrows, *Journal of Applied Mechanics*, Trans. ASME, vol. 71, 1949, pp. 55–73.

Report of the Engineering Research Department, ERR-A6-2, "The Stresses in a Pressure Vessel With a Conical Head," Standard Oil Company (Indiana), July 26, 1949.

5 "The Maximum Stresses in the Cylindrical Body of Pressure Vessels," by H. A. Lang, Property of Engineering Research Department, Standard Oil Company (Indiana).

6 API-ASME Code Unfired Pressure Vessels for Petroleum Liquids and Gases (1943 edition).

Discussion

T. McLEAN JASPER.[12] This paper gives a theoretical approach to a pressure-vessel problem which applies essentially to a totally elastic material. In steel, for instance, we have an excellent material for the adjustments of slight imperfections in fabrication, providing we have the material mass available in approximately the right location. Steel used in pressure vessels, in general, has great ductility in comparison to its natural elastic strain so that it can make adjustments to slightly imperfect shapes or designs. That is why steel is a most useful material for fabricated structures.

It is doubtful if before this there has been a paper in which so much sound thinking has been given to the theoretical details of an elastic problem of this kind. We are fast approaching a condition in the use of materials where the elastic details are of extreme importance because demands for high-strength materials at temperatures of 1500 to 2000 F are close to the engineer's present requirements. In general, such materials are very brittle even at those high temperatures.

This need also applies to pressure vessels of thick solid sections in which adjustments are not accommodated so easily. The stress-calculation system that the authors have used involves the simple formula for cylinders. The stresses due to internal pressure vary in a thick-wall high-pressure cylinder so that the difference between the inside and outside surface stresses is equivalent to the pressure P. In strain measurements on the outside surface of cylinders under pressure the maximum stress on the outside surface should have the pressure value P added if the stress value on the inside is to be obtained. In the case of precompressed cylinder adjustments, knowing the value of precompression will be required for the actual stresses in a cylinder. In stress measurements at the junction between cylinder and heads, strain gages are needed on both of the steel surfaces if a check on this analysis is to be made.

This paper should be appreciated greatly because it helps the strain-measuring setup for obtaining test results. Our factors of so-called safety should accommodate the designs and the slight fabrication difficulties in steel.

AUTHORS' CLOSURE

The authors wish to thank Mr. Jasper for his discussion. He points out that high local stresses in steel vessels are frequently relieved by plastic flow. Unfortunately, a designer cannot always rely on ductility as insurance against the bad effects of sharp corners and other stress raisers. Numerous failures have occurred because of brittleness at low temperatures; and as Mr. Jasper points out, many steels also become brittle at high temperatures.

[12] A. O. Smith Corporation, Milwaukee, Wis. Mem. ASME.

The authors believe that current design requirements will tend, in many cases, to reduce the available ductility. One frequently heard proposal is to take advantage of the higher yield strengths of low-alloy steels. It is well known that these higher yield strengths are inescapably linked to lower ductility values. The only other alternatives are higher working stresses or thicker walls. Although the problem of size effect is not yet entirely clarified, it is generally agreed that the thicker the plate, the greater the tendency toward brittle failures, because of welding difficulties, greater triaxial tensile stresses, greater temperature differences through the plate, and so on.

One of the main purposes of the present paper is to point out the superiority of hemispherical heads, compared to flat or conical heads, as a means of avoiding high local stresses. If stresses throughout a pressure vessel can be held at fairly uniform levels by using the best available shape, it is unnecessary to rely on ductility to relieve sore spots.

Mr. Jasper also points out that the authors' analysis is reasonably accurate only when applied to vessels with rather thin walls. Even so, it represents a considerable advance over present textbooks in making the results of advanced mathematical analysis more available to engineering designers. Although a limited amount of elasticity theory exists for thick-walled cylinders and spheres, it is not yet in a sufficiently manageable form to permit satisfaction of the boundary conditions at a sphere-cylinder junction. This problem may yield more easily to approximations of the lattice type, rather than the formal mathematics of elastic theory.

Flame Velocities in Carbon Monoxide-Oxygen Mixtures

By T. W. PRICE[1] and J. H. POTTER,[2] URBANA, ILL.

One of the ideal theoretical devices for determining flame velocities is the constant-pressure adiabatic bomb. In practice this has been realized in the form of a soap bubble filled with a premixed gas-oxidant combination, centrally ignited by a spark, and observed by high-speed photography. However, the aqueous soap film imposed certain restrictions, in that moisture content was not controllable, and that the film itself might have taken some part in the combustion reaction. The present paper reports (*a*) on a search for a substitute material for the bomb, and (*b*) the development of a technique in which a very thin transparent rubber balloon was used. The new method was then used to determine flame velocities in carbon monoxide-oxygen mixtures saturated with water vapor. These velocities were found to increase with increase of initial mixture temperature.

Introduction

KNOWLEDGE of flame velocities is important in the general understanding of combustion phenomena. The burning speed of a given fuel-oxidant combination is one of the basic parameters to be considered in the design of burners, flame tubes, furnaces, and combustion chambers.

A distinction is to be made between the velocity of a flame front past a given fixed point, and that with relation to the unburned gases just ahead of the front. In the first instance a "spatial velocity" is measured. When the burning speed is referred to the unburned gases ahead of the flame front the true "flame velocity" is found. In general, the experimental problem has been that of measuring a spatial velocity by one of several methods, and then reducing this to a flame velocity by calculation. If one accepts flame velocity as a basic property of a given fuel-oxidant mixture under specified starting conditions of *P-V-T*, then the flame velocity should be the same regardless of the method of measurement.

In the past, many variations on the Bunsen-cone method have been used. This type of measurement, stemming from the original work of Guoy (1)[3] has been developed and extended by others (2) (3:35) (4), although differences in the interpretation of the test data have led to fairly wide variations in the reported values of the flame velocities.

In simplest terms, the Bunsen-cone method involves the measurement of the surface area of the blue cone at the base of the flame, and the total rate of flow of gas and oxidant. Dividing the second by the first gives a mean value of the flame speed. The cone-area measurement is done differently by the various investigators in this field, and is the principal source of divergence among them.

Burning velocities also may be determined from combustion in tubes (3:103). Here the flame travel is measured, the spatial velocity found, and the burning velocity is computed. The gas-oxidant mixture may be at rest or in motion at the time of ignition, although the interpretation is more complicated in the latter case. Experiments involving an appreciable length of travel of a flame are apt to yield results which are reproducible only in a given apparatus. In general, the flame tube is least used as a means of determining burning velocity.

The constant-volume bomb (5, 6, 7, 8) affords another method for finding flame velocity. Here a spherical steel or glass vessel is usually used. It is fitted with central ignition electrodes, and the progress of the flame is observed photographically. The advantage of the constant-volume bomb technique lies in the fact that only a small volume of mixture is required; the disadvantage, the fact that the velocity and pressure of the unburned gases ahead of the flame front are unknown.

The method of determining flame velocity that is least affected by details of experimental apparatus (9) is that found by photographic observation of the travel of a flame front from a centrally ignited gas-oxidant mixture enclosed in a soap bubble. Such a method for containing the reaction constitutes a constant-pressure adiabatic bomb, and has found wide application in experimental studies (5:227) (6) (10, 11, 12, 13, 14, 15, 16, 17) (18:67). Observation of the combustion process has been effected by high-speed moving pictures, or by drum-camera techniques. The latter method offers the better research tool. Light enters the drum camera only through a narrow slit, so that the pattern left on the film is the locus of the diameter of the expanding spherical flame front. As a result, the diameter of the burning sphere can be found from the width of the V at a given time, which in turn is fixed by the linear speed of the film.

The theory of the constant-pressure adiabatic bomb is quite simple, and the drum-camera photographs are interpreted readily. Let

S_s = speed of flame in space, relative to a fixed point (spatial velocity)
S_u = speed of flame relative to unburned gases (flame velocity)
ρ_u = density of unburned gases
ρ_b = density of burned gases
E = volumetric expansion ratio
a = initial bubble radius
A = final flame radius

The spatial velocity S_s is found from the slope of the flame trace on the film. The mass of gas entering and leaving a given moving area of a combustion front per unit time is

$$S_u\rho_u = S_s\rho_b, \quad S_u = \frac{S_s\rho_b}{\rho_u}$$

And, as the process takes place at constant pressure

---

[1] Research Associate, Engineering Experiment Station, University of Illinois. Jun. ASME.

[2] Professor of Mechanical Engineering, University of Illinois. Mem. ASME.

[3] Numbers in parentheses refer to the Bibliography at the end of the paper. Where two or more numbers are cited in a single reference, those following the colon are the pages referred to.

Contributed by the Process Industries and Fuels Divisions and presented at the Semi-Annual Meeting, Cincinnati, Ohio, June 15–19, 1952, of The American Society of Mechanical Engineers.

Note: Statements and opinions advanced in papers are to be understood as individual expressions of their authors and not those of the Society. Manuscript received at ASME Headquarters, March 13, 1952. Paper No. 52—SA-65.

$$\frac{\rho_u}{\rho_b} = E = \left(\frac{A}{a}\right)^3$$

from which

$$S_u = \frac{S_r}{E} \quad \ldots\ldots [1]$$

In the actual experiments, the process deviates from isobaric to a negligible degree. Also, the expansion is very nearly adiabatic, as there is very little heat loss during rapid growth under conditions of radial symmetry. Turbulence is eliminated effectively as a variable, and only small batches of the combustible mixture are required. All of the foregoing factors made the constant-pressure bomb the most promising of the available methods for measuring flame velocity. In practice, however, two serious drawbacks were discovered. It was not possible adequately to control the humidity of the mixture inside the soap bubble. Then too the soap film itself had an effect on the combustible mixture, and in some cases may have taken part in the reaction. These two considerations placed such severe limitations on the method that it has been largely abandoned.

Present Investigation

The research reported in this paper had the following objectives in view:

(*a*) To find a substitute material for the soap film which could perform the functions of an isobaric adiabatic bomb.

(*b*) To develop around this material a satisfactory experimental technique for flame-velocity determination.

(*c*) To explore the effects of moisture on varying mixtures of carbon monoxide and oxygen.

The various substitute materials which were tried in the course of this investigation are listed in the Appendix, and the shortcomings of each material are given in Table 1. The material which finally proved successful was rubber, and very thin transparent rubber balloons were used throughout this research.

TABLE 1 FLAME VELOCITIES IN CO-O_2 MIXTURES

Type of material	Deficiencies
Bar soap	9, 13, 15, 16
Detergent soap powder	9, 15
Plastic toy balloon	10, 11
Rubber toy balloon	4
Cellophane bag	2, 3
Polyvinyl alcohol	2, 3
Polyvinyl acetate	10, 11
Plastisol	4, 10, 18
Latex rubber	4, 18

Some early experiments on soap-bubble bombs showed the importance of central ignition and pointed out the necessity for supporting the bomb in such a manner as to be centered in the field of the camera during the combustion process. In the case of the rubber bombs, it was decided to support them on the electrodes.

To assure purity, the CO was generated in the laboratory just prior to use by the interaction of formic and sulphuric acids. To remove possible acid and CO_2 traces, the CO was bubbled through potassium hydroxide before entering the mixture burette. Commercially pure oxygen was used. The mixture of CO and O_2 was carefully proportioned in a burette, using water as the leveling agent.

The gas was then introduced into a clean dry balloon which previously had been washed in distilled water to remove the powder in which it had been shipped. In order to check the isobaric characteristics of the balloon a manometer was connected to it near the neck. The pressure was checked while the balloon diameter was increased from 3 in. to 8 in. and showed a variation of less than 2 in. of water. As the walls of the balloon had very small mass, and as the gas velocities just ahead of the flame front were small,[4] the pressure required for acceleration of the walls and unburned gases was considered to be negligibly small. Tests also showed that the flame front traveled at substantially a constant velocity relative to the burned gases. All of the factors mentioned in the foregoing were considered to confirm the isobaric nature of the combustion process.

The problem of piercing the walls of the balloon with the electrodes was solved by the use of aluminum sleeves $^5/_8$ in. long, terminating in a thin flange of $^3/_4$ in. diam. There was a clearance of 0.0005 in. between the inside diameter of the sleeve and the outside diameter of the electrode. Two such sleeves were coaxially attached to the balloon 180 deg apart, with cellulose tape. The electrodes were sharpened lengths of $^1/_{16}$-in. drill rod. With the sleeves taped in place it was possible to force the electrodes through the walls of the balloon without causing rupture of the whole structure.

The balloon was carefully set in front of a black target as shown in Fig. 1, the friction between the sleeves and electrodes being sufficient to hold the balloon in place. In order to trace the progress of the balloon wall simultaneously with that of the luminous flame front, the outer walls of the balloon were illuminated by reflected light as shown in Fig. 2. The fact that this wall trace on the moving film closely approximated a cubic curve further substantiated the contention that the combustion process was isobaric. The balloon with target, lighting, and drum camera is shown in Fig. 3. The ignition circuit was synchronized with the shutter on the drum camera.

Fig. 1 Balloon Ready for Firing
(Note positions of electrodes and target.)

The temperature of the laboratory was varied from 35 F to 92 F. The combustible mixture was assumed to be saturated with water vapor at the temperature of the laboratory. The percentage of CO in the mixtures was varied from 30 to 90 per cent by volume.

[4] Of the order of 40 ips.

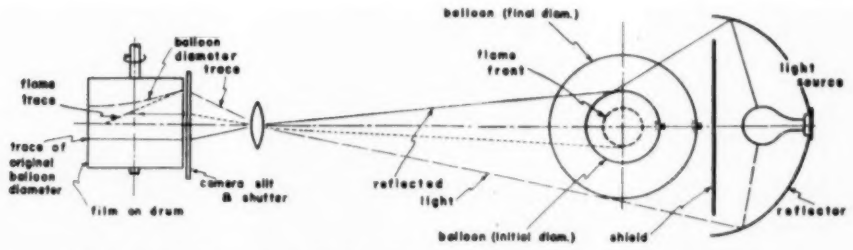

FIG. 2 TEST APPARATUS, SHOWING LIGHT PATHS AND TRACES OF DRUM-CAMERA FILM

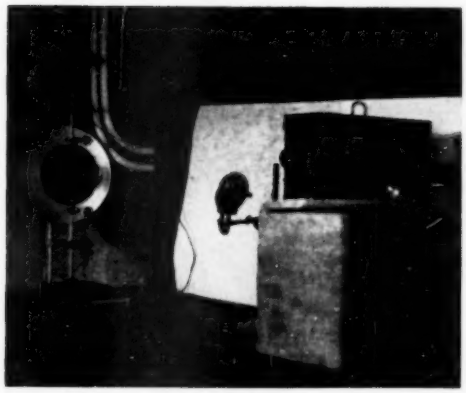

FIG. 3 BALLOON PRIOR TO FIRING, SHOWING RELATIVE POSITIONS OF DRUM CAMERA, TARGET, AND REFLECTOR

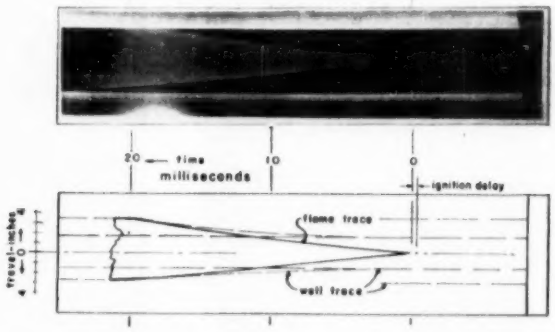

FIG. 4 PHOTOGRAPHIC RECORD OF LIGHT TRACES ON DRUM-CAMERA FILM

RESULTS AND DISCUSSION

A sample drum-camera picture for 85 per cent CO mixture is shown in Fig. 4. The white lines parallel to the axis are the traces of the original diameter of the balloon. These appear because the shutter was opened for about one revolution just prior to firing. After combustion has been initiated the wall traces are seen to move outward, expanding at a rate somewhat less than that of the flame front. Eventually, the flame traces overtook the wall traces and the spherical growth of both the flame front and balloon ceased. Thereafter, the flame front was in actual contact with the walls of the balloon for a period of time. This was terminated by the rupture of the balloon. These conclusions were also verified by high-speed motion pictures taken in an auxiliary study.

Fig. 4 also shows a nonsymmetrical flame trace caused by ignition from off-center electrodes. There is a measurable delay between the dot marking the point of ignition and the establishment of the luminous flame trace. This indicates an absence of sufficient luminosity in the earliest phase of the combustion process to show up on the film.

Three "pathological" cases are shown in Figs. 5, 6, and 7. In Fig. 5 the balloon was larger than usual at the time of ignition. The wall traces are very well defined, but the balloon burst before the flame front touched the walls. For this reason the final diameter cannot be fixed with certainty, and neither the expansion ratio nor the flame velocity can be determined.

In Fig. 6 the traces of an undersized balloon are shown. In addition to the extended length of the time of contact of the flame and wall, some characteristics which render this run unsuitable are noted. The point of ignition was not exactly in the center of the sphere, and as a result the flame front tended toward the closer wall, extending it disproportionately. The balloon then swung in the opposite direction and executed complicated oscillations. The black central line is the shadow of one of the electrodes. Its motion was caused by the motion of the balloon.

When the friction between the electrodes and the sleeves was too great, the top and bottom of the balloon could not expand as rapidly as the sides. This caused the balloon to take on an ellipsoidal shape, having a horizontal major axis. This case is illustrated in Fig. 7. (The bright white horizontal line in Fig. 7 is meaningless.) After the flame front reached the walls of the balloon, the whole mass drew itself into a more nearly spherical shape, causing the decrease in the width of the flame trace on the drum-camera film.

In order to avoid these difficulties, it is necessary that care be taken (*a*) to blow the balloon to approximately the proper initial diameter (about 3 in. for balloons used here), (*b*) to center the electrode gap at the center of the spherical bomb, (*c*) to center the camera on the electrode gap, (*d*) to align the two electrode sleeves exactly coaxially, and (*e*) to clean the electrode rods and sleeve bearings thoroughly.

After a number of successful runs, the data were collected and plotted. Fig. 8 shows the measured values of the expansion ratio E, plotted against the percentage of CO in the combustible mixture. The test points are shown as circles, and, in general, fall below the theoretical curve of Lewis and von Elbe (5).[5]

The half-shaded points are test values of Fiock and Roeder (15) based on soap-bubble experiments. It is interesting to note that some of the latter experimental values exceed the theoretical. Speculation suggests that the soap film took some part in the combustion process, either directly or in some catalytic manner. The open circles, representing the results of this study, tend to confirm the theoretical curve in the range of higher CO concen-

[5] Calculated values including effects of dissociation, for CO-O_2 mixtures having an H_2O mol fraction of 0.0269, and with initial gas conditions of 298 K, at 755 mm Hg.

FIG. 5 PATHOLOGICAL CASE, SHOWING EXPLOSIVE RUPTURE OF BALLOON BEFORE FLAME FRONT AND BALLOON WALL CONTACT

FIG. 6 PATHOLOGICAL CASE, SHOWING SMALL BALLOON IMPROPERLY CENTERED WITH RESPECT TO POINT OF IGNITION AND VERY LONG FLAME-WALL CONTACT

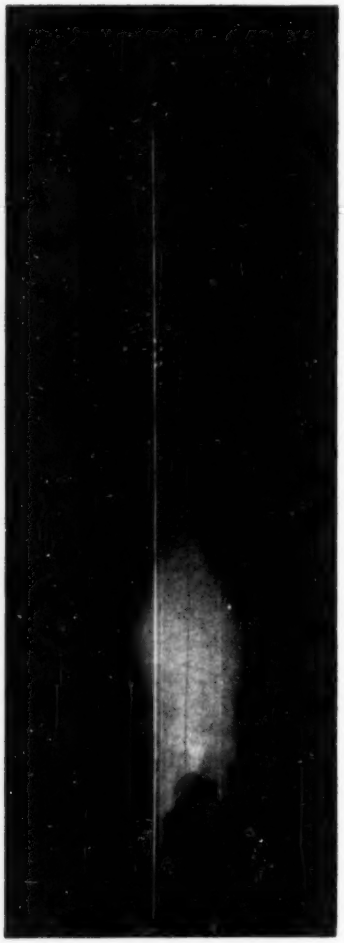

FIG. 7 PATHOLOGICAL CASE, SHOWING EFFECTS OF SLEEVE FRICTION ON DRUM-CAMERA TRACES

tration. Elsewhere the test points lie below the theoretical curve, suggesting either nonadiabatic performance or unstable chemical equilibrium.

Because the moisture concentrations were controlled by the use of saturated gas at varying temperatures, it is impossible to separate the effects of moisture from those of initial temperature. The curves in Fig. 9 indicate that the spatial velocities increased with increase in moisture, but these vapor increases were accompanied by higher initial temperatures.

By using Equation [1] the flame velocities were computed. These are shown plotted in Fig. 10. In general, the flame velocities reported here were slightly greater than those determined by Jahn by the Bunsen-cone method (5:463), but below those found from soap-bubble tests.

Fig. 11 shows some of the test curves of Jahn and is introduced for comparison purposes. Curves (*a*) and (*b*) contained 1.35 per cent H_2O; however, the upper curve shows the effect of an additional 1.5 per cent hydrogen. The two lower curves (*c*) and (*d*) were for CO-air mixtures, with the same additions of water and hydrogen. The marked increase in flame velocity due to the presence of even a small quantity of hydrogen presents an interesting challenge and suggests a field for further investigation.

CONCLUSIONS

In the range of variables explored in this investigation:

1 A thin, transparent rubber balloon was found to be a satisfactory substitute for the soap film in the spherical constant-pressure bomb.

2 A satisfactory technique was developed for handling, filling, supporting, igniting, and photographing the bombs made under 1.

3 A procedure was developed for interpreting the photographic record obtained with the drum camera to yield the flame velocity relative to the burned gas, that relative to the unburned gas, and the ratio of expansion.

4 Flame velocities in mixtures of carbon monoxide and oxygen increase with increase in the initial temperature of the moisture-saturated explosive mixture. It was not possible to determine

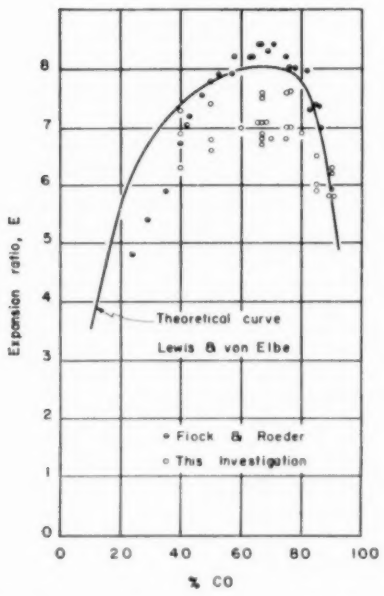

FIG. 8 EXPANSION RATIO AS RELATED TO PER CENT CO IN GAS MIXTURE

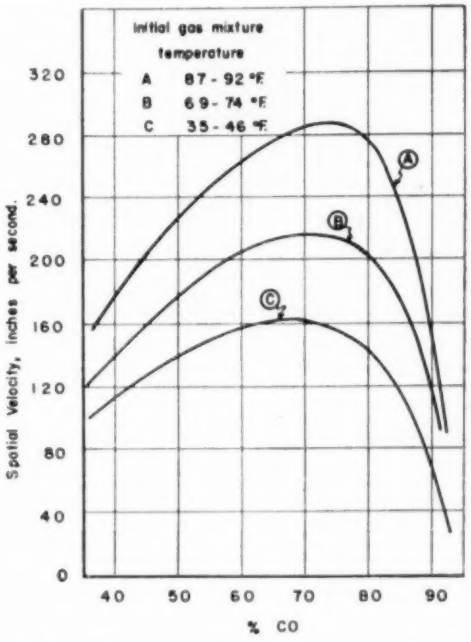

FIG. 10 FAIRED VALUES OF FLAME VELOCITY AS A FUNCTION OF PER CENT CO IN MIXTURE AND INITIAL MIXTURE TEMPERATURE
(All mixtures saturated with water vapor.)

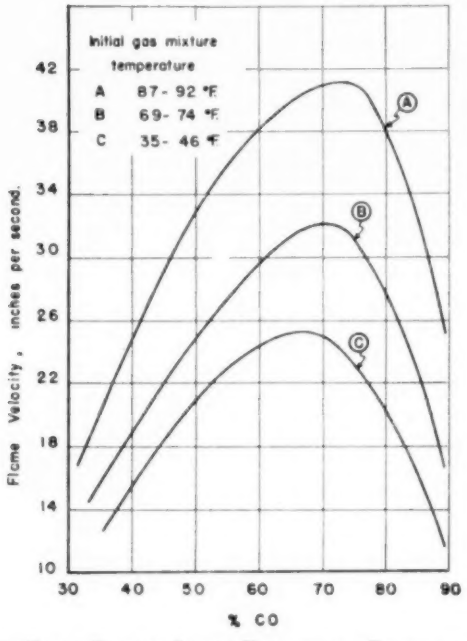

FIG. 9 FAIRED PLOTS OF SPATIAL VELOCITY AS A FUNCTION OF PER CENT CO IN MIXTURE AND INITIAL MIXTURE TEMPERATURE
(All mixtures saturated with water vapor.)

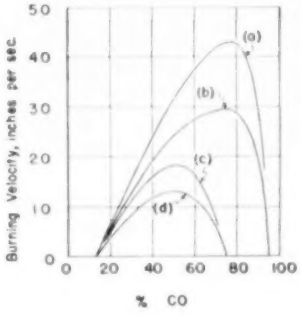

(*a*) CO plus O_2
(*b*) CO (with 1.5 per cent H_2) plus O_2
(*c*) CO plus air
(*d*) CO (with 1.5 per cent H_2) plus air

FIG. 11 EFFECT OF HYDROGEN ON FLAME VELOCITY IN CARBON-MONOXIDE COMBUSTION
(CO contained 1.35 per cent H_2O; O_2 contained 1.5 per cent N_2.)

whether this increase was due to the presence of additional water vapor or to the higher temperature of the unburned CO-O_2 mixture.

BIBLIOGRAPHY

1 "Recherches photometriques sur de flammes colorees," by M. Guoy, Ann. Chim. Phys. (5 series), vol. 18, 1897, pp. 5–101.

2 "Measurements of Flame Velocity by a Modified Burner Method," by F. A. Smith and S. F. Pickering, *Journal of Research*, National Bureau of Standards, vol. 17, 1936.

3 "Flame and Combustion in Gases," by W. A. Bone and D. T. A. Townsend, Longmans Green and Company, London, England, 1927.

4 "Fellowship Report on Flame Ignition Velocities," by J. E. Garside and G. W. Culshaw, Trans. of the Institution of Gas Engineers, vol. 91, 1941, p. 52.

5 "Combustion, Flames, and Explosions," by B. Lewis and G. von Elbe, Academic Press, New York, N. Y., 1951.

6 "Some Effects of Argon and Helium Upon Explosion of Carbon Monoxide and Oxygen," by E. F. Fiock and C. H. Roeder, Tech. Report No. 553. NACA, 1936.

7 "A Photographic Study of Combustion and Knock in a Spark Ignition Engine," by A. M. Rothrock and R. C. Spencer, Tech. Report No. 622, NACA, 1938.

8 "An Investigation of the Mechanism of Explosive Reactions," by C. Z. Rosecrans, Bulletin No. 157, University of Illinois Engineering Experiment Station, 1926.

9 "Fuels, Combustion, and Furnaces," by J. Griswold, McGraw-Hill Book Company, New York, N. Y., 1946, p. 205.

10 "A Constant Pressure Bomb," by F. W. Stevens, Tech. Report No. 176, NACA, 1923.

11 "The Gaseous Explosive Reaction—The Effect of Inert Gases," by F. W. Stevens, Tech. Report No. 280, NACA, 1927.

12 "The Gaseous Explosive Reaction—A Study of the Kinetics of Composite Fuels," by F. W. Stevens, Tech. Report No. 305, NACA, 1929.

13 "The Gaseous Explosive Reaction—The Effect of Pressure on the Rate of Propagation of the Reaction Zone and Upon the Rate of Molecular Transformation," by F. W. Stevens, Tech. Report No. 372, NACA, 1930.

14 "Effect of Water Vapor on Flame Velocity in Equivalent CO-O_2 Mixtures," by E. F. Fiock and H. K. King, Tech. Report No. 531, NACA, 1935.

15 "The Soap Bubble Method of Studying the Combustion of Mixtures of CO and O_2," by E. F. Fiock and C. H. Roeder, Tech. Report No. 332, NACA, 1935.

16 "The Measurement of Flame Speeds," by E. F. Fiock and C. F. Marvin, Jr., *Chemical Review*, vol. 21, 1937, pp. 367–387.

17 "Textbook of Inorganic Chemistry," by J. M. Friend, C. Griffin and Company, London, England, vol. 5, 1921, p. 102.

18 "Explosion and Combustion Processes in Gases," by W. Jost, McGraw-Hill Book Company, New York, N. Y., 1946.

Appendix

A material to substitute for the soap film in the isobaric adiabatic bomb would have to meet the following requirements:

1 Easily formed into a spherical shape.
2 Retention of spherical form during expansion.
3 Able to withstand diametric increase without a measurable pressure rise.
4 Transparency.
5 Good optical reflectivity.
6 Small refractive index.
7 Able to withstand necessary handling when blown.
8 Capable of penetration of electrodes for central ignition.
9 Nonaqueous in composition.
10 Freedom from volatile solvents.
11 Either noncombustible or slow burning.
12 Sufficiently high melting point.
13 Chemical inertness.
14 Substantial impermeability to gaseous interchange.
15 Relatively high impermeability to passage of water vapor.
16 Small gas absorptivity.
17 Readily obtainable.
18 Can be processed easily in laboratory.

The materials given in Table 1 were found to be unsuitable for use in an isobaric bomb. Unsuitable qualities of each substance are listed under Deficiencies, the numbers referring to those in the foregoing.

Operating Experiences With Mechanical Joints in High-Pressure High-Temperature Steam Piping

By E. C. BAILEY,[1] H. C. SCHROEDER,[2] AND I. H. CARLSON,[3] CHICAGO, ILL.

Because of the uncertain life expectancy of austenitic-ferritic steel welds for joining the 2¼ per cent chromium, 1 per cent molybdenum alloy-steel main steam piping to Type 347 stainless alloy steel at the throttle valves of the turbines, two types of mechanical transition joints were installed in the Ridgeland Station of the Commonwealth Edison, Chicago, Ill. The joints, the pressure-seal and the bellows-type were designed for operation on steam at 1800 psig and 1050 F. These joints have operated satisfactorily since the units were put in service. The pressure-seal joints have been in service a total of 1 year and 5 months and the bellows-type joints 1 year.

Introduction

THE Commonwealth Edison Company started installing high-temperature high-pressure (925 F/1250 psig) units in 1935. For this size unit at Fisk Station and the following two installations at Northwest and Fisk Stations, the carbon-molybdenum alloy-steel steam-piping systems were metal-arc-welded and flanged joints at the turbine were of the ring-joint type. No trouble has been experienced with the ring joints in the headers up to the present time; however, graphitization has taken place in the weld-contact zones of the piping and the valve castings. The carbon-molybdenum steel piping has been replaced within the past 2 years with 1 per cent chromium, ½ per cent molybdenum alloy-steel material. The ring joints used on the valve bonnets in these original installations leaked as a result of creep and thermal shock and were replaced with bellows-type gaskets.

The next unit of the system went into service at Calumet Station in 1947. The piping system for this unit was completely welded, and it was of 1 per cent chromium, ½ per cent molybdenum steel. The turbine casings were also of ferritic alloy. One pressure-seal joint and three bellows-type joints were installed in the turbine piping of this unit for a study of their performance under actual operating conditions. Experience to date has been very good, as none of the joints has leaked nor has it been necessary to restress the bolts. Visual inspection of the joints in the spring of 1952, while the unit was being overhauled, after 4 years and 9 months of operation, showed that all the machined surfaces were in excellent condition. The bellows-type gaskets and flanged surfaces required only superficial cleaning to remove magnetic-iron-oxide scale. The pressure-seal joint also required only superficial cleaning to remove magnetic-iron-oxide scale. A new gasket was installed in this joint upon reassembly, although the old gasket appeared to be in good condition.

Authorization for the first unit at the new Ridgeland Station was for the use of 1800 psig and 1050 F steam conditions. The main steam piping for this unit, because of the size, pressure, and temperature, was forged and bored 2¼ per cent chromium, 1 per cent molybdenum steel tubing. The turbine manufacturer used 18 per cent chromium, 8 per cent nickel, columbium-stabilized stainless steel for the high-temperature and high-pressure parts with the result that the terminal points on the throttle valves were austenitic material. The uncertain life expectancy of austenitic-ferritic welds subjected to stress and temperature fluctuations,[4] and the conflicting opinions as to the proper preheat and post-heat-treatment and welding-electrode compositions for these dissimilar welds required to make welds having satisfactory performance life, all combined to make the use of welded connections at the throttle valves questionable.

Based on our experience with flanged joints in the various stations, it was decided to investigate the suitability of several mechanical joints for joining these dissimilar materials. Tests were made on pressure-seal and bellows-type joints of the actual size required for the original installation. The results of these tests were very satisfactory, and it was decided to use pressure-seal joints on the first unit, designated Unit 2 at Ridgeland Station.[5,6]

Description of Unit No. 2

Piping System

Fig. 1 shows the high-pressure high-temperature steam-piping layout for this 150,000-kw unit, using 1800 psig, 1050 F steam. The pressure-seal joints between the 8.5-in-ID, 13.578-in-OD ferritic low-alloy forged and bored steel-tubing steam leads and the 8.5-in-ID 11 13/16-in-OD austenitic stainless forged-steel nozzles on the throttle valves are subjected to resultant moments of only 230,100 in-lb and 208,500 in-lb during operation.

Owing to the cold spring that had to be set up in the piping system and the desirability of blowing it out prior to initial operation of the turbine, it was decided to make the final connection at the first weld upstream from the pressure-seal joints in the 10-in. nominal diameter steam leads. The austenitic halves of the joints were shop-welded to the throttle-valve nozzles by the Westinghouse Electric Corporation, manufacturer of the turbine. The ferritic halves of the joints were shop-welded to the ferritic, forged and bored, steam-lead closure sections by Crane Co., the piping fabricator.

The entire steam-piping system, from the superheater-outlet

[1] Assistant to the Manager of Power Production, Commonwealth Edison Company. Mem. ASME.

[2] Partner, Sargent and Lundy, Engineers. Mem. ASME.

[3] Field Engineer, Engineering Division, Crane Co.

Contributed by the Steam Power Panel of the Joint ASTM-ASME Committee on Effect of Temperature on the Properties of Metals and presented at the Semi-Annual Meeting, Cincinnati, Ohio, June 15–19, 1952, of The American Society of Mechanical Engineers.

Note: Statements and opinions advanced in papers are to be understood as individual expressions of their authors and not those of the Society. Manuscript received at ASME Headquarters, June 25, 1952.

[4] "Review of Thermal Fatigue and Thermal Shock," by Helmut Thielsch, Welding Research Council (to be published soon but available in draft form).

[5] "Performance Tests of Pressure-Seal Pipe Joints," by I. H. Carlson and W. S. Black, *Valve World*, vol. 44, April-May, 1947, pp. 34–44.

[6] "Joints for High-Pressure High-Temperature Piping," by I. H. Carlson and W. S. Black, Trans ASME, vol. 73, 1941, pp. 237–246.

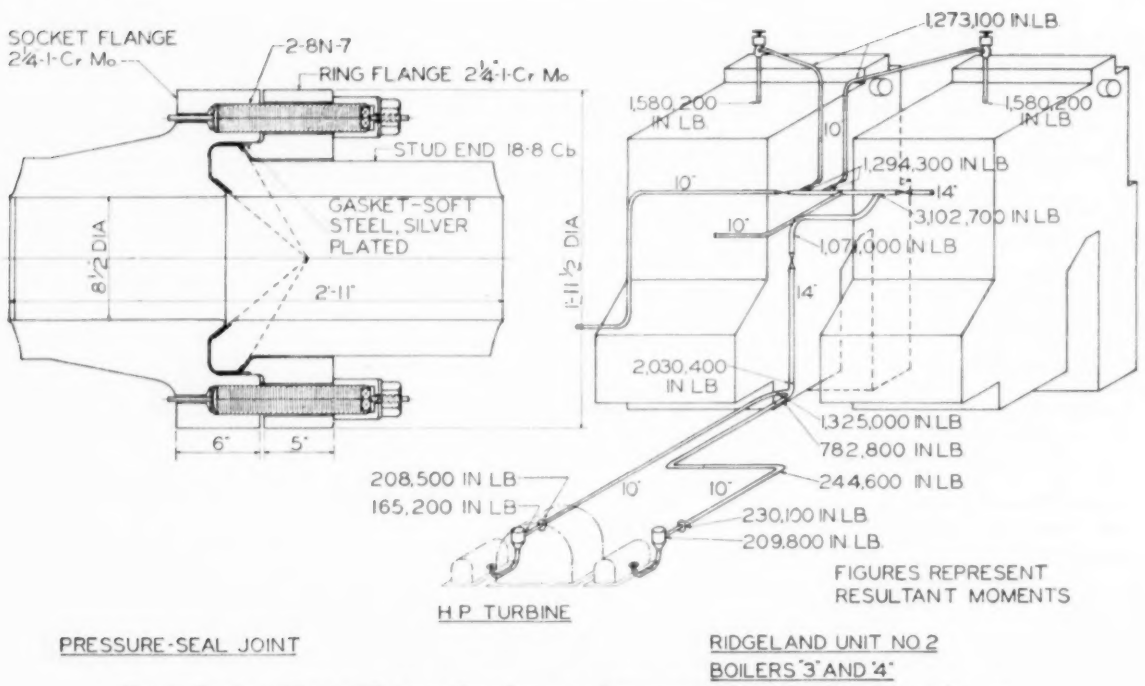

FIG. 1 SECTIONAL VIEW OF PRESSURE-SEAL JOINT AND LOCATION IN PIPING, UNIT 2 RIDGELAND STATION

(Pressure-seal joint is patented and additional patents are pending.)

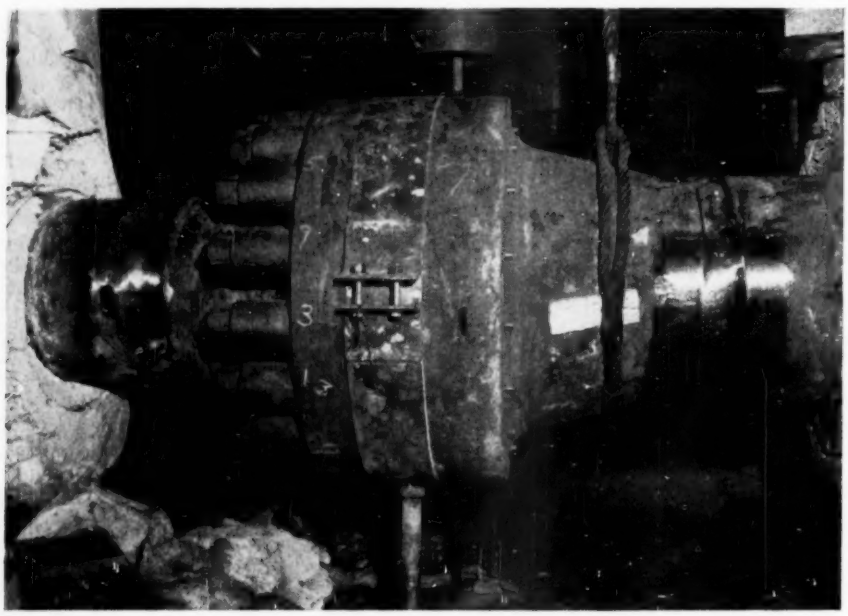

FIG. 2 VIEW OF 10-IN. NOMINAL DIAMETER PRESSURE-SEAL JOINT AT EAST THROTTLE VALVE OF UNIT 2 HIGH-PRESSURE TURBINE AT RIDGELAND STATION

headers down through the manifold and the 14-in. and 10-in. nominal diameter sections of the steam leads to the first welds upstream from the pressure-seal joints was erected, welded, and thoroughly blown out with low-pressure steam. The throttle valves were hung in place and the interconnecting piping to the steam chests was erected and welded. The ferritic halves of the joints with their welded sections were raised into place and the joints were made up.

Fig. 2 shows the 10-in. nominal diameter pressure-seal joint at the east throttle valve of Unit 2 high-pressure turbine. The extension rods fitted into the ends of the bolt studs, the turbine-type nuts, and the strap around the joint, which is part of the leak detector device, can be seen.

Description of Unit No. 1

Piping System

The authorization of Unit 1 at Ridgeland Station again brought up the subject of joining dissimilar metals in the high-pressure high-temperature steam piping. This unit, furnished by the General Electric Company, also uses steam at 1800 psig, 1050 F, and the steam-piping and stop-valve materials are the same as those previously described for Unit 2. Erection and welding of the steam-piping system was performed in the same sequence as was the case in Unit 2. However, instead of welded dissimilar-metal joints or "pressure-seal" dissimilar-metal joints, it was decided to use "bellows-type" dissimilar-metal flanged joints to attach the ferritic steam leads to the austenitic stop-valve-inlet nozzles.

Fig. 3 shows the piping system and the joint details for this unit. These flanged joints adjacent to the turbine stop valves are subject to only 161,700 in-lb resultant moments when the unit is in operation. In the course of erection of this piping, the cold pull required and the necessity of blowing out the system thoroughly with wet steam before installing the closure pieces at the turbine stop valves made it desirable to install the closure pieces, make up the flanged joints, and make the final closure at the first weld upstream from the flanged joints.

Fig. 4 shows the 10-in. nominal diameter, bellows-type joints at the stop valves of Unit 1 high-pressure turbine. The stop valves, the turbine-type nuts on the flanged joints, and the extension rods fitted in the end of the bolt studs can be seen. The leak-detector devices were installed after this view was taken.

Assembly of Joints

The methods of assembling the pressure-seal and the bellows-type joints were quite similar.

All contacting surfaces of component parts of the transition joints were cleaned thoroughly just before assembly and the bolt threads and bottom of nuts lubricated with Crane high-temperature thread compound. The seal ring, bellows gasket, and other contacting surfaces were lubricated with a light oil upon assembly. In the assembly, care was taken to insure that the bolt studs were tightened evenly all around so that the flange faces were kept parallel.

The bolt studs were tightened using slugging wrenches until elongation necessary for the desired stress was produced. Elongation was measured, across center-punched ends of extension rods fitted into the ends of the bolt studs, by means of an extensometer equipped with a 1/1000-in. indicating dial.

Bolting

Westinghouse K-42-B alloy steel, a chromium-nickel-cobalt alloy, was selected as the material for the bolt studs because of its satisfactory physical characteristics at high temperature and a coefficient of expansion slightly higher than that of the ferritic alloy-steel flanges. The nuts are "turbine type" of 2¼ per cent chromium, 1 per cent molybdenum alloy steel.

In order to prevent the possibility of the bolt studs freezing in the tapped holes of the flanges, the threads were cut in accordance with American Standard B1.4 1945, Class 7 fit, which provides for a clearance between the pitch diameters of the stud and hole. Tests and experience have indicated that threads cut in this manner can be disassembled with ease, even after prolonged periods of service and numerous cycles of heating and cooling, providing that the proper thread compound is employed. Care must be exercised at assembly to avoid bottoming the stud in the tapped hole or engaging the imperfect threads due to tap lead.

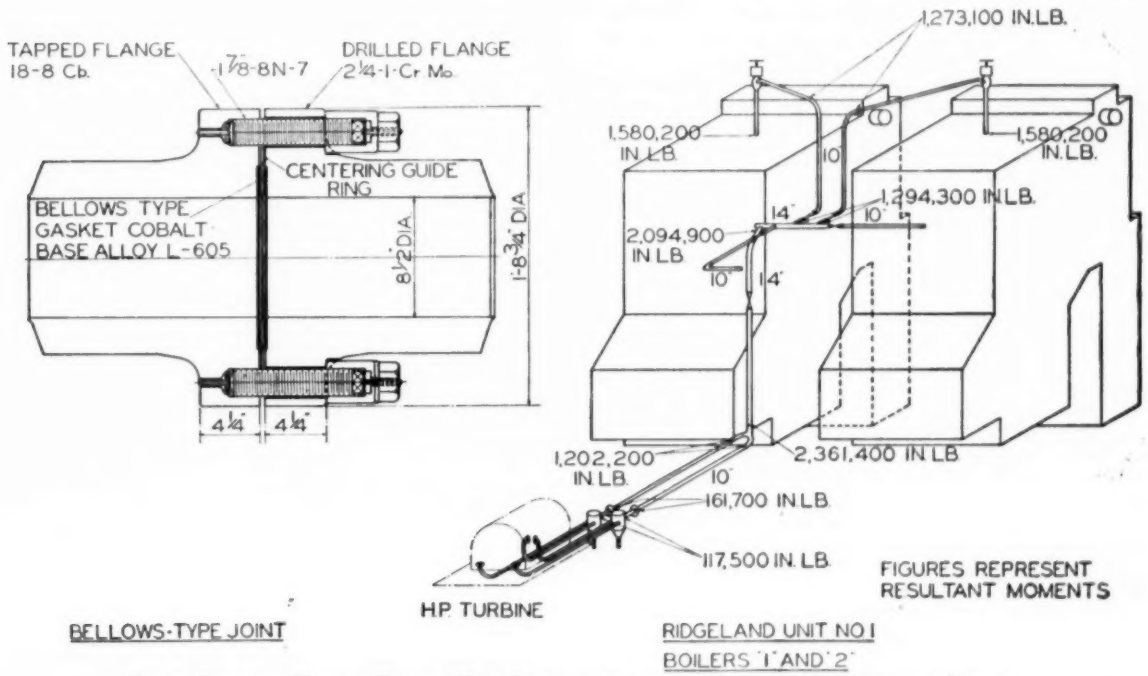

Fig. 3 Sectional View of Bellows-Type Joint and Location in Piping, Unit 1 Ridgeland Station
(Patent pending on bellows-type joint.)

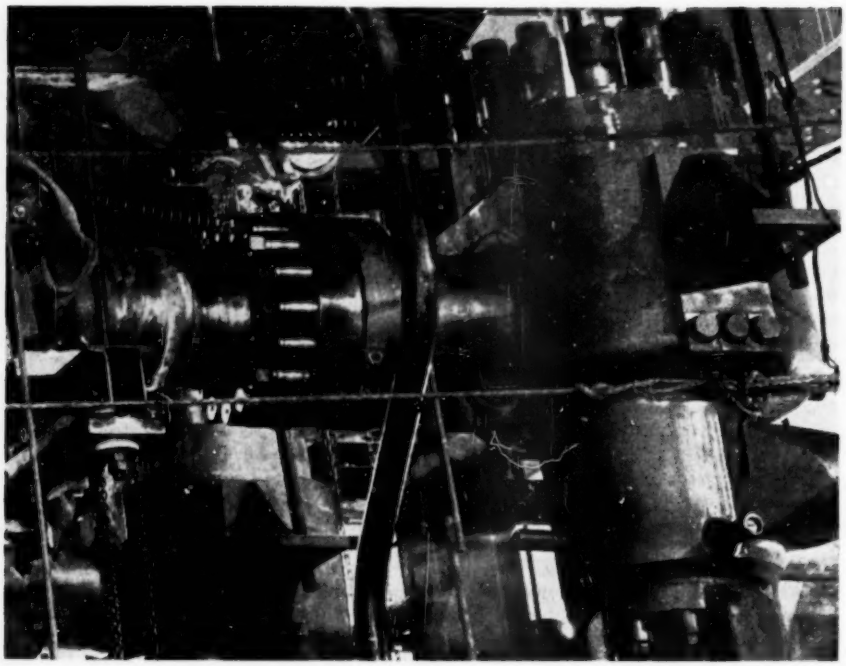

FIG. 4 VIEW OF 10-IN. NOMINAL DIAMETER BELLOWS-TYPE JOINTS AT STOP VALVES OF UNIT 1 HIGH-PRESSURE TURBINE AT RIDGELAND STATION

SERVICE RESULTS

Pressure-Seal Joints. The bolting in the pressure-seal joints on Unit 2 was initially stressed to 20,000 psi, and after a period of 32 hr at 860 F an opportunity arose to check the stress in the bolt studs. At this time the average residual stress was found to be 14,000 psi, a loss of 6000 psi stress, which is about normal for this type of joint after being made up and in service a while. This loss is due primarily to the "coining" of the soft-steel seal ring when initially placed in service. The bolting was then restressed to 20,000 psi and the joints placed back in service.

In checking the relaxation, all of the studs were measured for a check against the original stressed readings at the time the joints were assembled. Then four bolt studs 90 deg apart were loosened so that their free length could be measured to determine the amount of creep. The bolting was then restressed on the basis of the average relaxation found in the four bolt studs. Thread lubricant was not used at this time.

During the inspection and overhaul of this unit in April, 1952, the bolt stress was again checked. It was found that the residual stress in the bolt studs averaged 6200 psi. Also, measurement of the free length of the bolt studs revealed that no creep had occurred. When disassembling the bolt studs, once the nuts were broken loose, they could be unscrewed easily from the bolt studs by hand. The bolt studs also unscrewed easily and required only hand power for breaking loose. All nuts and bolts were in excellent condition, with no evidence of galling. Further data will have to be obtained after additional time in service before any definite conclusions can be drawn.

These pressure-seal joints which have been in service a total of 1 year and 5 months, at 1800 psig 1050 F, have been tight at all times.

Bellows-Type Joints. Because of the unavailability of K-42-B alloy at the time Unit 1 was ready to go into operation, it was necessary to employ temporarily Templex chromium-molybdenum-vanadium alloy steel, Grade B14 ASTM A-193 bolt studs in the two bellows-type joints. In this interim period, the bolting was restressed once. The same procedure as for the pressure-seal joints was followed in checking for relaxation and restressing. Later, they were replaced with bolt studs of the K-42-B alloy. In replacing the Templex bolt studs with K-42B alloy, four bolts 90 deg apart were removed at a time. Upon disassembly, it was noted that once the nuts were broken loose, they could be unscrewed from the bolt studs by hand. The bolt studs also unscrewed easily and required only hand power for breaking loose. All nuts and bolts were found to be in excellent condition, with no evidence of galling. Average initial and residual stresses for each period of operation are given in Table 1.

TABLE 1 ASSEMBLY DATA ON BELLOWS-TYPE JOINTS IN MAIN STEAM PIPING TO TURBINE OF UNIT 1

Bolting material	Description of assembly conditions		East joint	West joint
Crane Templex chromium-molybdenum-vanadium alloy steel Grade B14 ASTM A-193	Bolt stress, psi	Initial loading	21700	23100
		Residual after 432 hr at 1050 F	13500	10600
		Retightened after 432 hr at 1050 F	21800	21800
		Residual after 1032 additional hr at 1050 F	11100	9700
Westinghouse K-42-B chromium-nickel-cobalt alloy	Initial bolt stress loading, psi		21400	21000
	Total number of hours in service at 1800 psi 1050 F steam up to June, 1952		7268	

The bellows-type joints on this unit have been in service at 1800 psig, 1050 F, a total of 8700 hr, up to June 1, 1952, and have been tight at all times.

A comparison of stress data on the Templex steel bolt studs with relaxation test data on the material from the same heat is given in Fig. 5. The relaxation curves have been estimated for

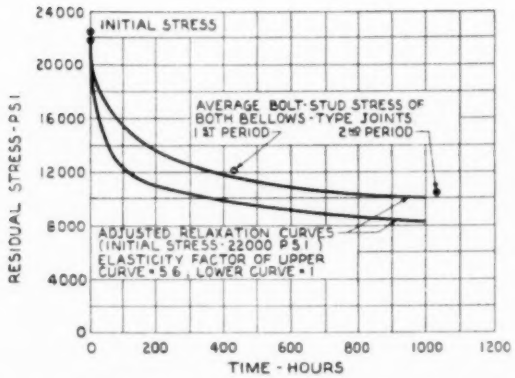

FIG. 5 COMPARISON OF BOLT STUD STRESS WITH RELAXATION DATA FOR TEMPLEX STEEL—1025 F TEMPERATURE

1025 F, average temperature of bolt studs as determined by thermocouples.

It should be noted that the two methods of stressing the bolt material differ somewhat. With a flanged joint, the bolting is pulled up at room temperature and measurement of residual bolt stress is made after cooling to room temperature. In the relaxation test, stress is applied to the test bar only after temperature equilibrium has been attained, and all measurements are made while the bar is at temperature.

Relaxation data were obtained on a testing unit, Fig. 6, designed essentially to simulate conditions existing in the bolting of high-temperature flanged joints. The initially applied stress decreases as creep occurs in the test bar. However, the machine itself acts as an elastic flanged member and tends to prevent the load from falling off. The ratio of elasticity of the machine to that of the test bar is 5.6. The data for unity elasticity factor was obtained in a conventional-type creep-test unit by reducing the applied load from time to time, so as to maintain the initial strain in the test bar.

As indicated by the data in Fig. 5, good agreement was obtained between the bolt stud and relaxation-test data, providing that the ratios of elasticity of the machine and of the flanged joint were about the same. These data indicate that at 1025 F temperature with Templex bolting material, the residual stresses would decrease to a relatively low value after more prolonged service exposure. In a period of 10,000 hr (about 1 year), the residual stress may amount to no more than 6000 psi.

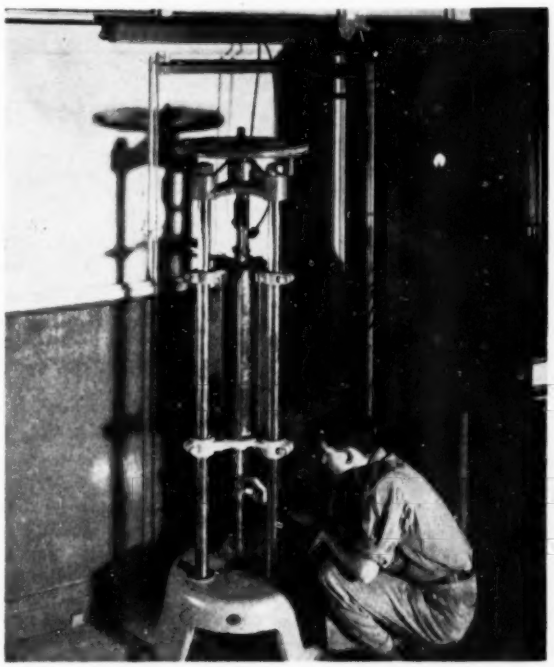

FIG. 6 RELAXATION TESTING UNIT

CONCLUSION

This progress report indicates that both pressure-seal and bellows-type joints have given satisfactory service for a period of 1 year and 5 months and 1 year, respectively.

Relative Abrasiveness of the Cast Surfaces of Various Gray-Iron Castings on Single-Point Tools of High-Speed Steel

By JOSEPH DATSKO[1] AND O. W. BOSTON,[2] ANN ARBOR, MICH.

This study reveals that plain gray-iron castings made in sand molds have a very abrasive surface that results in a low tool life when machining the surface. This condition can be eliminated almost completely by pickling the castings prior to machining. Annealing improves the machinability of the casting, but it also results in a more pronounced "skin effect." By means of an annealing and pickling treatment, the cutting speed for removing the surface was increased by 230 per cent.

DURING the past 50 years a great deal of machinability data have been compiled on many compositions of cast gray iron. Many studies have dealt with the effects of the various microstructures, such as pearlite, ferrite, and graphite. In most of these machinability tests, based on the cutting speed-tool life relationship, it has been customary to remove the cast surface with the outer $^1/_8$-in. to $^1/_2$-in. layer of material to make certain that the iron being tested was uniform and free from surface defects. Although these data make it possible for the metallurgical engineer to compare and select the various compositions of gray iron according to their relative ratings, it does not indicate to the production engineer, whose chief concern is the removal of the outer $^1/_8$ in. of the casting, what the optimum or proper cutting speed should be for his particular conditions.

The surface of any casting made in a sand mold has impregnated in it particles of sand, clay, oxides, and silicates as a result of the contact of the liquid iron with the surface of the mold cavity. Ever since cast iron has been machined, it has been known that the skin of the casting is more detrimental to a cutting tool than the interior. Experience has shown that if a depth of cut of 0.010 to 0.030 in. is used when removing the scale, the cutting tool fails very rapidly; if the casting is of the high-strength type, the tool will not cut at all. However, if a cut approximately $^1/_8$ in. deep is taken, the surface can be removed. It is believed by many men engaged in the machining of castings that it is possible to alleviate the detrimental effects of the skin upon the cutting tool simply by taking a deep cut.

On the contrary, some preliminary work[3] showed that the interior of No. 1 gray-iron castings could be machined at a cutting speed 85 per cent higher than that used in removing the surface for the same tool life. Furthermore, it demonstrated that the machinability of a cast surface could be evaluated and that the detrimental effects could be overcome by a pickling process. Consequently, a more extensive study was undertaken.

Test Procedure

A study of this problem by means of photomicrographs discloses simply that there is a thin, decarburized layer beneath the oxide and silicate scale. Therefore it was decided that it would be more convenient and beneficial to evaluate the relative abrasiveness of the surface after subjecting it to various treatments such as tumbling, shot-blasting, pickling, annealing, and oxidizing.

Castings. The castings used in this project had the following dimensions: 6 in. OD, 4 in. ID, and 18 in. length. The cylinders were poured in a horizontal plane. To insure sound castings, four gates were provided to feed the castings and particular care was taken to keep the mold cavity as clean as possible of all loose sand. The metal contained 3.25 per cent total carbon and 2.28 per cent silicon with a tensile strength of 36,000 psi and a hardness of 190 Bhn. The sulphur, phosphorus, and manganese were 0.12 per cent, 0.25 per cent, and 0.62 per cent, respectively. The combined carbon varied from 0.56 per cent to 0.78 per cent. Castings were made both in molds coated with facing sand and also molds using floor sand throughout.

Cutting Tools. The cutting tools used were of the 18-4-1 high-speed-steel type, $^3/_8$ in. square. They were finish-ground on the flank with a 60-grit wheel, and on the face with a 46-grit wheel to the following shape: 8, 14, 6, 6, 6, 15, $^3/_{64}$ (ASA designation). The surface quality was 4 microinches rms on the flank and 19 on the face as read on the profilometer.

Cutting Conditions. All cutting was done dry on a heavy-duty 14-in. American "Pacemaker" engine lathe having a 15-hp Reliance variable-speed drive. To duplicate the commercial cutting practice as much as possible, a depth of cut of 0.100 in. and a feed of 0.00625 ipr were used. In determining the tool life, the tools were run to complete failure by allowing the flank abrasion to develop sufficient heat between tool and work to cause the sudden breakdown of the tool as shown in Fig. 1.

Cutting Forces

It was desired to measure cutting forces under conditions approaching as closely as possible those used in industry. This required having the dynamometer of the same size and shape as the commercial toolholders and of equivalent rigidity to eliminate the possibility of excessive vibrations and chatter. Therefore a two-component electric-resistance strain-gage dynamometer was made from an SAE 1040 steel, size $^3/_4 \times 1^1/_4 \times 6$ in. Four active gages were mounted near the top and bottom fiber axes enabling permanent force readings to be made on an oscillograph tape in the range of $^1/_2$ to 1000 lb. Both the cutting force F_T and feeding force F_L were measured on the castings.

Effect of Hardness. In cutting a metal, it is clearly shown by a dynamometer of this type that the cutting force is not uniform, but that it regularly increases and decreases within two definite

[1] Instructor in Production Engineering, University of Michigan.
[2] Professor of Mechanical and Production Engineering; Chairman of Department of Production Engineering, University of Michigan. Fellow ASME.
[3] "Acid Pickle Doubles Tool Life on CI," by Joseph Datsko, *American Machinist*, vol. 95, June 11, 1951, pp. 140-141.

Contributed by the Production Engineering Division, Metal Cutting Data and Bibliography, and Cutting Fluids Research Committees, and presented at the Semi-Annual Meeting, Cincinnati, Ohio, June 15–19, 1952, of The American Society of Mechanical Engineers.

Note: Statements and opinions advanced in papers are to be understood as individual expressions of their authors and not those of the Society. Manuscript received at ASME Headquarters, March 10, 1952. Paper No. 52—SA-17.

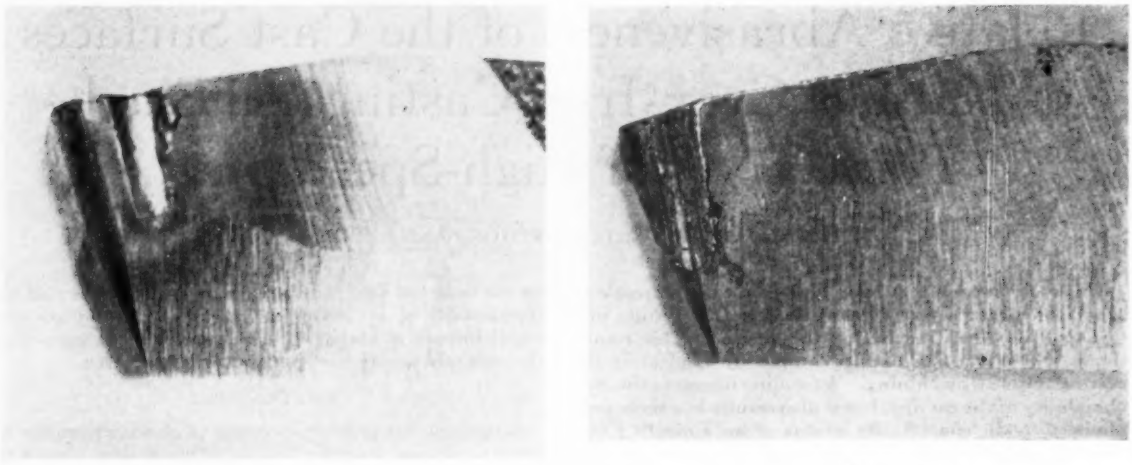

(a) (b)

FIG. 1 TYPICAL TOOL FAILURES

In *a* is shown nature of failure when machining surface of as-cast castings. Actual failure occurs 0.100 in. back of point while point itself is worn only a few thousandths of an inch. The tool failure when machining the interior is illustrated in *b*.)

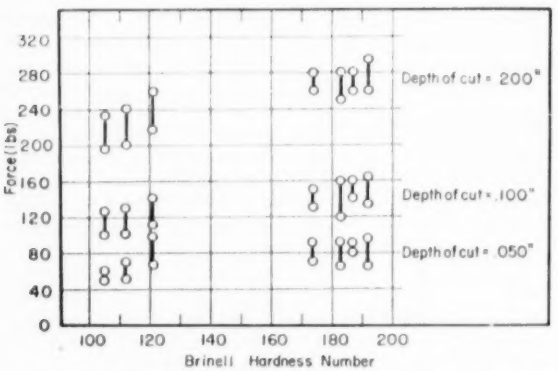

FIG. 2 EFFECT OF BRINELL HARDNESS OF GRAY IRON UPON CUTTING FORCE

(Maximum and minimum values are indicated. Cutting was done dry with a feed of 0.00625 ipr and cutting speed of 25 fpm with a tool shape of 8, 14, 6, 6, 6, 15, 1/16. Average force may be expressed as a function of hardness as follows: $F = 0.64B + 155$ for 0.200 in. depth; $F = 0.43B + 67$ for 0.100 in. depth; and $F = 0.34B + 17$ for 0.050 in. depth.)

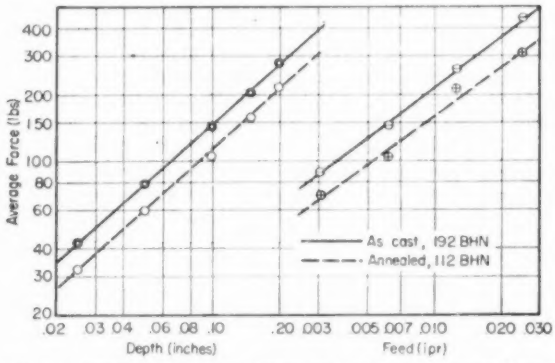

FIG. 3 EFFECT OF FEED AND DEPTH OF CUT UPON CUTTING FORCE

(Feed was constant at 0.00625 ipr when evaluating effect depth; depth was constant at 0.100 in. when evaluating feed. Cutting speed was 25 fpm with a tool shape of 8, 14, 6, 6, 6, 15, 1/16 in.)

limits as indicated in Fig. 2. Apparently this is due to the nature of the chip formation which may be described as a series of intermittent slippages of one part of the metal with respect to an adjacent area.

Fig. 2 shows the nature of the relationship between the hardness of gray iron and the cutting force at each of three depths of cut. The cutting force increases more or less linearly with the Brinell hardness number from an average value of 218 lb for a hardness of 105 to 275 lb for a hardness of 193. These values are for a 0.200-in. depth and a 0.006-ipr feed. By successively decreasing the depth of cut by one half, the force decreases by slightly more than 50 per cent.

Effect of Feed and Depth. The manner in which the cutting force varies with the size of cut may be seen in Fig. 3 which typifies the results obtained on both the as-cast pearlitic material and the annealed ferritic material. These may be expressed by the equations $F_T = 51{,}400\ f^{0.75}\ d^{0.89}$, and $F_T = 36{,}100\ f^{0.73}\ d^{0.90}$ for the as-cast and annealed irons, respectively. Thus it is evident from this figure that the cutting force is decreased by approximately 25 per cent for an average-size cut by annealing the pearlitic gray iron. However, no definite trend of the cutting forces was observed between the surface and the interior cuts.

CUTTING SPEED AND TOOL LIFE

The main emphasis of this investigation was on tool life, or more correctly, on the cutting speed for a constant tool life, since industry is interested in the cutting speed at which an operation can be performed, as this necessarily influences the cost of the manufactured article. On the other hand, the cutting forces determine the power consumed, which is insignificant compared to the cost of the labor.

Heat No. 1—170 Bhn. Fig. 4 shows the results obtained in the turning of six test cylinders—three tumbled castings, and three castings whose surfaces were pickled in hydrofluoric acid for 45 min. It is readily apparent that the machinability of the surface of a casting is noticeably inferior to the interior. That this surface is more abrasive than the interior is proved by the nature of the tool failure which is illustrated in Fig. 1. There it is seen that the tool failure when removing the surface with a 0.1 depth of cut occurs by flank wear at that part of the tool that contacts

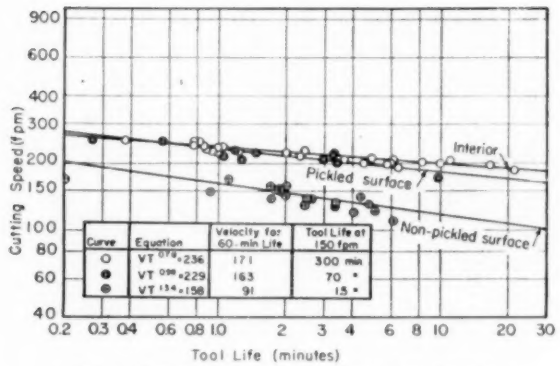
Cutting Speed (fpm)
Tool Life (minutes)
Interior
Pickled surface
Non-pickled surface
Curve | Equation | Velocity for 60-min Life | Tool Life at 150 fpm
O | VT^0.76=236 | 171 | 300 min
● | VT^0.98=229 | 163 | 70 "
◉ | VT^1.34=158 | 91 | 15 "

FIG. 4 CUTTING-SPEED VERSUS TOOL-LIFE CURVES

(Composition of these irons is as follows: Total carbon, 3.45 per cent; graphitic carbon, 2.81 per cent; silicon, 2.94 per cent; sulphur, 0.12 per cent; phosphorus, 0.26 per cent; manganese, 0.58 per cent.)

the thin skin with very little wear at the point or radius of the tool. On the other hand, the tool failure when cutting the interior of the casting occurs at the point of the tool where the heat of the cutting operation is concentrated.

For a comparison of the machinability of this iron, the data in Fig. 4 reveal that the cutting speed for a 20-min tool life (referred to as V_{20}) is 105 fpm for the tumbled surface, 173 fpm for the pickled surface, and 184 fpm for the interior of the casting. Thus it is apparent that the interior of a casting can be machined 75 per cent faster than the abrasive surface, and that by means of an acid pickle the machinability of the as-cast surface may be increased by 65 per cent.

Heat No. 2—190 Bhn. Figs. 5 and 6 portray the machinability of No. 2 gray-iron castings after various annealing and pickling treatments and the velocities for 20-min tool life are summarized in Table I.

TABLE I CUTTING SPEEDS FOR A 20-MIN TOOL LIFE

Cutting condition	Bhn	Velocity (fpm) for 20-min tool life	Increase, per cent
As-cast surface	190	94	Base
As-cast, interior	190	144	53.2
Pickled surface	187	135	43.7
Annealed surface	105	160	61
Annealed, oxidized interior	121	190	102
Annealed interior	121	287	208
Annealed, pickled surface	116	310	230
Annealed interior	105	390	315

Fig. 5 shows that the surface of the No. 2 iron is about as abrasive as that of the No. 1 iron previously discussed. Also, by means of an electrolytic[4] pickle, the surface is made almost as machinable as the interior. Thus, for a 20-min tool life, the as-cast surface can be machined at 94 fpm while the interior may be machined at 144 fpm, which is an increase of 53 per cent. However, by pickling the surface, it may be machined at 135 fpm or 44 per cent faster than the nonpickled surface.

Since many companies anneal their castings before machining to improve their machinability, an important aspect of this project was to determine whether annealing removed the skin effect that is present in the unannealed castings. The curves designated as A in Fig. 5 showed that the machinability of the casting is improved by annealing, but it also results in a more pronounced skin effect because the machinability of the interior is increased to a greater extent than that of the surface. To illustrate, V_{20} is increased from 94 fpm for the as-cast surface to 160 fpm for the annealed surface, and 390 fpm for the annealed interior. Thus

[4] The electrolytic pickling was done by the Kolene Treating Company, Detroit, Mich.

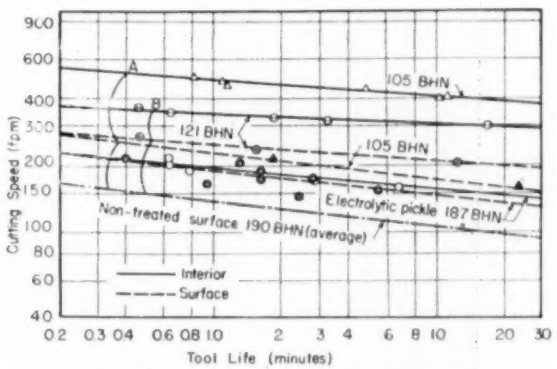

FIG. 5 CUTTING-SPEED VERSUS TOOL-LIFE CURVES

(The average composition of these irons is: Total carbon, 3.28 per cent; graphitic carbon, as-cast, 2.60 per cent; graphitic carbon, annealed, 3.18 per cent; silicon, 2.28 per cent; sulphur, 0.12 per cent; phosphorus, 0.25 per cent; manganese, 0.62 per cent. Lower hardnesses are result of annealing. Curves designated as A and B each refer to same casting.)

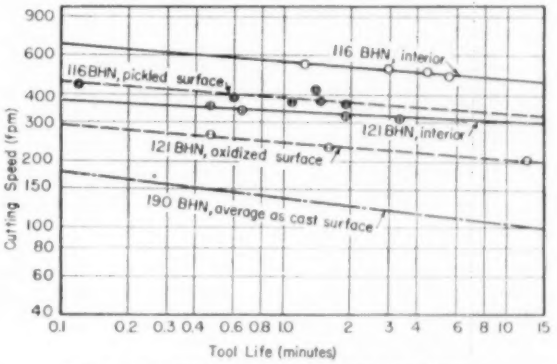

FIG. 6 CUTTING-SPEED VERSUS TOOL-LIFE CURVES

(Composition of iron is the same as shown in Fig. 5. Oxidized surface is sand-free.)

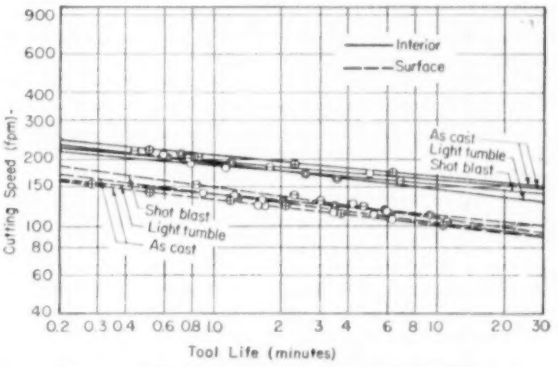

FIG. 7 CUTTING-SPEED VERSUS TOOL-LIFE CURVES

(The "light-tumble" and "shot-blast" designations with interior curves are simply to identify castings. Interiors were not subjected to these treatments prior to machining.)

the machinability of the surface is increased 61 per cent by annealing whereas the interior can be machined 315 per cent faster.

Naturally the next question to consider is whether pickling will improve the machinability of the annealed surface. Fig. 6 shows that by means of a 20-minute electrolytic pickle, the V_{20} is raised to 310 fpm, which is a 230 per cent increase over the as-cast con-

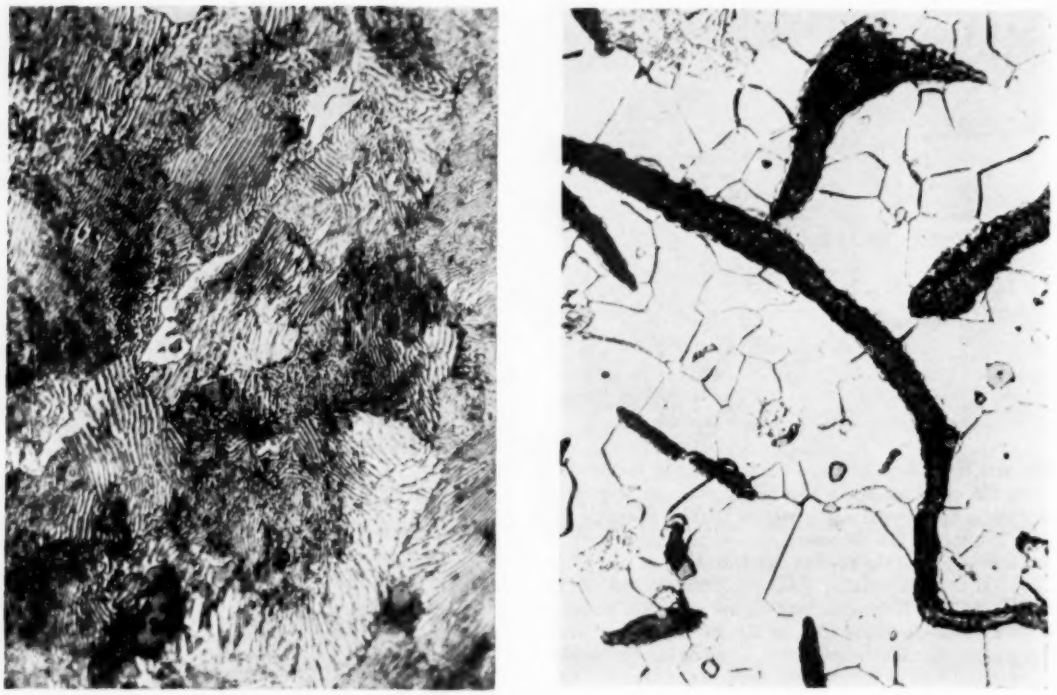

(*a*) (*b*)

FIG. 8 PHOTOMICROGRAPHS OF INTERIOR OF GRAY-IRON; ×500
(As-cast condition *a* is pearlitic. Annealed iron is ferritic as in *b*.)

dition and a 95 per cent increase over the annealed, unpickled surface. In other words, by means of a pickling treatment, the cutting speed while machining the surface can be nearly doubled.

To determine whether iron oxide without the presence of sand or silicates on the surface would result in a tool failure of the type shown in Fig. 1(*a*), a sand-free oxidized surface was obtained on a casting by first removing the outer 1/4 in. and then annealing the casting in an oxidizing atmosphere. The results of this test are shown in Figs. 5 and 6 by the curves designated with 121 Bhn. The fact that the oxidized surface is very abrasive can be readily discerned from these two figures. On the basis of V_{20}, the interior of this casting can be machined 50 per cent faster than the oxidized surface.

Fig. 7 illustrates the relative merits of shot-blasting and tumbling compared to the as-cast surface. The reason for the spread in the lines indicating the machinability of the interiors is a slight difference in the microstructure of the castings, since they are identical in every other respect. It appears that shot-blasting and tumbling do not increase the machinability of the surface by any appreciable amount.

Microstructures and Surface Conditions. Fig. 8(*a*) shows the microstructure of the interior of the as-cast iron consisting almost completely of pearlite. Although graphite flakes are present, they are not visible in this photomicrograph. The V_{20} for this microstructure is 144 fpm with a hardness of 190 Bhn. In Fig. 8(*b*) is seen the microstructure of the interior of an annealed casting, which consists of ferrite, flake graphite, and less than 5 per cent pearlite. Hardness of this iron was 105 Bhn; the V_{20} was 290 fpm.

In Fig. 9 (on the facing page) are photomicrographs revealing the nature of the surface condition of iron castings. Photomicrographs (*a*) and (*b*) show the same area in the unetched and etched condition, respectively, of a tumbled casting. An idea of the surface roughness and minute defects that are present may be obtained from (*a*). Also, the lack of graphite flakes near the surface indicates a thin decarburized layer. From (*b*) it is seen that the surface consists mainly of pearlite with a small amount of ferrite. The flake graphite, of course, is present.

Photomicrographs (*c*) and (*d*) portray the same area on the surface of a shot-blasted casting. The microstructure is the same as in (*a*) and (*b*). However, a marked improvement in the surface roughness is obtained by means of shot-blasting, which eliminates most of the sharp jagged peaks visible in photomicrograph (*a*).

CONCLUSIONS

The scope of this project was to compare the relative abrasiveness of some gray-iron surfaces on high-speed-steel tools. As previously noted, all tests were run at 0.100 in. depth and 0.00625 ipr feed with encouraging results. However, heavier cuts, especially feeds, may yield different results. In fact, some previous investigators[5] have found in cutting iron, alloyed with nickel and chromium, that the surface was more machinable than the interior. This work was done on much larger castings with a 0.050-in. depth and a 0.0255-ipr feed.

The fact that a pickling treatment prior to machining is advantageous is borne out by several manufacturing firms that installed electrolytic pickling units to remove sand from internal cores of components of sealed-in hydraulic systems. It was found that their tool life was noticeably increased when machining these treated parts.

[5] "Metal Processing," by O. W. Boston, John Wiley & Sons, Inc., New York, N. Y., 1951, second edition, p. 159.

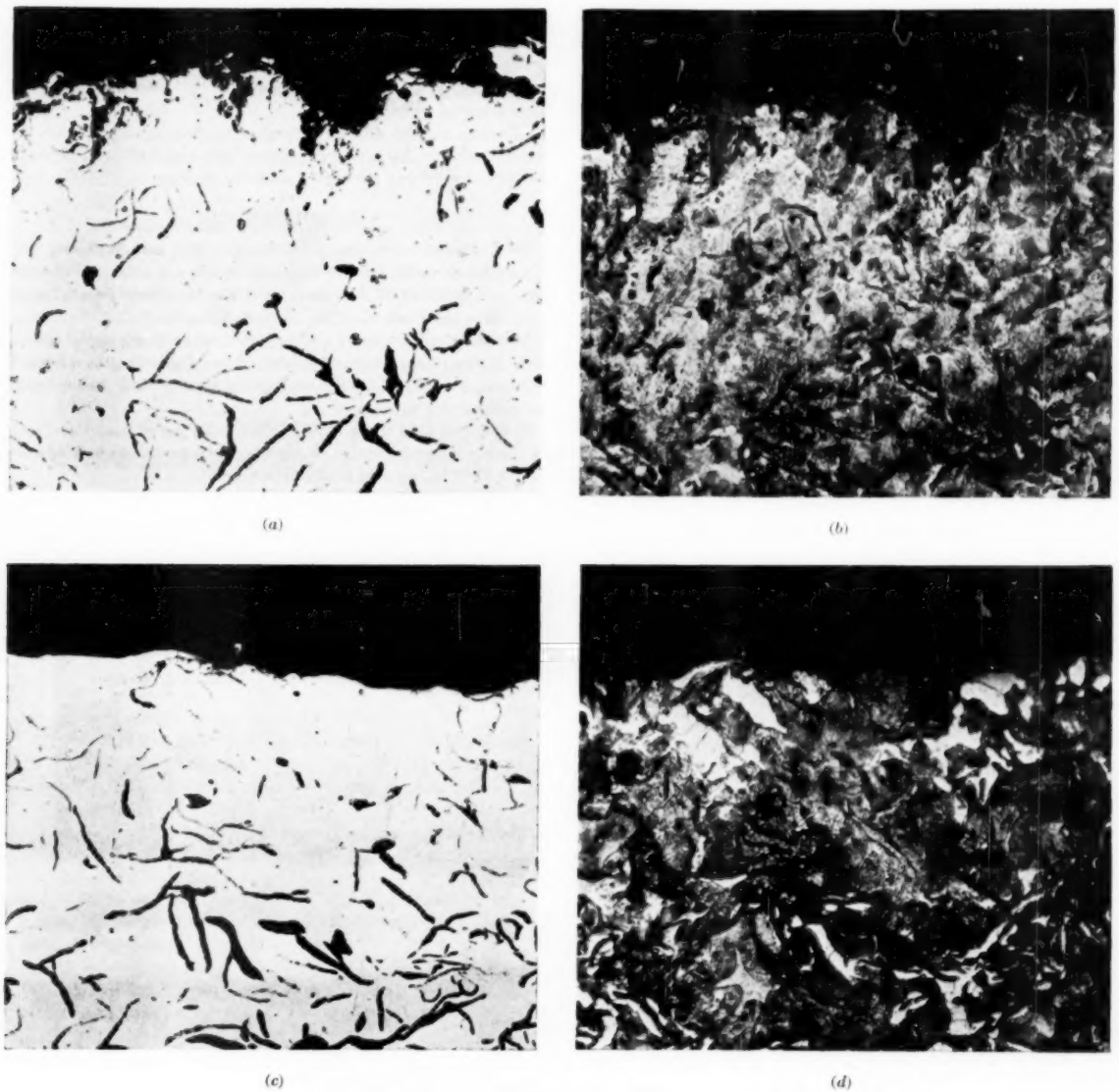

(a) (b) (c) (d)

FIG. 9 PHOTOMICROGRAPHS OF CAST SURFACES; ×100

(a, Unetched tumbled surface reveals rough decarburized surface. b, Etched tumbled surface reveals pearlitic structure. c, Unetched shot-blasted surface. Shot-blasting produces a smoother surface than tumbling. d, Etched shot-blasted surface shows pearlite and ferrite.)

Discussion

J. A. FALER.[8] We wish to commend the authors of this paper for their excellent observation of a subject generally ignored by metallurgists. Since a large percentage of production machining is the removal of the cast surface, an evaluation of the machinability of these surfaces is of genuine interest to production engineers.

Our personal interest in this information is a result of the observation of the operation of electroytic salt-bath processes installed for the removal of burned-in sand, scale, and so forth, from castings used in hydraulic and lubrication systems.

It was observed at one plant, on an operation involving facing, boring, and chamfering stress-relieved gray-iron housings with single-point carbide tools, that there was approximately a 100 per cent increase in tool life, with electrolytic salt cleaning of the surfaces over sandblasting.

With brass and bronze, the removal of sand inclusions much more noticeably affects tool life. In one case an improvement of several hundred per cent was noted.

It is apparent that much faster cutting speeds and longer tool life can be obtained by the removal of scale, burned-in sand, and sand inclusions. This is especially noticeable in making forming cuts. On an experimental setup it was determined that a gray-iron cast surface that had been prepared in an electrolytic salt bath had only slightly more abrasiveness than the base metal

[8] Chief Engineer, Kolene Corporation, Detroit, Mich. Mem. ASME.

(as determined by tool wear). At the same time, the tool wear was less than one tenth that experienced with the same type of casting prepared by tumbling only. An even more pronounced difference has been shown to exist in a spot-facing operation.

Preliminary estimates of one company show a possible tool saving of over $350,000.00 per year on machining three parts for one engine alone if the abrasiveness of the "as-cast" surfaces could be made to approach that of the base metal.

D. H. Mills.[7] In reply to this excellent paper the writer concurs heartily with the authors. His research experience is limited, however, to the heated sodium-hydroxide process of dissolving the sand from the surface of castings. Further experience with tool life in machining high-alloy cast valves shows a parallel condition after making proper allowance for the more-difficult-to-machine alloy.

Microscopic examination of castings showed that a minimum of shot blasting and tumbling prior to the sand-dissolving process is desirable because the tumbling and blasting can and do peen the metal right over some of the sand particles. This prevents the solution from contacting the impacted sand particles and they constitute an abrasive trapped in a softer matrix and are therefore capable of making score lines on the tool bit which, in effect, is accelerated wear.

Cleaning out the skin sand resulted in making these high-alloy castings machinable where previously grinding had been the only method of reducing them to usable dimensions.

[7] Ford Motor Company, Manufacturing Research, Dearborn, Mich.

Authors' Closure

The authors very much appreciate the comments of Mr. Faler who gives additional evidence on the advantage of electrolytic salt cleaning of cast surfaces. The results in general seem to confirm those based on the tests of the authors.

Mr. Mills' discussion is also appreciated as he gives the results of additional experience when machining high-alloy cast metals and compares shot blasting and tumbling and their value to the sand-dissolving processes.

It is hoped that the results given in this paper may be of help to those concerned with the machining of cast metals where retained sand in the skin is objectionable.

The Significance of the Thermal Number in Metal Machining

By B. T. CHAO[1] and K. J. TRIGGER,[2] URBANA, ILL.

The theoretical analysis of heat flow in conjunction with cutting data in high-speed orthogonal metal-machining operations reveals that, for a given tool rake, the temperature distribution along the shear plane is solely dependent on the thermal number, $V_c t/k$. An explanation is offered for the difference in chip curvature as the cutting conditions are changed. Further significance of the thermal number in metal machining is presented.

Nomenclature

The following nomenclature is used in the paper:

- c = average specific heat of work material
- J = mechanical equivalent of heat
- k = thermal diffusivity of the work material = $\frac{K}{c\rho}$
- K = average thermal conductivity of work material
- q = rate of heat liberation per unit area of shear plane
- r = distance
- R_t = thermal number = $\frac{V_c t}{k}$
- S_s = dynamic shear stress of work material
- t = thickness of "chip" before removal from workpiece
- V_c = cutting velocity
- x, y = co-ordinate axes fixed in space
- α = tool rake
- β = fraction of heat generated at shear zone conducted back into workpiece
- ϵ = shear strain
- ξ, η = co-ordinate axes moving with heat source
- θ, θ_0 = variable and initial temperature of workpiece, respectively
- ϕ = shear angle
- ρ = weight density of work material
- τ, τ' = time

Introduction

The cutting of metals is invariably accompanied by the generation of heat. Except for the small amount of latent energy stored in the deformed chip, and in the surface of the workpiece, all of the energy expended in cutting is converted into sensible heat which is distributed in the tool, chip, and workpiece. Previous work (1, 2)[3] has disclosed the intimate relationship which exists between the mechanism of chip formation and the tool-chip-interface temperature. This latter temperature also plays a very significant role in the life of a cutting tool.

In metal-cutting operations where a type 2 chip is produced, heat is liberated essentially in two distinct regions, namely, (*a*) the shear zone, and (*b*) the tool-chip interface. The generation of the interface temperature due to rubbing of the heated chip on the tool face has been analyzed and approximate equations for its evaluation have been given (3). In that analysis, the temperature of the chip as it left the shear zone was tacitly assumed to be uniform. In orthogonal cutting operations, the shear zone constitutes, essentially, an oblique band source of heat moving in the direction of the cutting velocity vector through the metal of the workpiece. The problem of the calculation of the temperature field in a solid due to moving sources of heat has been treated by Blok (4), Jaeger (5), Rosenthal (6), and others. Special cases of interest involving plane sources of heat moving either parallel or perpendicular to the plane of the source have been studied and results have been given by these investigators. Recently, Hahn (7) has extended the treatment to a particular two-dimensional case where the plane of the band source is inclined to its direction of motion in an infinite medium. The result of his analysis was applied directly to the calculation of the temperature distribution in the work material along the shear plane in the metal-cutting process. While Hahn's final expression for the "dimensionless temperature" along the shear plane is correct for the case of an infinite solid, a slightly different derivation is given in succeeding paragraphs. The results so obtained are modified by the findings relating the shear angle (which is the angle of inclination of the band source to its direction of motion) to a dimensionless product, $V_c t/k$, the thermal number.

Temperature Distribution Along Shear Plane in Orthogonal Cutting Operations

Referring to Fig. 1, the co-ordinate axes x and y are fixed in space with the origin coincident with the mid-point of the shear zone at zero time when cutting starts. Terms ξ and η are a moving pair of axes traveling with the source. Three positions of the moving band source are shown at time $\tau = 0$, τ', and τ, respectively. Within the conventional speed and feed range for carbide tools, the process of heating due both to main chip shear and to rubbing at the tool-chip interface is quasi-stationary in nature (8). In other words, an observer located at the source fails to notice any change in the surrounding temperature distribution with respect to time. The present objective is to find this quasi-stationary temperature distribution along the shear plane. The first step consists of calculating the temperature rise at any point $P(\xi, \eta)$ due to the continuous heating of the moving source when the latter occupies the position B, i.e., τ sec after heating starts. The required expression for the quasi-stationary temperature can then be obtained by investigating the limiting case when $\tau \to \infty$.

At any arbitrary instant $\tau'(\tau > \tau' > 0)$, which corresponds to position A for the band source in Fig. 1, the temperature rise at P due to an instantaneous line source of strength

$$\frac{\beta q \, d\xi' \, d\tau'}{c\rho}$$

---

[1] Assistant Professor of Mechanical Engineering, University of Illinois.

[2] Professor of Mechanical Engineering, University of Illinois. Mem. ASME.

[3] Numbers in parentheses refer to the Bibliography at the end of the paper.

Contributed by the Production Engineering Division, Metal Cutting Data and Bibliography, and Cutting Fluids Research Committees, and presented at the Semi-Annual Meeting, Cincinnati, Ohio, June 15–19, 1952, of The American Society of Mechanical Engineers.

Note: Statements and opinions advanced in papers are to be understood as individual expressions of their authors and not those of the Society. Manuscript received at ASME Headquarters, May 13, 1952. Paper No. 52—SA-58.

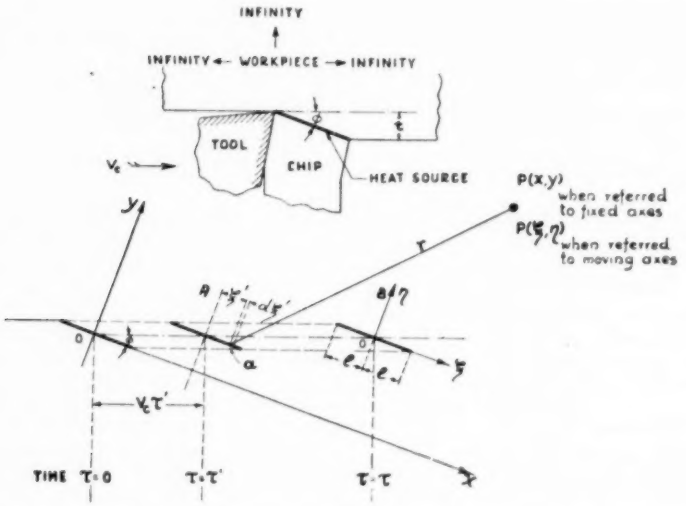

FIG. 1 MOVING BAND SOURCE OF HEAT DUE TO MAIN CHIP SHEAR IN ORTHOGONAL CUTTING PROCESS

situated at point a of the band source, $(\tau - \tau')$ seconds later, is

$$d\theta = 2\left[\frac{\beta q\, d\xi'\, d\tau'}{c\rho(4\pi k)}\right]\frac{1}{\tau - \tau'}\exp\left[-\frac{r^2}{4k(\tau - \tau')}\right] \quad \ldots\ldots [1]^4$$

The multiplying factor 2 in the foregoing expression is formulated on the basis that the temperature at any point in the workpiece (which is considered as a semi-infinite solid) will be twice as great as that in an infinite medium with identical strength of the heat source. This involves an approximation inasmuch as the temperature field in an infinite medium with an oblique band source is not symmetrical with respect to the trace 0-0, Fig. 1, in the direction of its motion. The relationship will be exact only if $\phi = 0$. However, in the majority of cutting processes, ϕ generally will not be greater than 30 deg. This simplification is reasonable and justifiable since no exact solution is yet known. In deriving Equation [1], it is also necessary to ignore any heat loss from the bounding surfaces of the work material, and any variations of the physical properties of the metal, such as K, c, and ρ, with temperature are neglected.

From the geometry of Fig. 1 it is evident that

$$r^2 = (x - V_c\tau' \cos\phi - \xi')^2 + (y - V_c\tau' \sin\phi)^2 \quad \ldots\ldots [2]$$

$$\left.\begin{aligned} \xi &= x - V_c\tau \cos\phi \\ \text{and} \qquad \eta &= y - V_c\tau \sin\phi \end{aligned}\right\} \quad \ldots\ldots [3]$$

Substituting Equations [2] and [3] into Equation [1], and simplifying, we get

$$d\theta = \frac{\beta q}{2\pi K}\frac{d\xi'\, d\tau'}{\tau - \tau'}\exp\left\{-\frac{(\xi - \xi')^2 + \eta^2}{4k(\tau - \tau')} + \frac{V_c}{2k}[(\xi - \xi')\cos\phi + \eta\sin\phi] + \frac{V_c^2(\tau - \tau')}{4k}\right\} \quad \ldots\ldots [4]$$

The final temperature rise at $P(\xi, \eta)$ when the band source occupies position B can be obtained by integrating Equation [4] as follows

$$\Delta\theta = \theta - \theta_0 = \frac{\beta q}{2\pi K}\int_{-l}^{l} d\xi' \int_0^{\tau} \exp - \left\{\frac{(\xi - \xi')^2 + \eta^2}{4k(\tau - \tau')} + \frac{V_c}{2k}[(\xi - \xi')\cos\phi + \eta\sin\phi] + \frac{V_c^2(\tau - \tau')}{4k}\right\}\frac{d\tau'}{\tau - \tau'} \quad \ldots\ldots [5]$$

For quasi-stationary state, we let $\tau \to \infty$, and since

$$K_0(m) = \int_0^{\infty}\frac{dz}{z}\exp - \left(m^2z^2 + \frac{1}{4z^2}\right) \quad \ldots\ldots [6]^5$$

where K_0 is the modified Bessel function of the second kind of zero order Equation [5] can be simplified to

$$\Delta\theta = \frac{\beta q}{\pi K}\int_{-l}^{l} K_0\left\{\frac{V_c}{2k}[(\xi - \xi')^2 + \eta^2]^{1/2}\right\} \exp\left\{-\frac{V_c}{2k}[(\xi - \xi')\cos\phi + \eta\sin\phi]\right\} d\xi' \quad \ldots\ldots [7]$$

Inasmuch as the temperature distribution in the shear plane is of prime interest in this analysis, let $\eta = 0$ in Equation [7] and obtain

$$\Delta\theta = \frac{\beta q}{\pi K}\int_{-l}^{l} \exp\left\{-\frac{V_c}{2k}[(\xi - \xi')\cos\phi]\right\} K_0\left(\frac{V_c|\xi - \xi'|}{2k}\right) d\xi' \quad \ldots\ldots [8]$$

Introducing the dimensionless quantities

$$E = \frac{V_c\xi}{2k},\ L = \frac{V_c l}{2k},\ \text{and}\ u = \frac{V_c(\xi - \xi')}{2k}$$

Equation [8] becomes

$$\Delta\theta = \frac{2}{\pi}\frac{\beta q}{c\rho V_c}\int_{E-L}^{E+L} e^{-u\cos\phi}\, K_0(|u|)\, du$$

or

[4] This expression can be found in standard textbooks on Heat Conduction, e.g., "Conduction of Heat in Solids," by H. S. Carslaw and J. C. Jaeger, Clarendon Press, Oxford, England, 1947, p. 218.

[5] See "Bessel Functions," by A. Gray and G. B. Mathews, Macmillan and Company, London, England, 1922, p. 51.

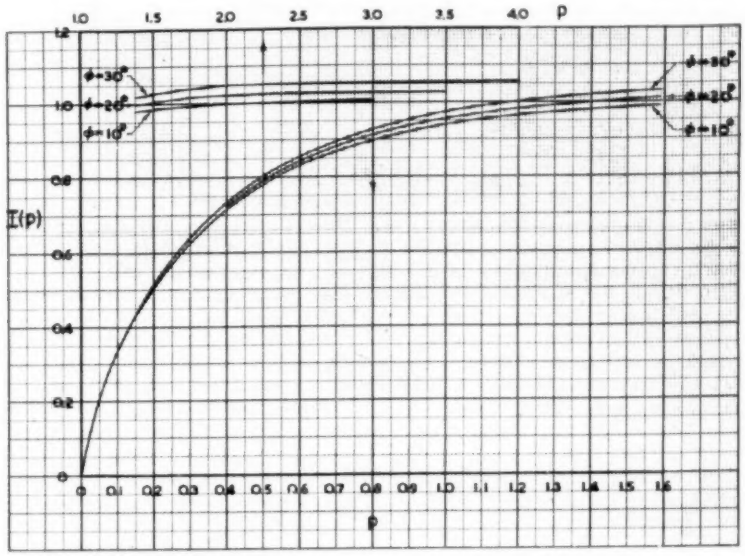

FIG. 2 VALUES OF DEFINITE INTEGRAL $I(p)$ BY EQUATION [10]

$$\frac{\pi}{2}\frac{c\rho V_e}{\beta q}\Delta\theta = I(E+L) - I(E-L)$$

$$= I\left[L\left(\frac{\xi}{l}+1\right)\right] - I\left[L\left(\frac{\xi}{l}-1\right)\right] \quad \ldots\ldots [9]$$

where

$$I(p) = \int_0^p e^{-u\cos\phi} K_0(|u|)\, du \quad \ldots\ldots [10]$$

$$I(-p) = -\int_0^p e^{u\cos\phi} K_0(|u|)\, du \quad \ldots\ldots [11]$$

The two definite Integrals [10] and [11] have been evaluated numerically for values of shear angle $\phi = 10°, 15°, 20°, 25°$, and $30°$. The results are presented graphically in Figs. 2 and 3, and can be used directly in Equations [9] and [13] for the calculation of temperature distribution.

The left-hand side of Equation [9] contains the quantity q which is the rate of heat liberation per unit area of the shear plane. Referring to Fig. 1, if the feed (the thickness of the "uncut" chip) is t, the width of the shear plane $2l$, will be $t/\sin\phi$. Thus

$$q = \frac{S_s \epsilon V_c t}{2Jl} = \frac{S_s \epsilon \sin\phi\, V_c}{J} \quad \ldots\ldots [12]$$

Only a fraction β_t of this heat will be transferred back into the workpiece by conduction. For orthogonal cutting, this fraction varies according to the thermal number (9).

If Equation [12] and the relationship $\epsilon = \cot\phi + \tan(\phi - \alpha)$ are substituted into Equation [9], it becomes

$$\frac{\pi}{2}\frac{c\rho J}{S_s}\Delta\theta = \frac{\beta}{\cos\phi + \sin\phi\tan\alpha}$$

$$\left\{I\left[L\left(\frac{\xi}{l}+1\right)\right] - I\left[L\left(\frac{\xi}{l}-1\right)\right]\right\} \quad \ldots\ldots [13]$$

where

$$L = \frac{V_c l}{2k} = \left(\frac{V_c t}{k}\right)\left(\frac{1}{4\sin\phi}\right) = \frac{R_t}{4\sin\phi}$$

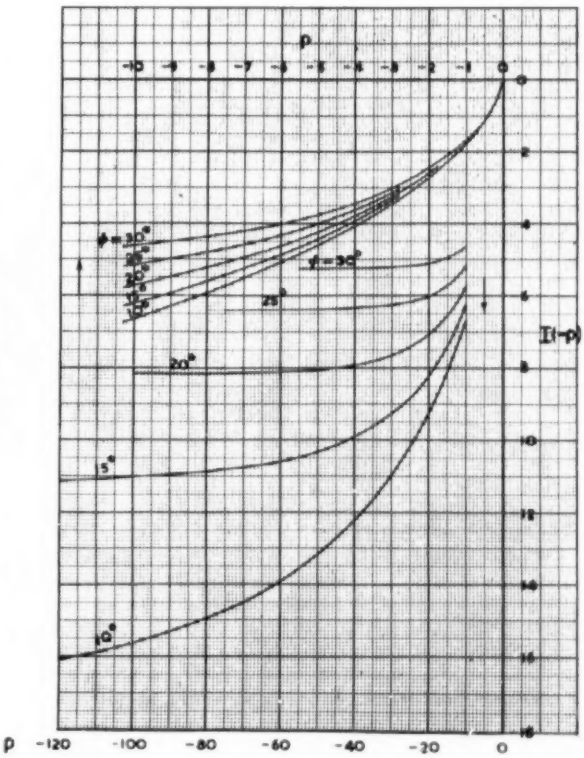

FIG. 3 VALUES OF DEFINITE INTEGRAL $I(-p)$ BY EQUATION [11]

All the previous equations are dimensionally compatible and they are applicable when any consistent system of units of measurement is employed. However, in most metal-cutting lit-

erature, S_s is usually given in psi, J in ft-lb/Btu, c in Btu/lb-deg F, ρ in pcf, and θ in deg F. If this "mixed" system is used, Equation [13] becomes

$$8.5\,\frac{c\rho}{S_s}\,\Delta\theta = \frac{\beta}{\cos\phi + \sin\phi\tan\alpha} \times \left\{ I\left[L\left(\frac{\xi}{l}+1\right)\right] - I\left[L\left(\frac{\xi}{l}-1\right)\right] \right\} \quad [13a]$$

It has been demonstrated that in commercial high-speed metal-cutting operations, the dynamic flow stress of the material S_s can be regarded as a constant except as modified by the size effect at very small feeds (2). It also has been found that with a given tool rake, the shear angle ϕ is uniquely determined by the thermal number. Fig. 4 shows a plot of the experimental data obtained when cutting spheroidized SAE 52100 steel with a triple-carbide tool of negative 2-deg rake angle. Results using a positive 10-deg rake tool are given in Fig. 5. In the latter case it is

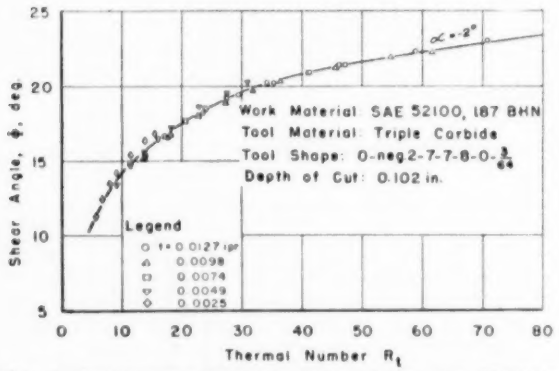

FIG. 4 RELATIONSHIP BETWEEN SHEAR ANGLE AND THERMAL NUMBER AT A FIXED TOOL RAKE IN ORTHOGONAL CUTTING

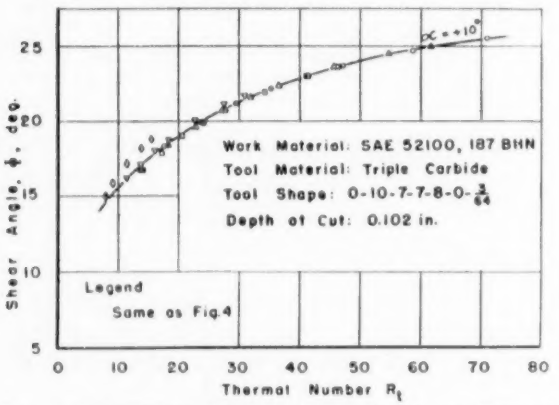

FIG. 5 RELATIONSHIP BETWEEN SHEAR ANGLE AND THERMAL NUMBER AT A FIXED TOOL RAKE IN ORTHOGONAL CUTTING

seen that some scattering does occur at the smallest feed employed. In general, however, the correlation is very satisfactory. The thermal diffusivity of SAE 52100 steel at room temperature has been found to be 1.03 sq in. per min.[6]

With these experimentally determined facts, Equation [13] can be written in the following form

$$M\Delta\theta = \psi\left(R_t, \frac{\xi}{l}\right) \quad [14]$$

where

$$M = \frac{\pi}{2}\,\frac{c\rho J}{S_s}$$

an invariant with respect to the cutting variables V_c, t, and α. Term ψ designates a possible functional relationship. This shows that at a given location on the shear plane, the temperature rise above initial temperature depends on the thermal number. In other words, the temperature distribution along the shear plane is governed entirely by this dimensionless number under the ideal conditions.

The fraction β is, unfortunately, not quantitatively known at present. In conventional turning operations, it will vary with cutting speed, feed, ratio of the size of cut to the diameter of the workpiece, and so on. Its analytical evaluation is extremely difficult owing to the fact that a part of the heat which flows into the workpiece by conduction will be present in the chip removed in the succeeding revolution. For orthogonal cutting, this fraction depends on the thermal number—the larger the number, the smaller the proportion of heat to the workpiece. This means that the proportion of the heat at the shear zone, which goes into the workpiece will become less and less with an increase in the cutting speed, or feed, or both.

In machining operations employing sintered-carbide tools and operating at relatively high cutting speeds, the change in β is usually not very great. Schmidt and Roubik (10) have reported that in the case of drilling, the heat going into the workpiece constitutes about 10 per cent of the total heat generated in cutting at speeds higher than 100 sfpm and a feed of 0.0091 ipr. However, because of the lack of quantitative data for single-point turning relating β to R_t, Equation [14] is modified slightly when the effect of cutting speed and feed on the temperature distribution along the shear plane is sought. Thus

$$\frac{M\Delta\theta}{\beta} = f\left(R_t, \frac{\xi}{l}\right) \quad [14a]$$

No generality will be lost, if one bears in mind that β is itself a function of R_t. Figs. 6 and 7 illustrate how the cutting speed and feed affect the shear-plane temperature distribution in terms of the thermal number. These curves are calculated from Equation [13] with the aid of Figs. 2 and 3 for the value of the definite integral I, and Figs. 4 and 5 for the appropriate shear angles at various thermal numbers. Cutting data were obtained by dry-turning spheroidized SAE 52100 steel (187 Bhn) using wide ranges of speeds and feeds and tool rakes of positive 10 deg and negative 2 deg. The test logs consisted of $5^1/_2$-in-OD tubing having a wall thickness of $^5/_8$ in. and approximately 30 in. long. Details of test procedure have been reported earlier (2).

It is seen from Figs. 6 and 7 that cutting at high speeds and large feeds will result in a large shear angle and a much more uniform temperature distribution on the shear plane (tool rake is unchanged). This phenomenon is directly opposite to the case when a plane slider moves on the surface of a semi-infinite solid and generates heat by frictional rubbing (5). In this latter case the temperature distribution becomes less uniform, with maximum shifts toward the trailing edge of the moving source as the velocity of sliding is gradually increased. The explanation lies in the obliquity of the source in the cutting process. With the plane slider, the temperature is higher toward the trailing edge due to the "cumulative" heating effect as the source moves. The higher the velocity the less will be the chance for the heat to be diffused away, and thus the stronger will be the cumulative

[6] From data in the "Metals Handbook," ASM, Cleveland, Ohio, 1948 edition.

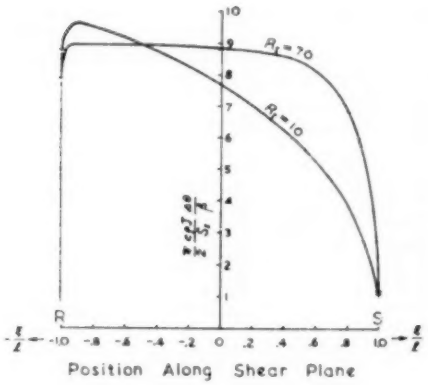

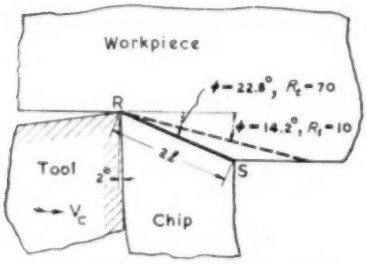

Work material: SAE 52100, 187 Bhn
Tool material: Triple carbide
Depth of cut: 0.102 in.
Tool rake: Negative 2 deg

FIG. 6 EFFECT OF THERMAL NUMBER ON TEMPERATURE DISTRIBUTION ALONG SHEAR PLANE

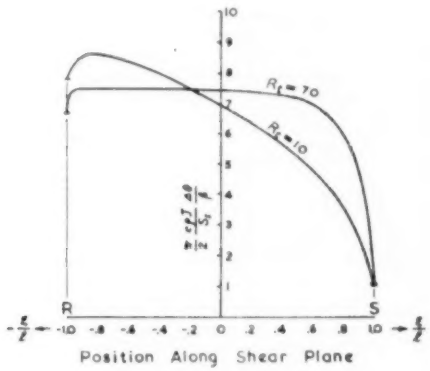

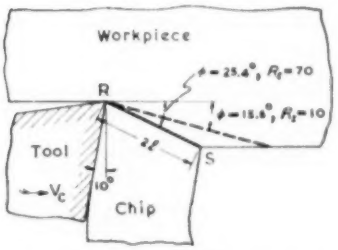

Work material: SAE 52100, 187 Bhn
Tool material: Triple carbide
Depth of cut: 0.102 in.
Tool rake: Positive 10 deg

FIG. 7 EFFECT OF THERMAL NUMBER ON TEMPERATURE DISTRIBUTION ALONG SHEAR PLANE

heating effect. However, when the plane of the source is inclined to its direction of motion, such a cumulative effect will practically vanish, especially when the speed is high. The higher the speed, the shallower will be the depth of temperature penetration in a direction perpendicular to the plane of the source (5). This may be what Hahn referred to as "quenching effect" in his discussion of a paper by the authors (2). With an excessive negative-rake tool (where ϕ is usually small) cutting at relatively slow speeds, the foregoing phenomenon of the effect of thermal number on the shear-plane temperature distribution ultimately might reverse itself. It is doubtful, however, whether such an extreme case would be met in practice.

The theoretical finding of the effect of the thermal number on the shear-plane temperature distribution may serve as a clue to explain the change in curvature of type 2 chips as cutting speed or feed is varied. At relatively low cutting speed, the nonuniformity of temperature distribution will result in a greater differential volumetric expansion of the material at the back of the chip. Consequently, the chip produced will be of larger curvature than it would with a more uniform temperature distribution. It is recognized that bending of the chip due to normal pressure on the tool face, heating effects due to interface rubbing, and so forth, are other possible factors influencing the degree of chip curl.

The significance of the thermal number in metal-machining operations has been reported earlier (2, 9). Of practical interest is the fact that there exists also a functional relationship between this number and the energy expended in cutting per unit volume of metal removed. This latter quantity has often been used to designate the efficiency of a machining operation. It is seen from Figs. 8 and 9 that the specific work done in metal removal decreases as either cutting speed or feed or both are increased. The decrease is rather rapid at small thermal numbers but gradually approaches a limit at large values of R_t. As is to be expected, at equal cutting speeds and feeds, the positive 10-deg-rake tool yields a higher efficiency, i.e., lower energy/unit volume of metal removed, than the negative 2-deg-rake tool. From a practical standpoint this greater efficiency may be offset in certain machining operations by the reduced mechanical strength and thermal capacity of the tool edge.

It appears that a better understanding of metal-cutting processes is possible when the full significance of the thermal number is appreciated. The correlation of the various observed "shear-zone" phenomena with the thermal number is very satisfactory, as shown in the foregoing sections of this discussion and in a previous paper (2).

The same degree of correlation does not exist between the thermal number and the tool-chip friction behavior. A previous analysis (3) has indicated that there is no mathematical relationship between the friction phenomena and the thermal number per se. The lack of correlation is thought to be due to changes in friction behavior as influenced by temperature and in the temperature-dependent properties of the chip material with steep temperature gradient. The tool-chip-interface temperature is influenced to a marked degree by the tool-chip friction aspects as reported earlier (2) and such frictional behavior is not solely dependent upon the thermal number. This is also evident from Fig. 10 in which two families of curves are shown for the separate effect of speed and feed.[3]

[3] The thermal number in Fig. 10 is calculated with thermal diffusivity of the chip material at chip-bulk temperature.

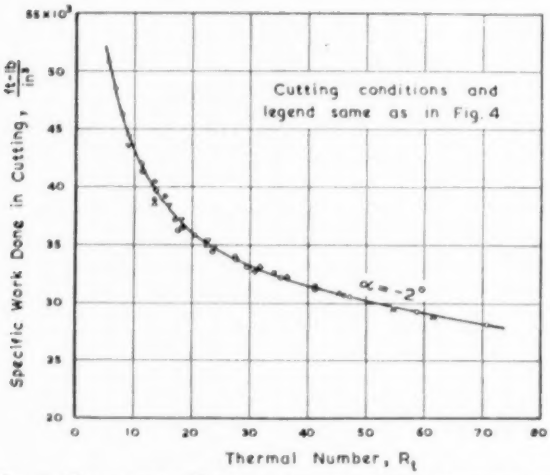

FIG. 8 RELATIONSHIP BETWEEN SPECIFIC ENERGY EXPENDED IN METAL REMOVAL AND THERMAL NUMBER

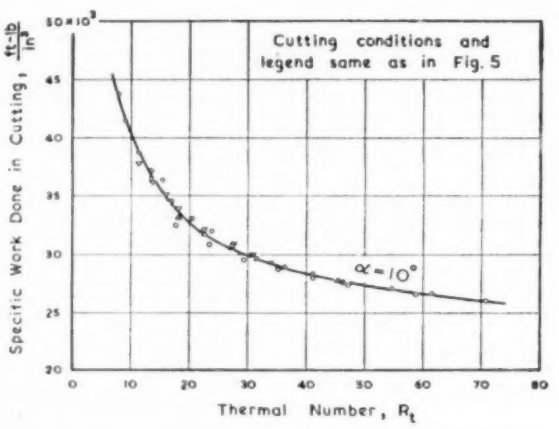

FIG. 9 RELATIONSHIP BETWEEN SPECIFIC ENERGY EXPENDED IN METAL REMOVAL AND THERMAL NUMBER

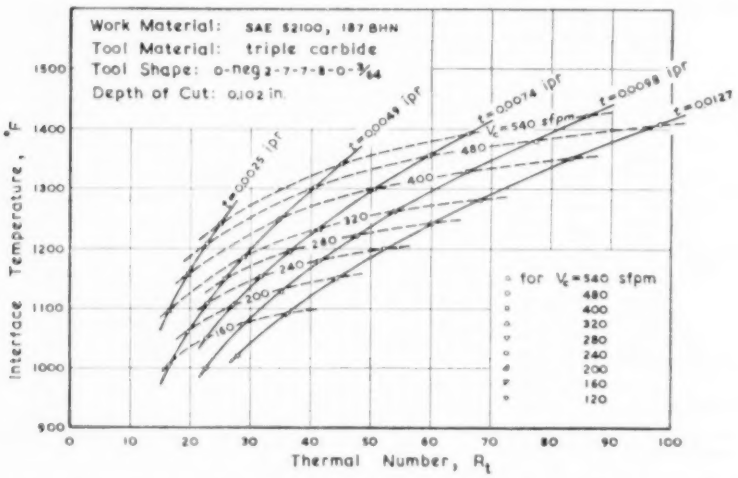

FIG. 10 EFFECT OF CUTTING SPEED AND FEED ON TOOL-CHIP-INTERFACE TEMPERATURE

From the standpoint of specific-energy requirements and rate of metal removal a high thermal number is desirable. However, it is necessary from a practical viewpoint to take into consideration the effect of an increase in speed and/or feed on the tool-chip-interface temperature—one of the important factors in the tool life of a given tool-work pair. Schallbroch, Schaumann, and Wallichs (11) have found that the tool life varies inversely as approximately the 20th power of the tool-chip-interface temperatures. Their empirical relationship, $Tt^n = K$ expressed tool life T in minutes, and temperature t in degrees Centigrade for high-speed-steel tools cutting chromium-molybdenum steel. While it is quite likely that the exponent is lower for carbide tools, still, relatively small changes in interface temperature will have a profound effect on tool life. Therefore it is necessary to consider the effect of speed and feed changes on the tool-chip-interface temperature.

Previous studies (1, 2, 3, 8) have shown that the tool-chip-interface temperature (type 2 chip) increases with cutting speed in accord with the relationship $T = CV^n$. Similarly, at least over the range investigated in this paper, an increase in feed increases the interface temperature in a manner expressible as $T = C'f^m$ (12). It can be deduced from Fig. 10 that the exponents m and n are not identical; i.e., the tool-chip-interface temperature is not solely dependent on the thermal number. An increase in speed and/or feed (in the usual range) increases the tool-chip-interface temperature and as a consequence reduces the ability of the tool to withstand the abrasive action of the chip, thereby shortening tool life.

An increase in the speed and/or feed decreases the proportion of the interface heat which is conducted into the tool. The quantity of heat to the tool per unit time remains nearly constant with an increase in cutting speed from 200 to 600 sfpm. The increase in tool-chip-interface temperature in this speed range results from the fact that the heat is concentrated on less tool area. The same general type of behavior obtains with increase in feed, i.e., while the proportion of interface heat to the tool decreases, the concentration on the tool face is more severe and higher interface temperatures result.

As a general trend the tool-chip-interface temperature increases with both speed and feed. An opposite trend is observed in specific-energy requirements—these opposing effects indicate an optimum combination of feed and speed for most economical removal of metal. (Depth of cut is of minor importance in fundamental considerations in orthogonal cutting though having, of course, practical significance.)

The ultimate economy of any metal-cutting process is then dictated by a compromise of these two opposing factors. An increase in speed and/or feed increases the rate of metal removal and reduces energy expended per unit volume. The same change increases the tool-chip-interface temperature and hastens tool failure for a given tool-work combination, thus necessitating more down time for tool changes.

Conclusions

1 In orthogonal cutting operations the temperature distribution along the shear plane is solely dependent upon the thermal number.

2 Under usual cutting conditions, a larger thermal number results in a more uniform temperature distribution along the shear plane.

3 Within the range investigated, the effect of cutting speed and feed on chip-thickness ratio, shear strain, shear angle, and specific energy of metal removal can be expressed in terms of the thermal number (constant rake angle).

4 The tool-chip-interface temperature is not solely dependent upon the thermal number.

5 Since an increase in speed and/or feed reduces the specific-energy requirements in metal removal and at the same time increases the tool-chip-interface temperature, the ultimate economy in a metal-cutting process is dictated by a compromise of these opposing factors.

Acknowledgment

The authors hereby express their appreciation to Prof. D. E. McFeron, Department of Mechanical Engineering, University of Illinois, for checking some of the calculations in this paper.

BIBLIOGRAPHY

1 "Cutting Temperatures and Metal-Cutting Phenomena," by B. T. Chao and K. J. Trigger, Trans. ASME, vol. 73, 1951, pp. 777–793.

2 "Thermophysical Aspects of Metal Cutting," by B. T. Chao, K. J. Trigger, and L. B. Zylstra, Trans. ASME, vol. 74, August, 1952, pp. 1039–1054.

3 "An Analytical Evaluation of Metal-Cutting Temperatures," by K. J. Trigger and B. T. Chao, Trans. ASME, vol. 73, 1951, pp. 57–68.

4 "Theoretical Study of Temperature Rise at Surfaces of Actual Contact Under Oiliness Lubricating Conditions," by H. Blok, Proceedings of the General Discussion on Lubrication and Lubricants, The Institution of Mechanical Engineers, London, England, 1938, pp. 222–235.

5 "Moving Sources of Heat and the Temperature at Sliding Contacts," by J. C. Jaeger, Proceedings of the Royal Society, London, England, vol. 76, 1942, pp. 203–224.

6 "The Theory of Moving Sources of Heat and Its Application to Metal Treatments," by D. Rosenthal, Trans. ASME, vol. 68, 1946, pp. 848–866.

7 "On the Temperature Developed at the Shear Plane in the Metal Cutting Process," by R. S. Hahn, to be published in the Proceedings of the Applied Mechanics Congress, 1950.

8 "Progress Report No. 1 on Tool-Chip Interface Temperatures," by K. J. Trigger, Trans. ASME, vol. 70, 1948, pp. 91–98.

9 "The Effect of Speed and Feed on the Mechanics of Metal Cutting," by B. T. Chao and G. H. Bisacre, Proceedings of The Institution of Mechanical Engineers, London, England, vol. 165, 1951, pp. 1–13 (WEP No. 63).

10 "Distribution of Heat Generated in Drilling," by A. O. Schmidt and J. R. Roubik, Trans. ASME, vol. 71, 1949, pp. 245–252.

11 "Testing for Machinability by Measuring Cutting Temperatures and Tool Wear," by H. Schallbroch, H. Schaumann, and R. Wallichs, Vortage der Hauptversammlung der Deutsche Gesselschaft für Metallkunde, Verein deutscher Ingenieure Verlag, 1938, pp 34–38.

12 Discussion of reference (10) by K. J. Trigger, pp. 249–250.

Discussion

R. S. Hahn.[8] The authors have presented an interesting analysis of shear-plane temperatures. There are, however, some features of their analysis which should be examined carefully. The authors claim that they derive the temperature distribution due to a band heat source (shear plane) moving obliquely over a semi-infinite solid and that their derivation is slightly different from that given in their reference (7) for a heat source moving obliquely through an infinite solid. Actually, their result given by Equation [8] is identical to the writer's Equation [3] of reference (7) (after setting $z = 0$) except for the factor β and a factor of 2. Consequently, their solution gives temperatures which are exactly twice that produced by a source moving obliquely through an infinite solid.

As a matter of fact, the writer originally did have the factor 2 in his equation but when he came to check the calculated shear-plane temperature against experimental determinations of it, the calculated temperature was nearly twice the experimentally determined temperature. It was at this time that he realized a heat source moving through an infinite solid was a much better approximation for the shear plane than one moving over a semi-infinite solid. The authors' Equation [9] is exactly equivalent to the writer's Equation [4] (7).

The introduction of the quantity β into Equation [1] seems improper. Any method which yields the temperature distribution on the shear plane immediately implies the fractional division of heat between chip and workpiece as a result, and this fraction need not be postulated. For example, referring to the temperature distribution shown in Fig. 6 of the paper, since the heat convected away from the shear plane is proportional to the area under the temperature-distribution curve and since the adiabatic shear-plane temperature (the temperature obtained by allocating the entire shear energy to the chip) can be computed readily, and may be represented by a horizontal line in Fig. 6, thereby enclosing an area proportional to the rate of heat convection when no heat is lost to the workpiece, a comparison of these areas immediately yields the fraction of heat, β lost to the workpiece.

The authors' statement that the shear angle is uniquely determined by the thermal number is quite a departure from the conventional theory of metal cutting. The plots in Figs. 4 and 5 do not prove that the shear angle is related to the thermal number because the thermal diffusivity has not been varied. Figs. 4 and 5 actually show that the shear angle is related to the numerator of the thermal number, i.e., to the product of cutting speed and depth of cut. It would seem rather strange that the shear angle depends on the thermal number and not, also, on tool-face friction as many have believed.

The authors also state, following Equation [14], that the temperature distribution along the shear plane is governed entirely by the thermal number. It should be emphasized that this is true only when the shearing stress S_s is independent of temperature (and/or speed V_s). This follows immediately from Equation [9] (or the writer's Equation [4] reference 7) as soon as it is realized that the ratio q/V_s is proportional to shear stress S_s (see Equation [12]).

[8] Heald Machine Co., Worcester, Mass. Mem. ASME.

E. G. Loewen[9] and M. C. Shaw.[10] The practical limitation in many machining processes is the temperature generated at the face of the tool. While this has been true for a long time, the problem has become accentuated in recent years by the difficulties encountered in machining high-temperature alloys and titanium. Therefore, any work that sheds light on the detailed mechanism of temperature development in the cutting process is of immediate interest.

In this paper the authors compute the temperature at points along the shear plane following the analytical procedure originally given by Hahn (authors' reference 7). Let us consider just what is involved in this analysis. In Fig. 11 of this discussion is shown a partially formed chip and shear plane. The shear plane is a heat source which moves relative to the workpiece. Hahn assumed this heat source to move horizontally with the cutting speed V_c, and hence set about to find the temperature at any point A in an infinite body in which a finite inclined heat source moved horizontally with a speed V_c, Fig. 12. This he did

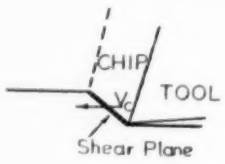

Fig. 11

Fig. 12

and the authors have retraced these steps. However, in solving for the temperature on the shear plane following the method of Blok we need to know the temperature at any point A for the case where the shaded region in Fig. 13 is a perfect insulator. In this paper the authors, again following Hahn, reason that the semi-infinite body in Fig. 14 (uncrosshatched region), is a good approximation for the uncrosshatched region in Fig. 13. The temperature at point A for the case of Fig. 14 is obviously just double that at point A for the case of the infinite body in Fig. 12. However, it should be noted that the foregoing procedure involves the assumption of a metallic region at C, Fig. 14, that

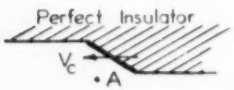

Fig. 13

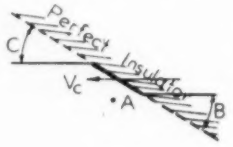

Fig. 14

actually does not exist, and the absence of a metallic region at B that in fact is present. When this approximation is made a temperature distribution across the shear plane is predicted as shown in Fig. 6 of the paper, which predicts a more uniform temperature across the shear plane as the speed (or thermal number) is increased.

We may arrive at a solution for the shear-plane temperature and its distribution with much less effort by making use of a solution by Jaeger[11] for a heat source moving in the surface of a semi-infinite body, Fig. 15, herewith. This procedure has already been given in slightly different form in a previous publication.[12] The assumption made in this case in solving the problem of Fig. 13 of this discussion is that the shear plane is moving with a velocity V_s along the semi-infinite body shown crosshatched in Fig. 16. This approximation likewise con-

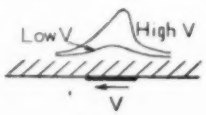

Fig. 15

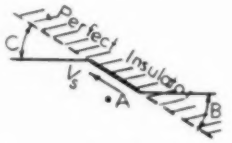

Fig. 16

siders that metal C is present when it really isn't and that metal B is not present when in reality it is. From Fig. 15 it is evident that this solution, unlike that of Hahn, predicts a less uniform temperature distribution along the shear plane with increased cutting speed.

In comparing the two solutions, the approximation involving regions B and C is common and is not considered to be a serious one. The major difference appears to be associated with the choice of velocity. When the Piispanen model of Fig. 17, he re-

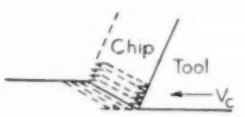

Fig. 17

with, is considered, velocity V_s would appear to be the one that should be adopted. By this picture, metal when cut behaves as a deck of cards, one card at a time sliding a finite distance across its neighbor. Heat is generated only when sliding occurs in direction V_s, and we might consider that one plate is always in motion and hence that the actual situation might be approximated by Fig. 16.

Direct evidence concerning the actual variation of temperature across the shear plane is difficult to obtain experimentally. The only worth-while attempt to measure temperatures over the shear-plane region was that of Schwerd[13] who used a very delicate radiation-measuring device. Unfortunately, the bulk of his data was never published, and the diagram shown in Fig. 18 of this discussion is the only one available to the writers.

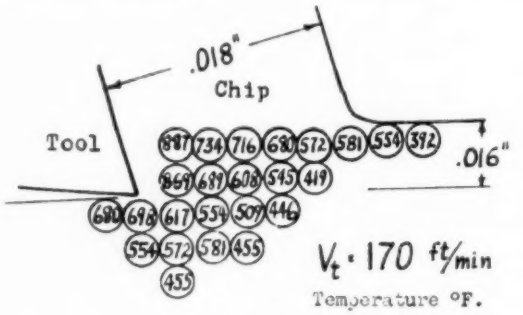

Fig. 18

[9] Assistant Professor, Mechanical Engineering, Massachusetts Institute of Technology, Cambridge, Mass. Jun. ASME.

[10] Associate Professor of Mechanical Engineering, Massachusetts Institute of Technology. Mem. ASME.

[11] "Moving Sources of Heat and the Temperature at Sliding Contacts," by J. C. Jaeger, Proceedings of the Royal Society of London, NSW, vol. 76, 1942, pp. 203–224.

[12] "Surface Temperatures in Grinding," by J. O. Outwater and M. C. Shaw, Trans. ASME, vol. 74, 1952, p. 73.

[13] "Über die Bestimmung des Temperaturfeldes beim Spanablauf," by F. Schwerd, *Zeitschrift des Vereines deutscher Ingenieure*, vol. 27, 1937, pp. 211–216.

While these results agree with both analyses with regard to the maximum temperature being at the tool point, a second result of this sort at a different speed would have to be obtained in order to determine whether the temperature distribution becomes more or less uniform with increased cutting speed.

It would appear that the case for the thermal number has been overstated. The thermal number R_t, except for a constant, is the same as the dimensionless parameter L that Jaeger[11] found so useful in describing the velocity behavior of a moving heat source. The authors suggest that for a given tool and workpiece the shear angle is uniquely determined by the thermal number, and present two curves with SAE 52100 steel to prove this point. This is quite contrary to the writers' experience, who could detect only a slight trend toward increased ϕ with thermal number in the case of free-machining sulphurized steel (SAE B-1113), and with wide scatter of points. When cutting stainless steel (18-8) the scatter was found to be just as great, even when using a good cutting fluid, and here the trend was reversed, the shear angle decreasing slightly with R_t.

The authors also claim a functional relationship between R_t and the specific work done in cutting, and their data on SAE 52100 seem to bear them out.

However, it should be observed that a decrease in specific work with increased speed and increased depth of cut will result from two different physical processes. The effect due to a change in depth of cut is a size effect while that due to a change in speed is probably thermal in nature. This being the case we should not expect the specific energy always to vary in the same way with thermal number regardless of whether the change in thermal number results from a change in speed or depth of cut.

In their concluding paragraphs the authors assert that the quantity of heat going to a tool is constant between 200 and 600 fpm cutting speed, and that the observed increase in tool temperature is due only to the decreased area of contact between chip and tool that takes place over this range. This is not held by the writers to be universally true, since in certain tests they have observed the contact area to change very little over this speed range, while the temperature increased considerably, as did the calculated energy going to the tool.

A. O. Schmidt[14] and B. F. Turkovich.[15] This paper is a welcome extension of previous work by the authors who have presented here a mathematical analysis of the metal-cutting process giving only the high points. Those of us working in this field appreciate the labor which has been expended in this case.

The thermal number R_t is a helpful figure determined from values which can be measured quite accurately. Much experimental work still is required to evaluate the amount of heat conducted into the workpiece during various cutting procedures. The amount of heat β conducted back into the workpiece after being generated at the shear zone, will be influenced primarily by cutting speed and feed. Within certain ranges of cutting speeds, e.g., 300 to 600 fpm in machining of steel, the value of β will be influenced by feed more than by speed. For the limited extent of cutting speeds from 10 to 175 fpm in drilling tubular magnesium test bars the value of β varied between 25 and 10 per cent for feeds of 0.0091 ipr and between 35 and 18 per cent for feeds of 0.0022 ipr (10).[16] This same general tendency has been established in turning steel at cutting speeds up to 750 fpm. Results of tests carried out at the Massachusetts Institute of Technology[17] clearly indicate a further decrease in β with higher cutting speeds. This was also found to be the case in milling tests in which aluminum was milled with carbide cutters at cutting speeds up to 15,000 fpm, no measurable heat being detectable in the workpiece at the high cutting speeds as long as the cutter remained sharp. Similar milling tests on steel at 15,000 fpm were impractical attempts in evaluating β, since tool wear was so rapid that the cutter tips and workpiece surface were literally "burnt up" within seconds of cutting time. The value β as defined by the authors must be determined with sharp cutters at cutting speeds which will not cause a too rapid rate of tool wear. As soon as noticeable tool wear occurs the workpiece will be heated not only by the fraction of heat generated at the shear zone and conducted back into workpiece but also by increasing friction of the dulling tool.

It is this increase in the amount of heat in the workpiece which can cause trouble when machining high-strength materials entailing high tool-tip temperatures and rapid tool wear.[18] In milling workpieces several feet in length and having comparatively thin wall thicknesses, dulling carbide cutters actually brought about such an increase in workpiece surface temperature that the pieces warped and buckled out of shape. Fortunately, in most cases, workpiece dimensions are large enough or coolant can be applied effectively to dissipate the heat from the machining process in order to maintain straight and accurate machined surfaces. However, it is experimentally possible to set up test conditions under which no appreciable heating of the workpiece due to increased friction between tool and workpiece takes place. This can be done by careful selection of tool materials, employment of sharp tools only, and operation at reasonable cutting speeds and feeds especially when using steel as the test bar material. Higher cutting speeds and feeds are feasible with many of the light alloys without affecting β in any appreciable degree as a result of tool wear.

Mathematically, β depends upon the thermal number R_t relative to cutting speed and feed in such a way that with increasing speed and heavier feeds β will asymptotically tend toward zero. It can be visualized that under such conditions, when no tool wear occurs, the separation of the chip from the workpiece can be so fast that no heat flow from the chip into the workpiece will take place. The only heat occurring then in the workpiece would be very small and caused by deformation of a thin layer near the surface due to the separation of the chip from the workpiece.

At cutting speeds which are practical for machining steel with carbide tools, usually between 200 and 800 fpm, we can assume that the average thermal conductivity K of the workpiece material remains constant, as well as its average specific heat c. Within these limits the thermal diffusivity k would be constant and it could be stated that

$$\beta = \frac{N}{R_t}$$

In order to determine N, only one value of β need be established experimentally because the "heat factor" N is a constant within certain limits of cutting speed. The foregoing formula will then permit β to be computed for different cutting speeds during which K, c, and k do not vary appreciably. Equation [13a] of the paper will then read

$$8.5\,\frac{c\rho}{S_s}\,\Delta\theta = \frac{N}{R_t(\cos\phi + \sin\phi\tan\alpha)} \left\{ I\left[L\left(\frac{\xi}{l}+1\right)\right] - I\left[L\left(\frac{\xi}{l}-1\right)\right] \right\}$$

[14] Research Engineer, Engineering Department, Kearney & Trecker, Milwaukee, Wis. Mem. ASME.

[15] Engineering Department, Kearney & Trecker Corporation.

[16] Refers to bibliography of paper.

[17] "Metal Cutting Principles," by M. C. Shaw, M.I.T., 1952, chapter XII.

[18] "Temperature Measurements in Workpiece, Chips and Tool," Conference on Metal Cutting, M.I.T., 1952; *The Tool Engineer*, July and August, 1952.

This transformation is introduced because, after a single value of β has been determined, the thermal number R_t and "heat factor" N define the specific conditions of the cut.

A numerical check of β gave a close correlation with values of β established experimentally as shown in the following sample computation:

When machining steel at 175 fpm with a chip thickness $t = 0.010$ in., the amount of heat going into the workpiece is about 12 per cent of the total energy of cutting or $\beta = 0.12$. At these cutting speeds the chips have an average temperature of 800 F which will give a specific heat for the chip, $c = 0.145$ Btu/(lb) (deg F) and a heat conductivity $K = 5.2 \times 10^{-4}$ Btu/(in²) (sec) (deg F/in). The density of the chip $\rho = 0.281$ lb/in³ and the thermal diffusivity

$$k = \frac{K}{c\rho} = \frac{5.2 \times 10^{-4}}{0.145 \times 0.281}$$
$$= 0.01276 \text{ in}^2/\text{sec}$$

For a cutting speed of 175 fpm

$$R_{t175} = \frac{V_s t}{k} = \frac{175 \times 12 \times 0.010}{60 \times 0.01276} = 27.5$$

$$\beta_{175} = N \frac{1}{R_{t175}}$$

$$N = \beta R_t = 0.12 \times 27.5 = 3.3$$

For a cutting speed of 600 fpm

$$R_{t600} = \frac{600 \times 12 \times 0.010}{60 \times 0.01276} = 94$$

$$\beta_{600} = \frac{N}{R_{t600}} = \frac{3.3}{94} = 0.035$$

This value of $\beta_{600} = 0.035$ indicates that only 3.5 per cent of the total energy expended during the cutting operation at 600 fpm goes into the workpiece. Experimental values indicate about 5 per cent. This may be due to the fact that a tool begins to wear as soon as cutting is started and even minute tool wear will cause more friction and thus additional heat in the workpiece surface.

Further experimental analysis of the heat distribution in metal-cutting operations and a better understanding of the effect of metal-cutting temperatures upon K and c will make it possible to determine R_t and N more accurately. It is hoped that this discussion will help to point out their importance.

Authors' Closure

The authors wish to thank the several discussers for their interest in the paper and for their many valuable suggestions, all of which contribute to a better understanding of the complicated metal-cutting process.

A major part of the theoretical analysis presented in this paper, including the lengthy calculations necessary for the plotting of Figs. 2 and 3, was completed in June, 1949. At that time the Mechanical Engineering Department of the University of Illinois was engaged in moving into the present quarters. Unfortunately, the original manuscript was misplaced during the transition and was not found until about a year ago. As a consequence the theoretical analysis in this paper was, in fact, entirely independent of the work by Hahn.

As pointed out at the beginning of the paper, the method of approach for the calculation of temperature distribution along the shear plane was not unlike that of Dr. Hahn's. In view of the fact that only sketchy, high points of the mathematical analysis had been published,[19] it was thought that a detailed derivation including such graphs as Figs. 2 and 3 might prove worth while to those working in the field. Furthermore, the introduction of the factors β and 2 in Equation [1] of the paper makes the numerical results different from those of Dr. Hahn. It is on these points that we must take issue now.

Dr. Hahn contends that the temperature distribution along the shear plane should be calculated as if the heat source were moving in an infinite medium. Fig. 1 of the paper illustrates the manner by which the heating of the workpiece and the chip takes place in an orthogonal cutting process. Inasmuch as the work material extends only on one side of the heat source which moves obliquely on its surface, it is difficult to see how it can be regarded as "infinite." If this were the case, the work materials must extend to remote distances on "both" sides of the source, which is obviously contradictory to what actually exists.

Dr. Hahn acknowledges that he originally did have the factor 2 in his expression for shear-plane temperature but when he came to compare the calculated values with experimentally determined temperatures, the former were nearly twice as great. The difficulty which he ran into apparently resulted from his failure to recognize the necessity of replacing q by βq in his expression for shear-plane temperature. This will be expounded further in the following paragraphs.

As defined in the earlier part of the paper, the quantity q in Equation [1] is the "total" rate of heat generation per unit area of the shear plane. Only a fraction of such heat goes into the workpiece by conduction. A major portion convects into the chip as a consequence of its motion. It is on this fact that the quantity β is introduced into the calculation of the temperature distribution along the shear plane.

When turning spheroidized SAE 52100 steel at a feed of 0.0074 ipr with a triple-carbide tool of negative 2-deg rake, the temperature distribution along the shear plane at cutting speeds of 116 and 811 sfpm can be represented by the two curves in Fig. 6 of the paper. The one identified with $R_t = 10$ corresponds to the lower cutting speed. Since β represents the fraction of the total shear-zone heat which passes into the workpiece, the fraction which leaves with the chip will be $(1 - \beta)$ if other heat losses are ignored. Therefore the mean temperature rise of the chip above the initial temperature as it leaves the shear zone is

$$(\Delta\theta)_{avg} = \frac{(1 - \beta)q\, 2l}{t\, V_s\, c\rho} \quad \ldots\ldots\ldots\ldots [15]$$

All quantities have been defined in the paper. Substituting Equation [12] into Equation [15], herewith, we obtain

$$(\Delta\theta)_{avg} = \frac{(1 - \beta)S_s\epsilon}{c\rho J} \quad \ldots\ldots\ldots\ldots [16]$$

The average temperature rise across the shear plane also can be found by measuring the area under the curves in Fig. 6. For a cutting speed of 811 sfpm, the mean "dimensionless temperature"

$$\frac{\pi}{2}\frac{c\rho J}{S_s}\frac{(\Delta\theta)_{avg}}{\beta}$$

has been found to be 8.4; or

$$(\Delta\theta)_{avg} = \frac{16.8}{\pi}\frac{\beta S_s}{c\rho J} \quad \ldots\ldots\ldots\ldots [17]$$

By equating Equations [16] and [17] we finally have

[19] Bibliography (7).

$$\beta = \frac{1}{1 + \frac{5.35}{\epsilon}} \quad [18]$$

For SAE 52100 steel, S_s = 100,000 psi, c = 0.128 Btu/lb deg F, ρ = 0.281 psi and under the given cutting conditions ϵ = 2.84. From this β = 0.347; $(\Delta\theta)_{avg}$ as given either by Equation [16] or [17] is 552 F. With an initial workpiece temperature of 79 F, the average temperature of the chip as it leaves the shear zone is 631 F which is in good agreement with actually measured temperatures reported. Quite evidently, Dr. Hahn's statement that our solution will give temperatures which are twice the actual values is in error. He also actually contradicts himself by first saying that there is no need of introducing the factor β and then suggesting a method for its determination, which, in fact, is not correct. (If there were not such a fraction as β, why bother to determine it?)

The authors agree with Dr. Hahn that the plots in Figs. 4 and 5 of the paper only prove that the shear angle is related to the numerator of the thermal number, i.e., to the product of cutting speed and feed because the thermal diffusivity has not been verified. However, as has been stated in the paper, the conclusion that the shear angle is uniquely determined by the thermal number is true only for a "given" set of cutting conditions, specifically rake angle and tool-work combination.

In commercial high-speed metal-cutting operations where a type 2 chip is formed, the dynamic flow stress of many materials has been found to remain constant except as modified by the size effect at very small feeds.[20] Consequently, the authors hold that the temperature distribution along the shear plane is solely dependent upon the thermal number.

That the use of the simple multiplying factor 2 in Equation [1] of the paper involves an approximation is clearly stated in the earlier part of the paper. An exact solution is difficult even though the constancy of such physical properties of metal, such as K, c, and ρ is assumed. Professors Loewen and Shaw suggest a different model for the heating process due to main chip shear, in which they claim that the shear-plane temperature distribution can be obtained with much less effort. Since heat is generated only when sliding occurs in the direction V_e, they reason that only this component of the cutting velocity has to be considered as illustrated in Fig. 16 of their discussion. Let us examine more carefully the validity of such an approach. The

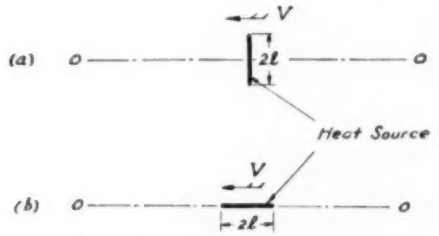

FIG. 19 MOVING-BAND SOURCE IN AN INFINITE MEDIUM

quasi-stationary temperature distribution surrounding a band source moving in an infinite medium depends on the direction of the "actual" velocity vector and the plane of the heat source irrespective of how the heat energy is generated.

Fig. 19 illustrates the two extreme cases. For identical strength of the heat source moving at identical speed, the temperature distribution along the plane of the source will be widely different. Fig. 14 of the discussion actually represents an intermediate case. It is apparent, therefore, that the replacing of the actual velocity vector V_e by V_s in Fig. 16 will result in serious error. In fact, one of the findings reported in this paper, namely, that cutting at high speeds and feeds will result in a more uniform temperature distribution across the shear plane, can never be derived by a heating model as portrayed in Fig. 16.

The statement that a functional relationship between the shear angle and the thermal number fails to exist in the case of free-machining sulphurized steel and 18-8 stainless steel cannot be answered by the authors without further experimental data. The decrease in specific work done with increased speed and feed cannot be accounted for by the size effect. The dynamic flow stress of the work material remains practically constant for all feeds employed in these tests (except the smallest, 0.0025 ipr).

With reference to the quantity of interface, (i.e., frictional heat)

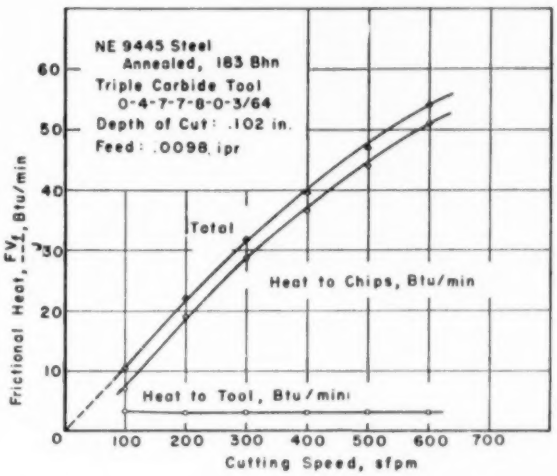

FIG. 20 DISTRIBUTION OF FRICTIONAL HEAT BETWEEN CHIP AND TOOL

conducted to the tool, the authors have investigated, in detail, the problem for annealed NE9445 steel under both conventional turning and orthogonal cutting conditions. The study has shown that the quantity of frictional heat conducted to the tool varies approximately 8 per cent for conventional turning over the range of 100 to 600 sfpm, Fig. 20 of this closure. The variation in contact area over the same speed range was about 40 per cent. It is the concentration of heat on the reduced contact area which is held to be primarily responsible for the higher interface temperatures at increased cutting speeds. The same trend was noted for orthogonal cutting—the quantity of frictional heat varied about 3 per cent and the contact area about 25 per cent over a range of 140 to 500 fpm. Similar effects have been observed with changes in feed. The authors agree that the observation should not be held to be universally applicable. Changes in the tool work pair (e.g., tungsten carbide on steel) tool angles, and other cutting variables may introduce modifying conditions.

However, in metal-cutting operations employing a suitable grade of carbide tool on steels it is believed that the contact area is of prime importance in interface temperatures.

It should be pointed out that reference to "depth of cut" by Professors Loewen and Shaw refers to "feed" as used by the authors. The factor is the amount the tool advances along the work per revolution and in the authors' opinion is best designated as feed even though depth of cut may appear more fitting in orthogonal cutting (the exception in most cutting operations).

[20] Bibliography (2).

Qualitatively, a decrease in β with higher cutting speeds and heavier feeds has long been known. Many men in the shop are aware of the fact that higher cutting speeds result in a cooler workpiece (unless the tool is dulled). However, no reliable quantitative data for single-point turning are yet available. Dr. Schmidt's and Mr. Roubik's report on the amount of heat conducted back to the workpiece in drilling magnesium bars was certainly a very welcome addition. More experimental work still needs to be done to ascertain accurately and completely the heat balance in a metal-cutting process.

An approximate mathematical relationship between β and the thermal number was derived by one of the authors five years ago.[21] It agrees with Dr. Schmidt's and Mr. Turkovich's viewpoint at least in a qualitative manner. However, the hyperbolic type of relationship, $\beta R_t = N$ (a constant), as suggested by Dr. Schmidt and Mr. Turkovich, has been found to be valid only within a relatively narrow range of speeds and feeds. For the case cited, extrapolation from a cutting speed of 175 sfpm to 600 sfpm by this assumed relationship is questionable.

[21] Bibliography (9).

AN ASME PAPER

Its Preparation, Submission and Publication, and Presentation

To a large degree the papers prepared and presented under the ASME sponsorship are evidence by which its professional standing and leadership are judged. It follows, therefore, that to qualify for ASME sponsorship, a paper must not only present suitable subject matter, but it must be well written and conform to recognized standards of good English and literary style.

The pamphlet on "AN ASME PAPER" is designed to aid authors in meeting these requirements and to acquaint them with rules of the Society relating to the preparation and submission of manuscripts and accompanying illustrations. It also includes suggestions for the presentation of papers before Society meetings.

CONTENTS

PREPARATION OF A PAPER—

General Information—Style, Preferred Spelling, Length Limitation, Approvals and Clearances.

Contents of the Paper—Title, Author's Name, Abstract, Body of Paper, Appendixes, Acknowledgments, Bibliographies, Tables, Captions, Photographs, Other Illustrations.

Writing the Paper—Outline Tabulations, Tables, Graphs, Charts for Computation, Drawings, Mathematics, Accuracy, Headings and Numbering, Lantern Slides, Motion Pictures, Typing, Number of Copies.

SUBMISSION AND PUBLICATION OF A PAPER—

Intention to Submit Paper Required in Advance, Meeting Dates, Due Dates for Manuscript, Discussers, Review and Acceptance, Proofs, Advance Copies and Reprints, Discussion and Closure, Publication by Others.

PRESENTATION OF A PAPER—

Time Limit, Addressing Your Audience, Public Address Systems, Use of Slides.

REFERENCES—

References on Writing and Speaking, Engineering Standards.

Price 40¢. No discount allowed. ***A remittance must accompany all orders for $5.00 or less. U. S. Postage Stamps are acceptable.***

THE AMERICAN SOCIETY OF MECHANICAL ENGINEERS

29 West 39th Street, New York 18, N. Y.